NASA CR-174923

LIGHTWEIGHT TWO-STROKE CYCLE AIRCRAFT DIESEL ENGINE TECHNOLOGY ENABLEMENT PROGRAM

VOLUME III
FINAL REPORT

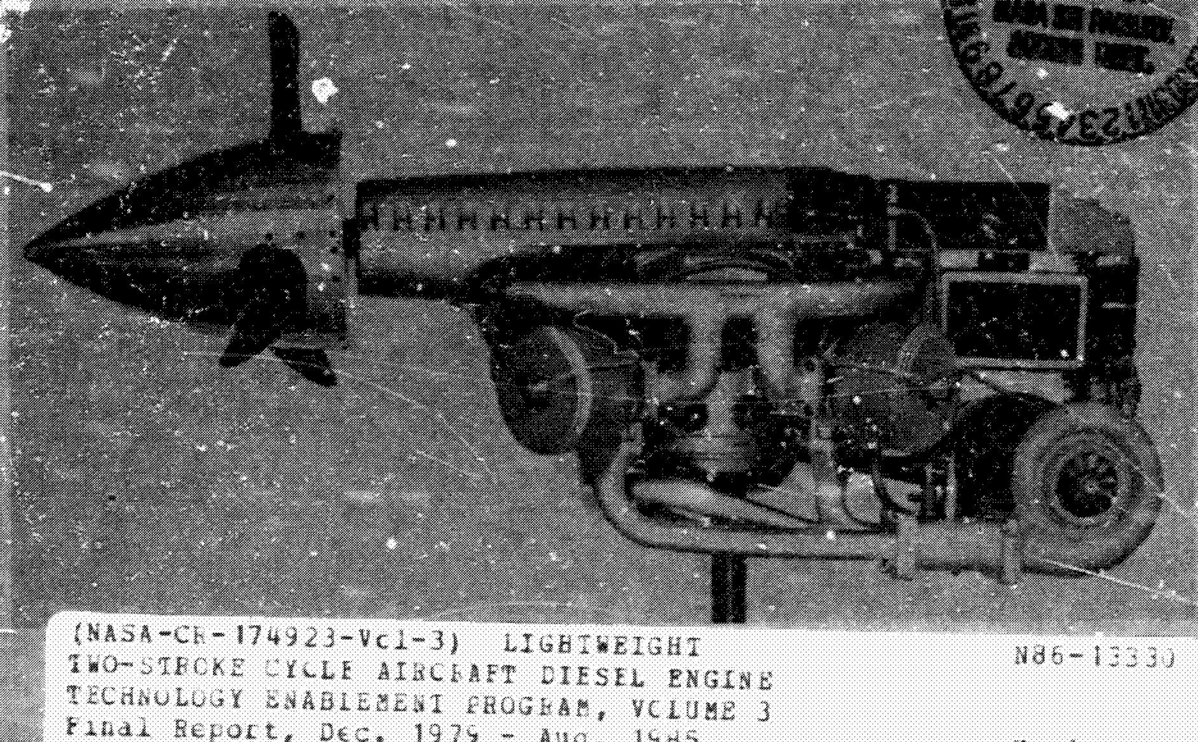

TELEDYNE CONTINENTAL MOTORS
General Products Division

P.D. FREEN, S.G. BERENYI, A.P. BROUWERS
M.E. MOYNIHAN

PREPARED FOR
NATIONAL AERONAUTICS AND SPACE ADMINISTRATION
NASA LEWIS RESEARCH CENTER

CONTRACT NAS3-22218

NASA CR-174923

VOLUME III

LIGHTWEIGHT TWO-STROKE CYCLE AIRCRAFT DIESEL ENGINE TECHNOLOGY ENABLEMENT PROGRAM

FINAL REPORT

TELEDYNE CONTINENTAL MOTORS
General Products Division

P.D. FREEN, S.G. BERENYI, A.P. BROUWERS
M.E. MOYNIHAN

PREPARED FOR

NATIONAL AERONAUTICS AND SPACE ADMINISTRATION
NASA LEWIS RESEARCH CENTER

CONTRACT NAS3-22218

NASA
National Aeronautics
and Space Administration

Scientific and Technical
Information Office

ORIGINAL PAGE IS
OF POOR QUALITY

1. Report No. NASA CR-174923	2. Government Accession No.	3. Recipient's Catalog No.
4. Title and Subtitle LIGHTWEIGHT TWO-STROKE CYCLE AIRCRAFT DIESEL ENGINE TECHNOLOGY ENABLEMENT PROGRAM		5. Report Date August, 1985
		6. Performing Organization Code 505-40-62
7. Author(s) P. D. FREEN, S. G. BERENYI, and A. P. BROUWERS, M. E. MOYNIHAN		8. Performing Organization Report No.
		10. Work Unit No.
9. Performing Organization Name and Address TELEDYNE CONTINENTAL MOTORS 76 GETTY STREET MUSKEGON, MICHIGAN 49442		11. Contract or Grant No. NAS3-22218
		13. Type of Report and Period Covered Contract Report 12/79 - 8/85
12. Sponsoring Agency Name and Address NATIONAL AERONAUTICS AND SPACE ADMINISTRATION WASHINGTON D.C. 20546		14. Sponsoring Agency Code NASA LEWIS RESEACH CENTER

15. Supplementary Notes

FINAL REPORT. PROJECT MANAGER, JOHN J. MCFADDEN, SMALL ENGINE PROPULSION BRANCH, NASA-LEWIS RESEARCH CENTER, CLEVELAND, OHIO

16. Abstract

An experimental Single Cylinder Test Engine Program was conducted to confirm the analytically projected performance of a two-stroke cycle diesel engine for aircraft applications. The test engine delivered 78kW indicated power from 1007cc displacement, operating at 3500 RPM on Schnuerle loop scavenged two-stroke cycle. Testing confirmed the ability of a proposed 4-cylinder version of such an engine to reach the target power at altitude, in a highly turbocharged configuration. The experimental program defined all necessary parameters to permit a detailed design of a multicylinder engine for eventual flight applications; including injection system requirement, turbocharging, heat rejection, breathing, scavenging, and structural requirements.

The multicylinder engine concept is configured to operate with an augmented turbocharger, but with no primary scavenge blower. The test program was oriented to provide a balanced turbocharger compressor to turbine power balance without an auxiliary scavenging system. Engine cylinder heat rejection to the ambient air has been significantly reduced and the minimum overall turbocharger efficiency required is within the range of commercially available turbochargers.

Analytical studies and finite element modeling was made of insulated configurations of the engine - including both ceramic and metallic versions. A second generation test engine was designed based on current test results.

17. Key Words (Suggested by Author(s)) Diesel Aircraft Engine; Advanced Engines; Adiabatic Diesel Engine; Diesel with independent turbocharger loop; Two-Stroke Cycle Aircraft Diesel; Radial Diesel Engine; High Pressure Fuel Injection	18. Distribution Statement UNCLASSIFIED - UNLIMITED STAR CATEGORY 07 AND GENERAL RELEASE

19. Security Classif. (of this report) UNCLASSIFIED	20. Security Classif. (of this page) UNCLASSIFIED	21. No. of pages	22. Price*

*For sale by the National Technical Information Service, Springfield, Virginia 22161

VOLUME III

This final report is subdivided into three specific volumes.

Volume I contains the following material:

- Lists of Figures, Tables, and Appendicies; and Metric System Conversion Table.
- Section 1.0 Summary
- Section 2.0 Introduction
- Section 3.0 Engine Design and Cycle Analysis

Volume II of the report covers:

- Lists of Figures, Tables, and Appendicies; and Metric System Conversion Table.
- Section 4.0 Development Testing
- Section 5.0 Multicylinder Performance Projections
- Section 6.0 Conclusions
- Section 7.0 Recommendations
- Section 8.0 References

Volume III of the report covers:

- Lists of Figures, Tables, and Appendicies; and Metric System Conversion Table.
- Section 9.0 Appendicies

TABLE OF CONTENTS

PAGE NUMBER

VOLUME I (CONTINUED)

VOLUME II

PAGE NUMBER

VOLUME II (CONTINUED)

VOLUME III

LIST OF FIGURES

LIST OF FIGURES (2)

LIST OF FIGURES (3)

LIST OF FIGURES (4)

LIST OF FIGURES (5)

LIST OF FIGURES (6)

PAGE NUMBER

LIST OF FIGURES (7)

LIST OF FIGURES (8)

LIST OF TABLES

LIST OF APPENDICES

Metric Conversion Factors

FROM:	MULTIPLY BY:	TO:	FROM:	MULTIPLY BY:	TO:
km	0.6214	mi	bar	100	kPa
km	3281	ft	bar	1.01972	kg/cm^2
m	3.281	ft	bar	14.50377	psi
m	39.37	in	MPa	1000	kPa
dm	3.937	in	MPa	10.1972	kg/cm^2
mm	0.03937	in	MPa	145.0377	psi
m^3	35.31	ft^3	kPa	0.14504	psi
m^3	61,023	in^3	kg/cm^2	9.812	N/cm^2
m^3	264.2	gallons	kg/cm^2	14.223	psi
ℓ	0.0353	ft^3	N-m	0.10197	kgm
ℓ	61.02	in^3	N-m	0.73759	ft-lb
ℓ	0.264	g	kgm	7.2333	ft-lb
m^2	10.76	ft^2	m^3/kW	26.331	ft^3/HP
metric ton	2.205	lb	m^3/kg	16.0165	ft^3/lb
kg	2.2046	lb	kW/ℓ	0.02198	HP/in^3
MN	224,810	lb	kg/kW	1.644	lb/HP
kN	224.81	lb	kg/ℓ	0.03613	lb/in^3
N	0.102	kg	kcal	3.9683	BTU
N	0.22481	lb	kcal/kg	1.8	BTU/lb
°K	1.8	°R	kcal/kg-°C	1	BTU/lb-°F
°C	1.8°C + 32	°F	g/kWh	0.00164	lb/HP-hr
kW	1.341	HP			

A P P E N D I X I

ENGINE CYCLE SIMULATION AND DETAILED HEAT TRANSFER ANALYSIS OF THE SINGLE CYLINDER TEST ENGINE WITH CORRELATION TO TEST MEASUREMENTS

Iapco
ANALYSIS & DESIGN APPLICATION CO., LTD

ENGINE CYCLE SIMULATION AND DETAILED HEAT TRANSFER ANALYSIS OF THE SINGLE CYLINDER TEST ENGINE WITH CORRELATION TO TEST MEASUREMENTS

Prepared for:

Teledyne Continental Motors
General Products Division

Prepared by:

Analysis & Design Application Company, Ltd.

Prepared by: David J. Purnell
David J. Purnell

Approved by: Peter S. MacDonald
Peter S. MacDonald

TABLE OF CONTENTS

1.0 INTRODUCTION

This report documents the engine cycle simulation and detailed thermal analysis for two operating points of the Single Cylinder Test Engine. Both the cycle simulation code and the detailed heat transfer model are correlated to test measurements. Basically, the analytical models are calibrated using the test data for one operating point. The input parameters are then changed to correspond to the second operating point, and the new analytical results are then compared to the test data for this second operating point. The two operating points will be referred to as "Run 659" and "Run 668", respectively.

The engine is an air-cooled, direct injection diesel operating on a loop-scavenged, two-stroke cycle. The basic engine geometry is summarized in Table 1. Figure 1 shows the layout of the cylinder, head insert and outer manifold ring. The intake air is piped to two openings in the manifold ring, each of which feeds three of the six intake ports. A third opening in the manifold ring receives the gases from the three exhaust ports. The exhaust gases are piped to a plenum designed to create the back pressure that would be caused by an exhaust turbine. A thin shroud covers the cooling fins, so that the cooling air flow can be controlled and monitored. In order to minimize temperature differences across the diameter of the cylinder, cooling oil is circulated around the exhaust ports through a passage in the cylinder wall.

The cycle analysis is carried out using the Benson cycle simulation code developed at the University of Manchester Institute of Science and Technology (UMIST).

The detailed heat transfer analysis is carried out using an ANSYS three-dimensional finite element model.

2.0 ENGINE CYCLE SIMULATION

The Benson code consists of a flow model, a combustion model, and an associated heat transfer model. Heat is added to the cylinder in accordance with the specified fuel burned schedule. Heat transfer to the walls of the combustion chamber is represented by the Annand correlation. The flow model includes the air pipes leading from the intake plenum, the ports with measured flow coefficient values, the cylinder, and the exhaust piping extending to the exhaust plenum.

The key engine operating variables represented in the Benson code are separated into various categories of input parameters, output parameters and calibration parameters as shown by the following outline:

Geometric Inputs

- Bore, Stroke, Connecting Rod Length
- Port Widths, Port Timing
- Compression Ratio
- Intake and Exhaust Piping

Inputs from Test Data

- Engine Speed
- Supercharge Temperature and Pressure
- Fuel Flow

Fuel Calorific Value

Fuel Burned Schedule

Instantaneous Port Flow Coefficients

Heat Loss Inputs

Annand Correlation Constants

Surface Areas and Temperatures for , Piston, Cylinder

Output Parameters (for comparison to test data)

Engine Power Output

Indicated Specific Fuel Consumption (ISFC)

Air Flow

Exhaust Temperature

Cylinder Pressure

Heat Loss

Calibration Parameters

Annand Constants (adjusted to match measured heat loss)

Back Pressure (adjusted to match measured air flow)

Charge Purity

Ratio of Specific Heats for Intake Air (γ_c)

Ratio of Specific Heats for Exhaust Gases (γ_e)

The key output parameters were not found to be sensitive to small variations in charge purity or specific heat ratios. For all runs subsequent to the sensitivity study, charge purity is assigned a value of 0.8, and the specific heat ratios are assigned the values: $\gamma_c = 1.390$, and $\gamma_e = 1.290$. Because the modeling of the exhaust system differs from the actual test set up in certain respects, the back pressure is adjusted in the cycle simulation in order to match the measured air flow. As shown in Tables 6 and 7, a reasonably good correlation with the test data was obtained for both air flow and the pressure ratio across the engine (intake/exhaust).

In the Benson code, the instantaneous rate of heat transfer from the gas to the surface of the combustion chamber is represented by the Annand correlation:

$$q = a \frac{k}{D} (Re)^b (T-T_w) + c(T^4-T_w{}^4)$$

where,

q = heat transfer rate, KW

k = thermal conductivity of fluid, KW/M-°K

D = cylinder bore, M

Re = Reynolds Number = $\rho VD/\mu$

ρ = density of fluid, KGM/M^3

V = mean piston speed, M/SEC

μ = dynamic viscosity of fluid, KGM/M-SEC

T = gas temperature, remote from wall, °K

T_w = surface temperature, °K

a,b = Annand coefficients for convective term

c = Annand coefficient for radiative term, $KW/M^2 - °K^4$

The Annand coefficients a and b are constant for the entire cycle. The radiative coefficient, c, is constant for the combustion and expansion stages, and is set equal to zero for the compression stroke.

Based on previous studies on two-stroke engines, the initial values for the Annand coefficients were:

a = 0.400

b = 0.700

c = 0.327E-10, $KW/M^2 - °K^4$

Only Annand coefficient "a" was treated as a calibration parameter in matching the measured heat loss. The measured heat loss for Run 659 was matched using a revised value of 0.480 for Annand "a". This value was left unchanged for Run 668.

The heat loss calculated by the Benson code is partially a function of the combustion chamber surface temperature distribution. Area-averaged constant temperatures are input for the head, the piston cap, and several zones on the cylinder bore. The program checks which cylinder zones are exposed to the gas on a crank-angle-by-crank-angle basis. The surface temperatures must be guessed for the initial few runs. The Annand contstant "a" is adjusted until the calculated heat loss matches the measured heat loss. The results of the cycle simulation are then used to derive the cycle-average boundary conditions for the detailed ANSYS finite element heat transfer model. The finite element model is then run in order to determine the detailed temperature distribution, which is then compared to the measured data. If necessary, some of the heat sink boundary conditions, such as the cooling air heat transfer coefficient, are adjusted to achieve better correlation. The heat loss predicted by the ANSYS model is then compared to the measured value. The area-average surface temperatures are also compared to those used in the latest cycle simulation. If the values do not compare satisfactorily, the surface temperatures used in the Benson code cycle analysis are updated, the Annand constant "a" is readjusted, and the entire process is repeated until satisfactory agreement of both models and test data is achieved. In this process, the heat losses to specific heat sinks predicted by the ANSYS model are also compared to test data.

The key output parameters of the cycle simulation are compared to measured data for the calibration run (Run 659) in Table 6. The correlation is judged to be satisfactory for all parameters except peak cylinder pressure, which is found to be over-predicted by 27.4 percent. (A somewhat better correlation is found on Run 668, where the peak pressure is over-predicted by 9.1 percent.) Assuming the measured value is correct, the calculated pressure may reflect an over-prediction of trapped mass by the Benson code. The over-prediction of trapped mass could be caused by inaccuracies in modeling the exhaust system, including the effect of delayed port closing due to the top ring land clearance. Another possible cause would be that the fuel burned schedule (also experimental) overpredicts the burn rate near TDC.

The key Benson code output parameters are compared to measured data for Run 668 in Table 7. The Run 668 data are used to test the model calibration performed for Run 659. Therefore, only one iteration is run with no adjustment of Annand constants to match measured heat loss. As shown in Table 7, the Benson code predicts a slight increase in heat loss and exhaust temperature, whereas the measured data show a larger increase in exhaust temperature and a very large reduction in heat loss. Hence, based on the test data, the Annand constants have not been successfully correlated. However, the reduction in experimental heat loss is suspect for the following reasons: (1) a drastic drop in the absolute rate of heat loss as the result of changing to an operating point with higher engine speed, fuel flow and power output is not consistent with general operating experience; (2) a large drop in the heat deposited in the combustion chamber should lead to a drop in measured heat loss through the cooling fins; however, there is essentially no measured change in the rate of heat removal by the cooling air.

As previously discussed, the modeling of the exhaust system differs from the actual test setup in certain respects. A number of different time-average "exhaust temperatures" are found as a function of location in the exhaust piping portion of the Benson model. Therefore, it was decided that the calculated exhaust temperatures as presented in Tables 6 and 7 should be derived from an overall energy balance on the Benson model. The details of the energy balance calculation are given in the Appendix.

3.0 DETAILED THERMAL ANALYSIS

3.1 Description of Thermal Model

The detailed finite element thermal model is depicted in Figures 1 through 5. The cylinder, head insert and manifold ring are modeled using three-dimensional solid elements (ANSYS STIF70). The cooling fins are not directly modeled, but are represented by effective heat transfer coefficients. A layer of solid aluminum at the base of the fins is included in the model, as indicated in Figure 1. As shown in Figure 5, the piston, piston cap and piston rings are represented by an axisymmetric model using two-dimensional solid elements (ANSYS STIF55). Surface contact resistances, and radiative and convective heat transfer in the enclosed spaces and narrow annuli are modeled using convection link elements (ANSYS STIF34). Convection link elements are also used to model the thermal communication between the piston and the cylinder.

3.2 Derivation of Thermal Boundary Conditions

The instantaneous gas temperatures and heat transfer coefficients produced by the cycle simulation code must be converted to equivalent steady thermal boundary conditions for purposes of the finite element analysis. The equivalent steady thermal boundary conditions are referred to as the "cycle-average temperature," and the "cycle-average heat transfer coefficient." For a surface which is at all times during the cycle exposed to the combustion gas, the cycle average values ($\bar{T},\bar{h}$) can be calculated from the instantaneous values ($T(\phi),h(\phi)$) by the following relations:

$$\bar{h} = \frac{1}{360} \int_0^{360} h(\phi)\, d\phi$$

$$\bar{T} = \frac{1}{360\bar{h}} \int_0^{360} h(\phi)\, T(\phi)\, d\phi$$

where,

ϕ = crank advance (degrees)

For elements of surface area on the cylinder bore, the above equations must be modified to account for sliding contact with the piston and/or exposure to crankcase oil on a crank-angle-by-crank-angle basis. For intervals corresponding to sliding contact with the piston, $h(\phi)$ is equated to zero, because heat input from the piston is accounted for by other means (see below). Figures 3 and 4 show the values of $\bar{h}$ and $\bar{T}$ as a function of axial location on the cylinder bore.

The heat flowing from the piston and rings to the cylinder bore is represented by the use of convection link elements. The governing equation for each convection link is:

$$q = hA\,(T_i - T_j)$$

where,

q = average rate of heat transfer from T_i to T_j

h = heat transfer coefficient

A = heat transfer surface area

T_i = temperature of node on piston where convection link originates

T_j = temperature of node on cylinder bore where convection link terminates

The heat transfer area for each convection link is computed from the following relation:

$$A = A_{TOT}(\phi_1 - \phi_2)/180$$

where,

A_{TOT} = Total heat transfer surface area associated with piston node where link originates

$(\phi_1 - \phi_2)$ = Crank angle interval during which the piston node is thermally linked to the cylinder node where the link terminates

The factor $(\phi_1-\phi_2)/180$ represents the fraction of cycle time that the piston node is linked to a particular cylinder node. The heat transfer coefficient represents the resistance to heat flow across the oil film between the piston and cylinder (excluding friction effects, which are handled separately). The numerical values used in the model are shown in Figure 5.

Since the head and the piston cap are always exposed to the gas, their forced convection cycle-average boundary conditions are computed using the relations for $\bar{T}$ and $\bar{h}$ given above, with $T(\phi)$ and $h(\phi)$ being provided by the cycle simulation code. $T(\phi)$ and $h(\phi)$ are shown in Figures 14, 15, 22 and 23. Values of $T(\phi)$ and $h(\phi)$ for the intake and exhaust ports are developed using a supplementary program which post-processes the port gas data provided by the Benson code. The port gas temperatures, mass flow rates and average velocities are shown in Figures 16 through 21, and 24 through 29. The cycle-average boundary conditions for the head insert, intake and exhaust ports, and manifold are given in Table 9.

The total heat load due to piston ring friction is shown for the two operating points in Table 9. The data represent experimental values obtained by motoring the engine. The friction heat load is represented in the model by specified heat generation rates at the nodes on the surface of the piston rings and cylinder bore. In loading the model, the friction heat is apportioned in the following manner:

Cylinder bore	50%
Oil ring	25%
Top ring	12 1/2%
Other rings	12 1/2%

The exhaust port oil cooling is represented in the model as illustrated in Figures 2A and 2C. The cooling rates, as shown in Table 9, are derived from measured data. In the final analytical runs, only 75% of the measured cooling rate was used, because the full values consistently caused an underprediction of measured temperature data near the exhaust ports. The exact reason for this lack of correlation is not known. There is a possibility that the cycle average heat transfer coefficients in the exhaust ports are too low. The heat transfer coefficients are developed using correlations for turbulent high speed flow near the leading edge of a flat plate. For portions of the cyle where the ports are partially open, the heat transfer coefficients for the lower port surfaces are developed from correlations for heat transfer in the wake region behind a flat plate.

The effective heat transfer coefficients for the circumferential cooling fins are given in Table 10. Heat dissipated from the wall area occupied by the fin is given by:

$$q = e\ h\ S\ (T_W - T_A)$$

where,

q = heat flow rate

e = fin efficiency

h = heat transfer coefficient between cooling air and fin surface

S = total fin surface area

T_W = temperature of wall area occupied by fin

T_A = temperature of cooling air

Since the fins are spaced one thickness apart, an effective heat transfer coefficient to represent the fins in the finite element model can be calculated from the following relation:

$$h_{eff} = e\ h\ S/A_W,$$

with A_W equal to twice the wall area occupied by the fin. The fin efficiency, e, is calculated by means of the following relation (Reference 1):

$$e = \frac{2}{m\ell(r_t/r_1+1)} \left\{ \frac{I_1(mr_1)K_1(mr_t)-I_1(mr_t)K_1(mr_1)}{I_0(mr_1)K_1(mr_t)+I_1(mr_t)K_0(mr_1)} \right\}$$

where,

r_t = outer fin radius

r_1 = inner fin radius

$\ell = r_t - r_1$

$m = \sqrt{2h/kt}$

k = thermal conductivity of fin material

t = fin thickness

I_n, K_n = n^{th} order modified Bessel functions of the first and second kind, respectively

A supplementary program was developed to calculate the effective heat transfer coefficients. The actual heat transfer coefficient, h, is assumed to be constant for all the fins. Its value was adjusted as part of the overall iterative process in order to match the measured heat flow rate to the cooling air. The value used in the final runs is 0.405 Btu/in²-Hr-°F.

3.3 Thermal Analysis Results

The overall heat balance for the detailed heat transfer model is given in Table 8. It is noted that the total friction heat load is dissipated by both the piston and the cylinder, with the piston taking a somewhat larger share. It is also noted that more than fifty percent of the total heat dissipated by the piston is caused by ring friction. This is due largely to the insulating effect of the air cavities under the piston cap, which suppress heat loss from the combustion gases.

The temperature results are presented in the form of color-coded temperature contour plots in Figures 6 - 8 for Run 659, and Figures 9 - 11 for Run 668. A comparison of calculated versus measured temperatures is presented in Figures 12 and 13 for Runs 659 and 668 respectively. The correlation between calculated and measured temperatures is judged to be generally satisfactory, since almost all of the calculated temperatures are within the expected range of accuracy of the thermocouple readings. The largest deviations occur for the thermocouples located near the interface between the heat insert and the cylinder. However, the steep thermal gradients in this area adversely affect the accuracy of the temperature measurements. It is noted that the three thermocouple readings nearest the manifold on the intake side of the cylinder dropped significantly for Run 668. This temperature drop is not predicted by the analytical model, and no physical explanation could be found other than experimental error.

4.0 CONCLUSION

The correlation of the cycle simulation results to experimental data is considered to be very good with respect to indicated power and airflow. The correlations for exhaust temperature and peak cyclinder pressure are not unreasonable, but do allow some room for improvement in the analytical model, assuming that the test measurements are correct. The heat loss was matched with the experimental value on Run 659 by adjusting the heat transfer correlation (Annand correlation). But the correlation did not then predict the drop in measured heat loss for Run 668. Some inaccuracy in the experimental heat loss values is suspected. Normally, the absolute rate of heat loss (not the rate of heat loss expressed as a fraction of fuel energy) is expected to go up for a higher power operating point. The experimental heat loss is subject to inaccuracy due to the fact that it is a relatively small percentage of the total energy, and its value is indirectly determined by subtracting the exhaust energy and indicated power output from the total energy. Finally, a large drop in the heat deposited in the combustion chamber should lead to a drop in measured heat loss to the cooling air; however, there is essentially no measured change in the rate of heat removed by the cooling air for Run 668.

The measured rate of heat removal by the cooling air was matched within five percent by the detailed thermal model for both Runs 659 and 668.

The correlation of calculated temperatures to experimental data is considered to be generally within the range of experimental error.

5.0 REFERENCES

1. "Handbook of Heat Transfer," McGraw-Hill Book Company, 1973.

2) Drawings and sketches of S.C.T.E. configuration provided by TELEDYNE.

3) S.C.T.E data for Run 659 and Run 668 provided by TELEDYNE.

Figure 1 Aircraft Diesel Single Cylinder Test Engine
Cylinder, Head, Manifold Ring Assembly
Three-Dimensional Heat Transfer Finite Element Model

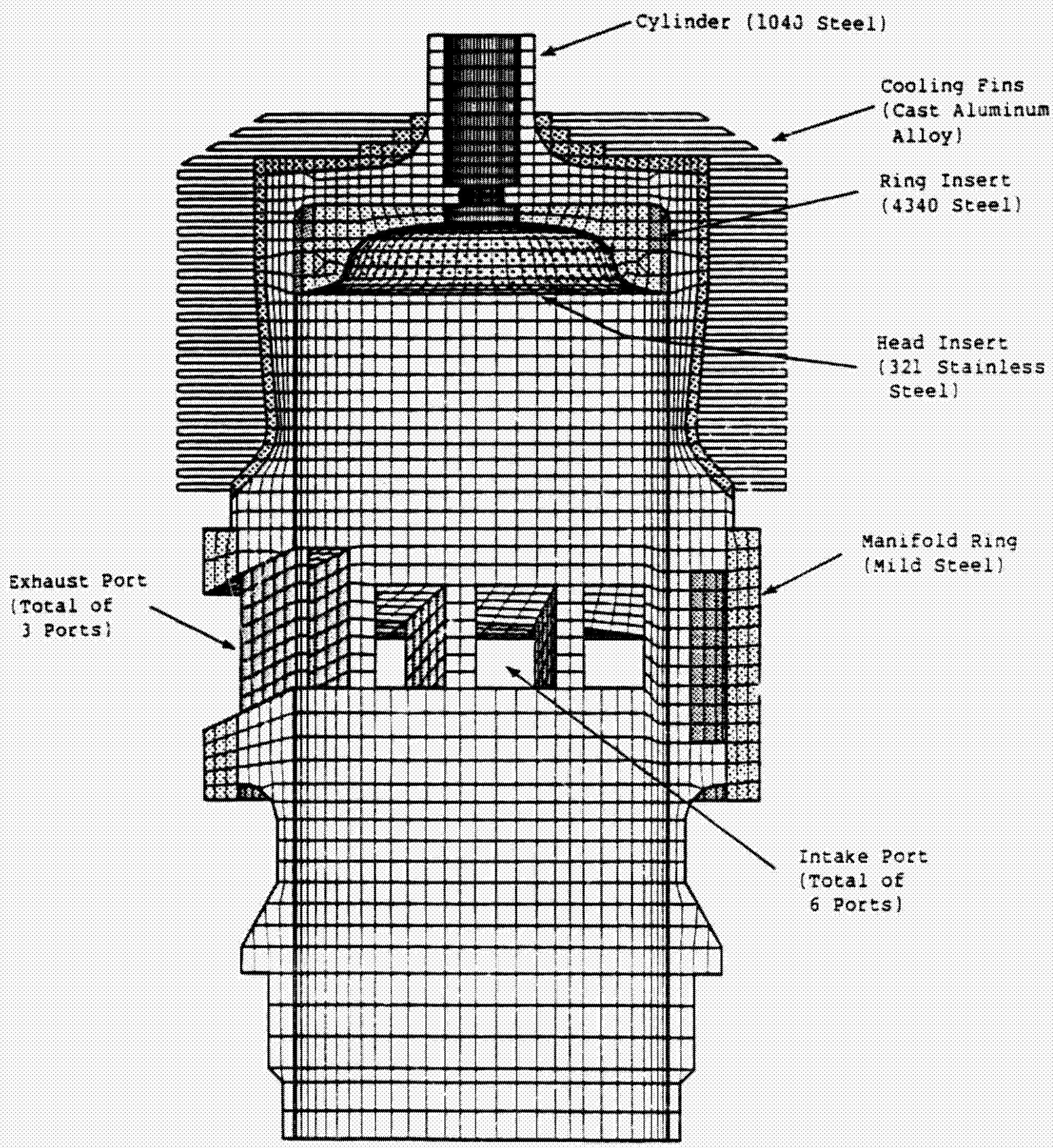

Note: The structure is shown cut on a vertical plane of symmetry. One-half of the engine is modeled. Symmetry boundary conditions are imposed on the cut plane.

ORIGINAL PAGE IS
OF POOR QUALITY

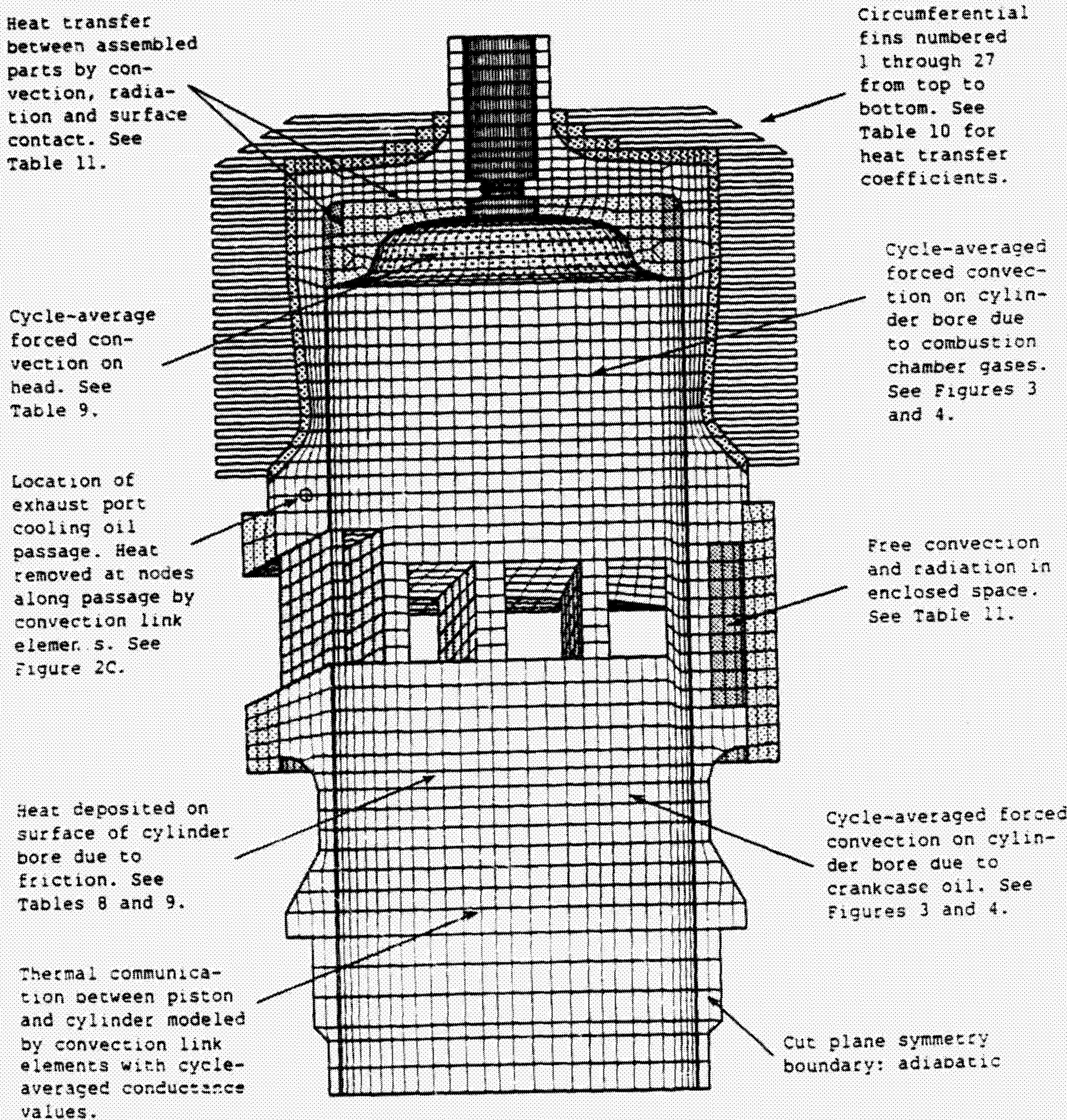

Figure 2A: SCTE Cylinder Assembly
Thermal Boundary Conditions

Figure 2B SCTE Cylinder
Fins and Manifold Removed

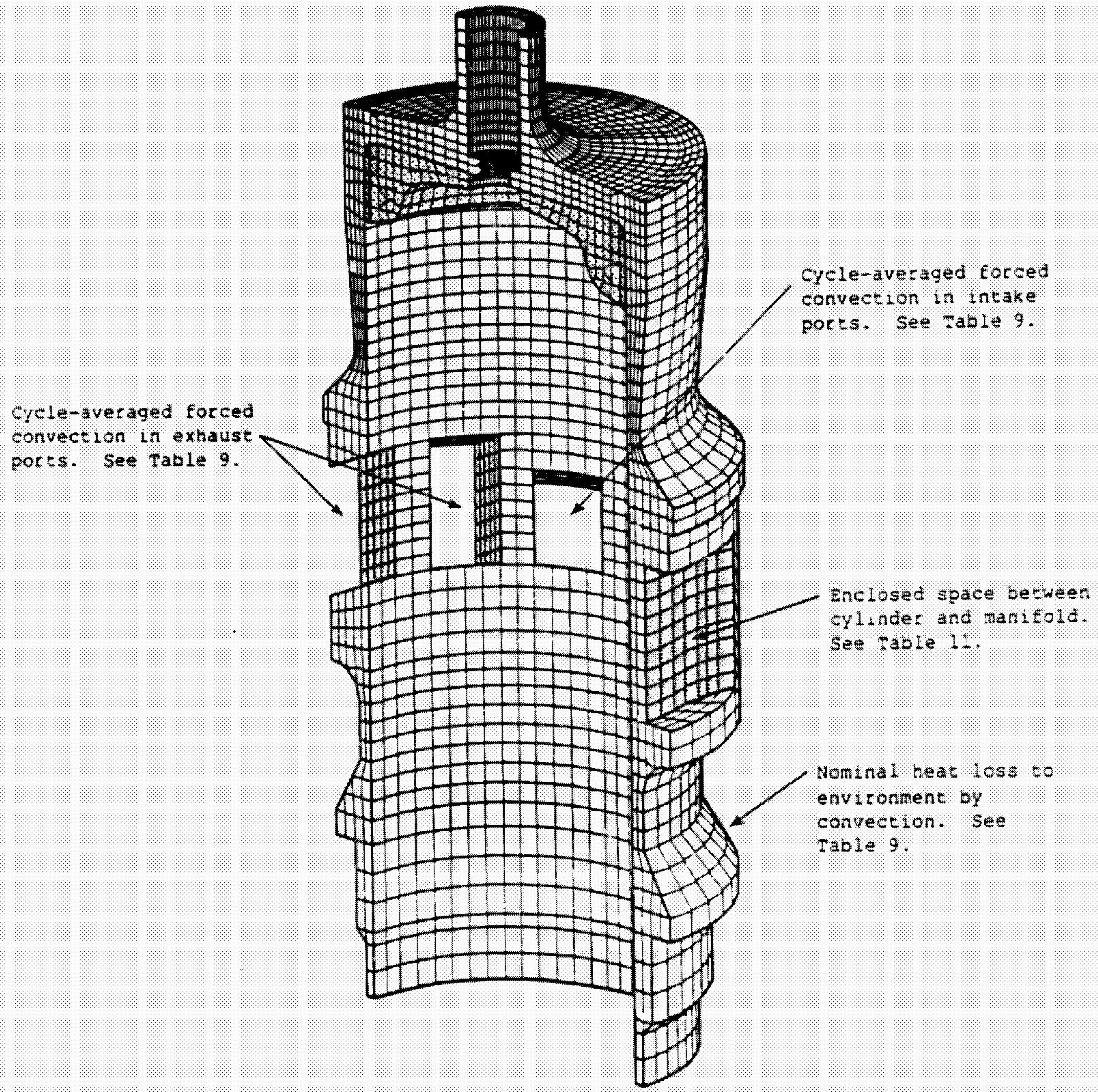

Figure 2C SCTE Cylinder
Fins and Manifold Removed
Modeling of Exhaust Port Oil Cooling

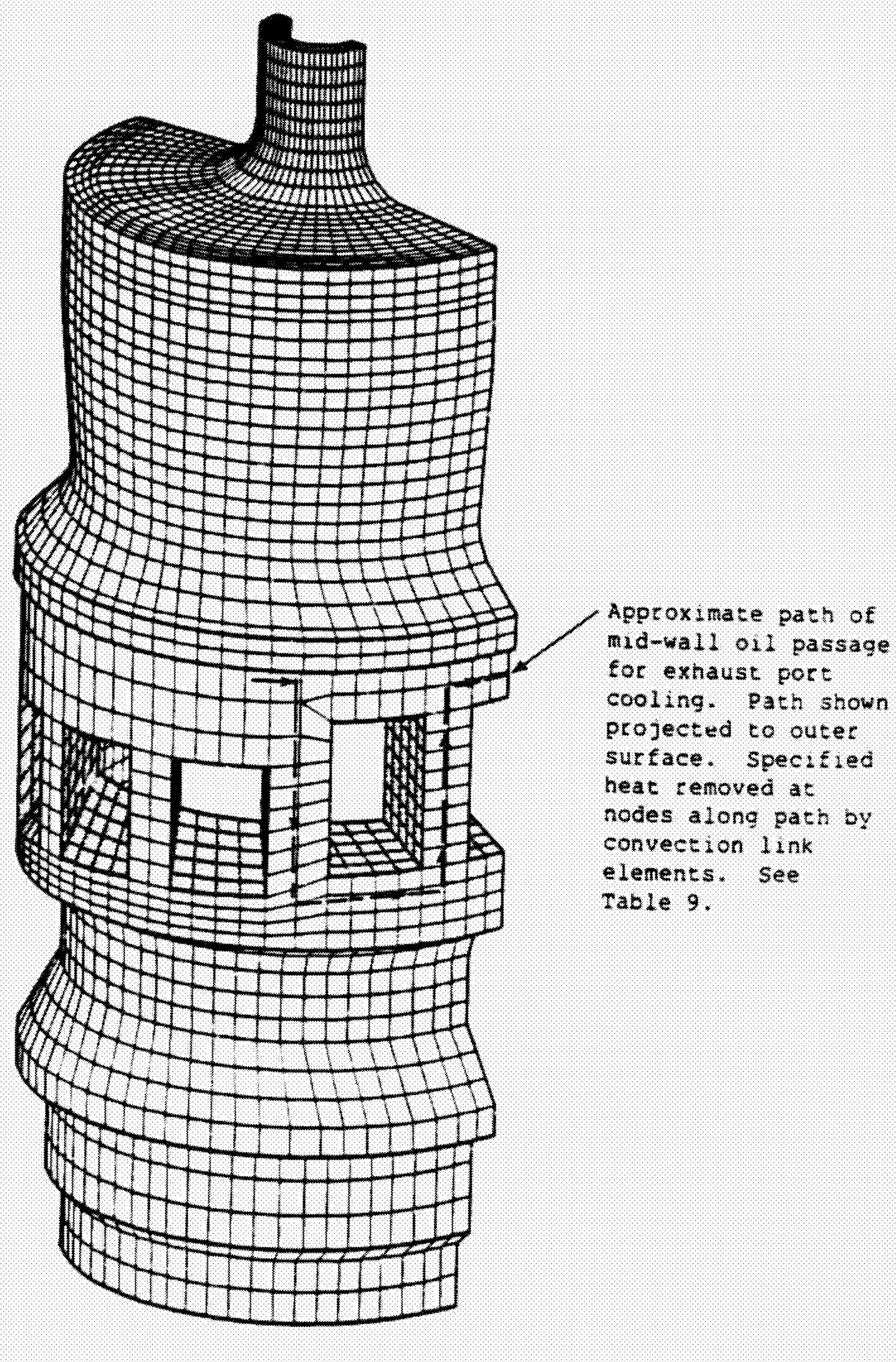

Figure 3 Cycle Averaged Forced Convection Boundary Conditions on Cylinder Bore; Run 659

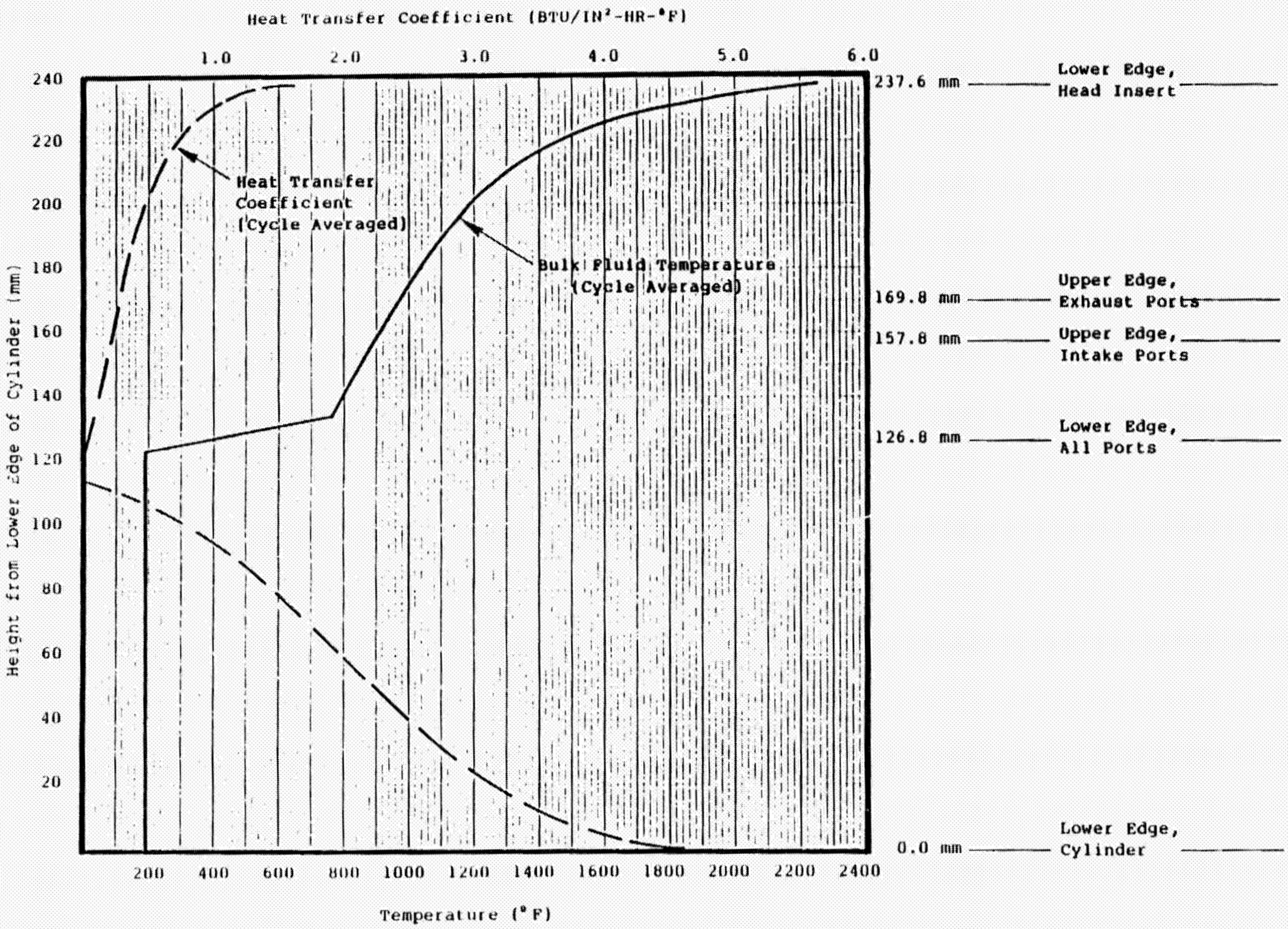

Figure 3 Cycle Averaged Forced Convection Boundary Conditions on Cylinder Bore; Run 659

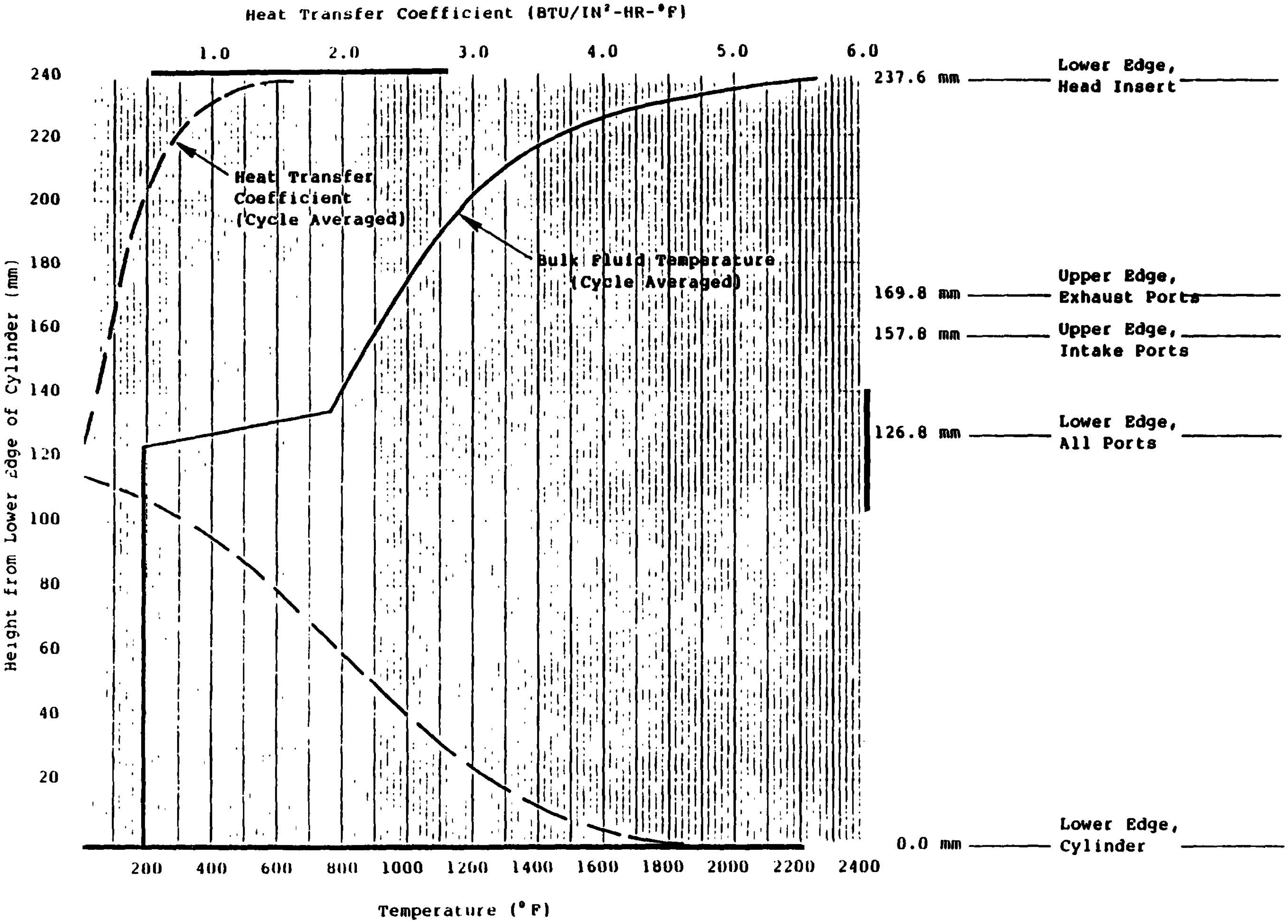

ORIGINAL PAGE IS OF POOR QUALITY

Figure 4 Cycle Averaged Forced Convection Boundary Conditions on Cylinder Bore; Run 668

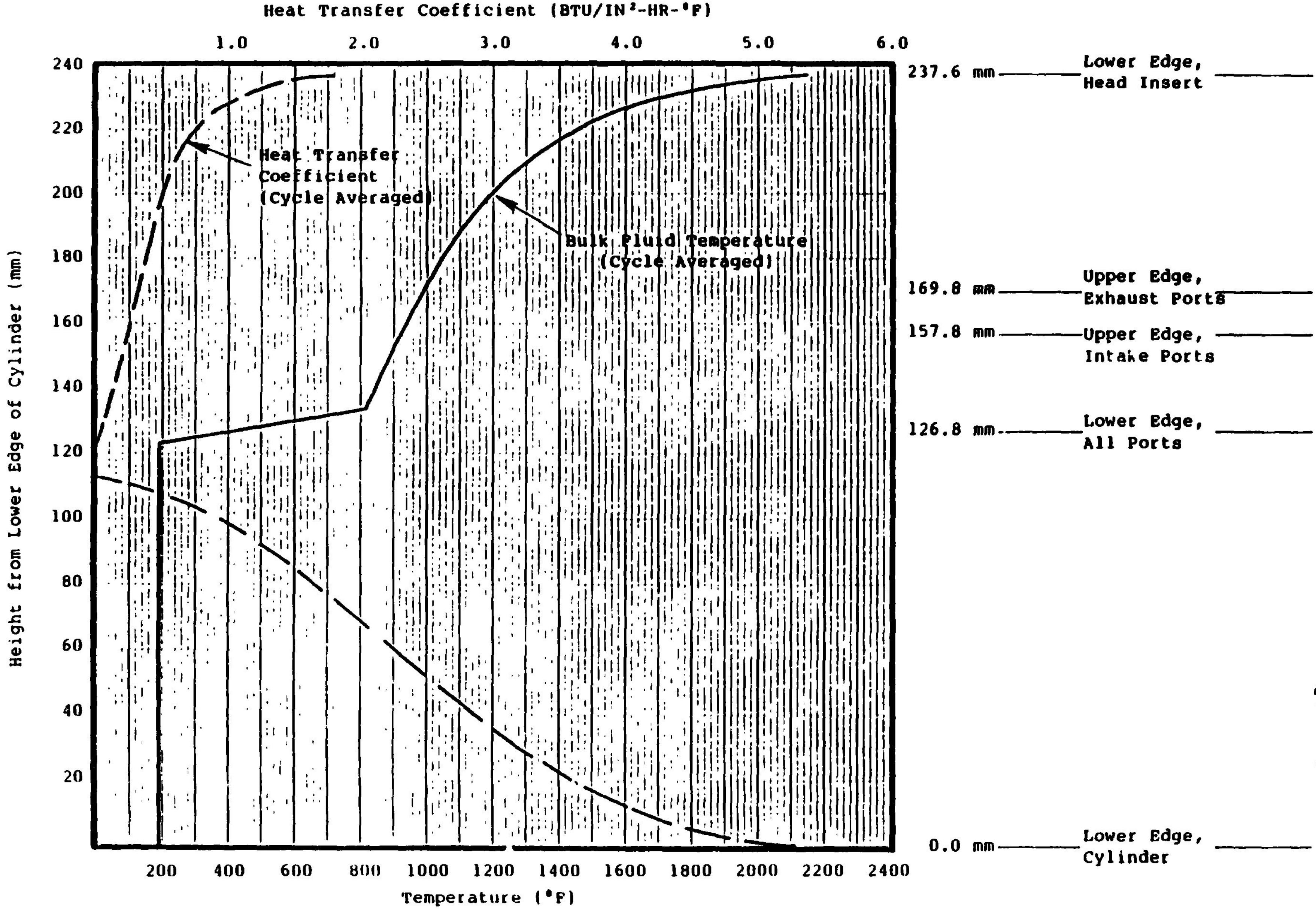

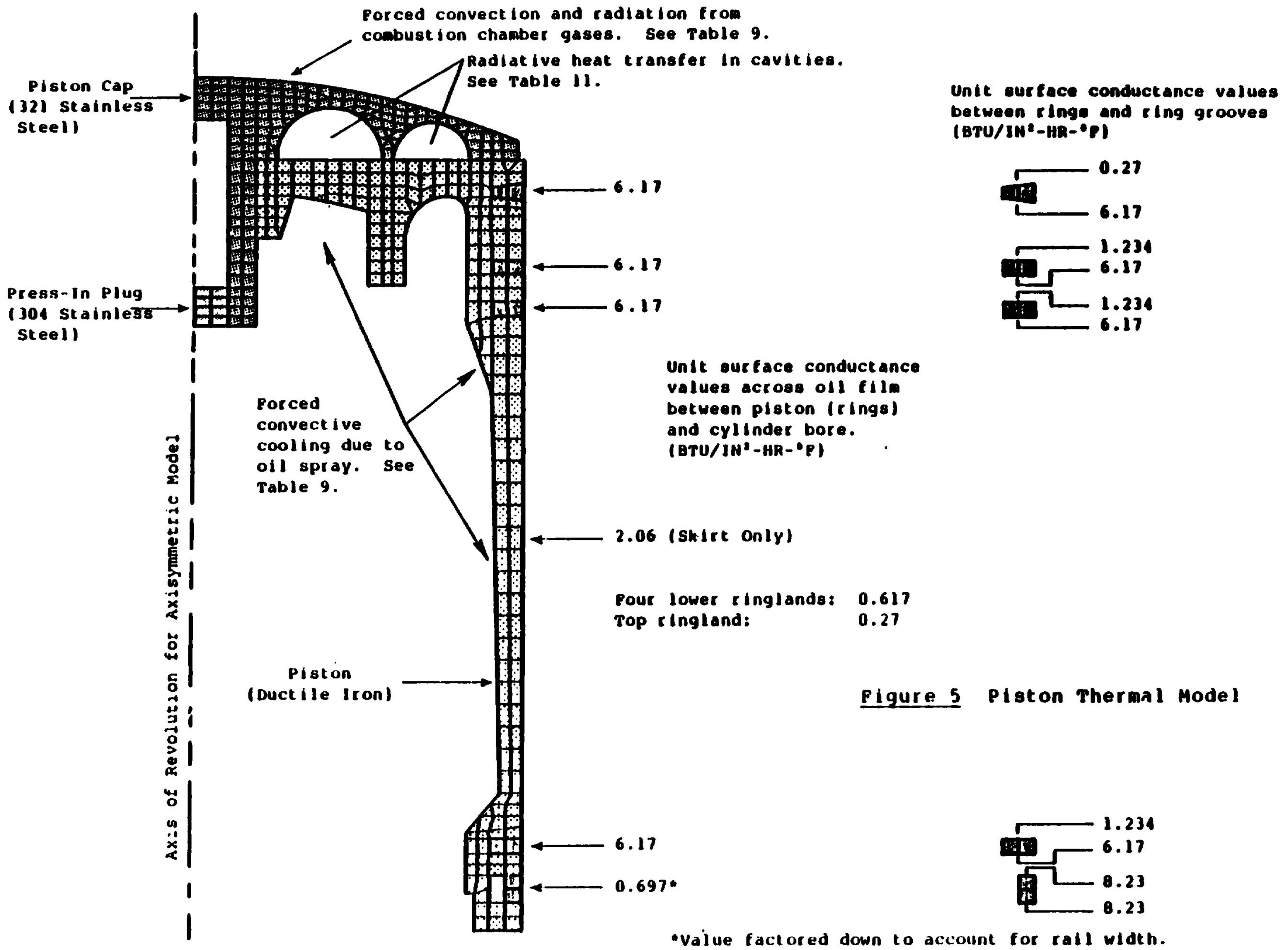

Figure 5 Piston Thermal Model

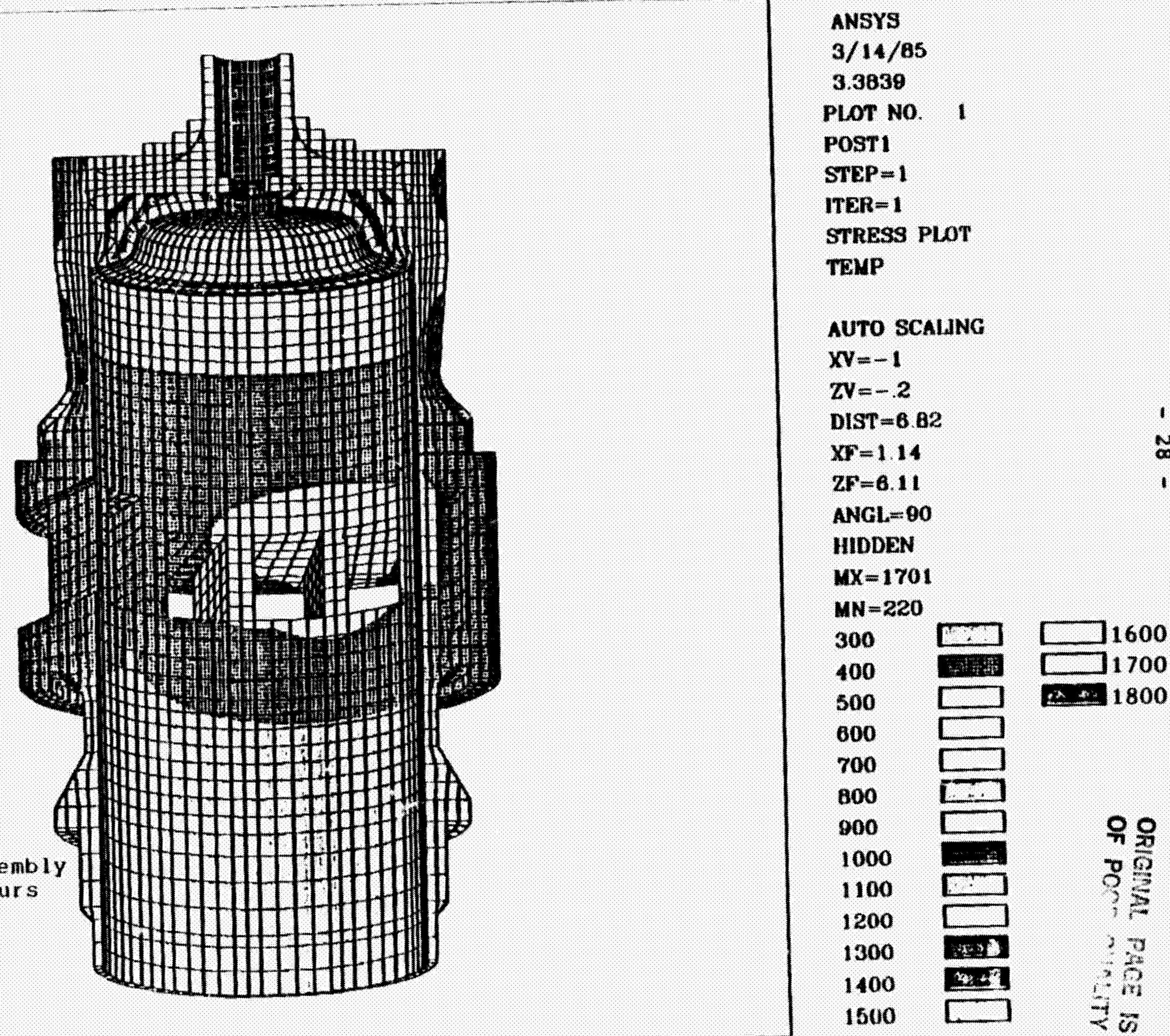

Figure 6

Cylinder, Head,
Manifold Ring Assembly
Temperature Contours
(°F)

RUN 659 G

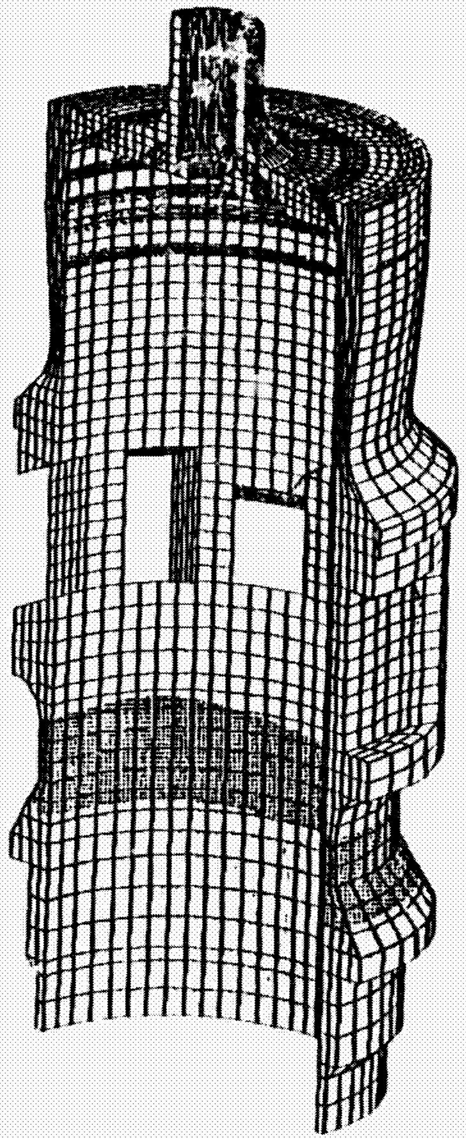

Figure 7A

Cylinder Temperature Contours (°F)

RUN 659 G

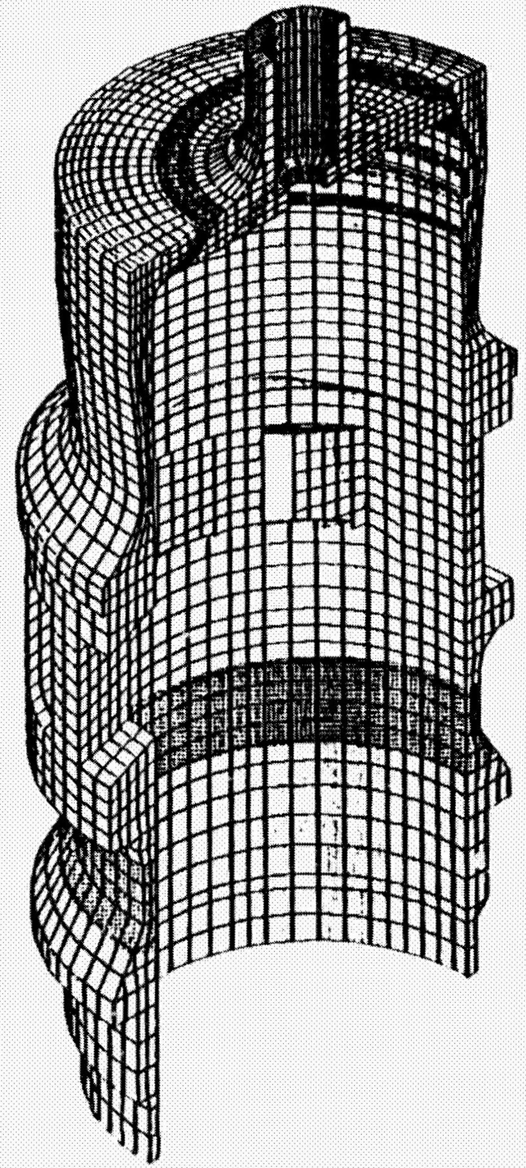

Figure 7B

Cylinder Temperature Contours (°F)

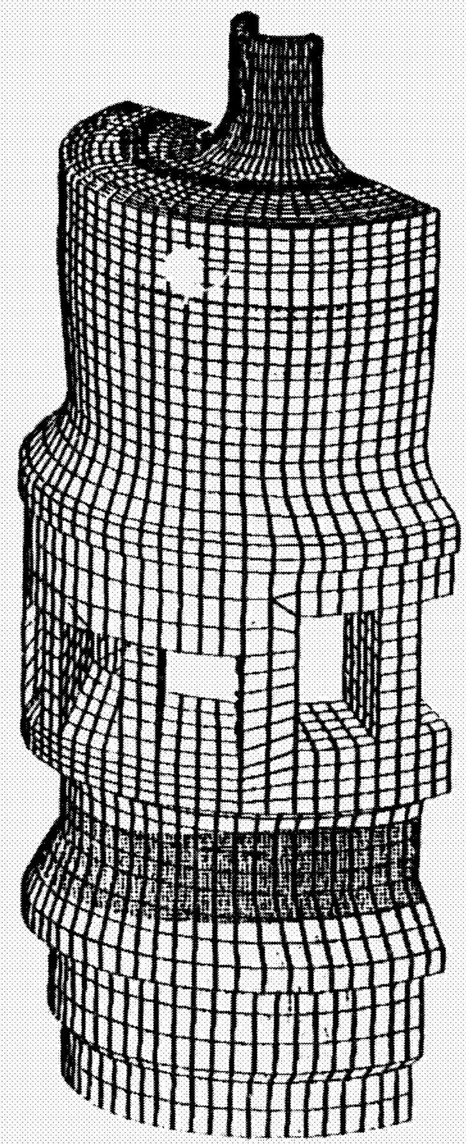

Figure 7C

Cylinder Temperature
Contours (°F)

RUN 659 G

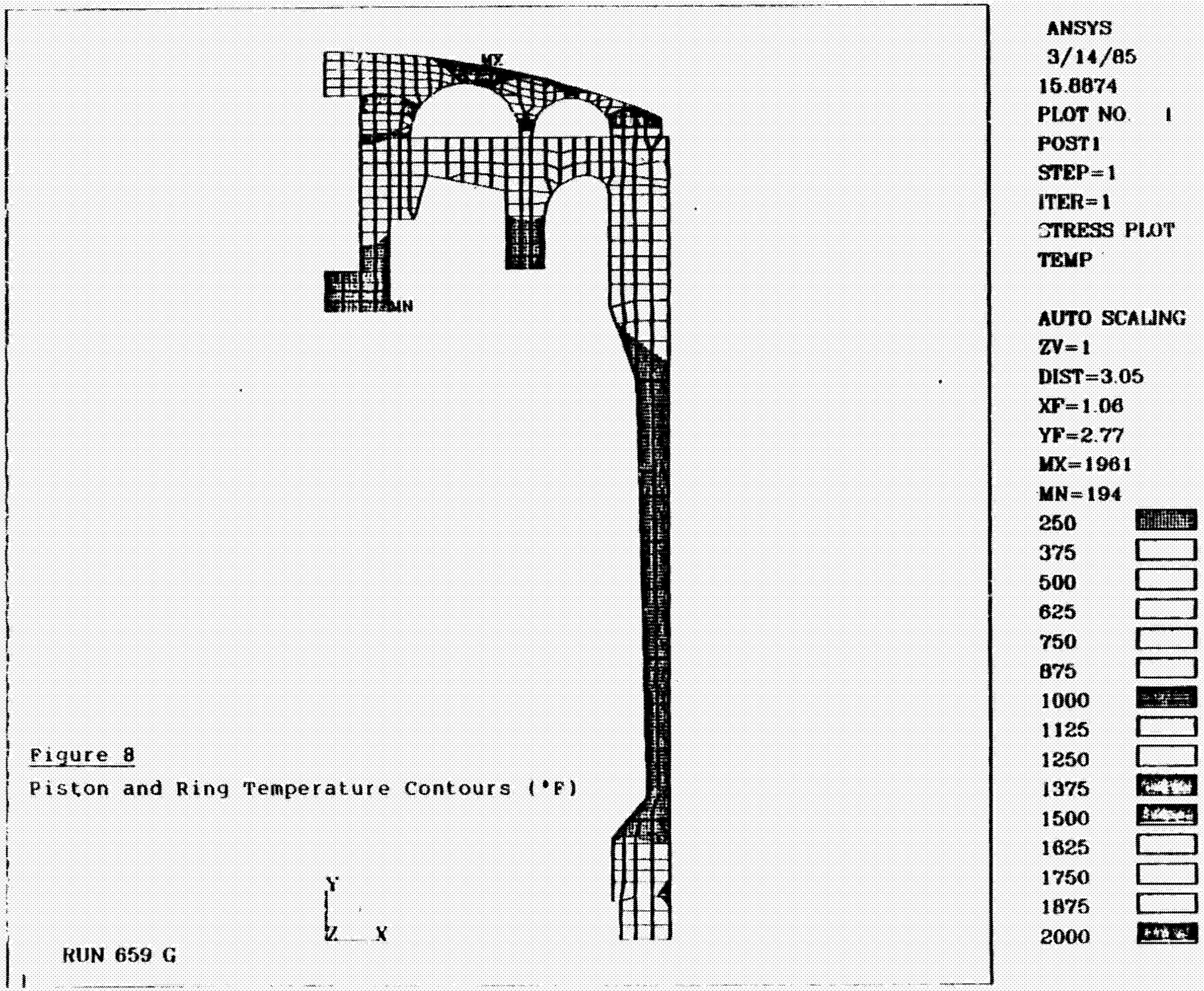

Figure 8

Piston and Ring Temperature Contours (°F)

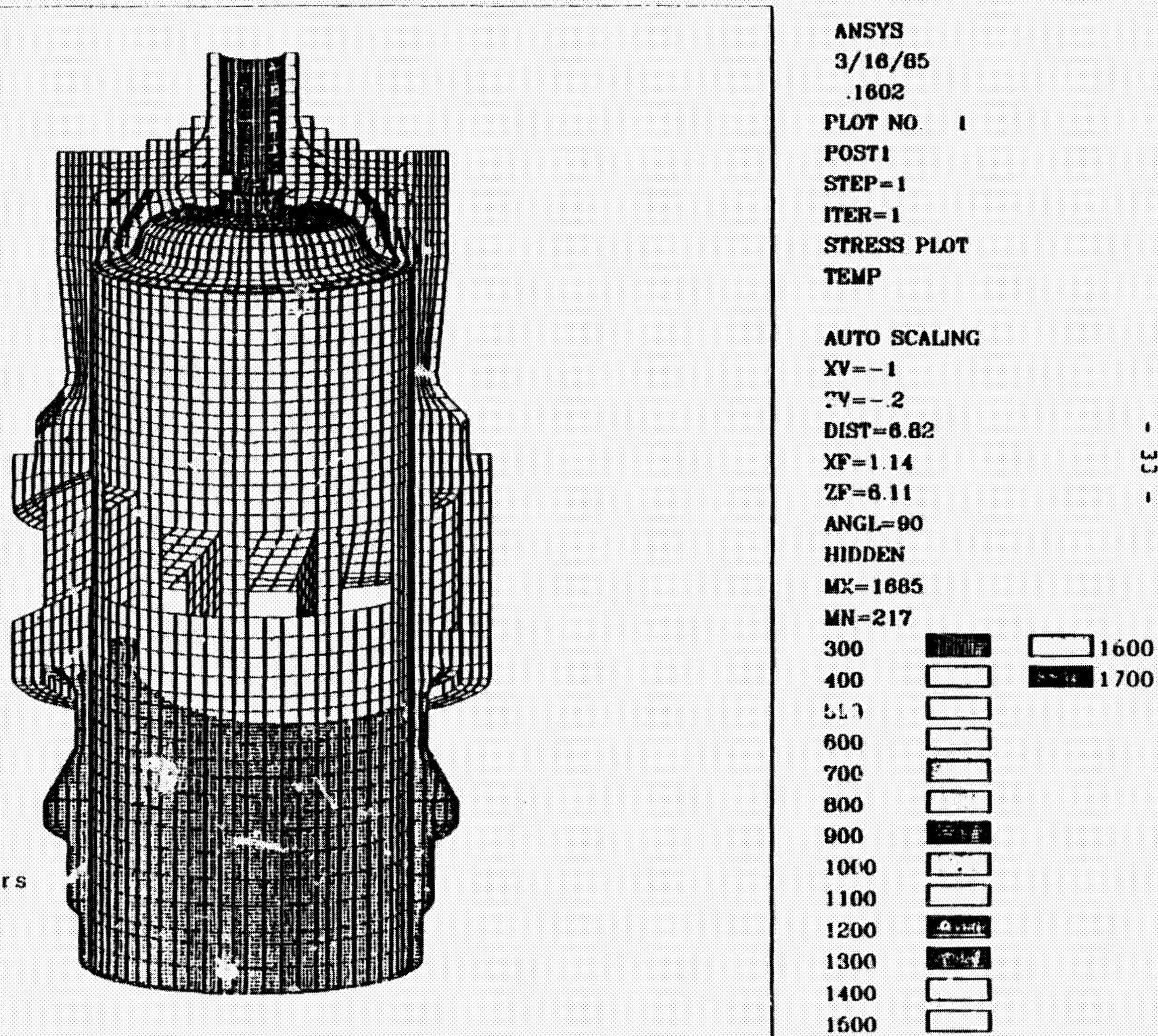

Figure 9

Cylinder, Head, Manifold Ring Assembly Temperature Contours (°F)

RUN 668 A

1

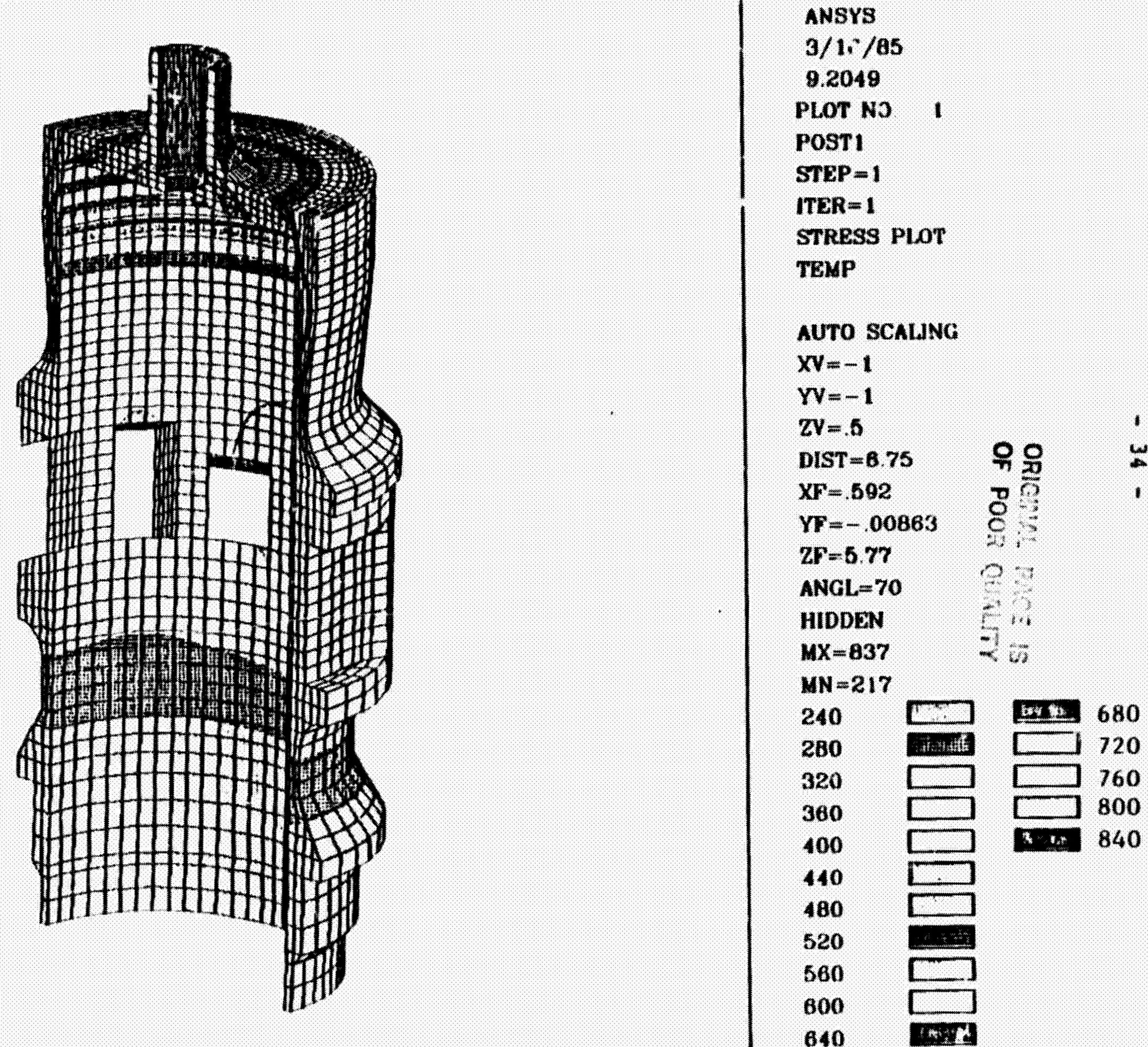

Figure 10A

Cylinder Temperature Contours (°F)

RUN 668 A

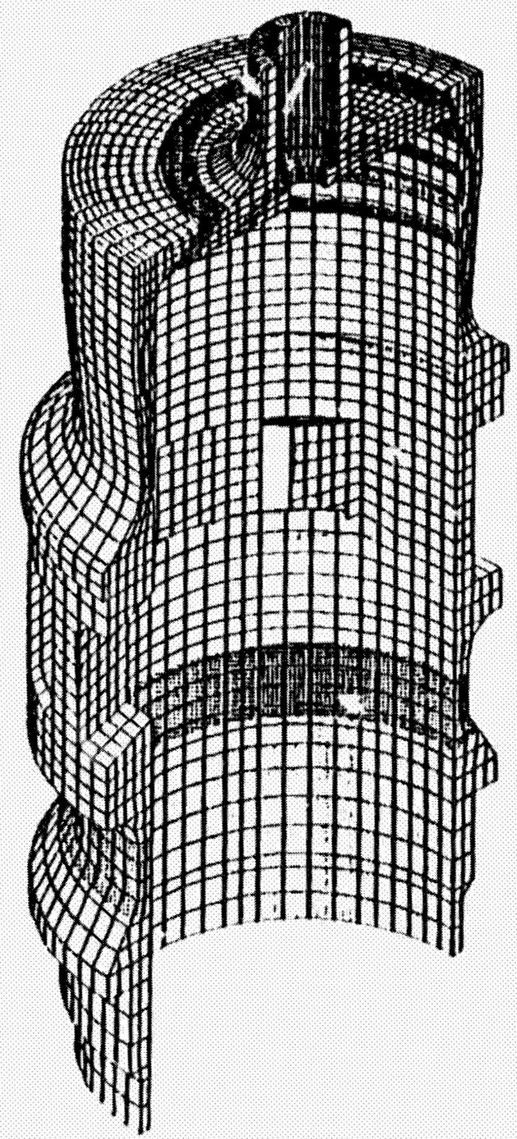

Figure 10B

Cylinder Temperature
Contours (°F)

RUN 660 A

ORIGINAL PAGE IS
OF POOR QUALITY

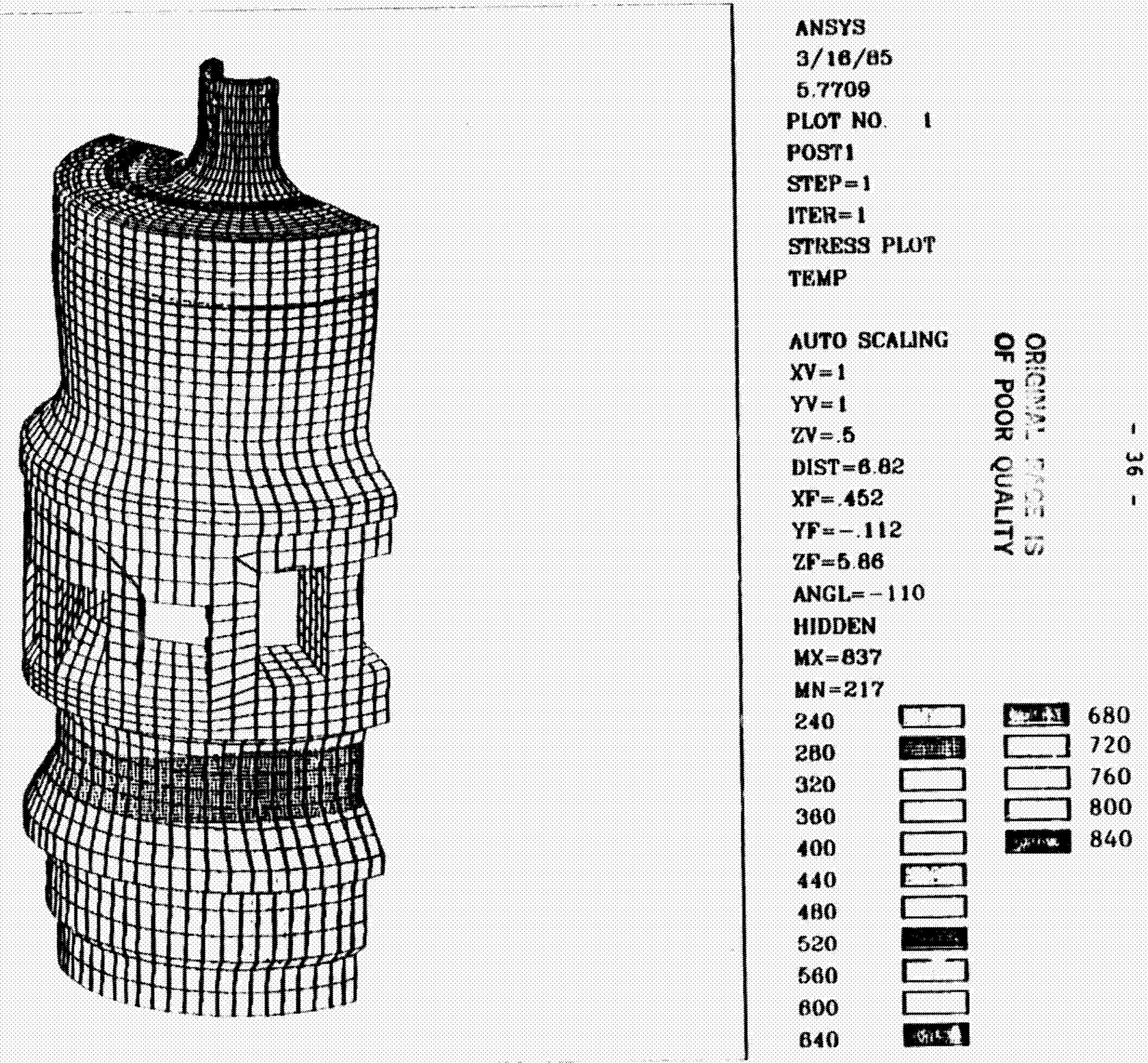

Figure 10C

Cylinder Temperature
Contours (°F)

RUN 668 A

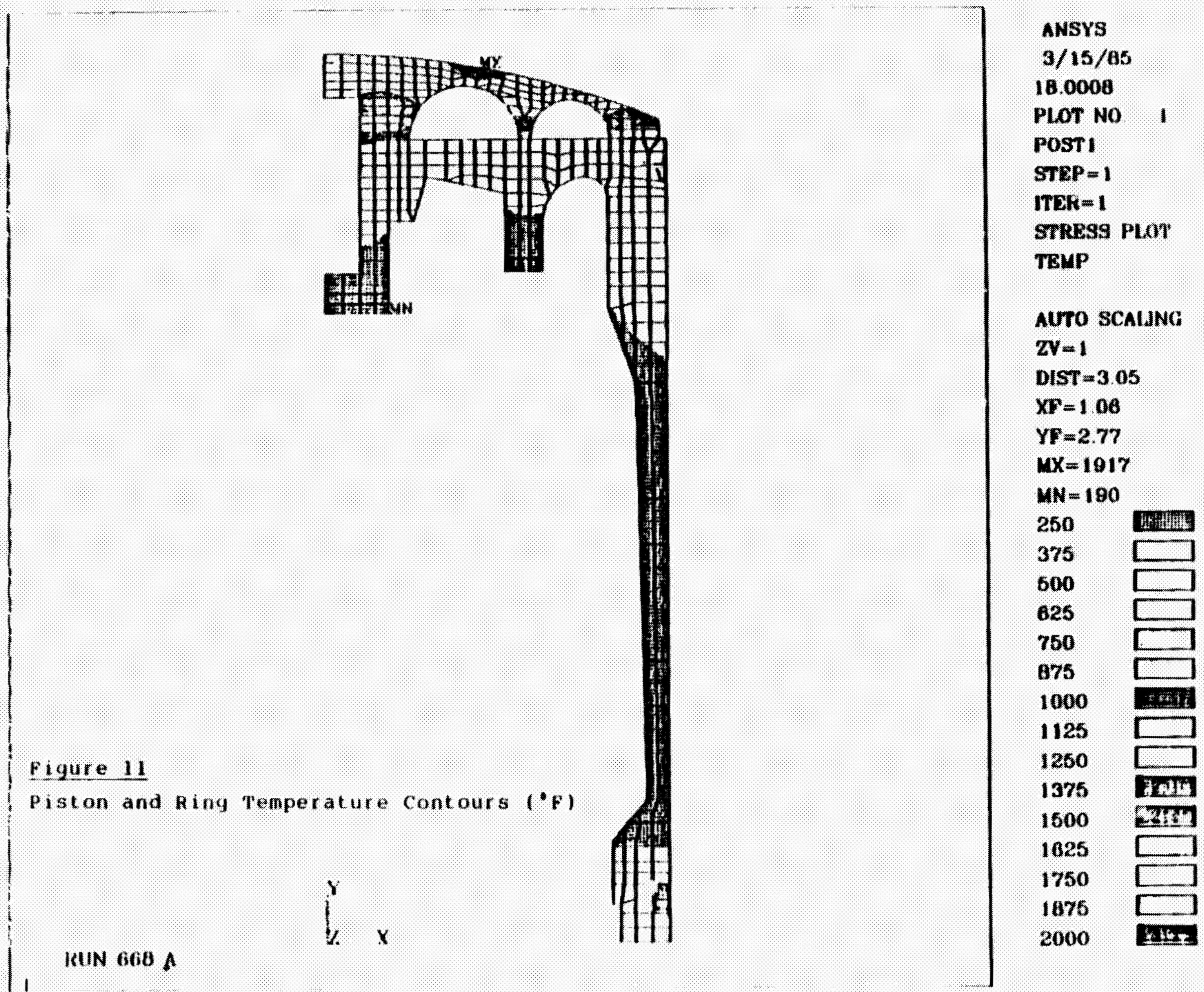

Figure 11

Piston and Ring Temperature Contours (°F)

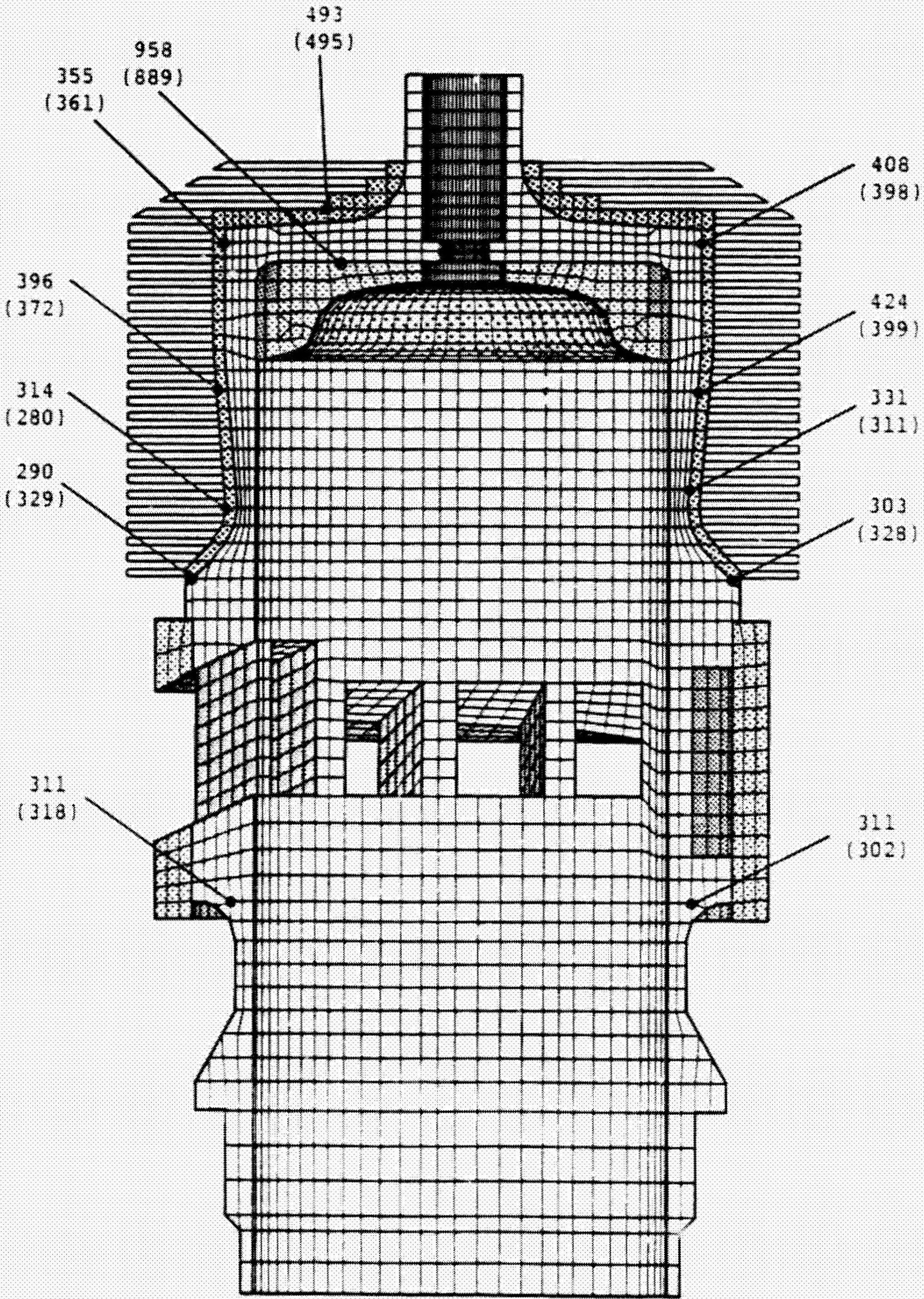

Note: Measured temperatures shown in parentheses

Figure 12 SCTE Cylinder
Comparison of Measured and Calculated Temperatures (°F)
Run 659

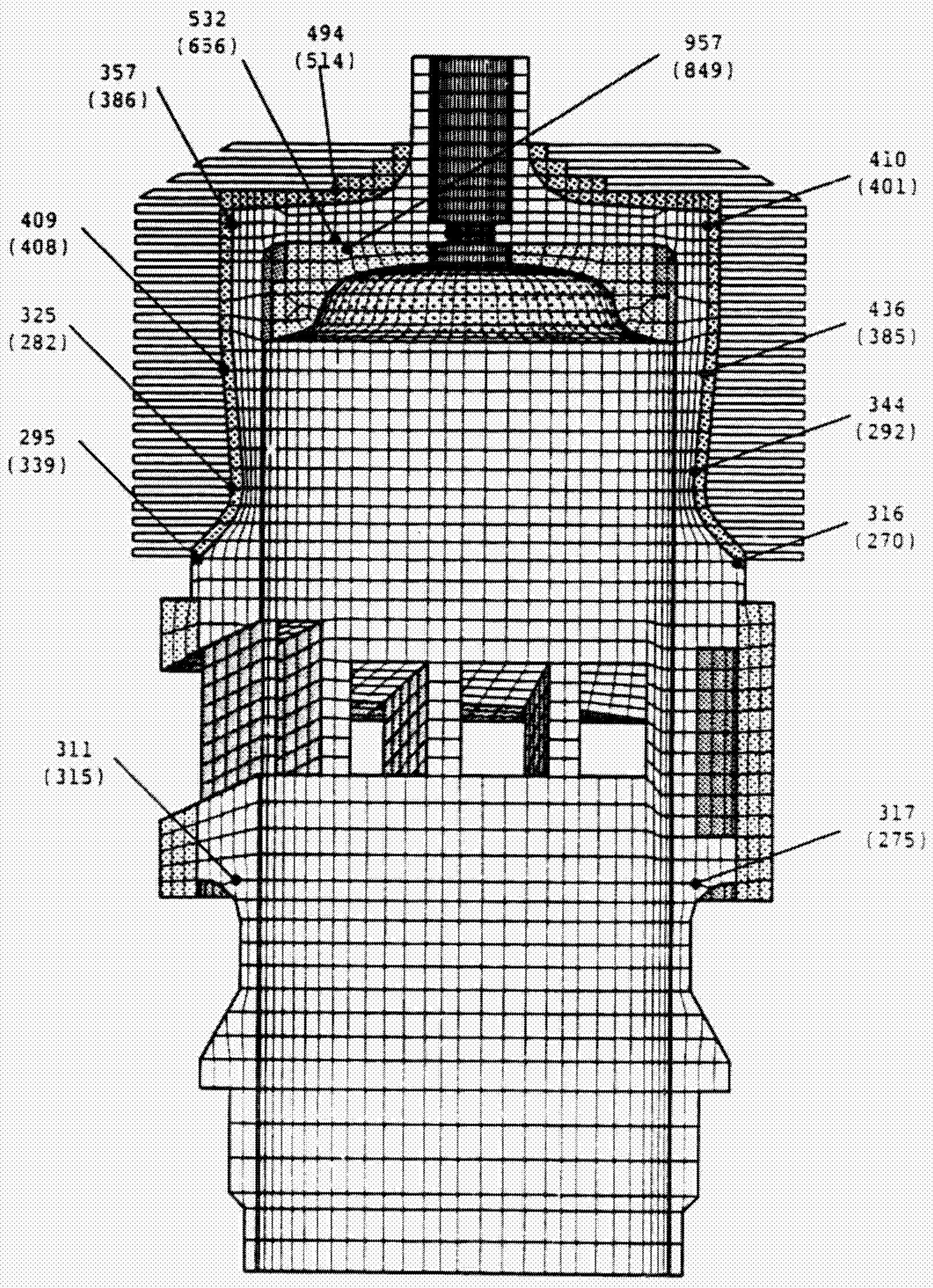

Note: Measured temperatures shown in parentheses

Figure 13 SCTE Cylinder
Comparison of Measured and Calculated Temperatures (°F)
Run 668

Figure 14 Cylinder Gas Temperatures
Run 659

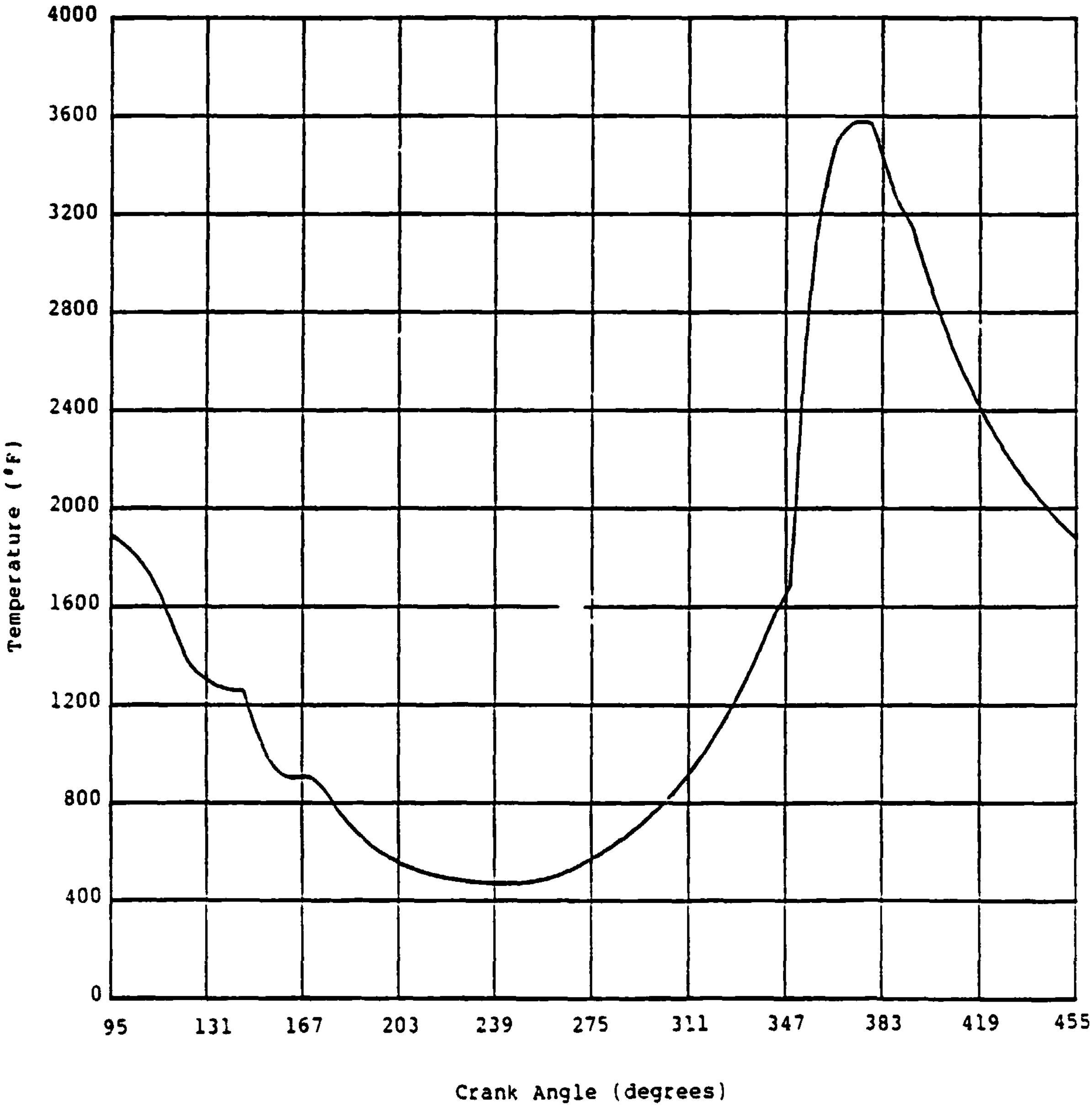

Figure 15 Cylinder Gas Heat Transfer Coefficient
Run 659

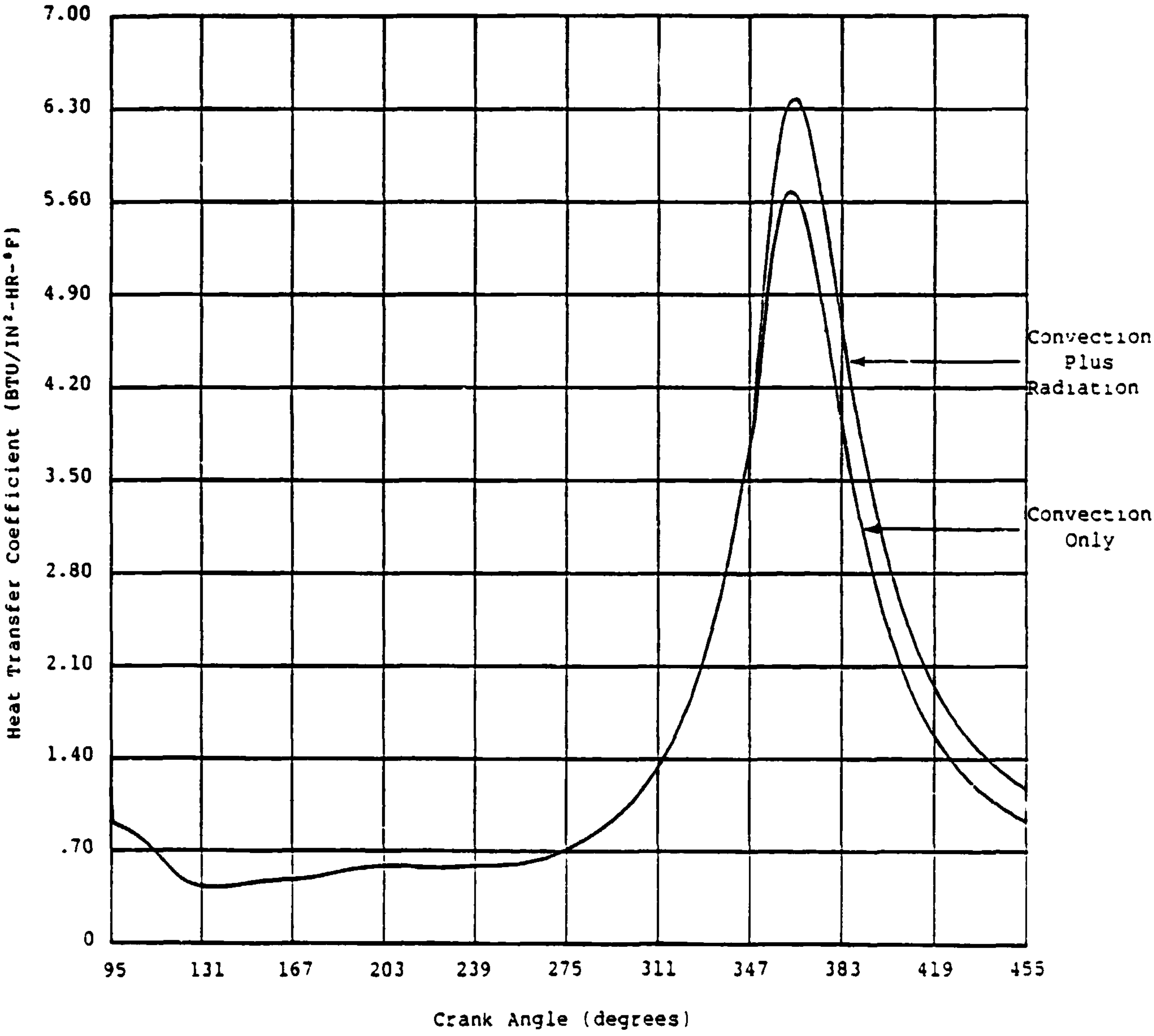

Figure 16 Intake Port Gas Temperatures
Run 659

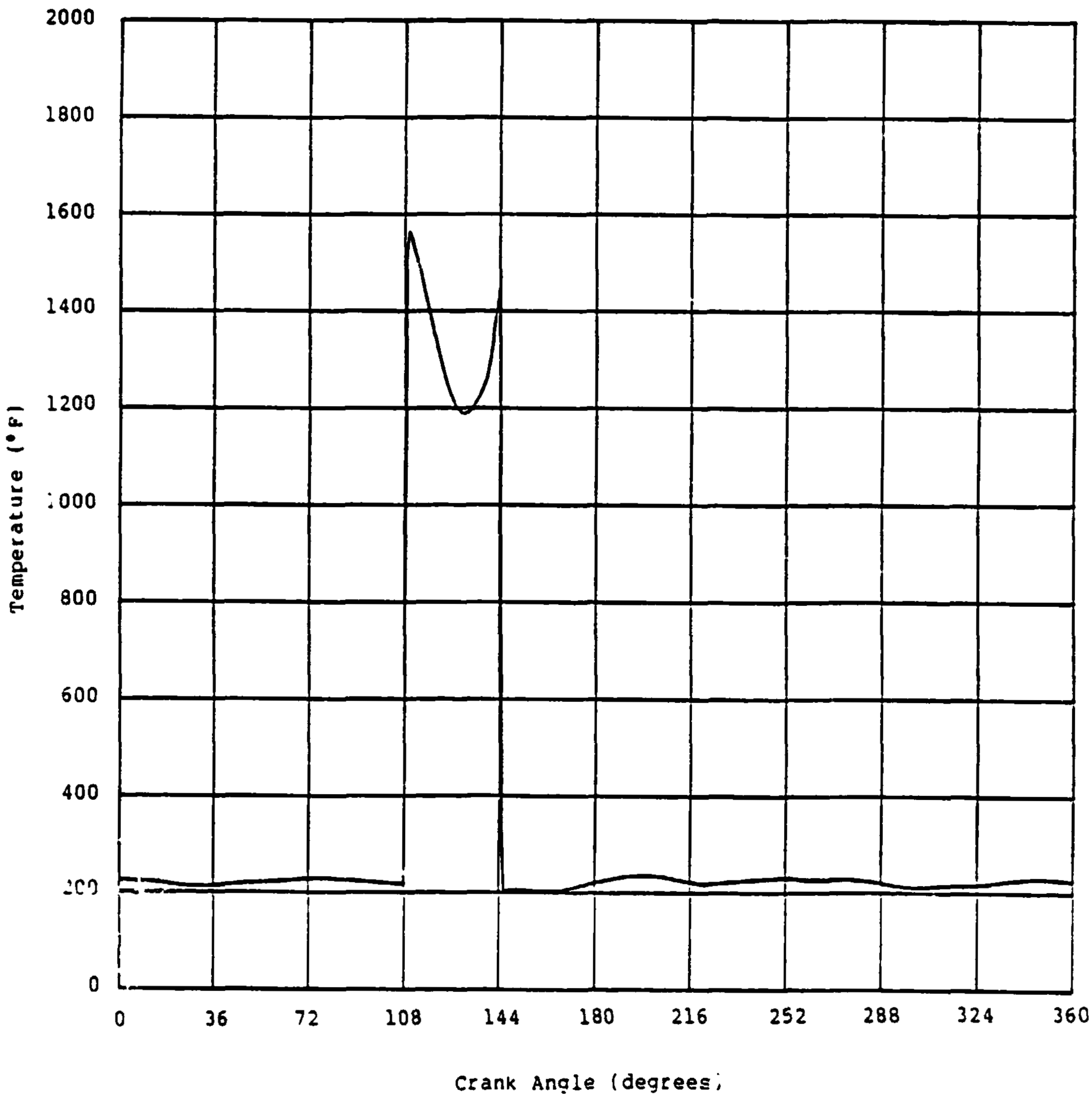

Figure 17 Intake Port Mass Flow Rate
Run 659

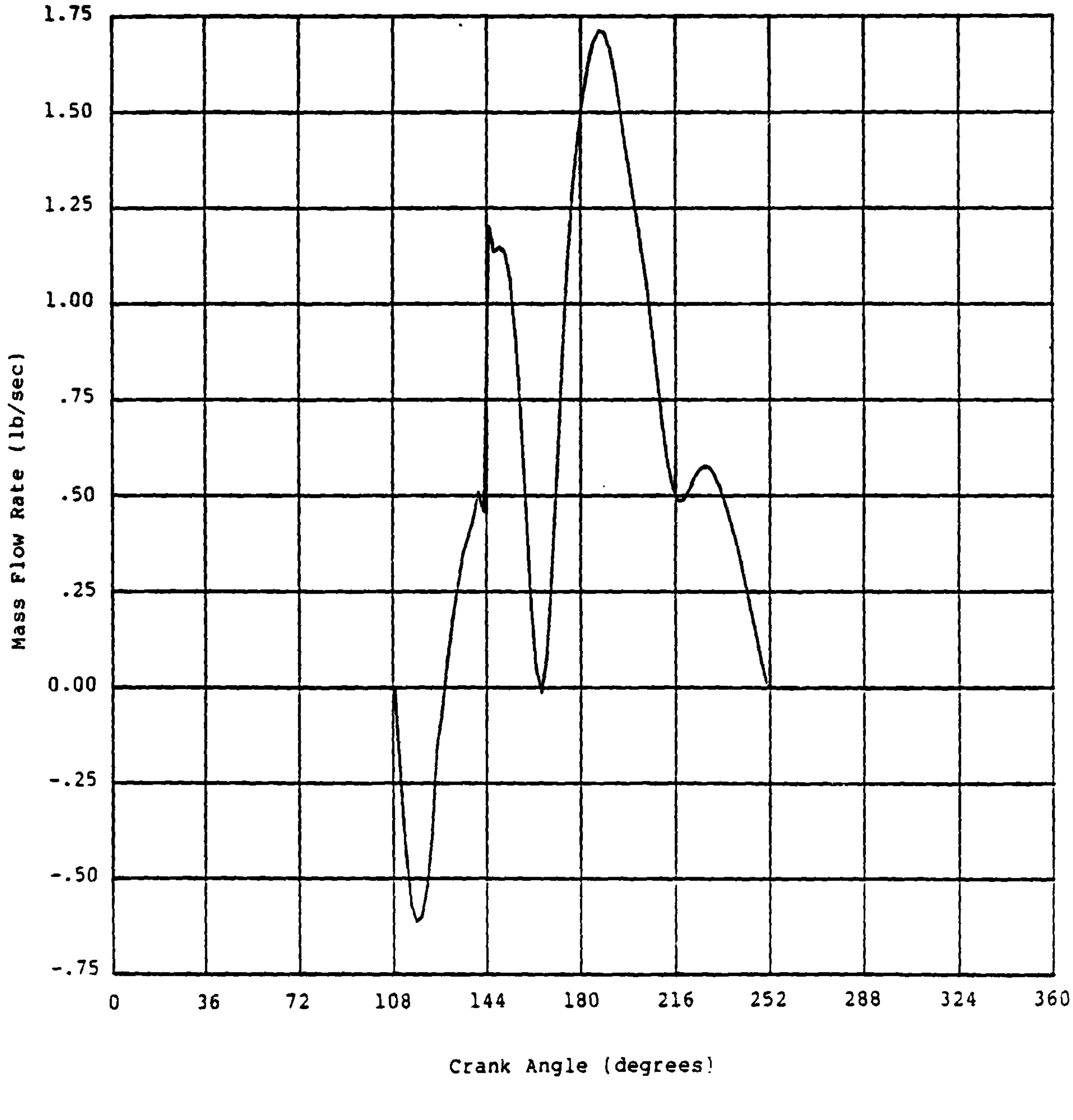

Figure 18 Intake Port Gas Average Veloc.ty
Run 659

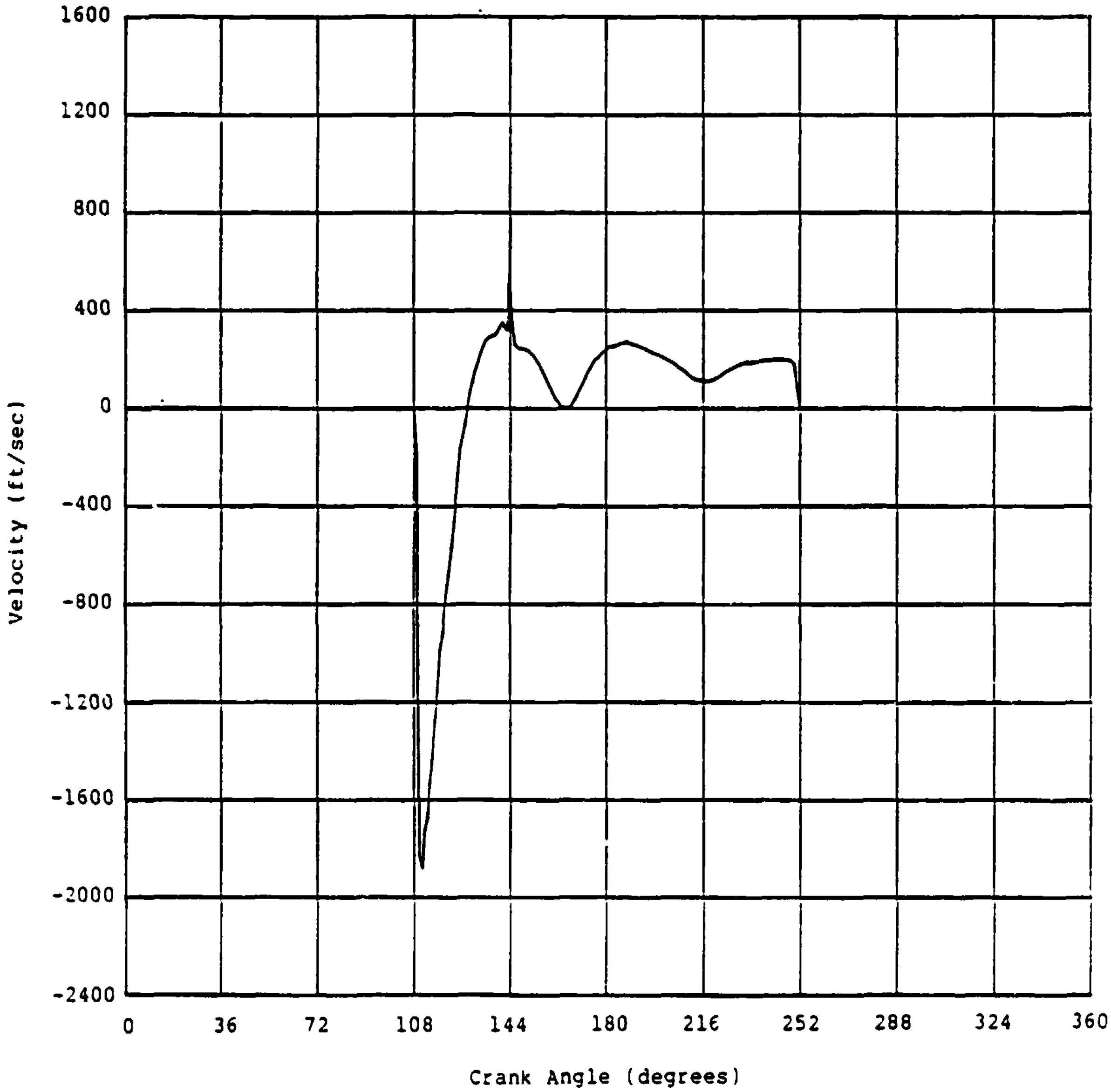

<u>Figure 19</u> Exhaust Port Gas Temperatures
Run 659

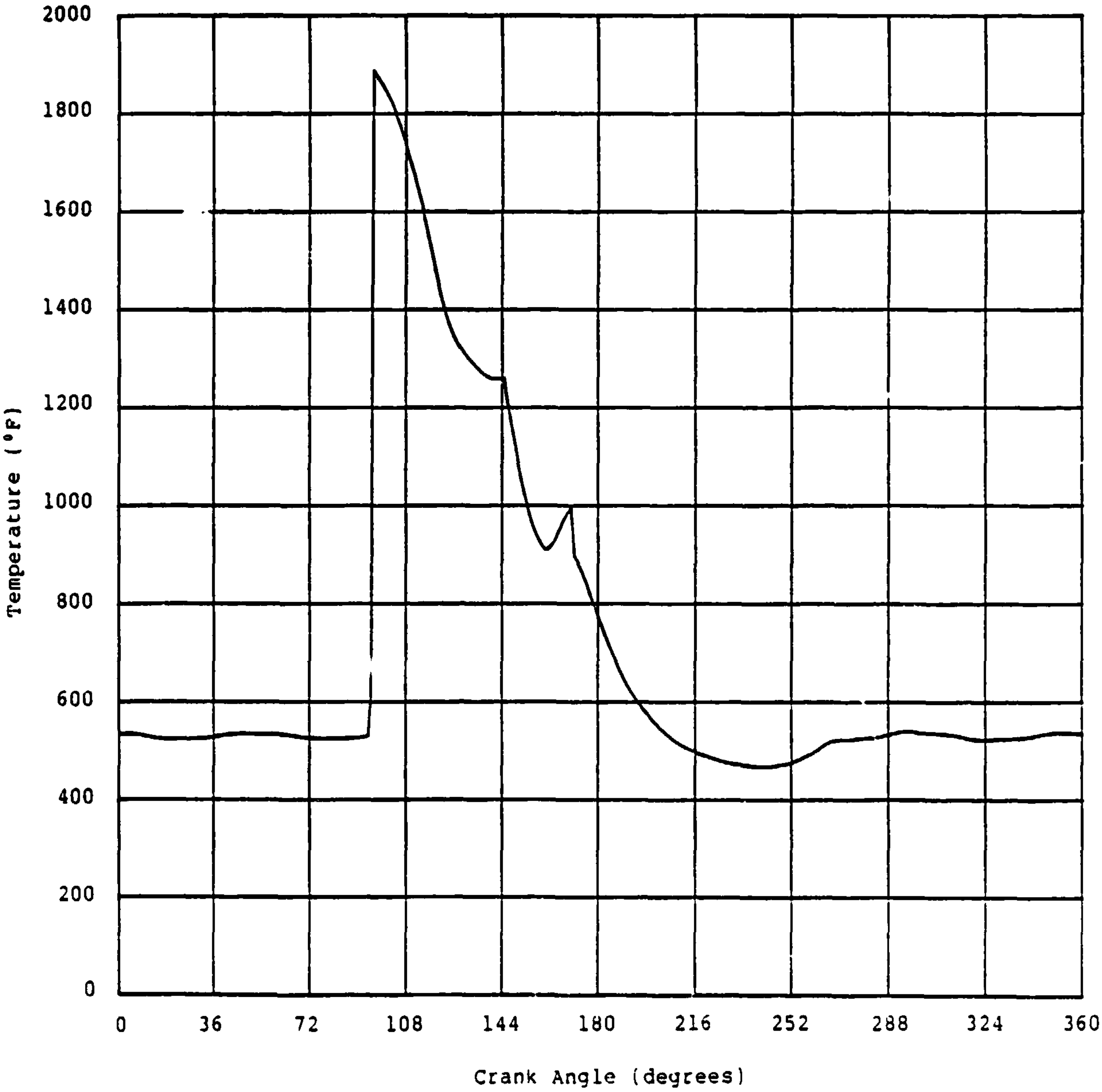

Figure 20 Exhaust Port Mass Flow Rate
Run 659

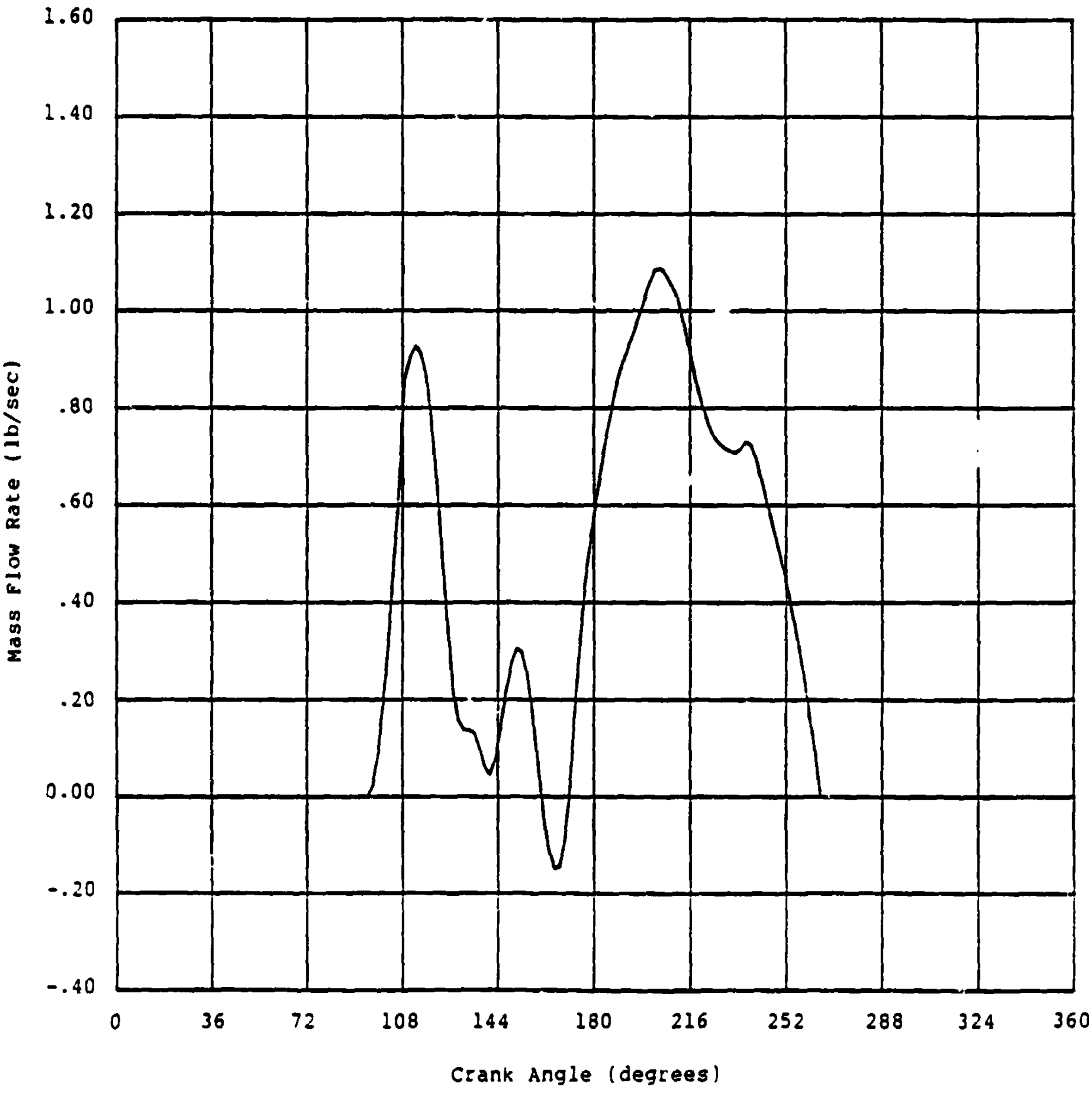

Figure 21 Exhaust Port Gas Average Velocity
Run 659

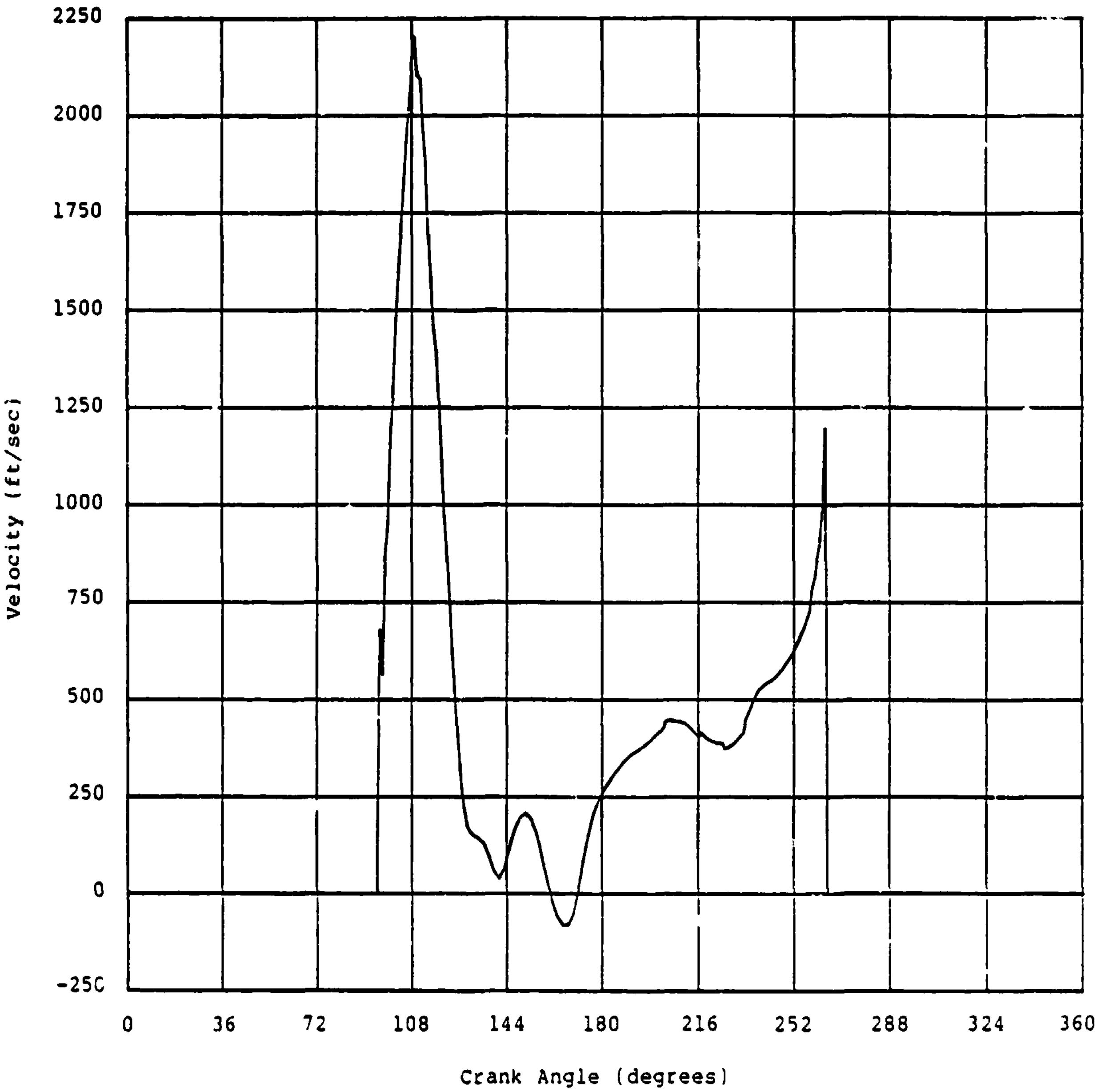

Figure 22 Cylinder Gas Temperatures
Run 668

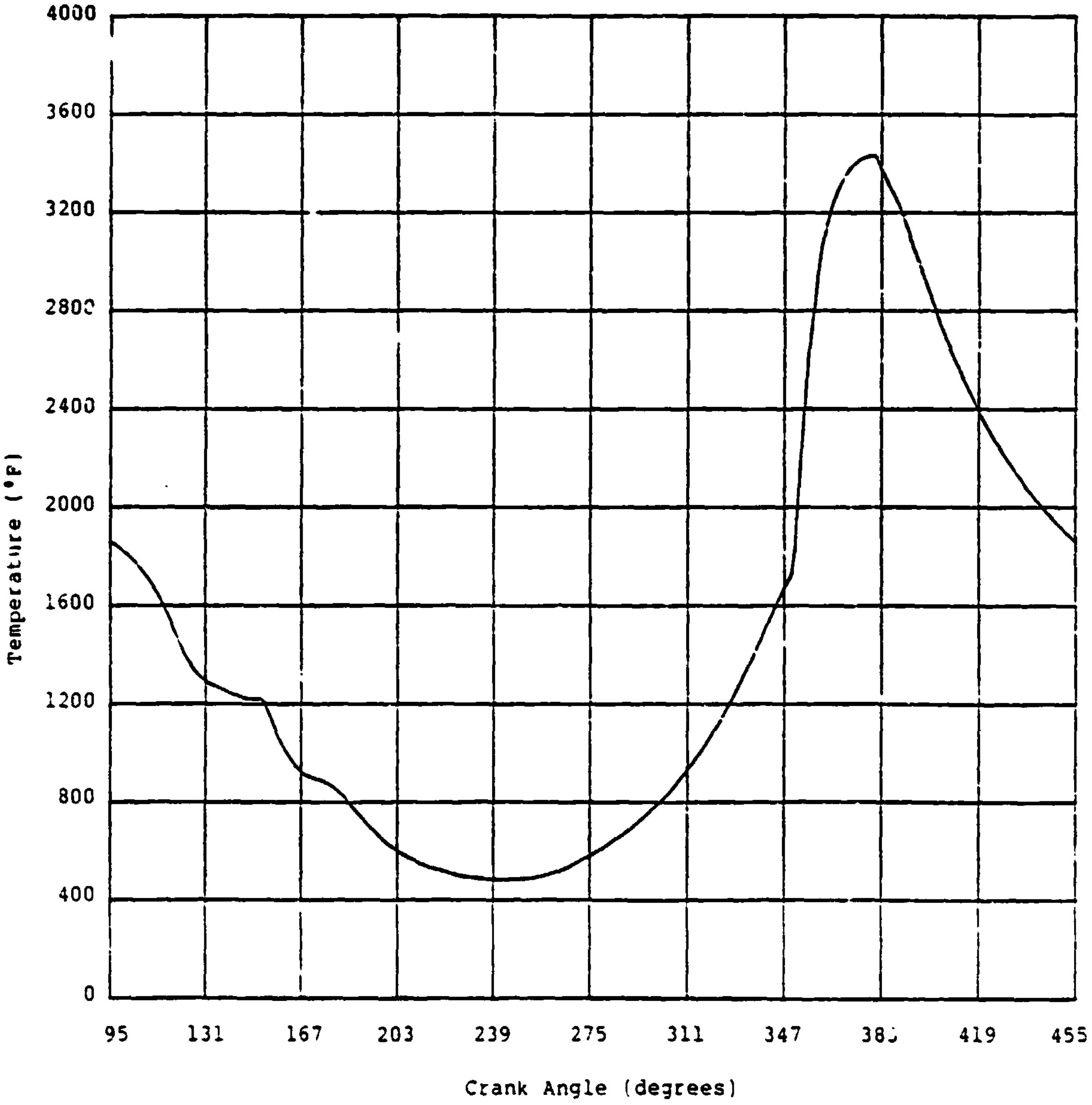

Figure 23 Cylinder Gas Heat Transfer Coefficient
Run 668

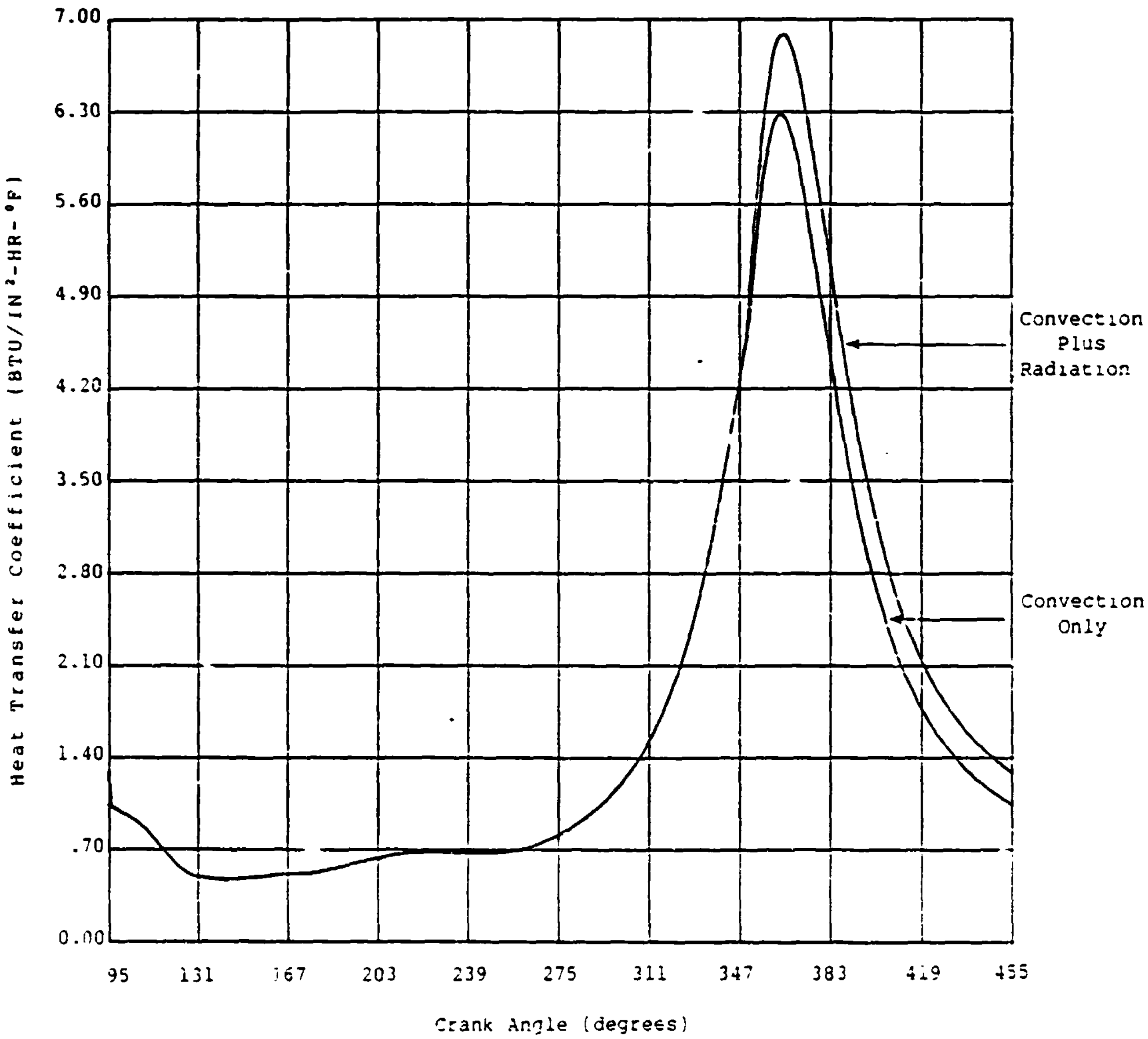

Figure 24 Intake Port Gas Temperatures
Run 668

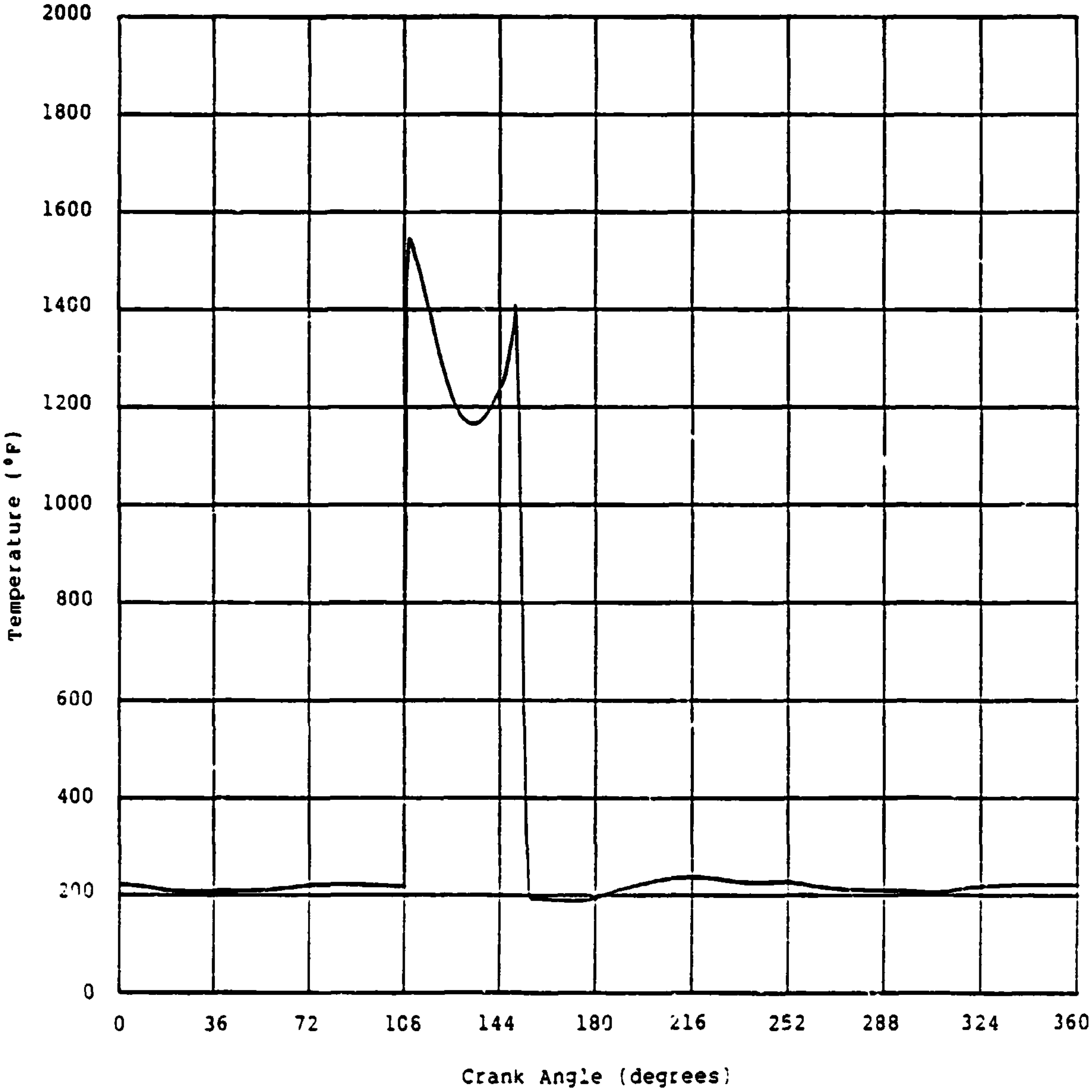

Figure 25 Intake Port Mass Flow Rate
Run 668

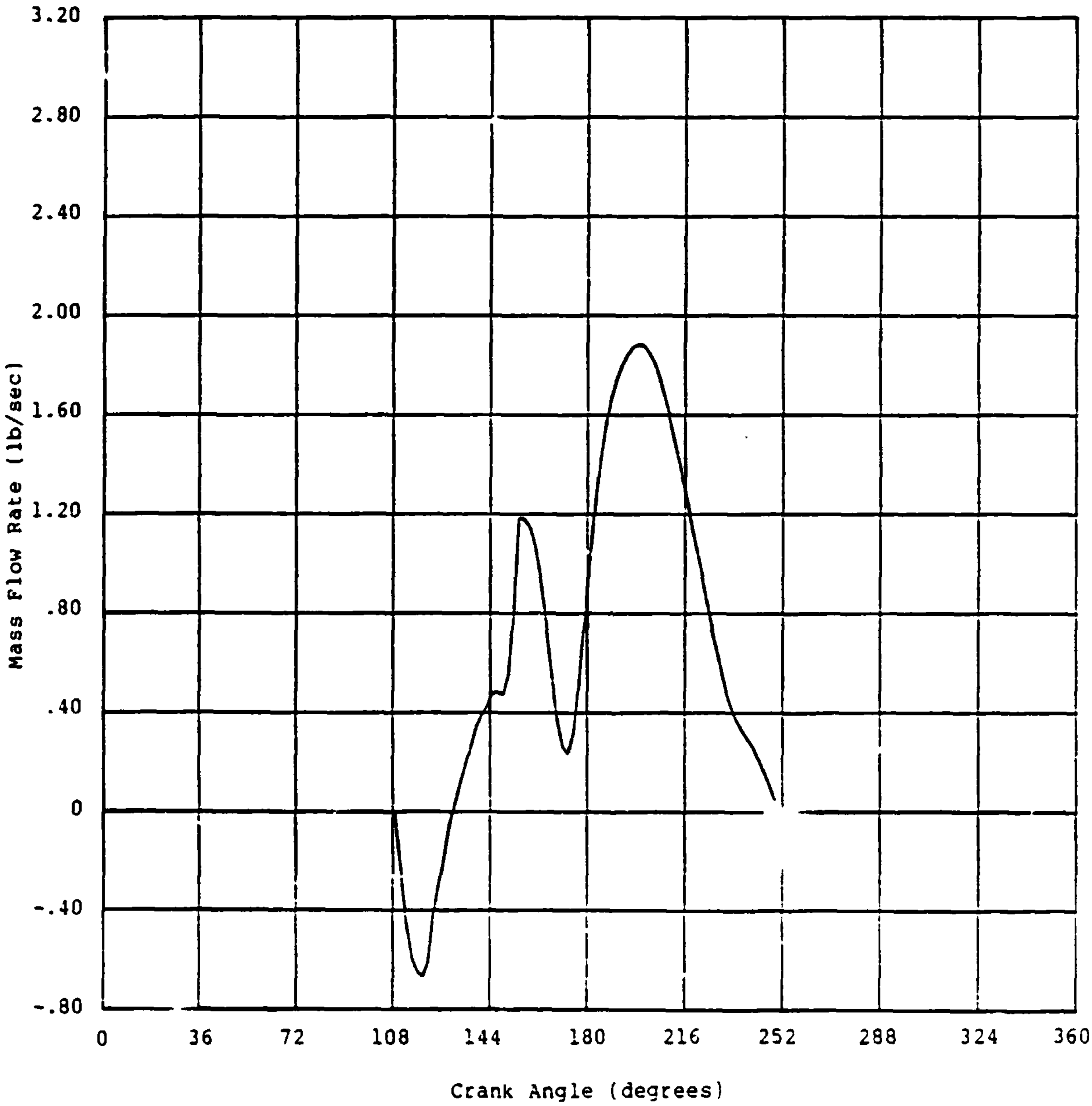

Figure 26 Intake Port Gas Average Velocity
Run 668

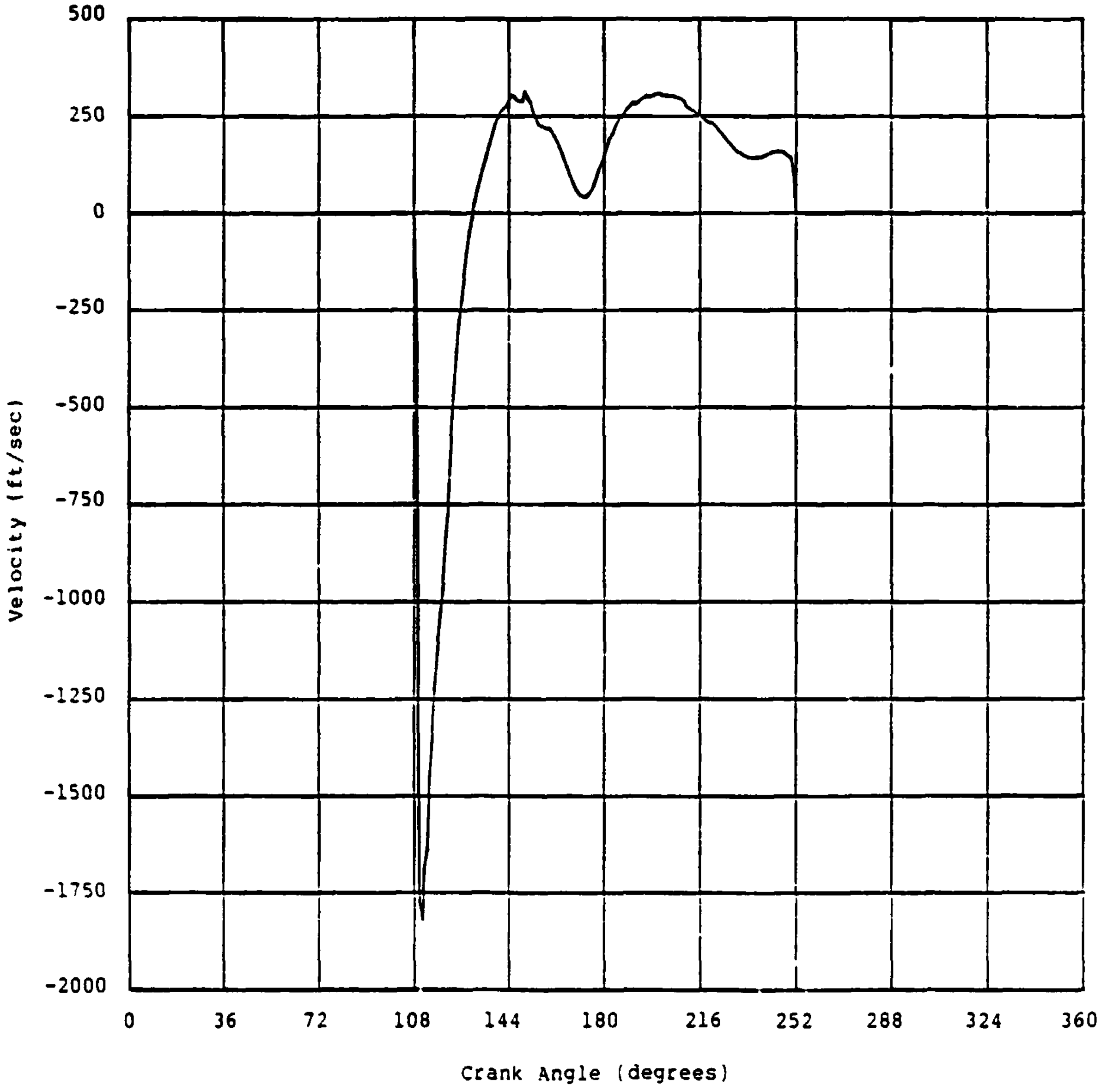

Figure 27 Exhaust Port Gas Temperatures
Run 668

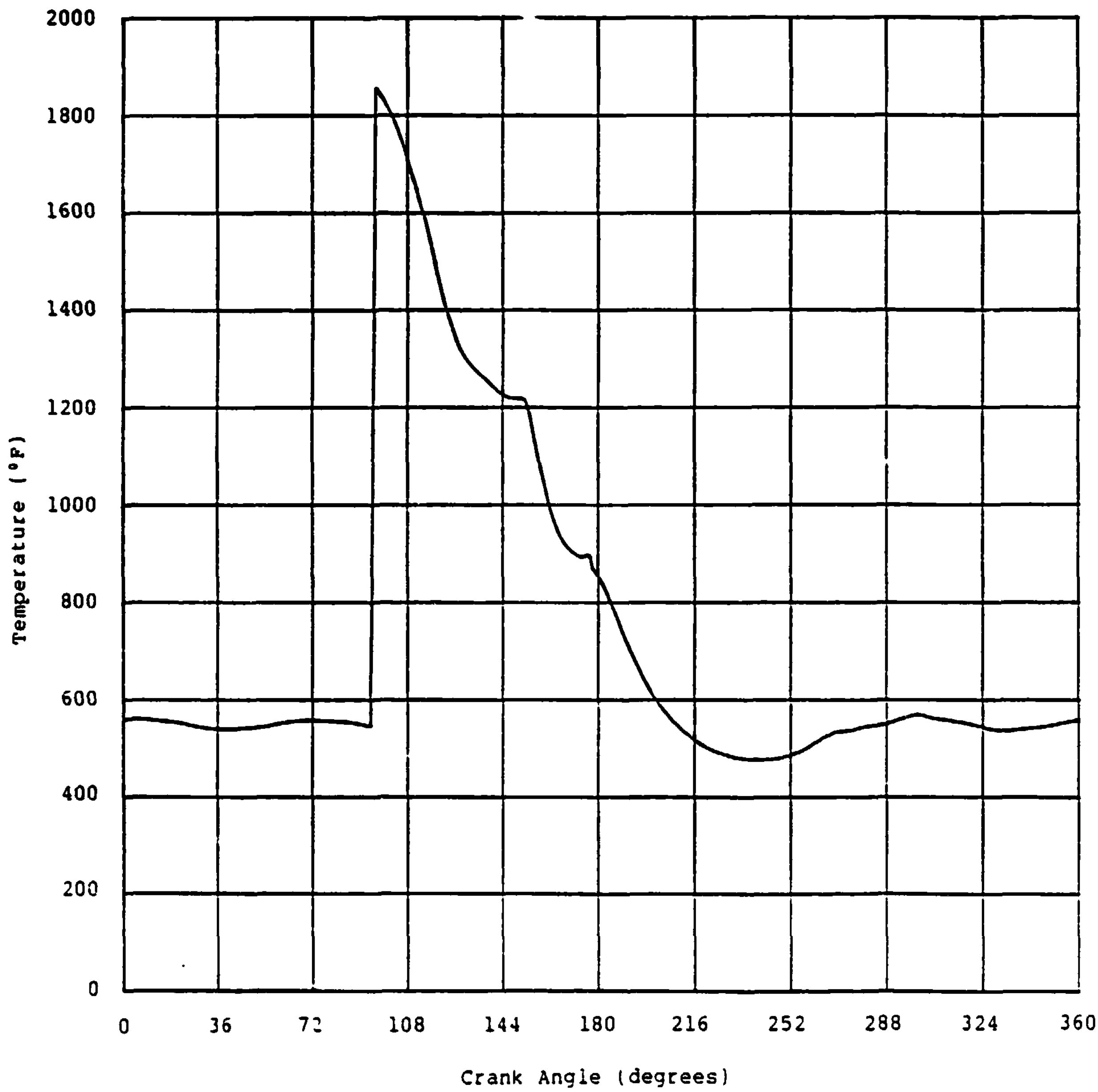

Figure 28 Exhaust Port Mass Flow Rate
Run 668

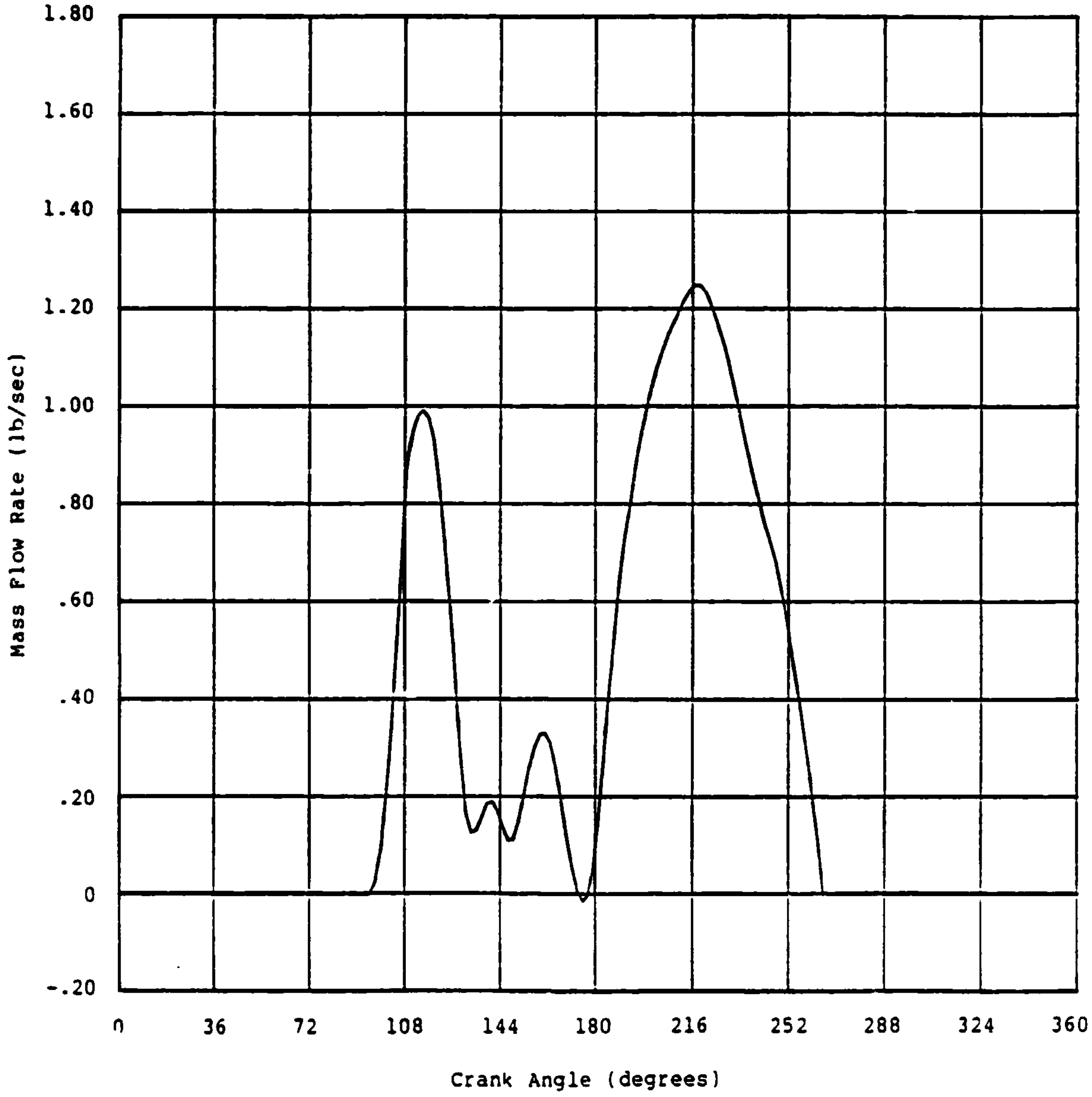

Figure 29 Exhaust Port Gas Average Velocity
Run 668

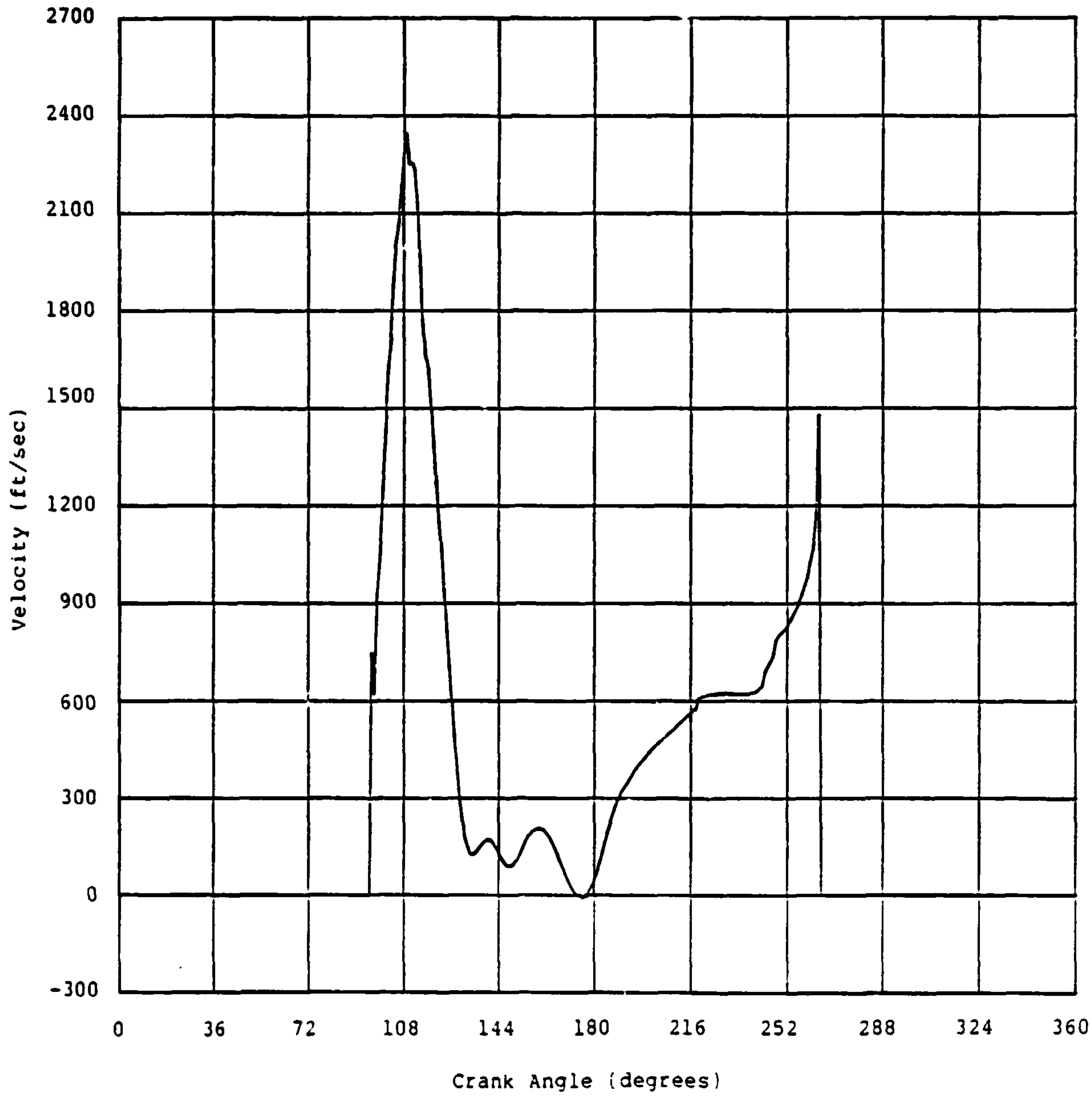

Figure 30 Cylinder Pressure
Benson Code Analysis
Run 659

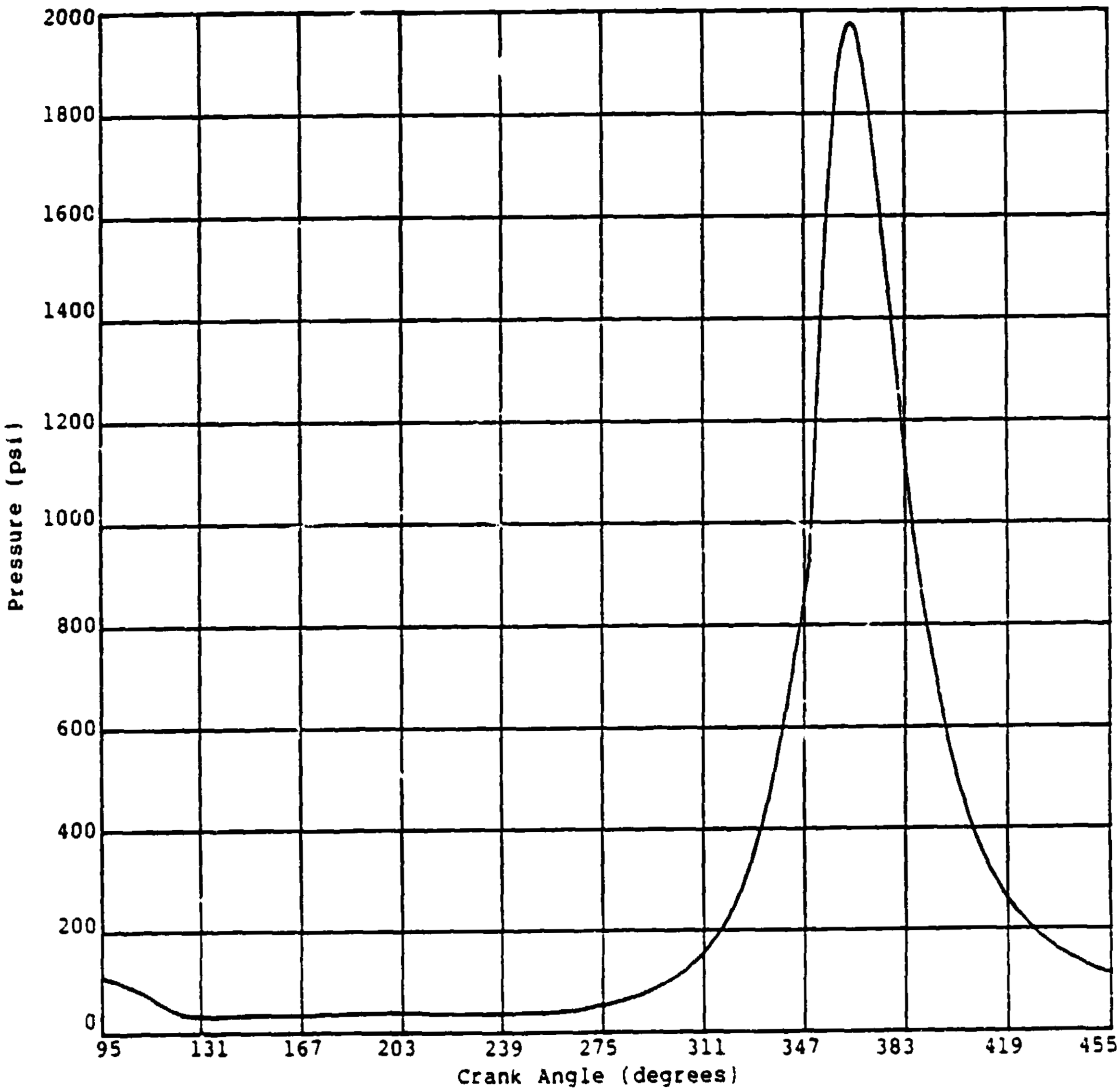

Figure 31 Cylinder Pressure
Benson Code Analysis
Run 668

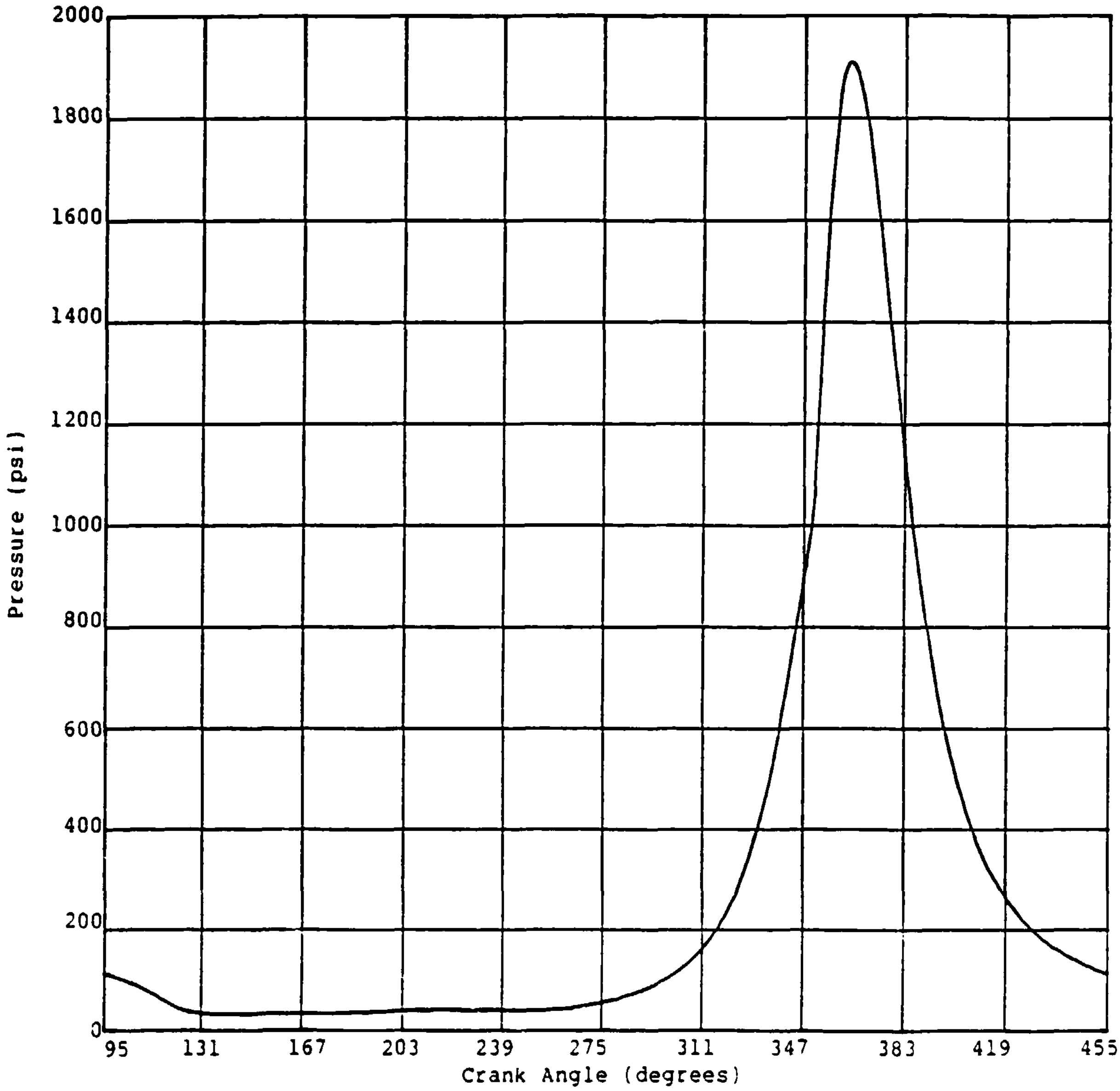

Table 1 Basic Engine Configuration

Engine type	Single piston two stroke diesel
Cylinder bore	108 mm
Stroke	110 mm
Connecting rod length	220 mm
Nominal compression ratio	17.85
Height intake ports	31 mm
Height exhaust ports	43 mm
Exhaust ports open	85° BBDC (C.A. = 95°)
Exhaust ports close	85° ABDC (C.A. = 265°)
Intake ports open	71° BBDC (C.A. = 109°)
Intake ports close	71° ABDC (C.A. = 251°)

Table 2 Summary of SCTE Test Data
Run 659

Parameter (Units)	Value
Engine Speed (RPM)	3004.00
Intake Temperature (°F)	222.00
Exhaust Temperature (°F)	957.00
Intake Pressure (In-Hg)	77.10
Exhaust Pressure (In-Hg)	72.00
Air Flow (Lb/Hr)	846.00
Fuel Flow (Lb/Hr)	20.66
Cooling Air (Lb/Hr)	1403.19
Temp. Cooling Air in (°F)	104.00
Temp. Cooling Air out (°F)	234.00
Port Oil Flow (Lb/Hr)	398.46
Temp. Port Oil in (°F)	178.00
Temp. Port Oil Out (°F)	201.00
IHP	64.14
BHP	46.26
ISFC (Lb/IHP-Hr)	0.322
Peak Cylinder Pressure (psi)	1550.0

Table 3 Summary of SCTE Test Data
Run 668

Parameter (Units)	Value
Engine Speed (RPM)	3501.00
Intake Temperature (°F)	215.00
Exhaust Temperature (°F)	1006.00
Intake Pressure (In-Hg)	78.00
Exhaust Pressure (In-Hg)	70.00
Air Flow (Lb/Hr)	974.48
Fuel Flow (Lb/Hr)	23.62
Cooling Air (Lb/Hr)	1416.06
Temp. Cooling Air in (°F)	108.00
Temp. Cooling Air out (°F)	238.00
Port Oil Flow (Lb/Hr)	382.31
Temp. Port Oil in (°F)	169.00
Temp. Port Oil out (°F)	197.00
IHP	76.15
BHP	52.34
ISFC (Lb/IHP-Hr)	0.310
Peak Cylinder Pressure (psi)	1750.0

Table 4 SCTE Energy Balance Derived from Test Data

ITEM	HEAT RATE AS A PERCENT OF FUEL ENERGY	
	RUN 659	RUN 668
Crankcase Oil	8.94	7.98
Transducer Oil	0.23	0.27
Port Cooling Oil	1.24	1.26
Cooling Air	11.65	10.28
Exhaust	43.97	47.80
BHP	30.81	30.48
Unaccounted	3.17	1.93
TOTAL	100.00	100.00

Table 5 Indicated Heat Loss Derived from Test Data

ITEM	HEAT RATE AS A PERCENT OF FUEL ENERGY	
	RUN 659	RUN 668
IHP	42.72	44.37
Exhaust	43.97	47.80
Heat Loss	13.31	7.83
TOTAL	100.00	100.00

Table 6 Comparison of Key Engine Parameters
Benson Cycle Code Versus Test Data
Run 659

ITEM	BENSON CODE	TEST DATA
IHP	67.02	64.14
IS C (LB/IHP-HR)	0.308	0.322
Airflow (LB/HR)	846.2	846.0
Exhaust Temperature (°F)	921.0	957.0
Peak Cylinder Pressure (psi)	1975	1550
Heat Loss (Btu/Hr)	50910	50872
Pressure Ra [illegible] (Intake/E[illegible]	1.104	1.07

Table 7 Comparison of Key Engine Parameters
Benson Cycle Code Versus Test Data
Run 668

ITEM	BENSON CODE	TEST DATA
IHP	77.60	76.15
ISFC (Lb/IHP/Hr)	0.304	0.310
Airflow (Lb/Hr)	959.2	974.48
Exhaust Temperature (°F)	933	1006
Peak Cylinder Pressure (psi)	1910	1750
Heat Loss (Btu/Hr)	52174	34215
Pressure Ratio (Intake/Exhaust)	1.15	1.11

Table 8 Heat Balance for Finite Element Model

SURFACE OR REGION	HEAT RATE (Btu/Hr)	
	RUN 659	RUN 668
Head	21446	21450
Cylinder (Combustion Chamber & Gases)	20664	22516
Piston (Cap)	10460	10388
Piston (Oil Spray)	-22176	-23966
Piston (Ring Friction)	11716	13578
Cylinder (Ring Friction)	8984	10422
Cylinder and Manifold (Exhaust Gases)	3058	3372
Cylinder and Manifold (Intake Ports)	1314	1384
Cylinder and Manifold (External Environment)	-518	-530
Cylinder (Cooling Air)	-45248	-47302
Cylinder (Splash Oil)	-6160	-7200
Cylinder (Exhaust Port Cooling Oil)	-3540	-4112
TOTAL	0	0

Note: Negative sign indicates heat flow out of surface.

Table 9 Forced Convection Boundary Conditions and Specified Heat Rates

REGION	RUN 659	RUN 663
Head Insert and Piston Cap (Combustion Side)	T = 2230.9 H = 1.620	T = 2153.5 H = 1.792
Exhaust Port: Top	T = 1018; H = 0.510	T = 1024; H = 0.560
Sides	T = 975; H = 0.400	T = 989; H = 0.435
Bottom	T = 1020; H = 0.293	T = 1032; H = 0.316
Intake Port: Top	T = 660; H = 0.323	T = 665; H = 0.350
Sides	T = 583; H = 0.265	T = 590; H = 0.288
Bottom	T = 661; H = 0.187	T = 672; H = 0.200
Manifold: Exhaust	T = 856; H = 0.206	T = 872; H = 0.224
Intake	T = 438; H = 0.108	T = 451; H = 0.120
Piston Ring Friction	20760 Btu/Hr	24000 Btu/Hr
Port Oil Cooling	-3554 Btu/Hr	-4130 Btu/Hr
Piston (Crankcase Side)	T = 191; H = 4.6	T = 188; H = 5.27
Natural Convection and Radiation to External Environment	T = 70; H = 0.018	T = 70; H = 0.018

Note: T = Bulk Fluid Temperature (°F)

H = Heat Transfer Coefficient (Btu/In^2-Hr-°F)

Table 10 Effective Heat Transfer Coefficient for Circumferential Fins

Fin Number	Fin Efficiency	Effective Heat Transfer Coefficient (Btu/In^2-Hr-°F)
1	0.334 (1.0)	6.179 (0.405)
2	0.331 (1.0)	5.862 (0.405)
3	0.387 (1.0)	5.377 (0.405)
4	0.774 (1.0)	3.514 (0.405)
5	0.719	3.845
6	0.719	3.845
7	0.719	3.845
8	0.719	3.845
9	0.719	3.845
10	0.719	3.845
11	0.719	3.845
12	0.719	3.845
13	0.719	3.845
14	0.710	3.897
15	0.701	3.949
16	0.692	3.998
17	0.683	4.046
18	0.674	4.093
19	0.665	4.138
20	0.656	4.182
21	0.656	4.182
22	0.656	4.182
23	0.656	4.[illegible]2
24	0.683	4.046
25	0.747	3.679
26	0.811	3.233
27	0.846	2.942

Note: The effective heat transfer coefficient is based on the actual heat transfer coefficient, the actual fin surface area, the fin efficiency, and a fin spacing of one thickness. The top four fins were broken off prior to the test, so the actual heat transfer coefficient is used with an efficiency of 1.0 in the finite element model for fins 1 through 4. This value is shown in parentheses. Based on the test data, an average cooling air temperature of 169°F is used in the model for Run 659 and Run 668.

Table 11 Free Convection, Radiation and Surface Contact Heat Transfer Coefficients

REGION OR INTERFACE	PRIMARY MODE OF HEAT TRANSFER	HEAT TRANSFER COEFFICIENT (BTU/IN^2-HR-$^\circ$F)
Enclosed Space between Cylinder and Manifold Ring	Free Convection	0.011
Head Insert/Cylinder:		
Slots	Radiation and Conduction across Air Gap	0.1124
Lands	Radiation and Conduction across Contact Resistance	3.0
Head Insert/Ring:		
Upper Land	Radiation and Conduction across Air Gap	0.384
Lower Land	Radiation and Conduction across Contact Resistance	3.0
Ring/Cylinder	Assumed coupled at interface due to interference fit	--
Piston Cap/Piston:		
Air Cavities	Radiation	0.106
Lands	Surface Contact	3.0
Shank Portion of Cap	Conduction/Radiation in Air Gaps	0.093

Table 12 Values of Thermal Conductivity Used in Detailed Heat transfer Model

PART	MATERIAL	CONDUCTIVITY (Btu/Hr-In-°F)
Cylinder	1040 Steel	2.25
Fins	Cast Aluminum Alloy	7.50
Piston	Ductile Iron	2.07
Piston Press in Plug	304SS	1.03
Piston Cap	321SS	0.708
Piston Rings	Ductile Iron	2.07
Head Insert	321SS	0.708
Ring Insert	4340 Steel	1.81
Manifcld Ring	Mild Steel	2.08

APPENDIX

Benson Code Exhaust Temperature Calculation by Energy Accounting

The following calculations assume 100% energy balance, and then derive the resulting exhaust temperature.

1.0 <u>Benson Code Energy Balance Calculation for Run 659</u>

Fuel Heating Value = 18500 BTU/LB

Fuel Flow = 20.66 LB/HR; Fuel Temperature = 70°F

Intake Air Flow = 846 LB/HR*; Intake Air Temperature=222°F

Heat Loss = 13.32% of Fuel Energy*

IHP = 67.02*

Energy Added = (18500 BTU/LB)(20.66 LB/HR) = 382210 BTU/HR

Indicated Power = (67.02 HP)(2545.2 BTU/HP-HR)=170579 BTU/HR

Heat Loss = (0.1332)(382210 BTU/HR) = 50910 BTU/HR

Exhaust = 382210 - 170579 - 50910 = 160721 BTU/HR

TE = Exhaust Temperature

Exhaust = 160721 BTU/HR =

(0.264 BTU/LB-°F)[(846 LB/HR)(TE-222)+20.66 LB/HR)(TE-70)]

TE = <u>921°F</u>

*Indicates value calculated by Benson Code

2.0 Benson Code Energy Balance Calculation for Run 668

Fuel Heat Value = 18500 BTU/LB

Fuel Flow = 23.62 LB/HR;   Fuel Temperature = 70°F

Intake Air Flow = 959.2 LB/HR*; Intake Air Temperature=215°F

Heat Loss = 11.94% of Fuel Energy

IHP = 77.60*

Energy Added = (18500 BTU/LB)(23.62 LB/HR) = 436970 BTU/HR

Indicated Power = (77.60 HP)(2545.2 BTU/HP-HR)=197507 BTU/HR

Heat Loss = (.1194)(436970 BTU/HR) = 52174 BTU/HR

Exhaust = 436970 - 197507 - 52174 = 187289 BTU/HR

TE = Exhaust Temperature

Exhaust = 187289 BTU/HR =

(0.264 BTU/LB-°F)[(959.2 LB/HR)(TE-215)+(23.62 LB/HR)(TE-70)]

TE = 933°F

*Indicates value calculated by Benson Code

A P P E N D I X   II

STRUCTURAL ANALYSIS
OF THE
SINGLE CYLINDER TEST ENGINE

adapco
ANALYSIS & DESIGN APPLICATION CO., LTD.

Report 26-02-002
April 12, 1985

STRUCTURAL ANALYSIS
OF THE
SINGLE CYLINDER TEST ENGINE

Prepared for:

TELEDYNE CONTINENTAL MOTORS

Prepared by:

Analysis and Design Application Company, Ltd.

Prepared by: David J. Purnell
David J. Purnell

Approved by: Peter S. MacDonald
Peter S. MacDonald

60 BROADHOLLOW ROAD, MELVILLE, NEW YORK 11747 516-549-2300

<u>TABLE OF CONTENTS</u>

1.0 INTRODUCTION

This report documents the structural analysis of the Single Cylinder Test Engine (S.C.T.E.) for the operating conditions represented by "Run 668" in Reference 1. For purposes of the stress analysis, the finite element heat transfer model of Reference 1 is converted to a structural model by changing the thermal continuum elements to structural continuum elements, and introducing the appropriate structural boundary conditions. As indicated in Figure 1, the boundary conditions include the peak cylinder pressure (1910 psi) as calculated by the Benson cycle simulation code. The temperature distribution (nodal temperatures) is obtained from the heat transfer analysis of Reference 1. The interface between the head insert and the cylinder is "double-noded" so that the mating surfaces may move in and out of contact. The solution of the contact problem requires the use of bilinear contact elements in an iterative process. As indicated in Figure 2, the contact elements are defined on nodal circles representing the loads where contact may occur. Each individual contact element is one-dimensional in that it operates in either a vertical or a radial sense. The initial as-fabricated clearance, if any, is included in the formulation of the contact elements. The stresses in the various parts are caused by the interaction, or interference, due to relative thermal expansion,. the internal temperature gradients, and

(NASA-CR-174923-Vol-3) LIGHTWEIGHT N86-13330
TWO-STROKE CYCLE AIRCRAFT DIESEL ENGINE
TECHNOLOGY ENABLEMENT PROGRAM, VOLUME 3
Final Report, Dec. 1979 - Aug. 1985 Unclas
(Teledyne Continental Motors, Muskegon, G3/07 04793

A P P E N D I X II

STRUCTURAL ANALYSIS
OF THE
SINGLE CYLINDER TEST ENGINE

ANALYSIS & DESIGN APPLICATION CO., LTD.

STRUCTURAL ANALYSIS
OF THE
SINGLE CYLINDER TEST ENGINE

Prepared for:

TELEDYNE CONTINENTAL MOTORS

Prepared by:

Analysis and Design Application Company, Ltd.

Prepared by: David J. Purnell
David J. Purnell

Approved by: Peter S. MacDonald
Peter S. MacDonald

60 BROADHOLLOW ROAD, MELVILLE, NEW YORK 11747 516 - 549-2300

TABLE OF CONTENTS

1.0 INTRODUCTION

This report documents the structural analysis of the Single Cylinder Test Engine (S.C.T.E.) for the operating conditions represented by "Run 668" in Reference 1. For purposes of the stress analysis, the finite element heat transfer model of Reference 1 is converted to a structural model by changing the thermal continuum elements to structural continuum elements, and introducing the appropriate structural boundary conditions. As indicated in Figure 1, the boundary conditions include the peak cylinder pressure (1910 psi) as calculated by the Benson cycle simulation code. The temperature distribution (nodal temperatures) is obtained from the heat transfer analysis of Reference 1. The interface between the head insert and the cylinder is "double-noded" so that the mating surfaces may move in and out of contact. The solution of the contact problem requires the use of bilinear contact elements in an iterative process. As indicated in Figure 2, the contact elements are defined on nodal circles representing the loads where contact may occur. Each individual contact element is one-dimensional in that it operates in either a vertical or a radial sense. The initial as-fabricated clearance, if any, is included in the formulation of the contact elements. The stresses in the various parts are caused by the interaction, or interference, due to relative thermal expansion, the internal temperature gradients, and the applied cylinder pressure. The assembly loads (bolt preload) are not considered in this analysis.

A structural interaction model, similar to that described above, is also defined for the piston and piston cap. This model is depicted in Figure 3.

2.0 STRUCTURAL MODEL DESCRIPTION

The cylinder, combustion dome insert, insert ring and manifold ring are modeled using three-dimensional solid elements (ANSYS STIF45). The material properties for each part are shown in Table 1. The cooling fins are represented by thin shell elements (ANSYS STIF63) with effective material properties. Contact elements (ANSYS STIF40) are used for the surface interaction effects. The piston and piston cap are modeled using axisymmetric solid elements (ANSYS STIF42).

The effective material properties for the thin shell elements representing the fins consist of the effective coefficient of thermal expansion (based on the wall temperature), and the effective elastic modulus (based on the thickness of the shell element and the stiffness of the fin). The mean fin temperature ($\bar{T}$) is related to the air temperature (T_A), the wall temperature (T_w), and the fin thermal efficiency (e) through the following relation:

$$\bar{T} = e\,(T_W - T_A) + T_A$$

The effective coefficient of thermal expansion (α_e) is related to the actual material coefficient of thermal expansion (α) by the following formula:

$$\alpha_e = \alpha \left\{ \frac{e\ T_w + (1-e)\ T_A - 70}{T_w - 70} \right\}$$

In the above relation, T_A and e are obtained from Reference 1, and T_w is obtained from the ANSYS temperatures on the wall outer surface where the thin shell elements are defined. The radial stiffness of the circumferential fins is calculated using equations (44) of Reference 2. The effective modulus is then calculated based upon the thickness of the shell elements and the fin spacing. This effective modulus is specified in the circumferential sense only. The shell elements are given a negligibly low modulus in the meridional direction. The Poisson's ratio is assigned a value of zero.

The surface contact elements are assigned initial gaps representing the as-manufactured clearances between the head insert and the cylinder. The initial gap sizes (from Reference 3) are as follows:

Vertical clearance between lands on head insert upper surface and cylinder.	0.001 in.
Diametral clearance between head insert upper land and ring insert upper land.	0.025 in.
Diametral clearance between head insert lower land and ring insert lower land.	0.010 in.

3.0 STRUCTURAL ANALYSIS RESULTS

Stress distributions for the cylinder and head insert are obtained for two loading conditions. The first loading condition represents the effects of the peak cylinder pressure, the temperature distributions of "Run 668", and the head insert-cylinder interaction. The second load case represents a "free thermal" condition. The stresses for the second case are caused by thermal gradients only, and do not include the effects of interaction (interference) due to relative thermal expansion of mating parts. The second load case is run for comparative purposes only.

The stress results are summarized in the form of color-coded stress contour plots (Figures 4 through 12). The von Mises effective stress distribution is shown for the cylinder, insert ring, combustion dome insert and manifold ring in Figures 4, 5 and 6. Comparison of these results with the free thermal stresses, as shown in Figures 8 and 9, reveals that the total stresses are largely associated with temperature gradients. The thermal stresses in the combustion dome insert are particularly high due to large temperature differences through the thickness. In addition, a strong radial interaction occurs between the head insert and the insert ring on their lower land surfaces. The effect of this interaction on the stresses can be seen by comparing Figures 7 and 10. As shown in Figure 10, the thermal gradients cause a free thermal compressive stress of about -160 ksi near the top of the combustion dome. As shown in Figure 7, the interaction with the insert ring increases the compressive stresses over the entire inside surface of the head, the largest value being -232 ksi near the lower inside edge of the dome.

The head-insert ring interaction analysis shows that there is a radial interaction on the lower land, but not on the upper land, except at the extreme upper corner. This contact status is consistent with the modeling assumptions of the heat transfer analysis of Reference 1. Reference 1 assumed an air gap on the upper land, and used a contact resistance on the lower land. In the vertical sense, only the inner two rings of contact elements on the head upper surface are closed. This contact status is also basically consistent with the thermal analysis of Reference 1, because contact on the outer rings could occur only on the surfaces of the very narrow lands between the slots cut in the top of the head insert. Bolt clamp-up could bring these outer lands into contact with the cylinder; however, bolt preload is not considered in the current analysis.

The piston and piston cap stresses are shown in Figures 11 and 12. The largest stresses occur in the outer land of the piston cap. As shown by Figure 12, these stresses are caused by hoop tension due to the fact that the outer land is relatively cold. The shank portion of the piston cap is also relatively cold; however in this region, the tensile stresses are partially relieved by the contact interaction between the cap shank and piston. The interaction analysis shows that all radially acting gap elements are closed on the cap shank. In the vertical sense, only the gap elements on the outer land are closed. Preload introduced by tightening of the retaining nut may keep the inner load in contact; however, this effect is not considered in the current analysis.

4.0 PISTON RING TEMPERATURE DISTRIBUTIONS

The temperature distributions in the piston rings are shown in Figures 13 and 14 for "RUN 668" and "RUN 659" respectively. The temperatures, as shown on each ring cross-section, do not vary around the circumference because they are modeled using axisymmetric elements. It is noted that the relative temperatures of the five rings are a strong function of the ring friction heat generation apportionment as given in Reference 1.

5.0 CONCLUSION

A three-dimensional finite element stress analysis of the Single Cylinder Test Engine has been performed for the pressure and temperature loadings of "Run 668" in Reference 1. The analysis shows that the highest stresses occur in the head insert and the piston cap, and that these stresses are largely associated with thermal gradients. Significant amounts of plasticity and creep relaxation can be expected in these two parts. A strong radial interference loading occurs on the lower land of the head insert, which could be eliminated by increasing the clearance between the head and the ring insert. The analysis shows that stresses in the deformation sensitive portion of the cylinder (below the insert ring) are generally less than 16000 psi. Since the temperatures in this region of the cylinder are less than 700 °F, plasticity and creep effects will not be important.

6.0 REFERENCES

1. adapco Report 26-02-001; "Engine Cycle Simulation And Detailed Heat Transfer Analysis of the Single Cylinder Test Engine with Correlation to Test Measurements", March 21, 1985.

2. Timoshenko and Goodier; "Theory of Elasticity", McGraw-Hill Book Co., 1970.

3. Drawings and sketches of S.C.T.E. Configuration provided by Teledyne.

Table 1 Material Property Values Used in Structural Models

PART	MATERIAL	ELASTIC MODULUS (psi)	COEFFICIENT OF THERMAL EXPANSION (IN/IN-°F)
Cylinder	1040 Steel	29000000	0.0000083
Fins	Cast Aluminum Alloy	10300000	0.0000130
Piston	Ductile Iron	17000000	0.0000058
Piston Press in Plug	304SS	22500000	0.0000090
Piston Cap	321SS	28000000	0.0000093
Piston Rings	Ductile Iron	17000000	0.0000058
Head insert	321SS	28000000	0.0000093
Ring Insert	4340 Steel	29000000	0.0000081
Manifold Ring	Mild Steel	29000000	0.0000075

Note: All materials are assumed to have a Poisson's ratio of 0.3

Figure 1 Aircraft Diesel Single Cylinder Test Engine
Cylinder, Head, Manifold Ring Assembly
Three-Dimensional Structural Finite Element Model

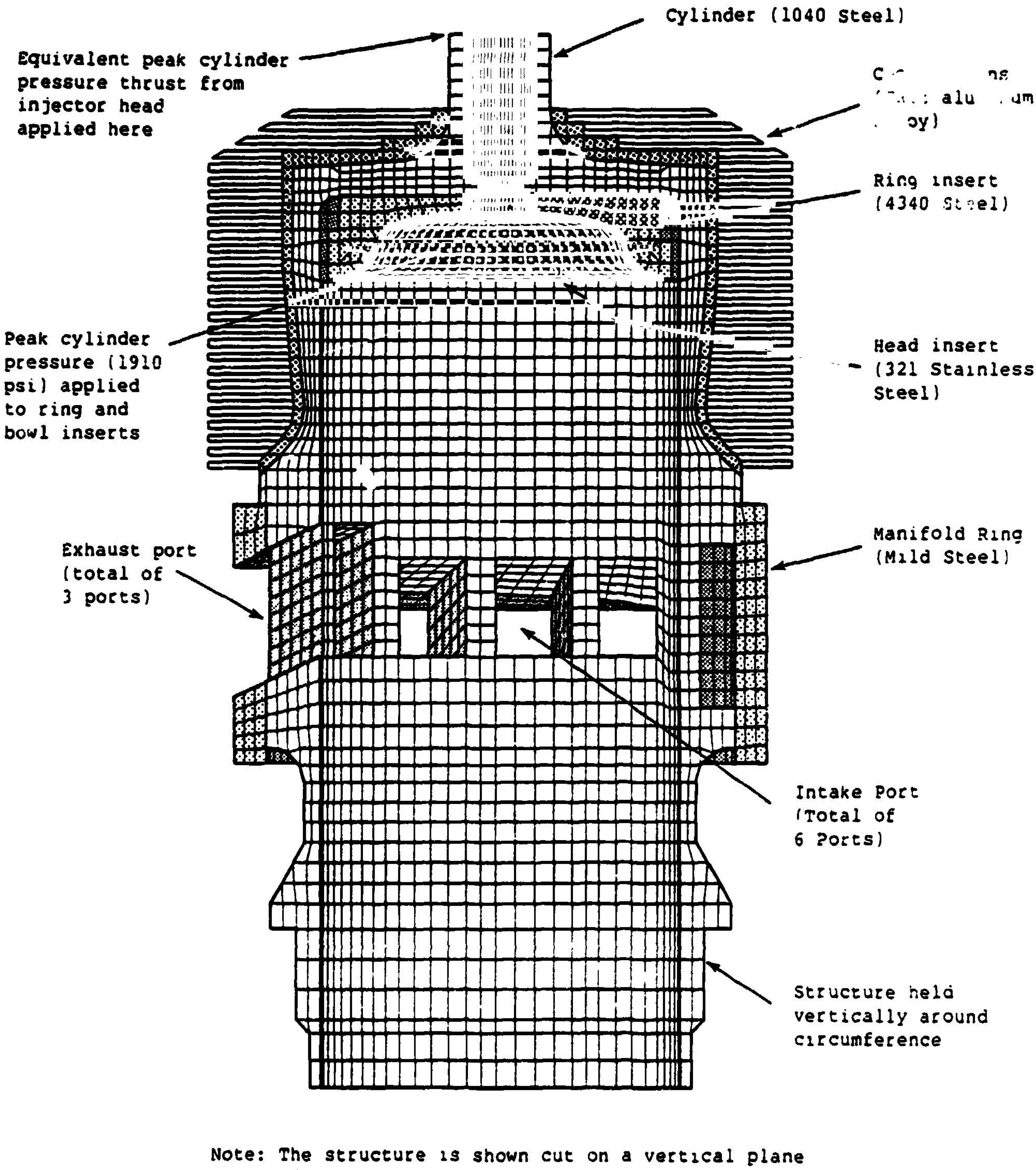

Note: The structure is shown cut on a vertical plane of symmetry. One-half of the engine is modeled. Symmetry boundary conditions are imposed on the cut plane.

Figure 2 Cylinder - Head Insert Interaction Analysis

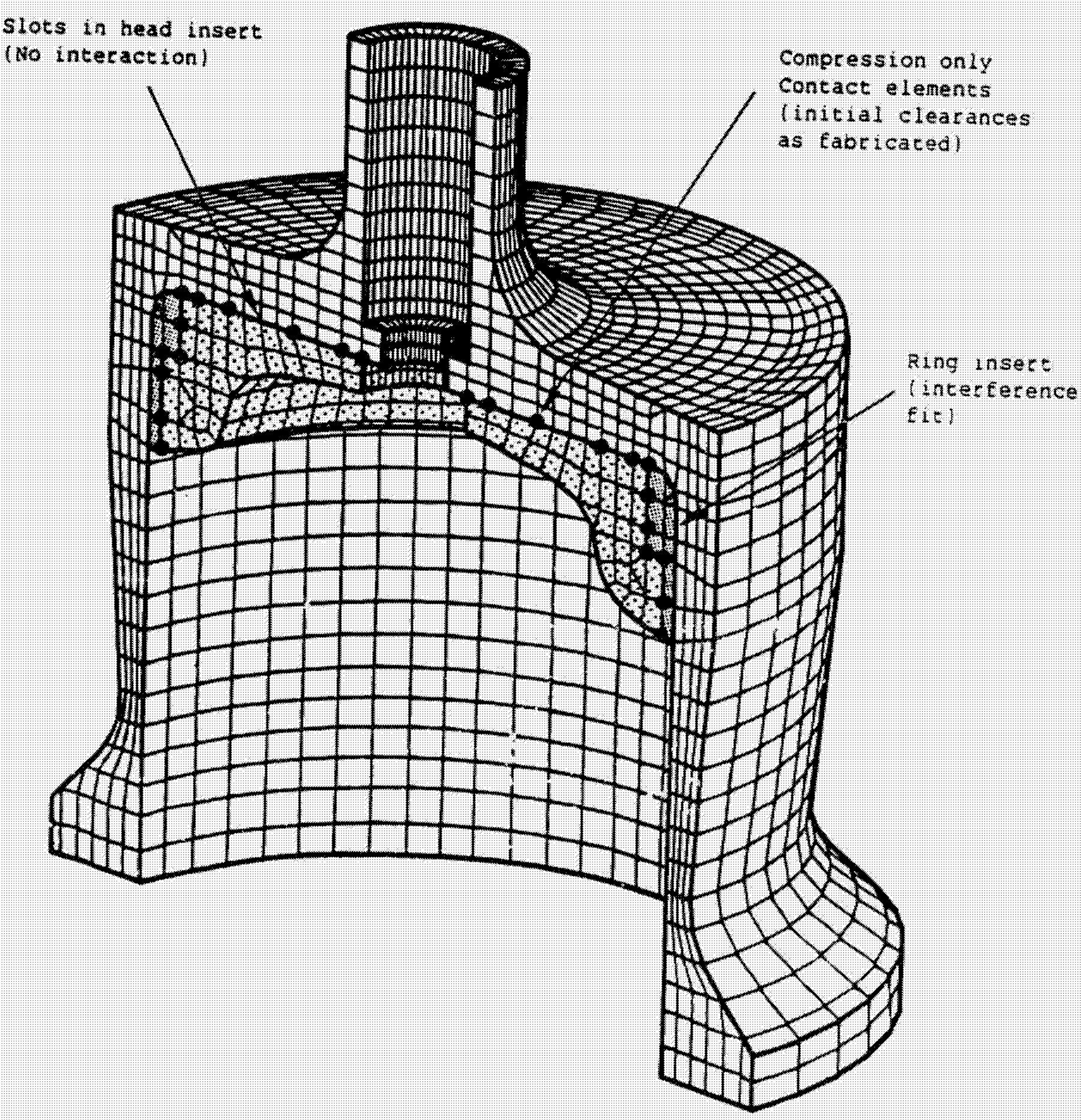

Figure 3 Piston - Piston Cap Structural Model

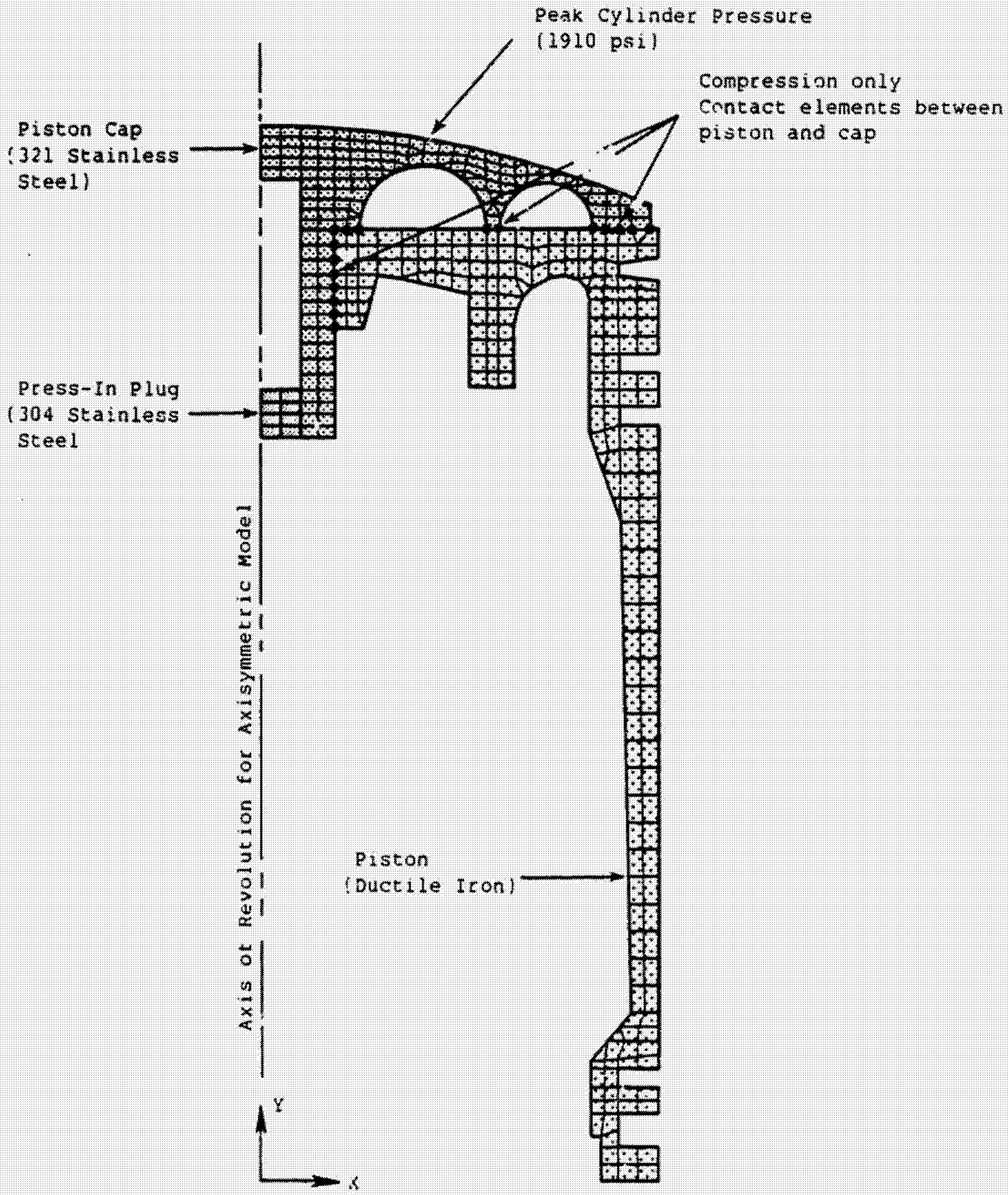

FIGURE 4: CYLINDER - RING INSERT
PEAK PRESSURE + THERMAL
EFFECTIVE STRESS (psi)

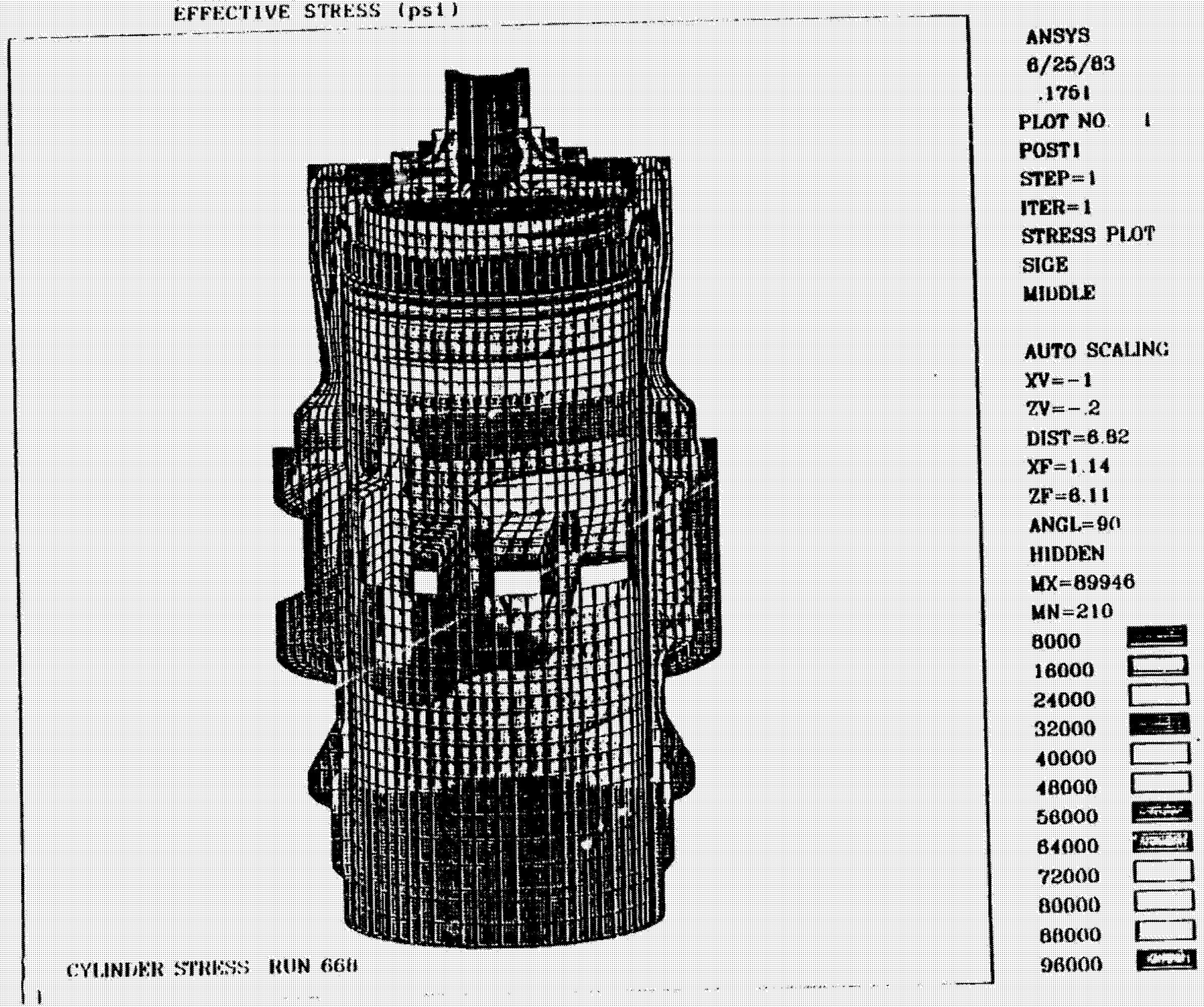

FIGURE 5: CYLINDER
PEAK PRESSURE + THERMAL
EFFECTIVE STRESS (psi)

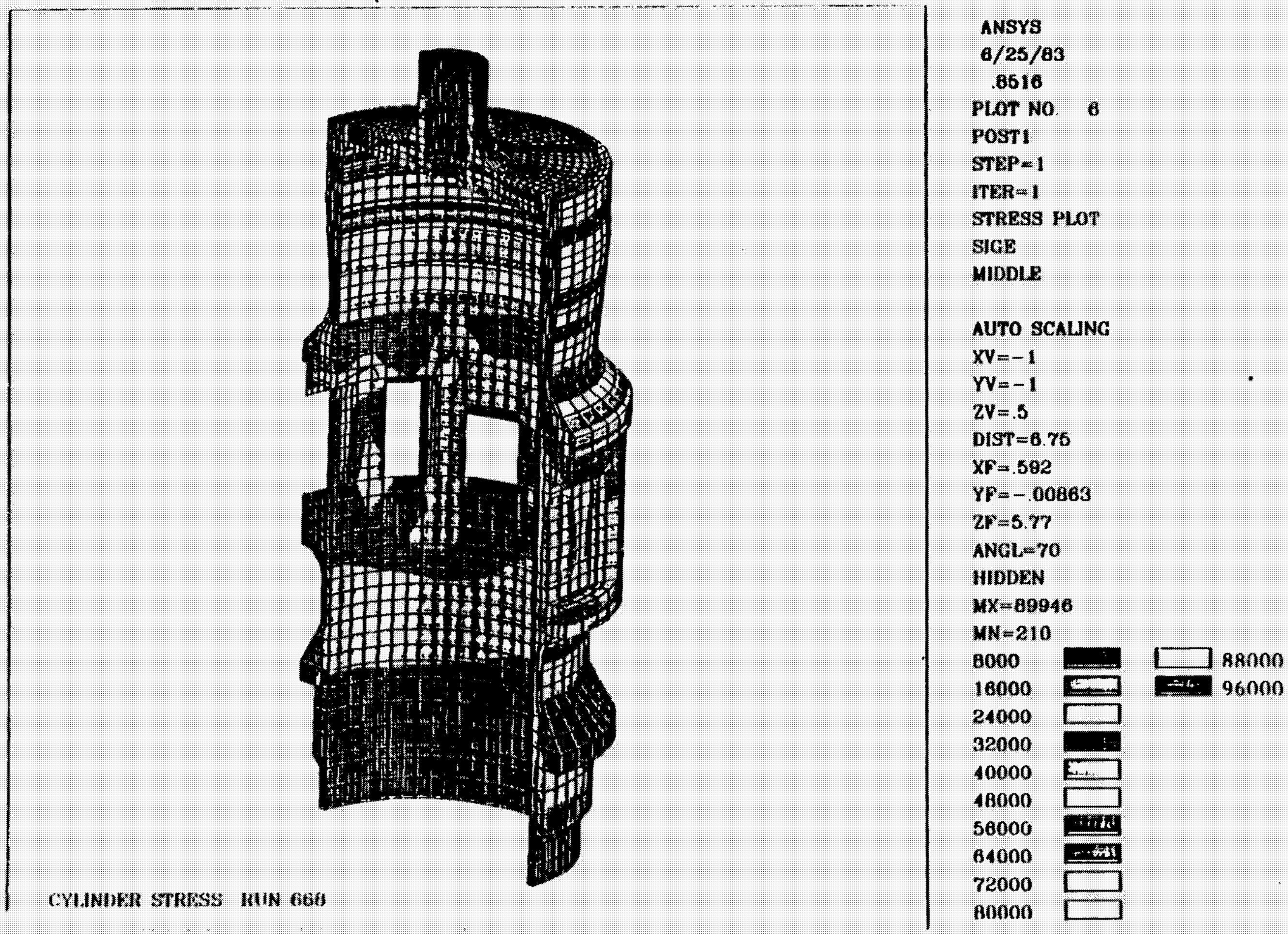

FIGURE 6: HEAD INSERT
PEAK PRESSURE + THERMAL
EFFECTIVE STRESS (psi)

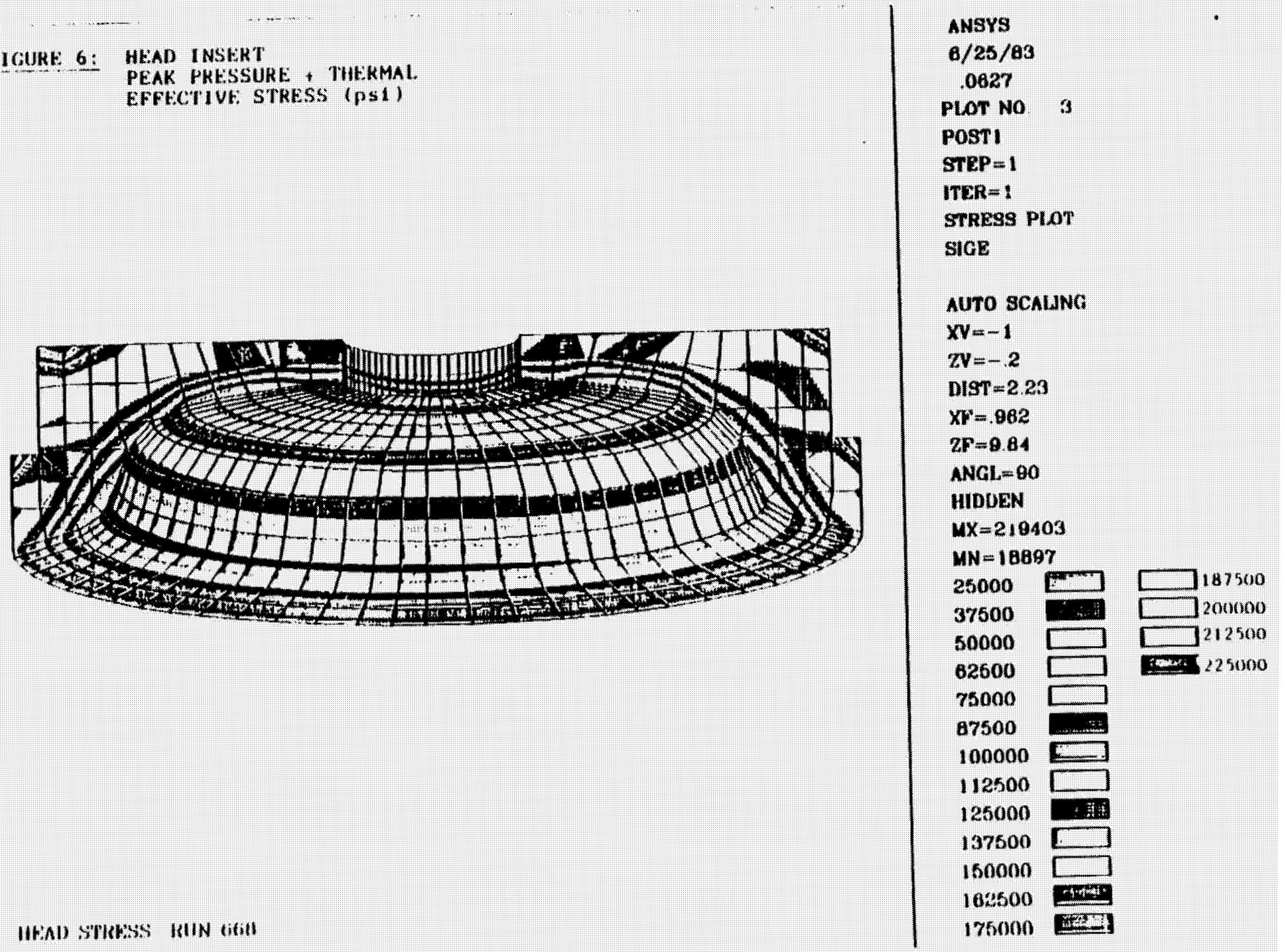

FIGURE 8: CYLINDER
FREE THERMAL
EFFECTIVE STRESS (psi)

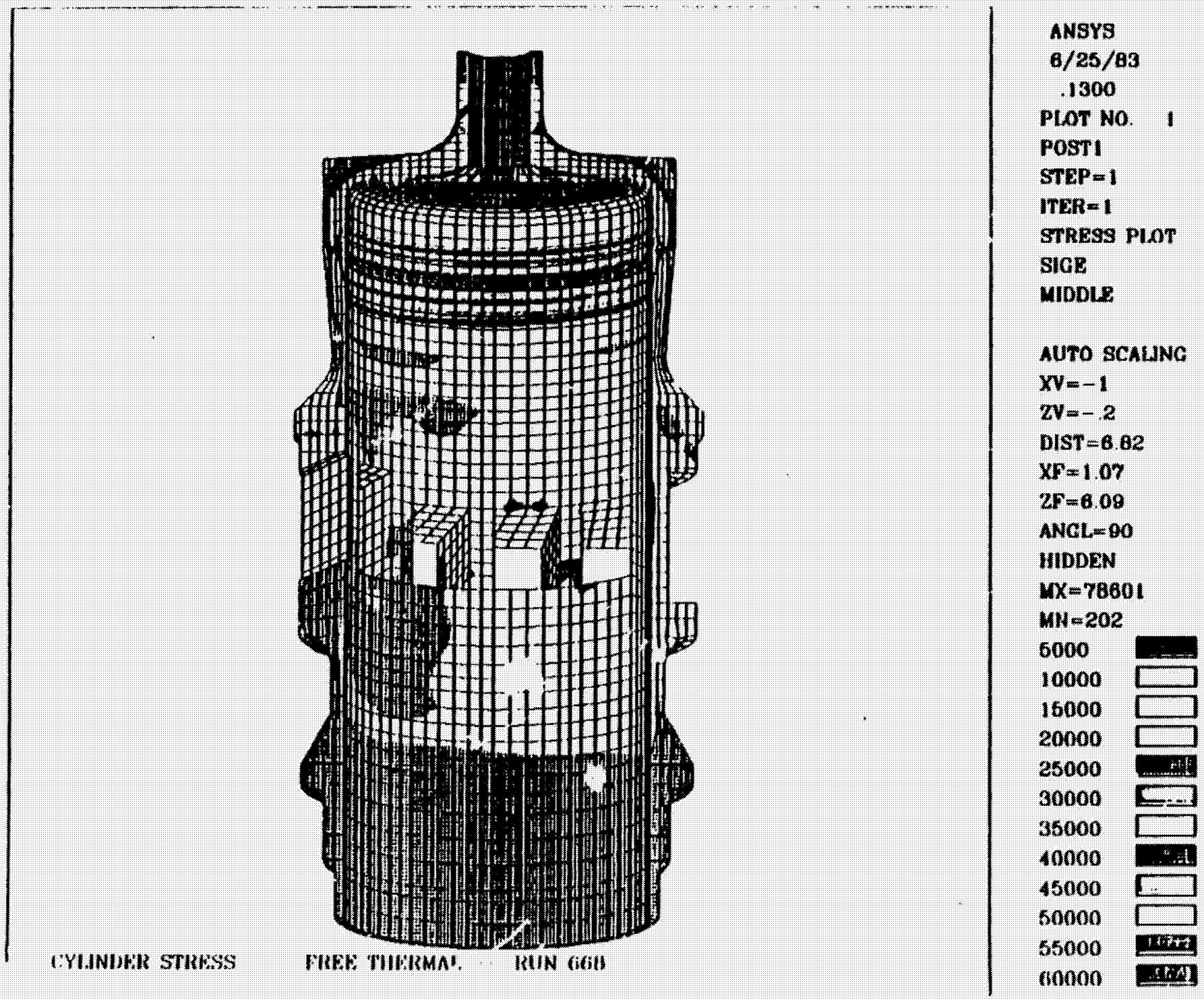

FIGURE 9 HEAD INSERT
FREE THERMAL
EFFECTIVE STRESS (p 1)

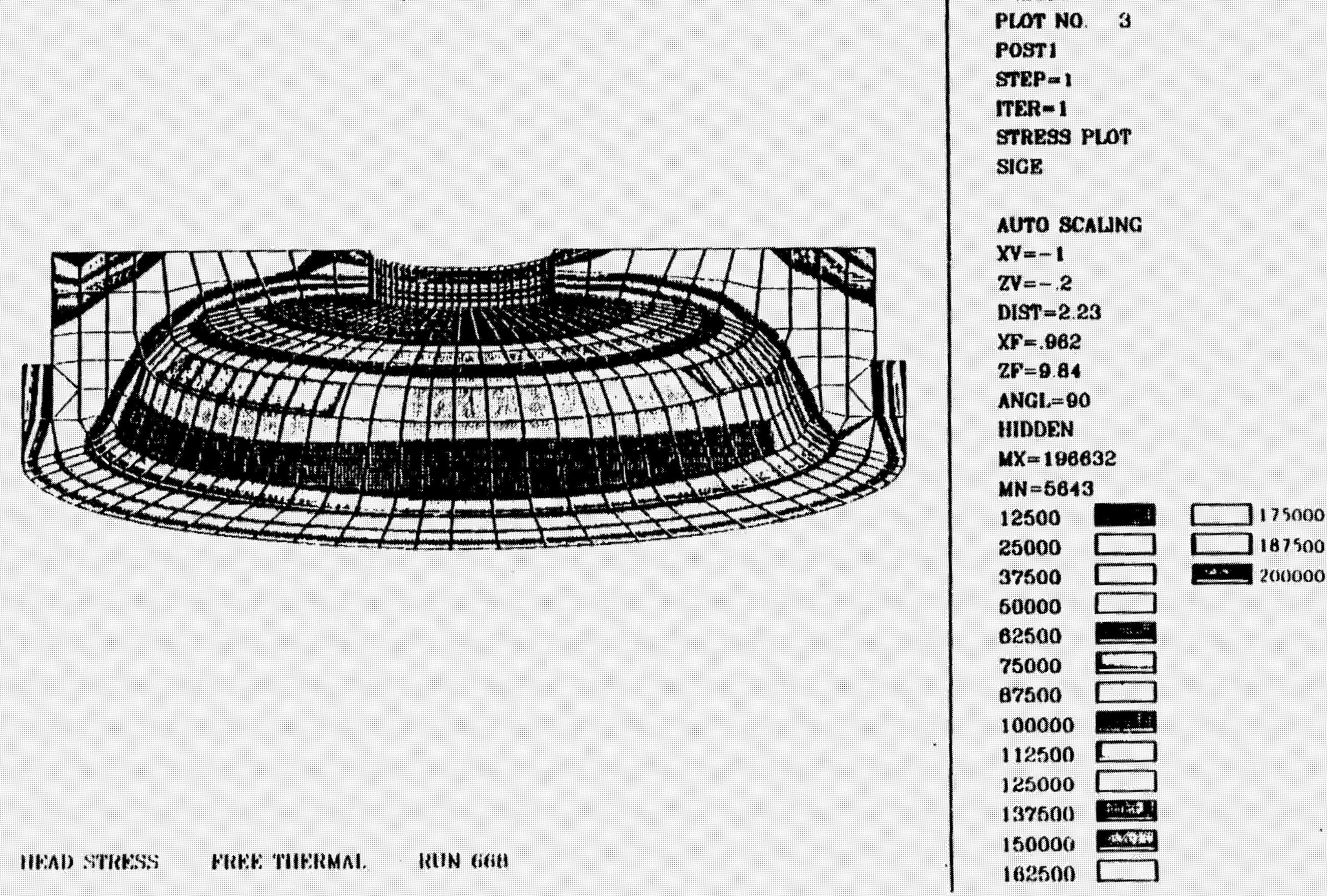

FIGURE 10: HEAD INSERT
FREE THERMAL
MINIMUM NEGATIVE PRINCIPAL STRESS (psi)

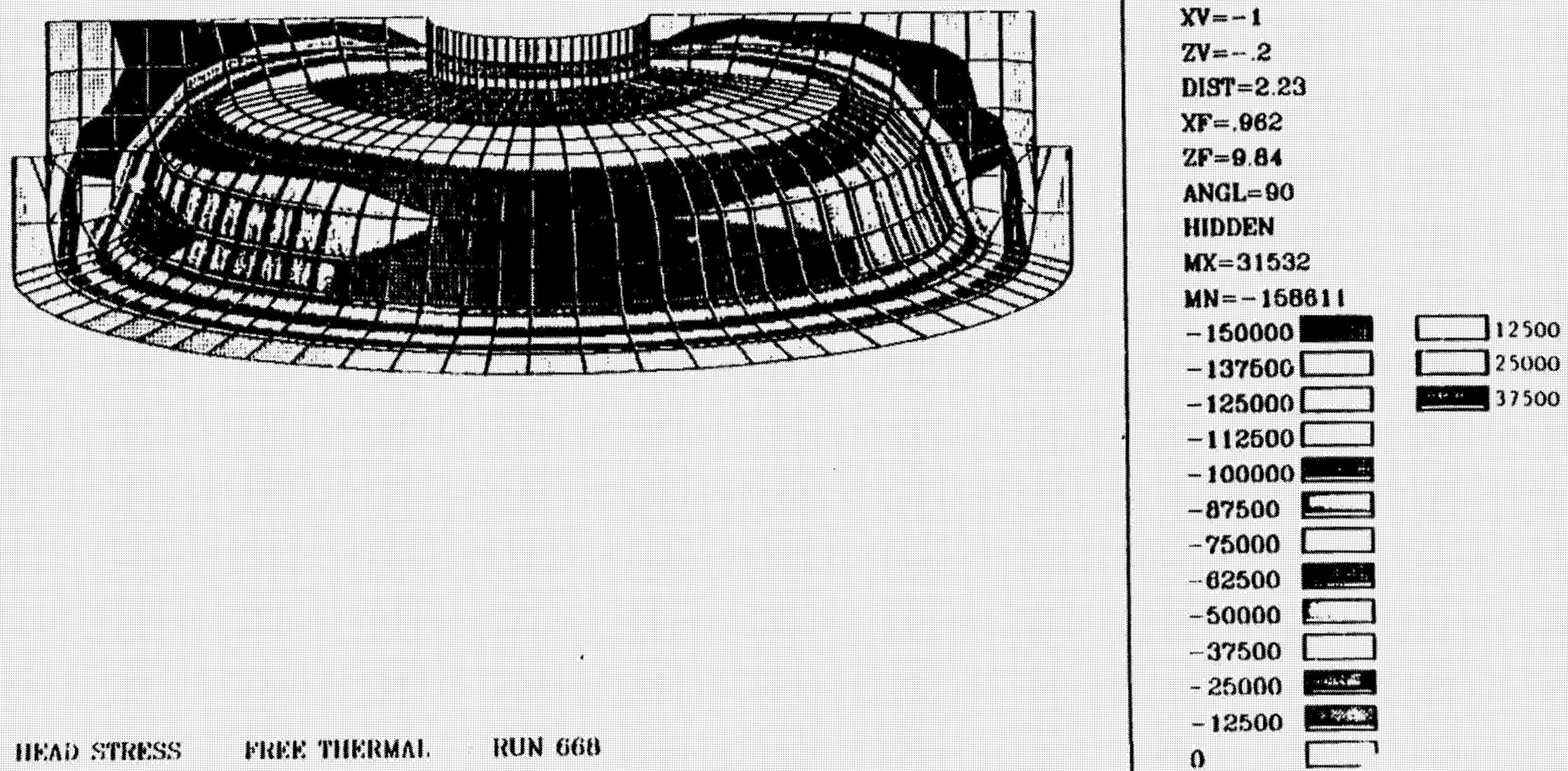

HEAD STRESS FREE THERMAL RUN 668

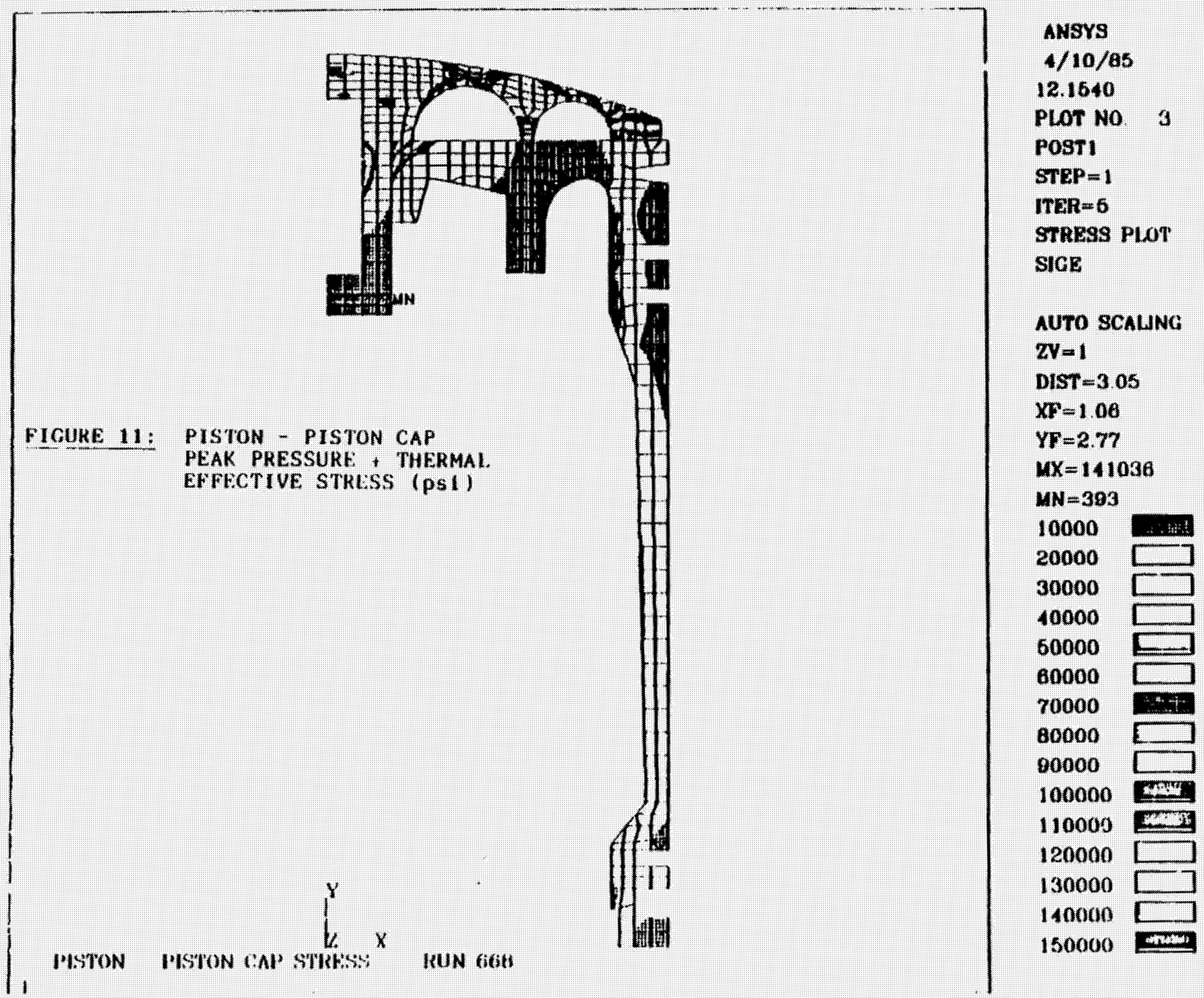

FIGURE 11: PISTON - PISTON CAP
PEAK PRESSURE + THERMAL
EFFECTIVE STRESS (psi)

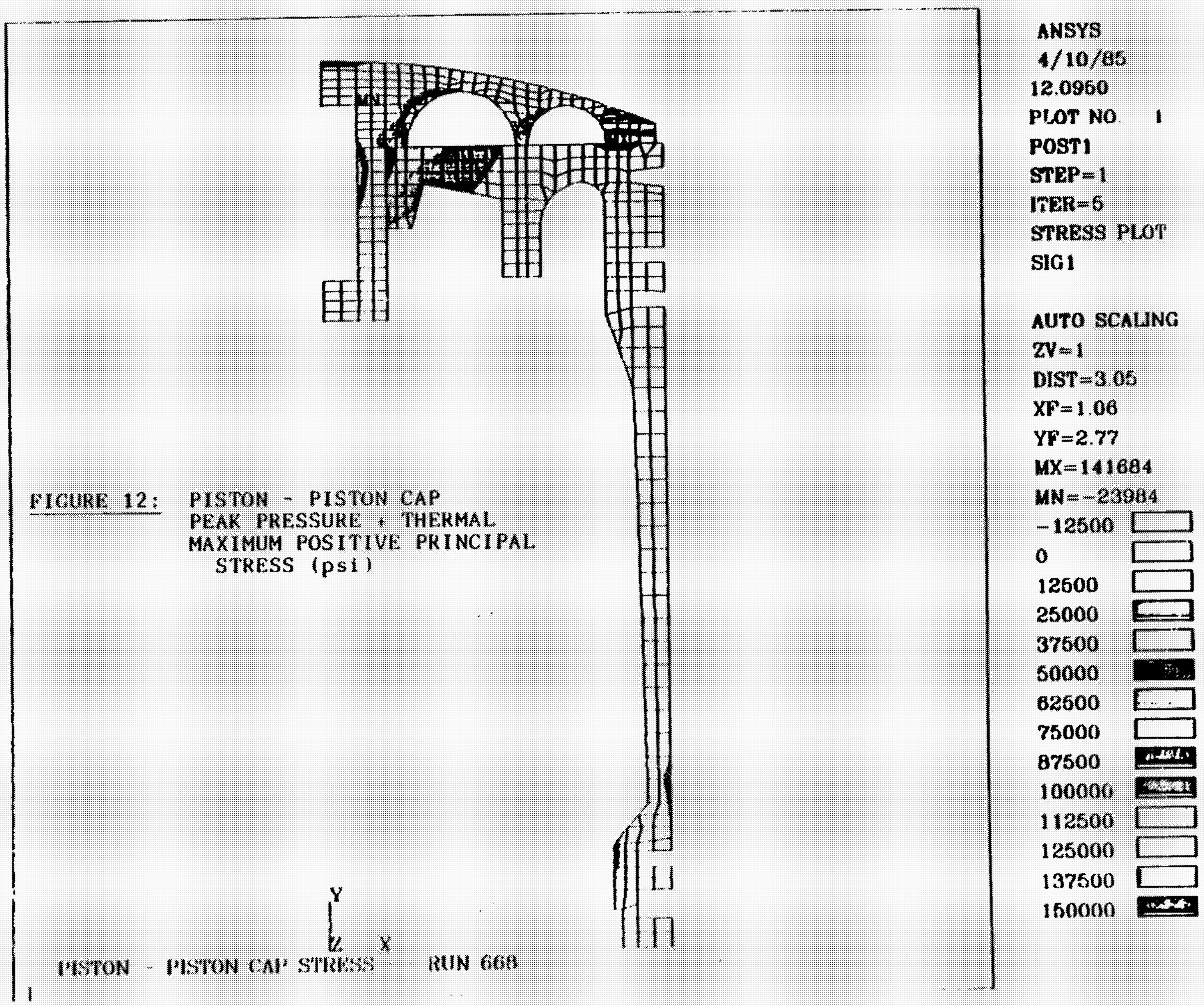

FIGURE 12: PISTON - PISTON CAP
PEAK PRESSURE + THERMAL
MAXIMUM POSITIVE PRINCIPAL
STRESS (psi)

FIGURE 13 PISTON RING TEMPERATURES (°F)
RUN 668

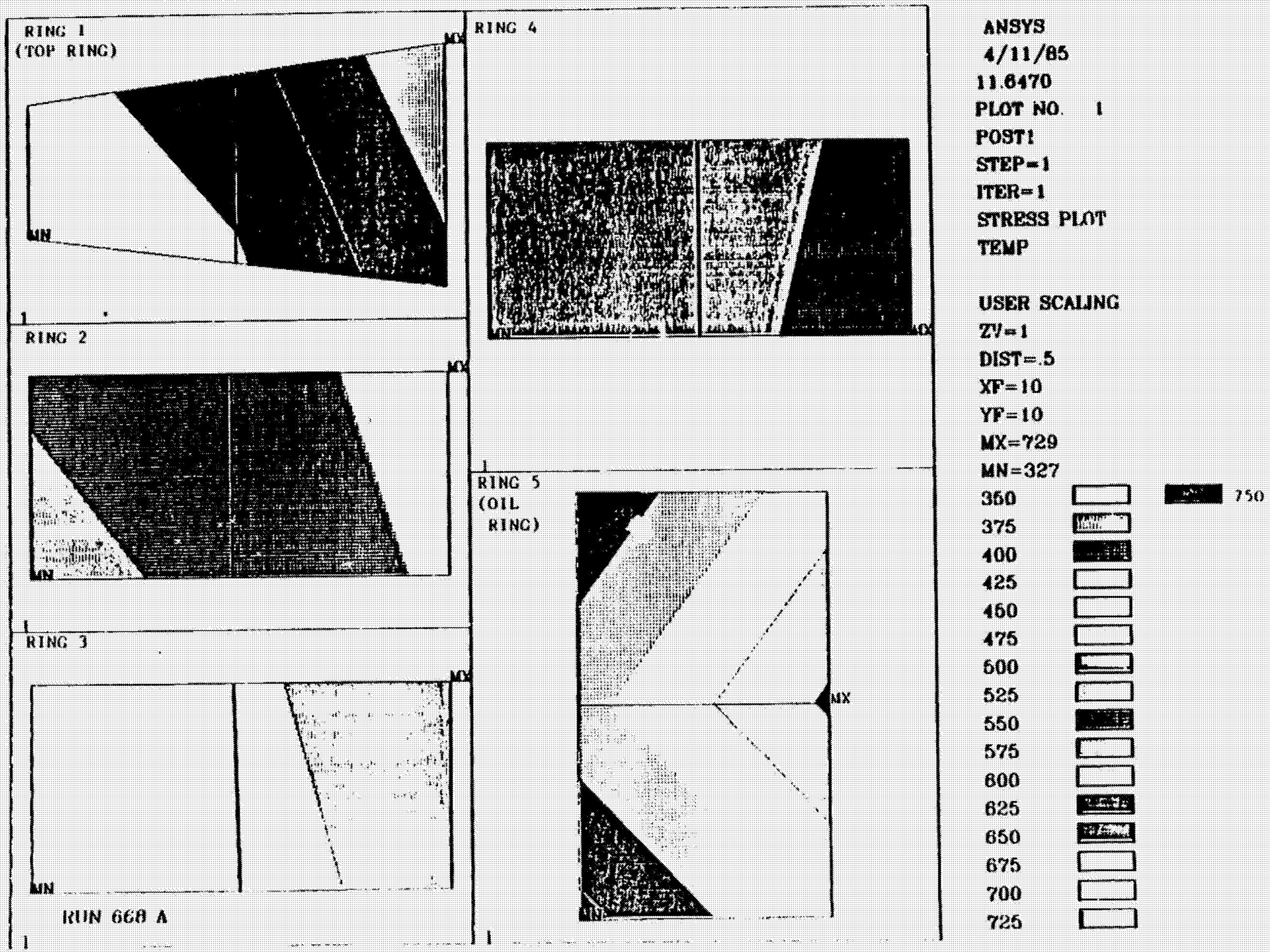

FIGURE 14 PISTON RING TEMPERATURES (°F)
RUN 659

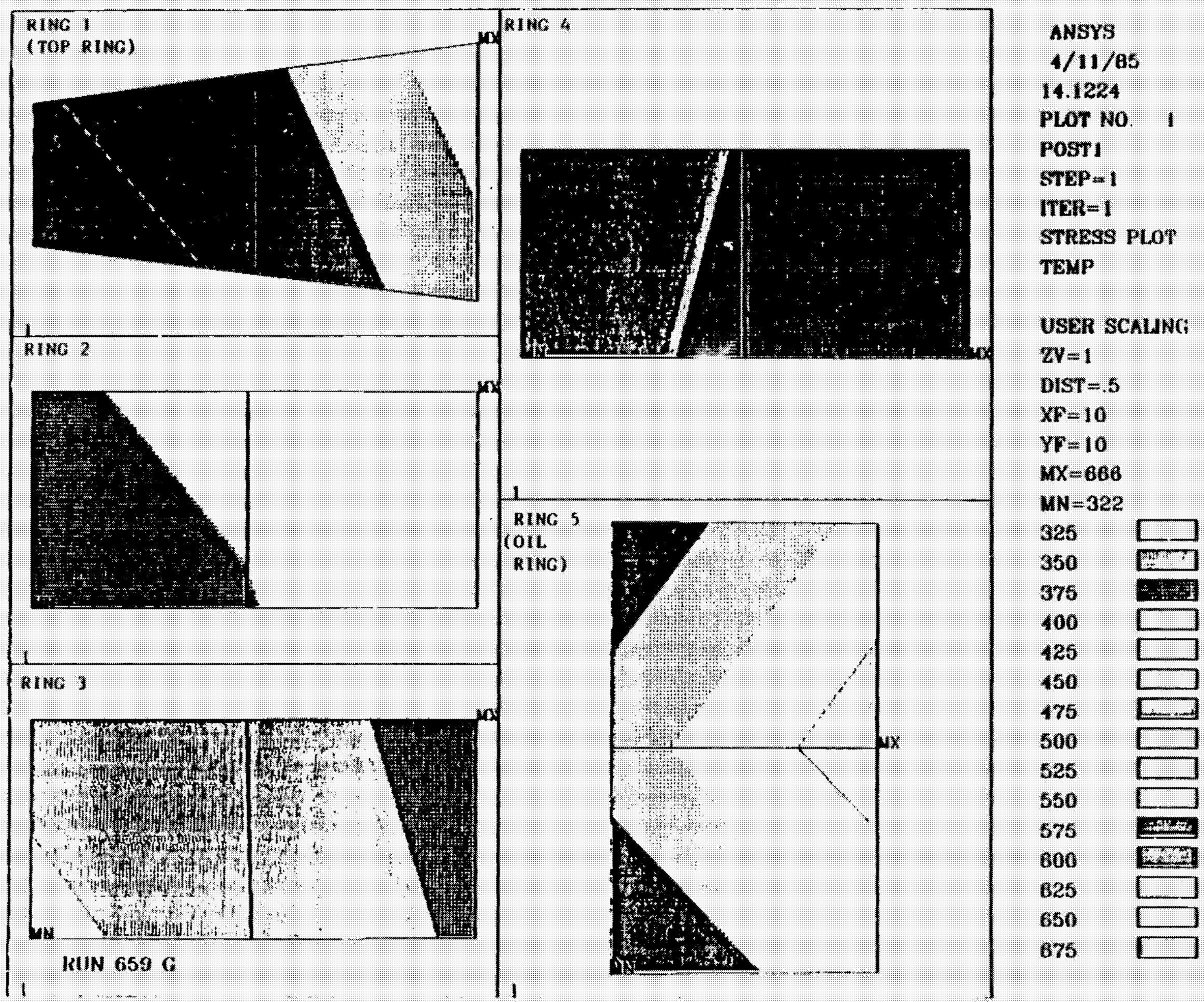

A P P E N D I X   I I I

SECOND GENERATION SINGLE CYLINDER TEST ENGINE PARTS LISTS

APPENDIX III

SECOND GENERATION SINGLE CYLINDER TEST ENGINE

PARTS LIST (INSULATED VERSION)

TITLE	DWG. SIZE	PART NO.
1. AIRCRAFT DIESEL ASSEMBLY SINGLE CYLINDER TEST	K	EACD104L-002
2. INJECTOR NOZZLE & HOLDER ASSEMBLY	*B	EACD100-001
3. CYLINDER HEAD	*F	EACD101-007
4. CYLINDER BARREL	F	EACD101-008
5. CYLINDER LINER	F	EACD101-009
6. PLATE, ENGINE TOP DECK	*F	EACD101-010
7. INSERT, CYLINDER HEAD	D	EACD101-011
8. PISTON CAP	D	EACD101-012
9. INSULATIVE DISC, CYLINDER HEAD	*C	EACD101-013
10. INSULATION RING, CYLINDER HEAD	*C	EACD101-014
11. INSULATION DISC, PISTON CAP	C	EACD101-015
12. NUT, INJECTOR NOZZLE HOLDER	*D	EACD101-016
13. PLATE, INJECTOR NOZZLE HOLD DOWN	*C	EACD101-017
14. COMFORMABLE SHIM, PISTON CAP	B	EACD101-018
15. NUT, 12 POINT 3/8-24 (24 REQUIRED)	*A	EACD101-019
16. GASKET, CYLINDER HEAD	*D	EACD101-020
17. PIN, LINER ALIGNMENT TO CYL. BARREL	B	EACD101-023

* ALSO USED ON COOLED VERSION

PAGE 2

TITLE	DWG. SIZE	PART NO.
18. CONNECTING ROD ASSEMBLY	*D	EACD102-009
19. PISTON	*C	EACD102-010
20. STUD, 3/8 X 4.00 LG. (12 REQUIRED)	*B	EACD102-018
21. STUD, 3/8 X 2.25 LG. (12 REQUIRED)		EACD102-019
22. PISTON REWORK		EACD102-020
23. WASHER, FLAT	B	EACD104-010
24. BOLT (SCREW) (PISTON CAP)	B	EACD104-011
25. DISC SPRING (BELLVILLE WASHER)	B	EACD104-012
26. NUT, JAM 3/8-34	B	EACD104-013
27. SCREW 3/8-16 (2 REQUIRED)	*	MS90725-73
28. O'RING, INJECTOR TO NUT (2 REQUIRED)	*	MS9388-016
29. O'RING, PLATE TO CRANKCASE	*	MS9388-168
30. O'RING, CYLINDER LINER TO BARREL (LOWER)	*	MS9388-248
31. O'RING, CYLINDER BARREL TO PLATE	*	MS9388-255

* ALSO USED ON COOLED VERSION

APPENDIX III

SECOND GENERATION SINGLE CYLINDER TEST ENGINE

PARTS LIST (COOLED VERSION)

TITLE	DWG. SIZ.	PART NO.
1. AIRCRAFT DIESEL ASSEMBLY SINGLE CYLINDER TEST	K	EACD104L-003
2. INJECTOR NOZZLE & HOLDER ASSEMBLY	*B	EACD100-001
3. CYLINDER HEAD	*F	EACD101-007
4. PLATE, ENGINE TOP DECK	*F	EACD101-010
5. INSULATION DISC, CYLINDER HEAD	*C	EACD101-013
6. INSULATION RING, CYLINDER HEAD	*C	EACD101-014
7. NUT, INJECTOR NOZZLE HOLDER	*D	EACD101-016
8. PLATE, INJECTOR NOZZLE HOLD DOWN	*C	EACD101-017
9. NUT, 12 POINT 3/8-24 (24 REQUIRED)	*A	EACD101-019
10. GASKET, CYLINDER HEAD	*D	EACD101-020
11. CYLINDER BARREL	F	EACD101-021
12. CYLINDER LINER	F	EACD101-022
13. PIN, LINER ALIGNMENT TO CYL. BARREL	*B	EACD101-023
14. INSERT, CYLINDER HEAD	D	EACD101-024
15. JACKET, CYLINDER HEAD COOLING	F	EACD101-025
16. PISTON	*C	EACD102-010
17. CONNECTING ROD ASSEMBLY	*D	EACD102-005

* ALSO USED ON CERAMIC VERSION

PAGE 2

TITLE	DWG. SIZE	PART NO.
18. STUD, 3/8 X 4.00 LG. (12 REQUIRED)	*B	EACD102-018
19. STUD, 3/8 X 2.25 LG. (12 REQUIRED)	*B	EACD102-019
20. PISTON CAP	D	EACD104-004
21. PISTON REWORK	C	EACD104-005
22. DISC, SPRING (BELLVILLE WASHER) (4 REQUIRED)	B	EACD104-006
23. NUT, JAM 1/2-13 UNC-28	B	EACD104-007
24. SPACER (PISTON CAP)	B	EACD104-008
25. INSULATION DISC, PISTON CAP	C	EACD104-009
26. SCREW, 3/8-16 X 3.75 LG. (2 REQUIRED)	*	MS90725-73
27. O'RING, INJECTOR TO NUT (2 REQUIRED)	*	MS9388-016
28. O'RING, PLATE TO CRANKCASE	*	MS9388-168
29. O'RING, CYLINDER LINER TO BARREL (LOWER)	*	MS9388-248
30. O'RING, CYLINDER LINER TO BARREL (3 REQUIRED) (UPPER)		MS9388-251
31. O'RING, CYLINDER BARREL TO PLATE	*	MS9388-255
32. O'RING, COOLANT JACKET TO CYLINDER HEAD		MS9388-262

* ALSO USED ON CERAMIC VERSION

A P P E N D I X   I V

FEASIBILITY ASSESSMENT OF LOW HEAT REJECTION CONFIGURATION OF THE TELEDYNE LIGHTWEIGHT DIESEL ENGINE

adapco
ANALYSIS & DESIGN APPLICATION CO., LTD

FEASIBILITY ASSESSMENT OF LOW HEAT REJECTION CONFIGURATION OF THE TELEDYNE LIGHTWEIGHT DIESEL ENGINE

Prepared for:

Teledyne Continental Motors

Prepared by:

Analysis and Design Application Company, Ltd.

Prepared by: Jerry Coffey
Jerry Coffey

Approved by: Peter S. MacDonald
Peter S. MacDonald

60 BROADHOLLOW ROAD, MELVILLE, NEW YORK 11747 516 - 549-2300

TABLE OF CONTENTS

1.0 INTRODUCTION

The objective of the engineering effort reported herein is to provide design guidance and feasibility assessment, through detailed thermal and structural analysis, in the development of a low heat rejection configuration of the Teledyne lightweight diesel engine for aircraft application. This phase of the overall development activity involves investigating a single cylinder engine which lends itself to testing of components plus establishing performance and emissions data.

The report presents the insulated single cylinder test engine configurations investigated followed by detailed descriptions of the thermal and stress analyses and presentation of their results. In the thermal analysis section, a description of the analytical model and the method of analysis is provided along with the boundary conditions used. The stress analysis section covers the structural assessment of the head, cylinder liner, and piston cap. The last section of the report addresses conclusions from the analytical results and recommendations with respect to a baseline configuration to be tested.

2.0 INSULATED TEST ENGINE CONFIGURATIONS

The low heat rejection, monolithic ceramic insulated, single cylinder test engine combustion chamber configuration is illustrated in Figure 1. As can be seen in the figure, the cylinder and head have been significantly changed from the air cooled one piece design. This was done both to facilitate testing of a number of components plus the need to accommodate the monolithic ceramic inserts. The metal portion of the bolt-on head is relatively massive to provide room for the head bolt circle plus sufficient hoop integrity to maintain a press fit on the combustion bow insert. The press fit is necessary to overcome the thermal induced tensile stresses on the back side (cold side) of the ceramic combustion bowl insert. The cylinder portion of the engine allows for easy replacement of cylinder liner assemblies. The outer cylinder block provides a bolting flange for the head with the intake/exhaust manifold torodial structure accommodated just under the flange. The liner assembly insert consists of a metal reinforcing outer cylinder and a ceramic inner cylinder. A radial interference between the parts provides retention of one to the other while reducing the pressure and thermal induced tensile stresses in the ceramic. The piston assembly is made up of a two piece ceramic cap and a cast iron base. The cap is broken up into two parts in order to reduce the tensile stresses caused by through thickness thermal gradients. The upper mushroom shaped cap is retained by a radial press fit at its base. The ceramic disk is retained by being trapped between the metal base and upper cap. There is a small ledge to keep the disk from moving in some radial direction. Note that in this design the piston is fully covered by ceramic insulation on its combustion surface face. This is typically not the case in the more classical low heat rejection diesel with the combustion bowl in the top of the piston and valves in the head. Full coverage of the top of the piston is important both from a heat loss point of view and the need to keep the rings cool. The thermal shield under the ceramic cap is optional. It is used to reduce the heat loss to the oil lubrication heat sink.

The configuration illustrated in Figure 1 was assessed using zirconia and alumina as the ceramic insulator material. Upon turning to silicon nitride as the ceramic, it was necessary to face the fact that press fits could not be counted upon due to the small thermal expansion coefficient for silicon nitride in comparison to metal. Figure 2 illustrates the modified low heat rejection, monolithic ceramic insulated, single cylinder test engine combustion chamber configuration. As indicated in the figure, the cylinder liner assembly has been replaced by a single piece ceramic cylinder of silicon nitride. This was done to eliminate an assembly problem. In addition, the metal outer reinforcement structure would not be in contact with the cylinder at operating temperatures due to coefficient of thermal expansion differences. The upper ledge of the cylinder insert was moved up towards the top, near the gasketed joint, to reduce problems with maintaining preload in the joint. This problem is the result of the axial differential growth of the liner versus the block, again due to expansion mismatch. The combustion bowl insert was increased in outer diameter and an insulating intermediate ceramic disk placed above it to help reduce the thermal induced tension stresses on the bowl's upper surface. The thermal shield under the piston cap was again used to reduce heat loss to the lubrication oil, since the silicon nitride is a much better conductor than the zirconia.

3.0 THERMAL ANALYSIS

Presentation of the thermal analysis is broken into four parts. First, the method of analysis is addressed and it is followed by a presentation of the ANSYS based finite element models. Next, the detailed boundary conditions used are illustrated. Last, the resulting component temperatures for three (zirconia, alumina, and silicon nitride) ceramic insulation configurations are presented.

3.1 Analytical Methodology

In the overall thermal analysis of the single cylinder engine, there are two coupled analyses which must be carried out. It is important to note that thermal distribution is far more important in an insulated engine than in a conventional engine since the temperature variation is what fails the ceramic. The first of the analyses is a cycle simulation which provides the thermodynamics of the combustion chamber gas. It is necessary in this cycle simulation to specify the combustion chamber wall temperatures. Temperatures to be specified are combustion bowl inner surface, piston cap top surface, and cylinder liner inner surface. Next, using the cycle simulation temperatures of the combustion gas as a function of crank angle, a cycle average thermal analysis of the overall engine is carried out. The resulting combustion surface temperatures are compared with those which were used in the cycle simulation analysis. If there is a significant difference, the new surface temperatures are input into the cycle simulation and the coupled analysis is repeated.

The cycle simulation analyses were carried out using the Benson program. The cycle simulation converged results were made available to **Teledyne** but are not included in what follows.

The combustion chamber temperatures can be calculated on a steady state basis provided that the effective steady state thermal boundary conditions are represented in the analytical model. In the case of the inner surface of the combustion chamber, the effective boundary conditions are called the "cycle-average temperature," and the "cycle-average heat transfer coefficient." The cycle-average temperature and the cycle-average heat transfer coefficient are the steady boundary values which cause the same total heat to cross the inner surface of the combustion chamber as the engine cycle.

The piston also dissipates heat in an unsteady process by virtue of its motion in the cylinder. The cylinder bore has a large axial thermal gradient, the upper portion being heated by the combustion gases and the lower portion being cooled by the mixture of air and oil in the crankcase. As the piston and rings slide up and down in the cylinder, they are alternately exposed to the high and low cylinder temperatures. In addition, the thermal boundary conditions on the cylinder bore are unsteady by virtue of the piston motion, as well as the unsteady conditions in the combustion chamber.

The purpose of this part of the report is to present the theoretical basis and methodology for reduction of the combustion chamber heat transfer analysis to fully steady state problem. This permits calculation of temperatures in the piston, cylinder, head, and other engine components by means of steady state three-dimensional finite element models.

Computation of Cycle Average Conditions in the Combustion Chamber

In deriving the effective steady state boundary conditions, the basic approach is to write down the unsteady equations governing the physical process and the steady equations governing the analytical model, then to combine the equations so as to conserve the total heat transferred during the engine cycle.

Equations (1) and (2) below are unsteady and the steady forms, respectively, of Newton's convective heat transfer equation as applied to the combustion chamber surface. The steady factors in equation (1) are the convection area, A, and the surface temperature, T_s, which we approximate as a constant in relation to the extremely unsteady gas temperature, T_g (ϕ). The unsteady factors are expressed as functions of crank angle, ϕ, rather than time to make the equations independent of engine speed. The rate of heat transfer is then measured per degree of crank angle, CA, rather than per unit time.

(1) $$q(\phi) = h(\phi)\ A\ [T_g(\phi) - T_s]$$

where,

$q(\phi)$ = rate of heat transfer (BTU/CA)

$h(\phi)$ = heat transfer coefficient, or unit thermal conductance (BTU/CA-Ft^2-°F)

A = heat transfer area (Ft^2)

$T_g(\phi)$ = gas temperature (°F)

T_s = surface temperature (°F)

ϕ = crank angle (deg.)

(2) $$\bar{q} = \bar{h}\ A\ [\bar{T}_g - T_s]$$

where,

$\bar{q}$ = cycle average rate of heat transfer (BTU/CA)

$\bar{h}$ = cycle average heat transfer coefficient (BTU/CA-Ft^2-°F)

A = heat transfer area (Ft^2)

$\bar{T}_g$ = cycle average temperature (°F)

T_s = surface temperature (°F)

In order to conserve the total heat transferred during the cycle, Q, we must satisfy the following relation:

(3) $$Q = 360\ \bar{q} = \int_0^{360} q(\phi)\ d\phi$$

Hence, the cycle average rate of heat transfer is defined by equation (4).

(4) $$\bar{q} = \frac{1}{360}\int_0^{360} q(\phi)\ d\phi$$

Similarly, the cycle average heat transfer coefficient is defined by equation (5).

(5) $$\bar{h} = \frac{1}{360}\int_0^{360} h(\phi)\ d\phi$$

Integrating equation (1) over the cycle, and dividing by 360, we obtain:

(6) $$\frac{1}{360}\int_0^{360} q(\phi)\ d\phi = \frac{A}{360}\int_0^{360} h(\phi)\ T_g(\phi)\ d\phi - \frac{A}{360}\int_0^{360} h(\phi) T_s\ d\phi$$

Combining equations (4), (5), and (6) we obtain:

(7) $$\bar{q} = \frac{A}{360}\int_0^{360} h(\phi)\ T_g(\phi)\ d\phi - \bar{h}\ A\ T_s$$

Comparing each term in equation (7) with the corresponding term in equation (2), it is evident that,

$$(8) \qquad \bar{h}\, A\, \bar{T}_g = \frac{A}{360} \int_0^{360} h(\phi)\, T_g(\phi)\, d\phi$$

Solving equation (8) for $\bar{T}_g$, we obtain the definition of the cycle average temperature:

$$(9) \qquad \bar{T}_g = \frac{1}{360\, \bar{h}} \int_0^{360} h(\phi)\, T_g(\phi)\, d\phi$$

By means of equations (5) and (9) we can calculate the cycle average boundary conditions for use in the steady state heat transfer model. The unsteady boundary conditions, $h(\phi)$ and $T_g(\phi)$, are generated in a tabular format by the engine cycle simulation program. These data are then integrated numerically according to equations (5) and (9). Hence, $\bar{h}$ and $\bar{T}_g$ can be calculated on any convection area, A, for which the unsteady conditions, $\bar{h}(\phi)$ and $\bar{T}_g\,(\phi)$ are given.

Modeling of Piston to Cylinder Heat Transfer

The problem of piston-to-cylinder heat transfer is similar in that it is an unsteady, cyclic process, which must be analytically reduced to an equivalent steady state process. However, in the previous case we were concerned only with forced convection, whereas in this case, we need to thermally link the piston (and rings) to the cylinder. In the finite element model, this thermal linkage is achieved by means of convection link elements. The governing equation for each convection link is as follows:

(10) $q = h\,A\,[T_i - T_j]$

Each convection link provides a heat conduction path of thermal conductance, hA, between node i and node j at temperatures T_i and T_j respectively. If node i is a node on the piston outer surface which slides past a node j on the cylinder bore, as the piston travels up and down, then a convection link element will need to be defined between nodes i and j. In this manner, a set of convection links will thermally link each piston node to an axial line of nodes on the cylinder extending from the TDC position of the piston node to the BDC position of the piston node. This is illustrated in Figure 3.

If both the piston and cylinder are modeled three-dimensionally, several hundred--if not several thousand--such links will be required. The problem then becomes one of finding the correct conductance, hA, for each link. As a matter of analytical convenience we separate the total conductance into its two factors, h and A, and assign each a different physical significance. The unit surface conductance, h, is treated as a steady factor, a measure of the quality of the contact between the piston, or ring, and the cylinder. For example, the model will usually have a relatively high h in the links originating on the compression rings. The unsteady component of the conductance is embodied in the second factor, A. The derivation of the convection link areas is discussed below.

In order to calculate the correct heat transfer areas for the convection links, we adopt the same general approach as in the previous part. That is, we write down the unsteady and steady forms of the heat transfer equations, and then combine the equations so as to conserve the total heat transferred. The unsteady form, equation (11), applies to the actual physical process, whereas the steady form, equation (12), applies to the analytical model.

(11) $q(\phi) = h\,A[T_p - T_c(\phi)]$

where,

$q(\phi)$ = rate of heat transfer out of area A on the piston surface (BTU/CA)

T_p = temperature of the surface A (°F)

$T_c(\phi)$= temperature of the cylinder surface to which heat is rejected as the piston travels (°F)

In equation (11), $q(\phi)$ and $T_c(\phi)$ vary with ϕ by virtue of the axial temperature gradient in the cylinder and the motion of the piston.

(12) $\bar{q} = h\,A_1(T_p - T_1, \; h\,A_2(T_p - T_2) + \ldots$
$+ h\,A_n(T_p - T_n)$

$\bar{q}$ = average rate of heat transfer out of area A on the piston surface (BTU/CA)

$A = A_1 + A_2 + \ldots + A_n$ = piston heat transfer area (Ft^2)

$A_1, A_2, \ldots A_n$ = areas associated with temperatures $T_1, T_2, \ldots T_n$

T_p = temperature of the surface A (°F)

$T_1, T_2, \ldots T_n$ = temperatures at discreet points (nodes) on the cylinder bore (°F)

In combining equations (11) and (12) we need to consider only one stroke ($0^\circ \leq \phi \leq 180^\circ$) instead of both strokes ($0^\circ \leq \phi \leq 360^\circ$). The crank advances through the same number of degrees as the piston descends from A to B on the downstroke as it does when the piston ascends from B to A on the upstroke. Furthermore, the piston "sees" the same temperature history on the cylinder from A to B as it does from B to A, only in reverse sequence. Hence, the cycle-average rate of heat transfer can be defined as follows:

(13) $$\bar{q} = \frac{1}{180}\int_0^{180} q(\phi)\, d\phi$$

Integrating equation (11) over one stroke and dividing by 180, we obtain:

(14) $$\frac{1}{180}\int_0^{180} q(\phi)\, d\phi = \frac{h\,A}{180}\int_0^{180} [T_p - T_c(\phi)]d\phi$$

In the physical process $T_c(\phi)$ is a continuous function. However, in the finite element model, $T_c(\phi)$ must be approximated by a step function (because there is a finite number of convection links in the model):

$$(15)\quad T_c(\phi) = \begin{cases} T_1\,, & \phi_1 \leq \phi < \phi_2 \\ T_2\,, & \phi_2 \leq \phi < \phi_3 \\ \vdots & \vdots \\ T_n\,, & \phi_n \leq \phi \leq \phi_{n+1} \\ & \phi_1 = 0° \\ & \phi_{n+1} = 180° \end{cases}$$

Combining equations (13), (14), and (15), the following relation is obtained:

$$(16)\quad \bar{q} = \frac{h\ A}{180}\left[180\ T_p - (\phi_2 - \phi_1)\ T_1 - (\phi_3 - \phi_2)\ T_2 - \ldots - (\phi_{n+1} - \phi_n)\ T_n\right]$$

upon re-arranging,

$$(17)\quad \bar{q} = h\ A\ \left[\left(\frac{\phi_2 - \phi_1}{180}\right)(T_p - T_1) + \left(\frac{\phi_3 - \phi_2}{180}\right)(T_p - T_2) + \ldots + \left(\frac{\phi_{n+1} - \phi_n}{180}\right)(T_p - T_n)\right]$$

Comparing each term in equation (17) with the corresponding term in equation (12), it is evident that,

$$A_1 = A\left(\frac{\phi_2 - \phi_1}{180}\right)$$

(18)
$$A_2 = A\left(\frac{\phi_3 - \phi_2}{180}\right)$$

$$\vdots$$

$$A_n = A\left(\frac{\phi_{n+1} - \phi_n}{180}\right)$$

Equations (18) are used to calculate the heat transfer areas $A_1, A_2, \ldots A_n$ for the convection links. Examination of equations (18) permits a simple physical interpretation of the convection areas. If 180° represents the total time that it takes for the piston node associated with surface area A to travel through one stroke, then each interval $\phi_{i+1} \leq \phi \leq \phi_i$ represents the time that the piston node is thermally linked to cylinder node i during the stroke. The ratio A_i/A is the fraction of cycle time that the piston node is linked to cylinder node i.

The piston nodal areas are computed as a function of the piston finite element mesh. The sum of the areas associated with all the nodes on the surface of the piston is equal to the total piston surface area. Only those areas and nodes which are in sliding contact with the cylinder bore are included in the convection link areas.

The intervals $\phi_{i+1} \le \phi \le \phi_i$ are a function of the cylinder finite element mesh as well as the crank radius and connecting rod length. As the piston descends from TDC to BDC each piston node inscribes an imaginary axial line on the cylinder surface. This line is broken up into a series of contiguous segments whose end-points lie mid-way between consecutive cylinder nodes. Each segment corresponds to an advance of the crank from ϕ_i to ϕ_{i+1}. The change in crank angle as a function of piston travel is calculated by the following equation:

$$(19) \qquad \phi = \cos^{-1}\left[\frac{1 - x_1}{1 - (2x_1/(1+\ell/r)} - x_1\right]$$

where,

ϕ = angle through which crank has advanced from TDC

x = distance through which piston has descended from TDC

r = crank radius

ℓ = connecting rod length

x_1 = fraction of stroke from commencement = $x/2r$

Piston travel and piston velocity as functions of crank angle are illustrated in Figure 4 for a piston assembly with $\ell/r = 3.5$.

Computation of Cycle Average Conditions on the Cylinder Bore

The cycle average heat transfer coefficients and cycle average temperatures on the cylinder bore can be calculated by equations (5) and (9). In general, however, the integrations must be carried out over separate intervals corresponding to exposure of the particular heat transfer area to crankcase conditions, sliding contact with the piston, and combustion chamber conditions. For intervals corresponding to sliding contact with the piston, $T_g(\phi)$ and $h(\phi)$ are set equal to zero, because the heat input from the piston is already accounted for. Typically, $\bar{h}$ and $\bar{T}_g$ are computed for each element face on the cylinder bore.

3.2 Finite Element Models

The detailed temperature distribution in the combustion chamber components was determined using an ANSYS based finite element model. The overall engine model consists of four major components: piston, head, block and cylinder assembly insert. Each of these components was substructured and used in the assembled analysis. Figure 5 presents the piston assembly which has been treated as axisymmetric. For the thermal analysis, the interfaces at A, B and C have been coupled, which means there is an assumed perfect condition. The same piston model was used in all three engine configuration cases considered. These various cases involve a change in the material properties for the ceramic parts only. Table I tabulates the thermal conductivity property for the materials of construction considered. Figures 6A and 6B present the axisymmetric model of the two head assemblies considered. Again, the interfaces D, E and F were assumed to be coupled. The block and insertable liner assembly were both modeled fully three dimensionally in order to be able to assess what happens in the intake and exhaust ports. Figures 7A and 7B present the inside and outside view of the insertable liner assembly, respectively. This assembly consists of a stainless steel outer reinforcing cylinder with a ceramic inner sleeve. The cylinders are assembled with an interference fit. The interference boundary G is assumed to be coupled. Figure 8 is an outside view of the solid monolithic ceramic liner. From a model standpoint, the solid monolothic liner is nothing but the liner of Figure 7 with the materials being the same and the upper ledge moved closer to the bolted joint. Figures 9A and 9B present the fully three dimensional ANSYS based thermal and structural model of the test engine block. Figure 10 illustrates the modification of the block model to accommodate the movement of the liner support ledge up close to the bolted joint.

The four basic structures presented were individually developed as substructures and then used in an overall thermal analysis.

3.3 Detailed Thermal Boundary Conditions

The combustion surface gas temperatures and associated forced convection heat transfer coefficient were obtained using the procedure set forth in section 3.1. For an all zirconia insulated engine, the cycle average film coefficient along the cylinder wall and the cycle averaged gas temperature are illustrated in Figures 11A and 11B, respectively. In developing this information it was also necessary to have a convection coefficient on the crank case side of the engine. The value used for zirconia and alumina is 7 BTU/HR-FT^2-°F with an oil mist temperature of 300 °F. For the silicon nitride engine a value of 423 BTU/HR-FT^2-°F was used with an oil mist temperature of 300 °F. The significant change in this boundary condition relates to shifting from an adiabatic concept to a low heat rejection concept with conventional lubricated rings. Figures 12A and 12B illustrate the convection coefficient and gas temperature, respectively, for alumina. Figures 13A and 13B present the same information for silicon nitride.

The convection coefficient and cycle average gas temperature which applies to the combustion bowl surface and top surface of the piston cap are the values presented in Figures 11 through 13 at top dead center. The conduction coefficients between the piston side walls and cylinder and the ring/ring groove interface were developed based upon information presented in the public domain literature. Figure 14 shows the values used in all three configurations. The conduction coefficient is highest between the piston rings and cylinder. Also note that for a given ring the conduction is highest on the lower interface. This is due to the gas pressure forcing the ring against the lower ring groove face. As noted in Section 3.1, these conduction coefficients which pass between the piston and cylinder must be distributed due to movement of one surface relative to the other during the cycle. Figure 15 illustrates the time weighting function values for one of the points on the piston relative to the cylinder wall. Note that the ring to ring groove conduction is not time weighted because they are always in contact.

The effect of heat generation at the rings was included in the analysis. A power loss of 7 horsepower (5BTU/SEC) was considered. The top ring generated thirty percent of the heat and the rest was evenly distributed to the remaining four rings. The air gaps between the piston cap and metal portion of the piston plus the combustion bowl and metal portion of the head were treated considering both conduction and radiation. The conduction accounted for the air conductivity. Radiation was modeled using the ANSYS radiation, so it was directly calculated in the overall solution. As noted earlier, all contacting interfaces between ceramic and metal parts were coupled. This means zero contact resistance was used.

The head was thermally coupled to the cylinder insert and block at the contact surfaces. Conduction and radiation was accounded for between the head and injector. An air gap of 0.075 inches used with conduction and radiation modeled. The injector coolant was assumed to be at 55 °F. The convection and radiation to test cell ambient was determined for both the head and block. The convection coefficient was computed using the vertical cylinder correlation

$$h_c = 0.555 \frac{k}{L} (G_r \cdot P_r)^{\frac{1}{4}}.$$

A surface temperature of 1000 °F was used for the engine. Radiation was added to the convection.

The heat transfer across the gap between the insert cylinder liner and the block was modeled as conduction with an air gap of 0.010 inches. In the area of the ports the two structures were coupled. The exhaust and intake ports gas temperatures were developed from the cyle simulation data. The heat transfer coefficient for the ports was computed using the mass flow rate, port temperatures, and pressure data with a correlation for turbulent tube flow:

$$(20) \qquad h = C \cdot D^{-0.2} P^{0.8} T^{-0.53} V^{0.8}$$

$$C = \frac{Nu}{Re^{0.8}}$$

D = effective port diameter

T = gas temperature

V = gas velocity

P = gas pressure

3.4 Temperature Distribution Results

For the three different ceramic insulation configurations of the basic test engine, the converged cycle averaged temperatures in the entire engine have been found. As noted earlier, this required an iterative process between the cycle simulation and the detailed engine temperature analysis.

Figures 16A, 16B and 16C present the temperature fields in the head assembly for zirconia, alumina, and silicon nitride, respectively. From these illustrations of the temperatures, it can be seen that the maximum ceramic temperature is dropping as the ceramic materials conductivity increases. The

2059 °F for the zirconia is outside the temperature range which this material can withstand for an extensive service time. That range is about 1800 °F. The silicon nitride is losing more heat than one would like, but this can be adjusted in two ways. First, the intermediate disk can be replaced with zirconia and second, the outer surface of the head assembly can be insulated as needed.

Figures 17A, 17B and 17C provide the detailed temperature distribution for the piston assembly for zirconia, alumina, and silicon nitride. Again, the zirconia is for hotter than the material can withstand. The maximum temperature for all three materials is greater on the piston than the head because the piston ceramic has been isolated more from the heat sinks. In all three cases the rings are running for hotter than any lubrication will allow. In the future, the crank case oil must be allowed to cool the ring area by removing the thermal shield (see Figures 1 and 2). Note that the stress in the ceramic will increase because the gradient in the material will significantly increase. The target for ring and adjacent metal temperature should be 600 ° F to 800 ° F.

Figures 18A and 18B present the ceramic liner temperatures, Figures 19A and 19B present the metal reinforcing cylinder temperatures, and Figures 20A and 20B present the block temperatures for the zirconia insulated engine. Figures 21, 22 and 23, respectively, do the same for the alumina insulated engine. For the solid ceramic (silicon nitride) cylinder insert configuration, Figures 24A and 24B present the detailed temperature distribution. The associated block temperatures are provided in Figures 25A and 25B.

4.0 STRESS ANALYSIS

Based upon experience with a number of ceramic lined (insulated) diesel engines, the significant loading condition to ' sider in assessing the feasibility of a given design configuration is assembly plus thermal plus peak cylinder pressure, all applied at one time. The finite element models used to establish the stresses are the same as those used in the thermal analysis (see Figures 5 through 10). While the overall thermal analysis was carried out us ng a complete combined model, the stress analyses were carried out using the various individual assemblies. From a screening analysis standpoint this is acceptable, but when working on a baseline final type design, it would be highly desirable to carry out an overall structural interaction analyses.

For the head assembly stress analysis, Figure 26 depicts the mechanical boundary conditions used. The contact elements noted in the figure transmit compressive loads across structural interfaces but unhook for tension. Friction has been set to zero on all contact surfaces. Figures 27A, 27B and 27C present the radial axial and hoop stress for the ceramic combustion bowl in, respectively, the zirconia, alumina, and silicon nitride insulated engines. In Figure 27A the large radial and hoop tensile stresses on the top surface of the bowl insert (cold side) are a direct result of the large through thickness temperature gradient in the part (see Figure 16A). The radial press fit (0.010 inches diametral) between the bowl and head reduces this tensile stress. It is important to note that increasing the press fit is good for the ceramic, but hard on the metal head. This is especially true when creep relaxation of the press fit is considered. The tensile stresses in the axial direction along with the press fit boundary are thermal induced. The large compressive stress in the same area is a passions effect. The large compressive stresses on the combustion surfaces are a result of press fit and thermal adding. This surface also sees a temperature change over the cycle, but at no time does the surface experience tension while operating. The peak pressure tends to increase the radial tensile stress on the upper surface of the bowl because it forces the bowl to contact the head. This contact reduces the amount of curling up the bowl can do, which in turn increases the radial tensile stress.

All the same things can be said for the alumina insulated engine head assembly (see Figure 27B). When moving to the silicon nitride head assembly, two modifications to the design occurred. First, an intermediate disk was placed between the bowl and head. The reason for this was to reduce the through thickness gradient in the bowl, which in turn reduces the radial and hoop tensile stresses on the bowl top surface. Second involved increasing the diameter of the bowl insert and having it sit on the cylinder liner. This was necessary because the radial press fit is lost at temperature due to the large thermal expansion difference between 410 stainless steel and silicon nitride (see Table I). From Figure 27C, it can be seen that the significant tensile stresses on the top surface of the bowl have been eliminated. This is due to both the design change and the material properties of silicon nitride. Note that the head temperatures have increased significantly (see Figure 16C). Figure 28 illustrates the radial, axial and hoop stress in the intermediate disk for the silicon nitride insulation configuration.

Figures 29A, 29B and 29C present the stresses for the metal portion of the head for the loading condition noted above. The large stresses at the press fit boundary are relieved by plasticity. The vertical lines in the hoop stress figures are due to the modeling of the bolt holes. This was done by setting the hoop elastic modulus to zero in the area of the bolt hole and adjusting the axial and radial modulus on an area basis.

The structural boundary conditions applied to the piston assembly are illustrated in Figure 30. The axial restraint of the bottom of the piston is necessary to carry the axial pressure induced load which actually passes out through the rod. This modeling is acceptable, since it is only the upper portion of the assembly, which is being assessed from a feasibility standpoint. Figures 31A, 31B, and 31C present the radial, axial and hoop stresses in the piston cap for the zirconia, alumina and silicon nitride, respectively. The large tensile stresses, both radial and axial, on the underside of the cap are similar in nature to those on the cold side of the combustion bowl. Axial retention of the cap is provided by the press fit on the cap stem. In the case of silicon nitride, this is not possible because of thermal expansion differences. Also, if the silicon nitride cap is retained axially on the stem, there is a large axial stress induced due to expansion mismatch. A properly tapered surface on the stem will reduce these problems. Figures 32A, 32B and 32C present the stresses in the piston intermediate insulation disk. The large stresses at the inside of the disks are a result of interaction with the centering lip on the metal piston. By providing a small initial clearance between the two parts, these stresses will be significantly reduced. Figures 33A, 33B and 33C provide the stresses in the upper region of the metal part of the piston assembly. These figures also show large stresses at the centering lip which will be eliminated with an easy design modification. The nominal stresses in the cast iron piston are important because of the relatively high temperature seen at operating conditions.

Figures 34 and 35 present the maximum and minimum principal stress in the zirconia cylinder liner for maximum power thermal induced loading and 0.010 inches of diametral interference. From these stress contour results it can be seen that the stresses around the intake and exhaust ports are relatively low. Even though the finite element model is coarse with respect to identifying peak stresses in the ports, it is adapco's opinion that the low stress level predictions are representative of what is happening. The large tensile stresses at the top of the ceramic liner are due to through thickness temperature gradients. The hoop tensile stresses at the top are countered by the press fit. The axial tensile stresses on the cold side are largest some distance down the cylinder due to the free edge at the top of the ceramic. Figures 36 and 37 provide the same information for the alumina inserted ceramic liner. The silicon nitride cylinder is not a liner backed up by a metal cyclinder and a press fit. It is basically a free standing solid ceramic cylinder which has sufficient thickness to carry the pressure loads. Figures 38 and 39 provide the maximum and minimum principal stress contours in the silicon nitride cylinder for maximum power induced thermal loads.

5.0 CONCLUSIONS AND RECOMMENDATIONS

From the thermal and stress analysis results presented above plus adapco's experience on other low heat rejection concepts involving monolithic ceramics, it is adapco's opinion that the insulation of the Teledyne lightweight diesel has a high probability of success. To date, the major problem in insulating low heat rejection engines has been the piston. In the case of the Teledyne engine, the elimination of the combustion bowl and giving it a spherical domed shape provides a configuration which has a high probability of not failing. In addition, the entire surface is covered. This is important from both a heat loss standpoint and being able to keep the rings cool.

The one problem identified in the thermal analysis is the high temperature (above 1750 °F) at which the zirconia insulated engine configuration is operating. This problem is important, since it is adapco's opinion that zirconia should be used as the insulator due to its high thermal expansion. Present zirconia cannot be used at temperatures above 1700° to 1800 °F. To provide some cooling while at the same time reducing cost, it has been recommended by Teledyne that the cylinder be metal. adapco agrees with this approach.

Figure 1 Low Heat Rejection - Monolithic Ceramic Insulated - Single Cylinder Test Engine Combustion Chamber Configuration

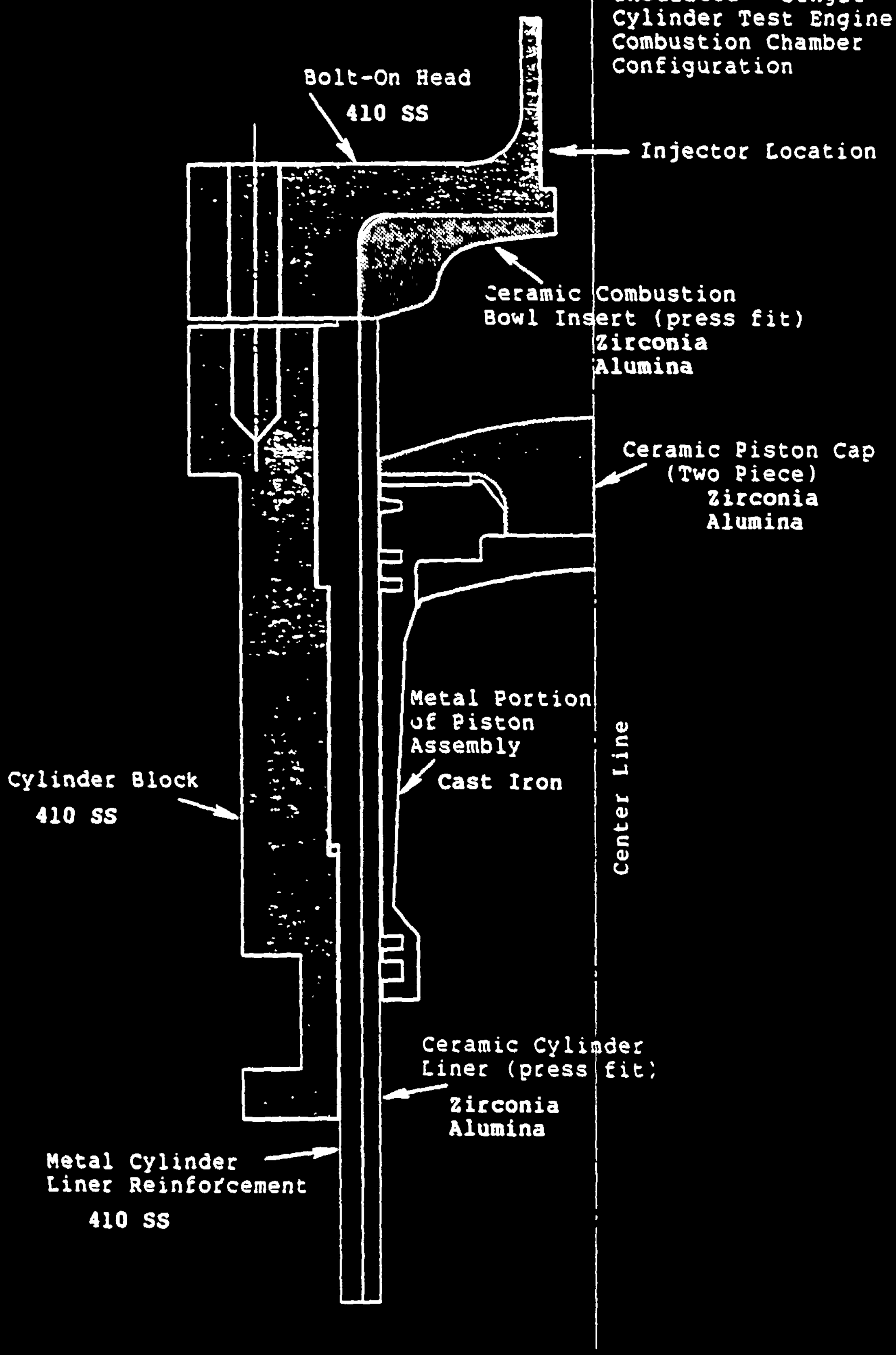

Figure 2 Modified Low Heat Rejection - Monolithic Ceramic Insulated - Single Cylinder Test Engine Combustion Chamber Configuration

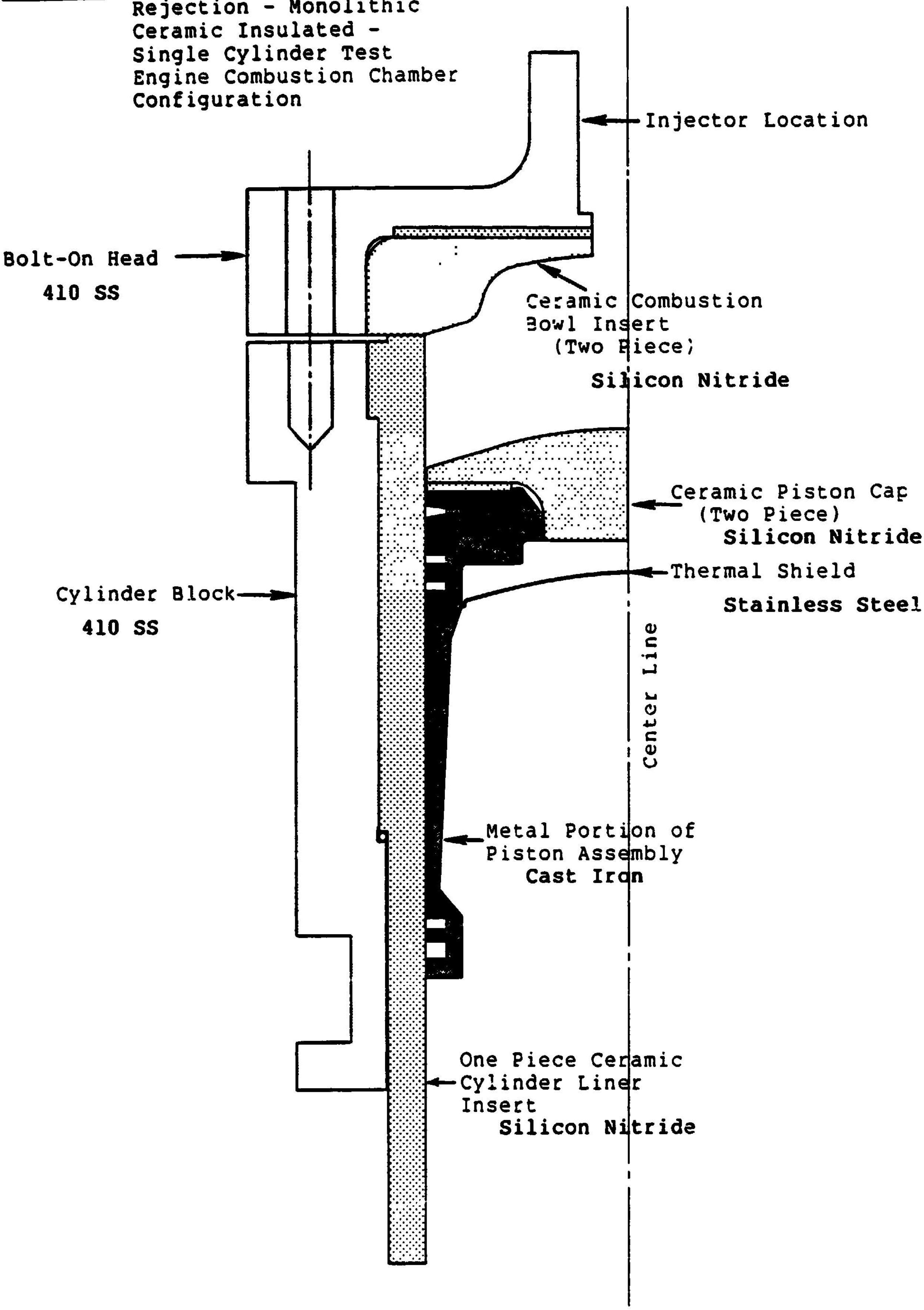

Figure 3 Piston to Cylinder Thermal Linkage

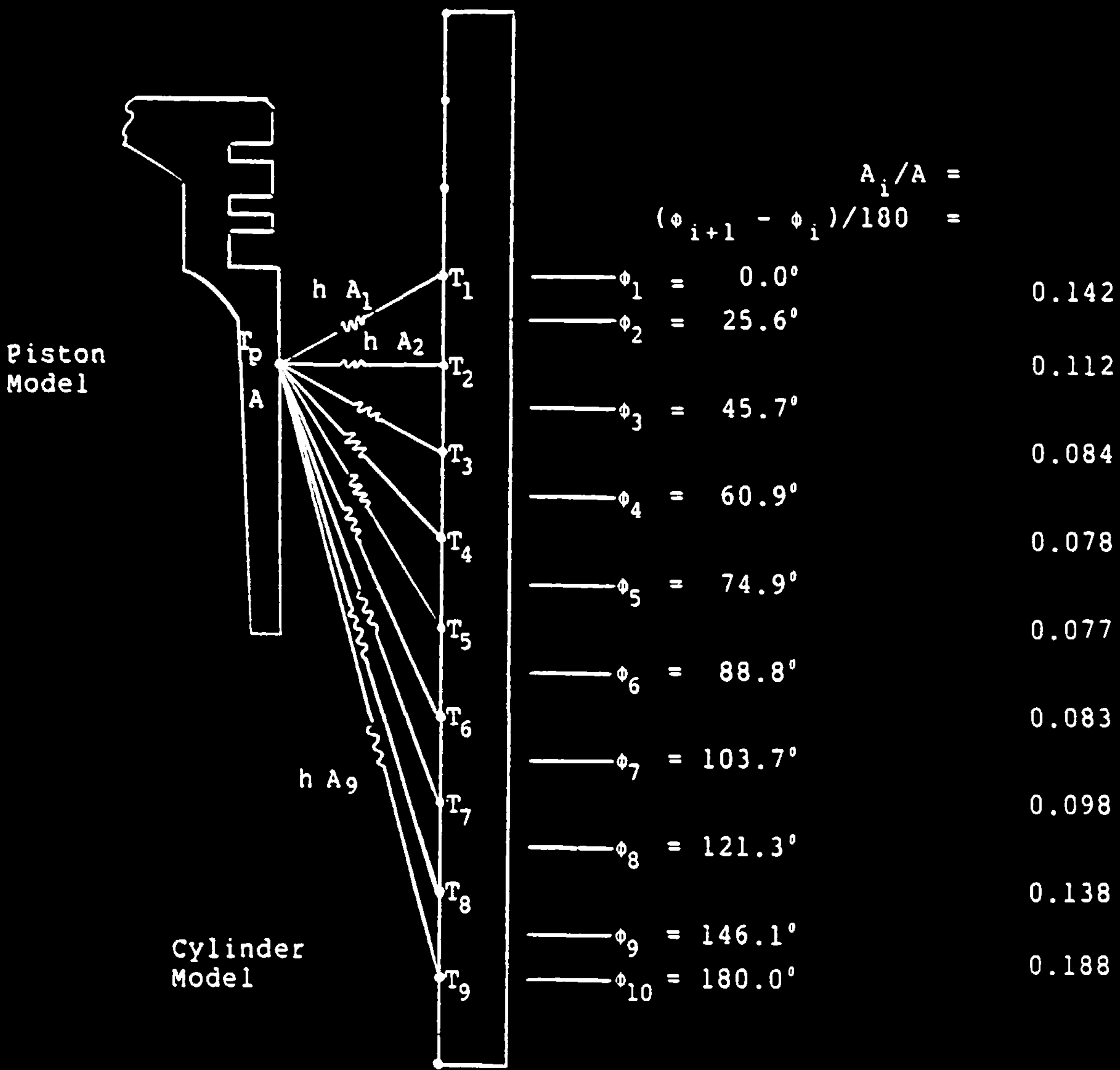

Figure 4 Piston Travel as a Fraction of Stroke (x_1) Versus Crank Angle
Piston Velocity as a Fraction of Crank Pin Velocity (c) Versus Crank Angle

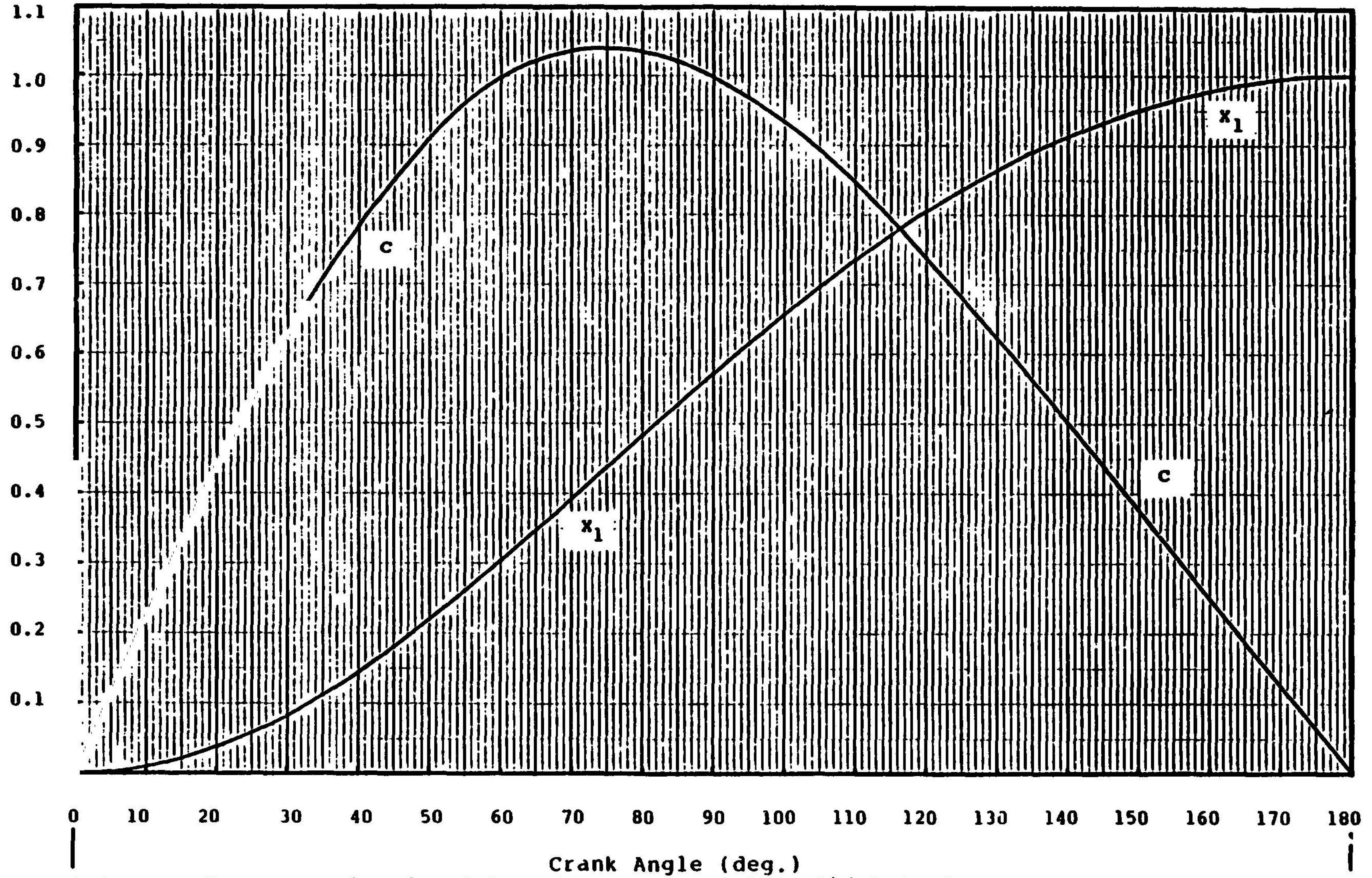

Note: Ratio of rod length to crank radius (ℓ/r) is 3.5

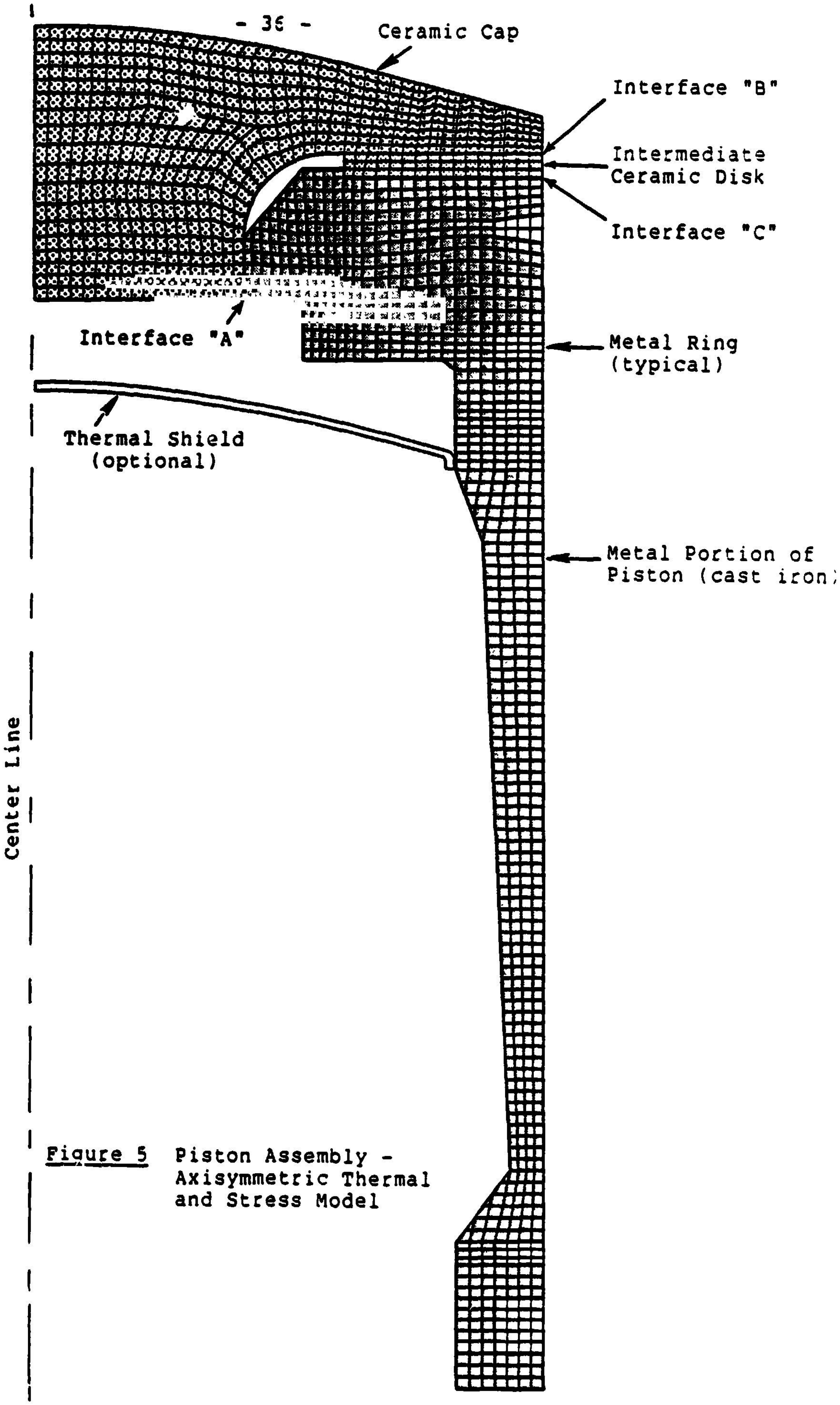

Figure 5 Piston Assembly - Axisymmetric Thermal and Stress Model

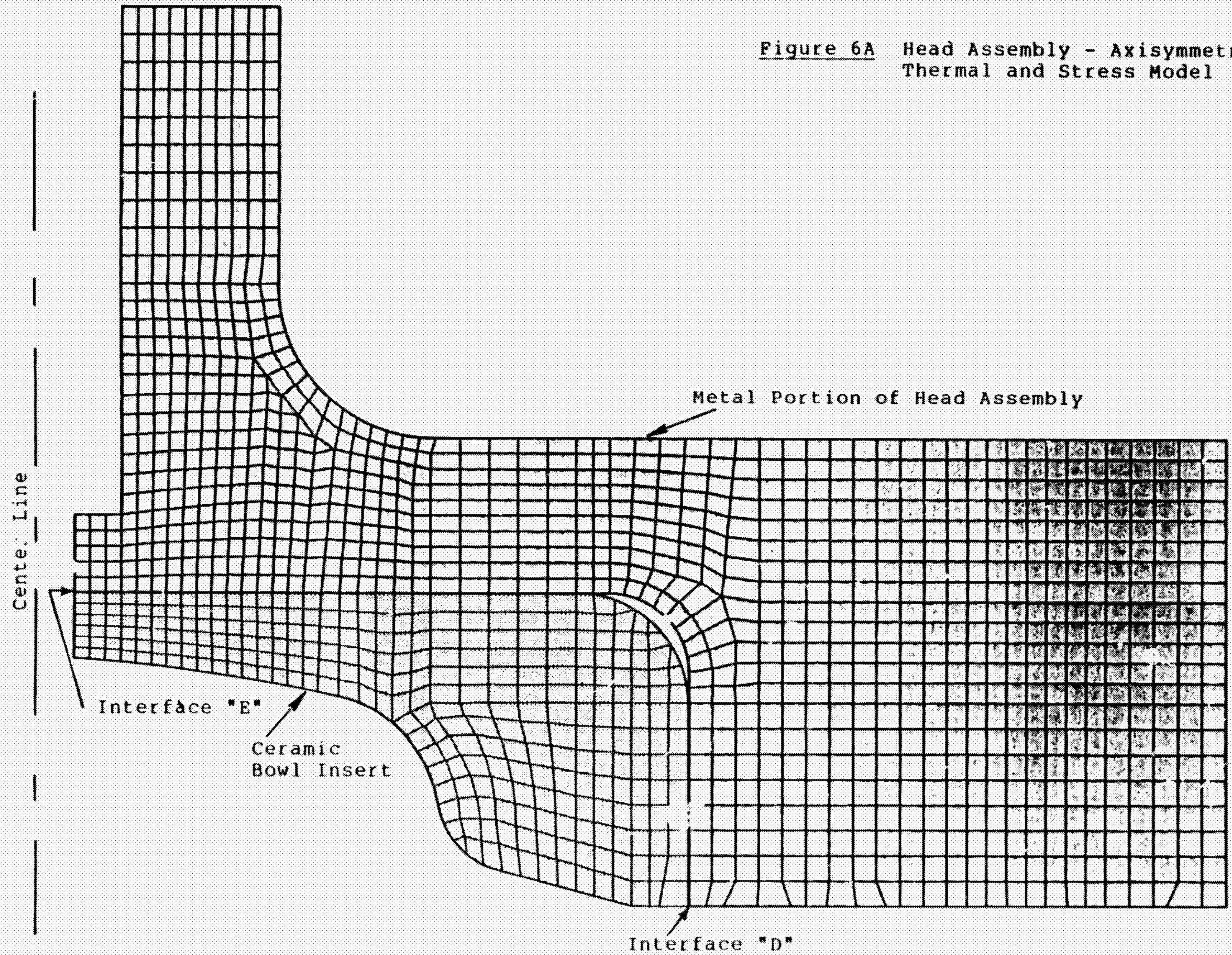

Figure 6A Head Assembly - Axisymmetric Thermal and Stress Model

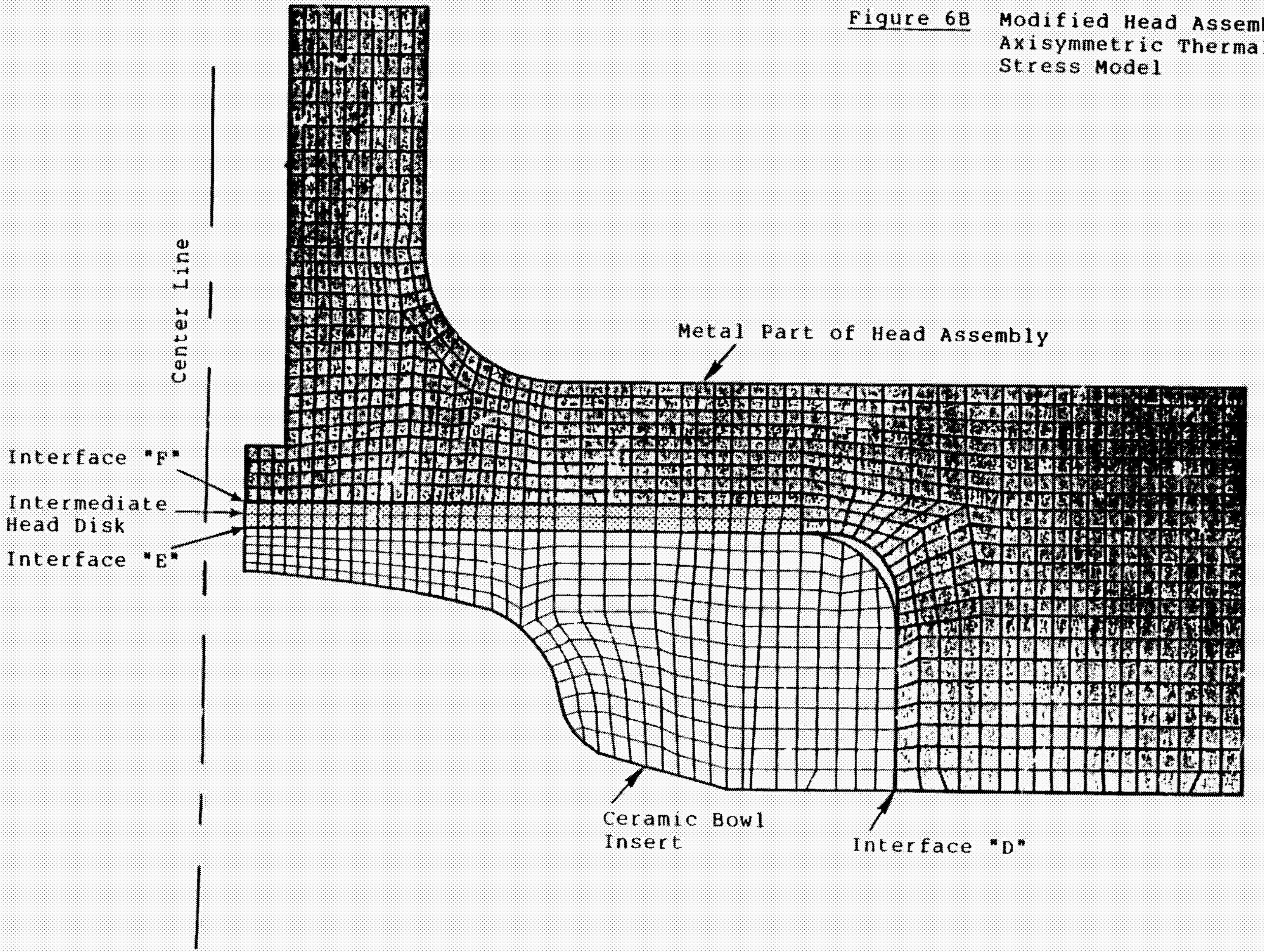

Figure 6B Modified Head Assembly - Axisymmetric Thermal and Stress Model

 Figure 7A Insertable Liner Assembly - Thermal and Stress Model

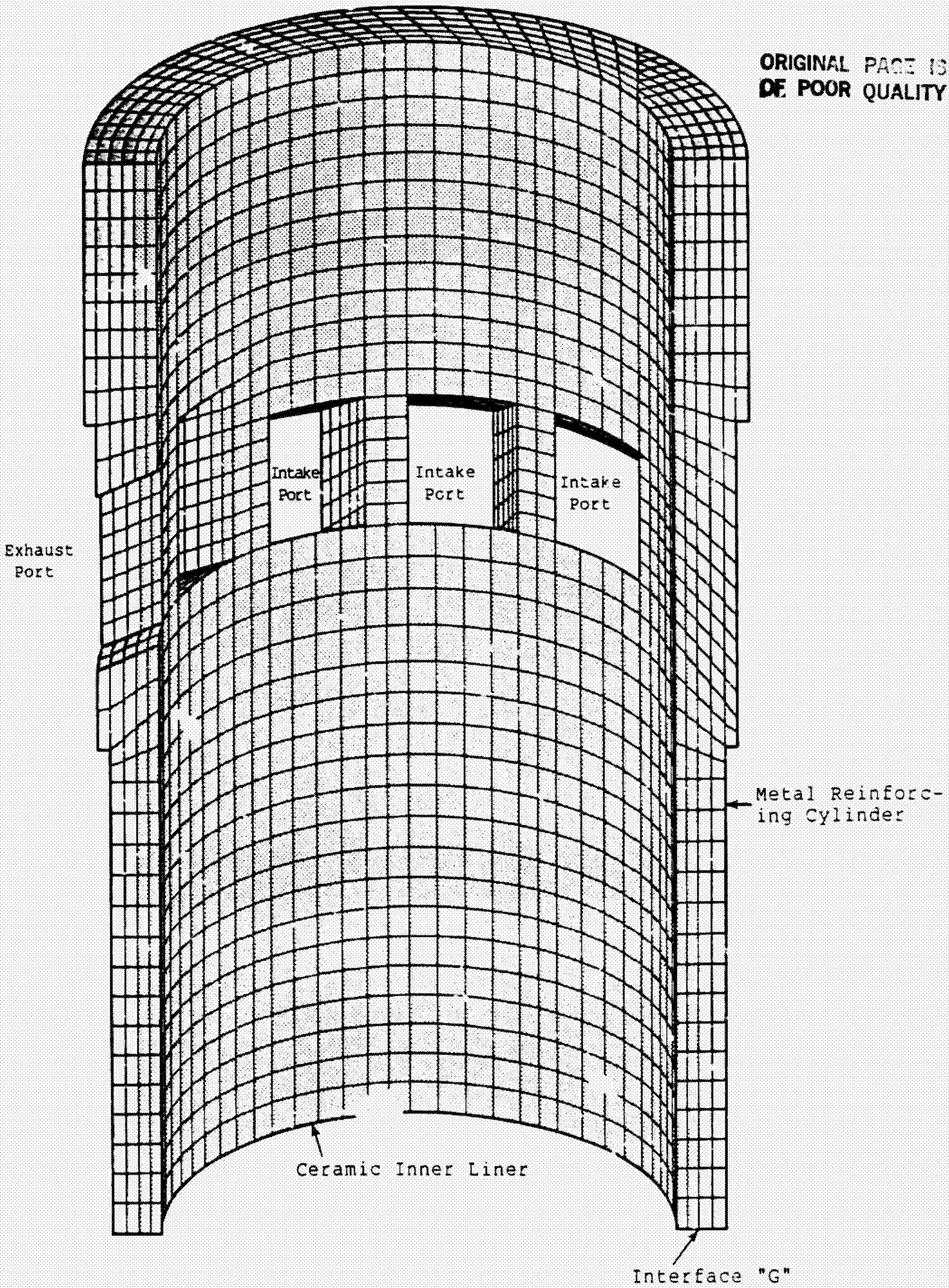

Figure 7B Insertable Liner Assembly - Thermal and Stress

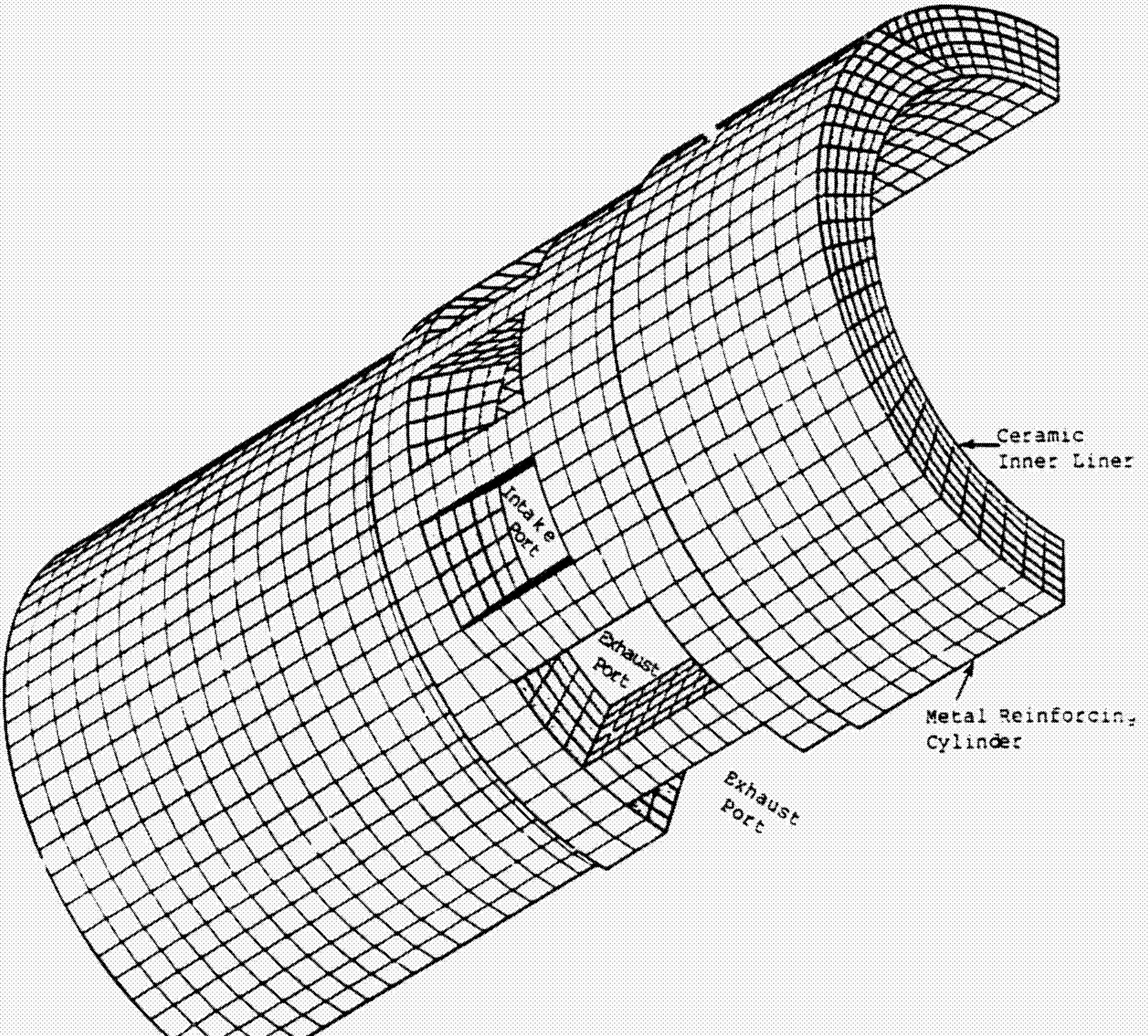

Figure 8 Insertable Monolithic Ceramic Cylinder

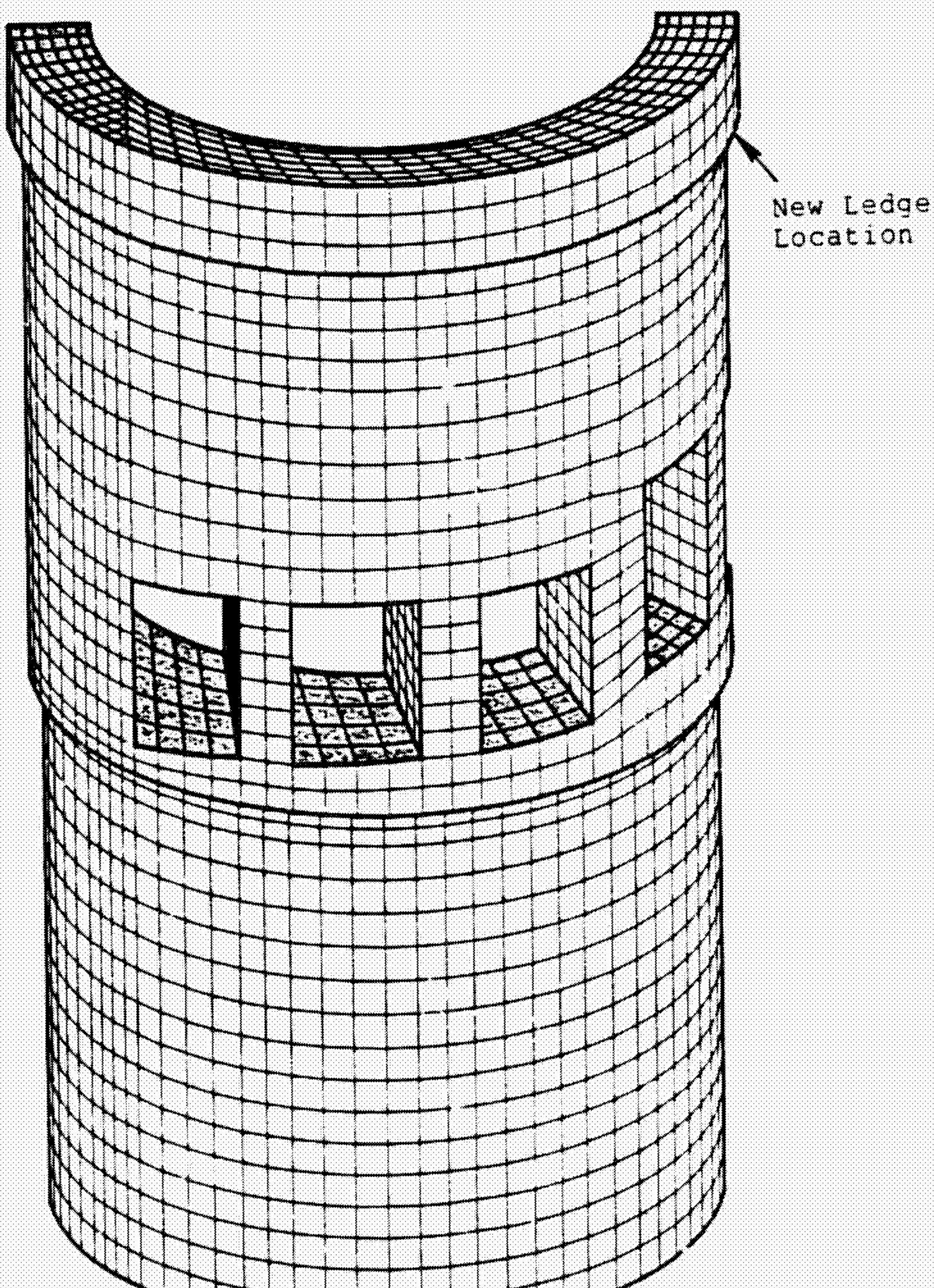

<u>Figure 9A</u> Engine Block - Thermal and Stress Model

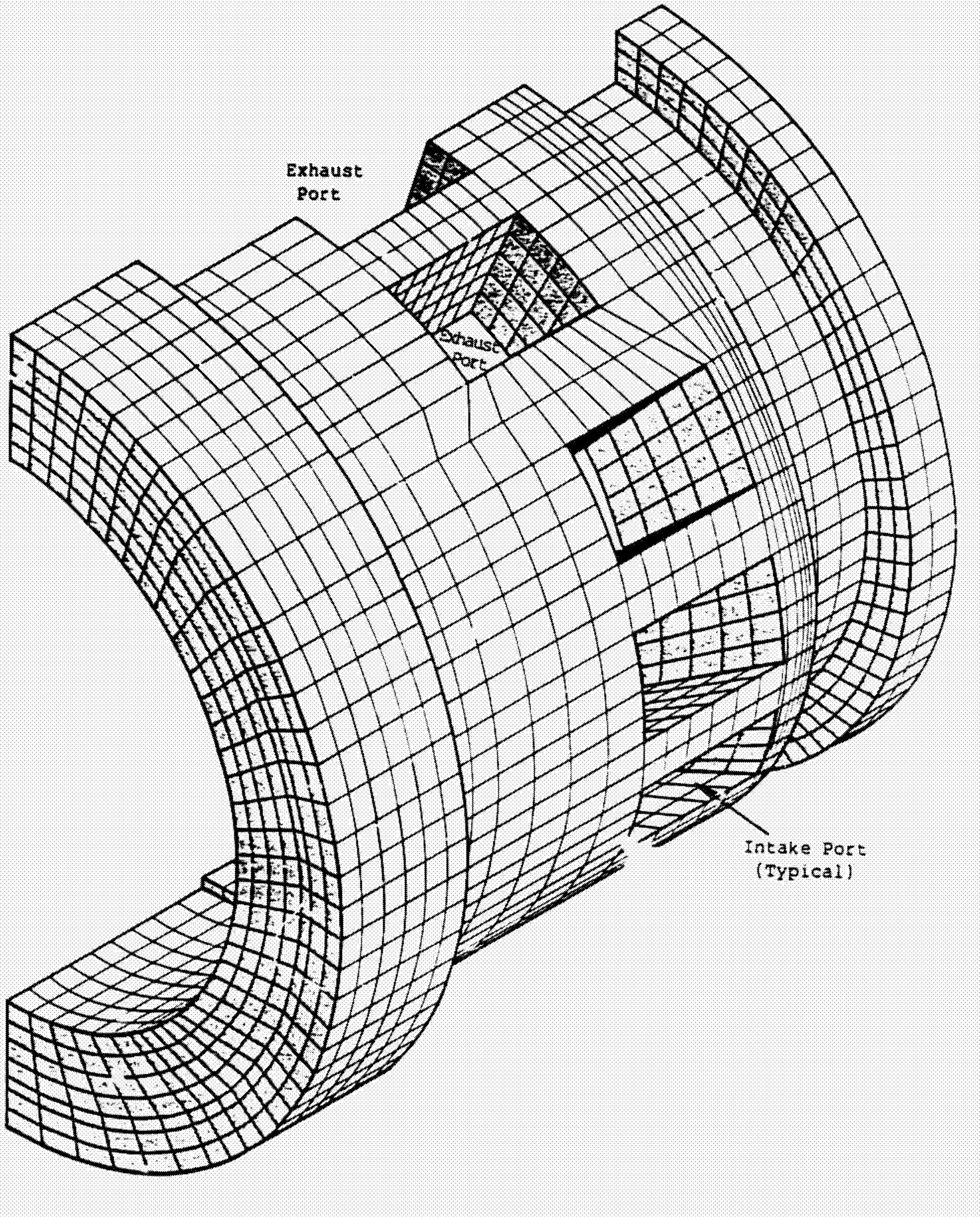

Figure 9B Engine Block - Thermal and Stress Model

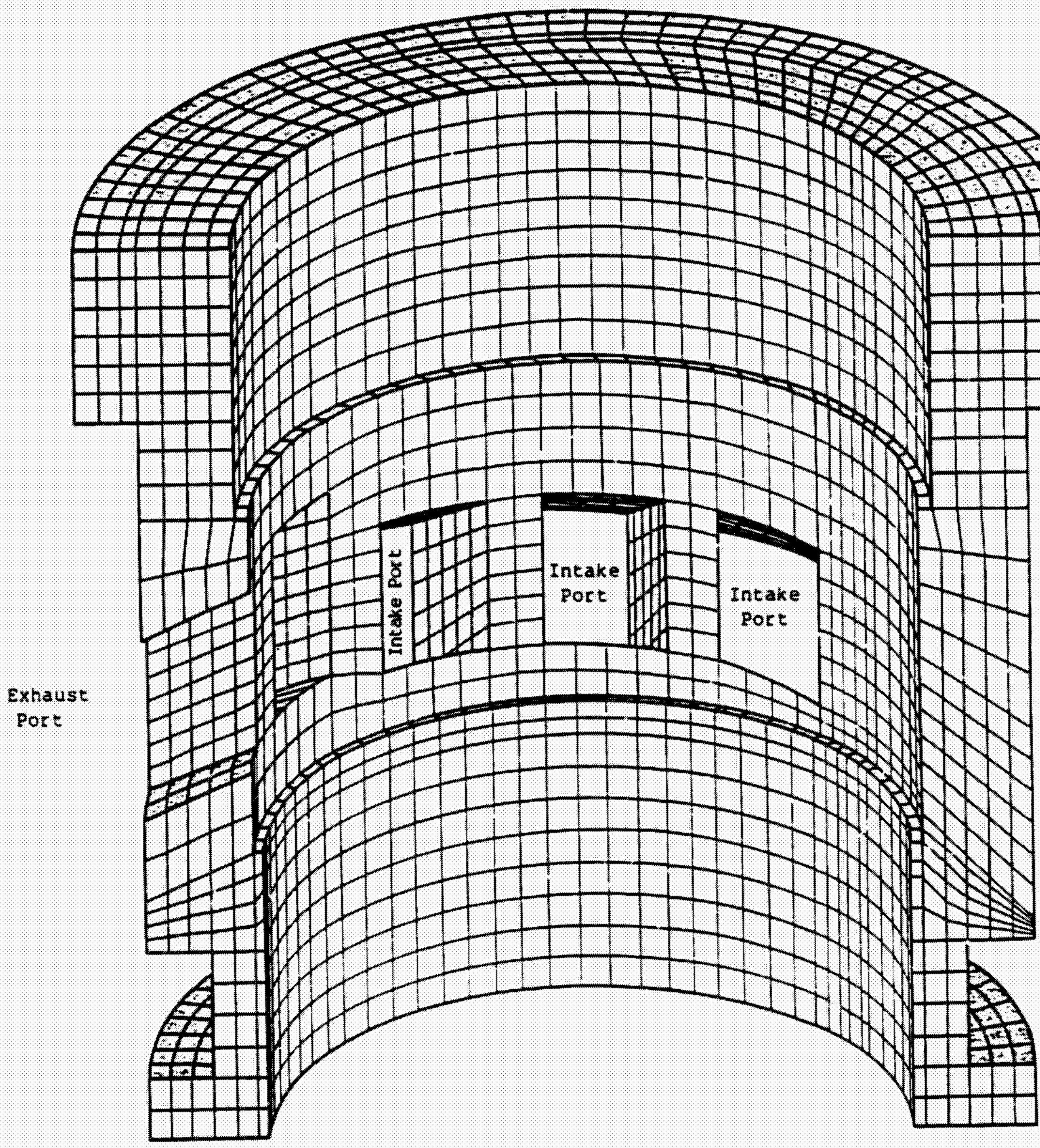

Figure 10 Modified Engine Block - Thermal and Stress Model

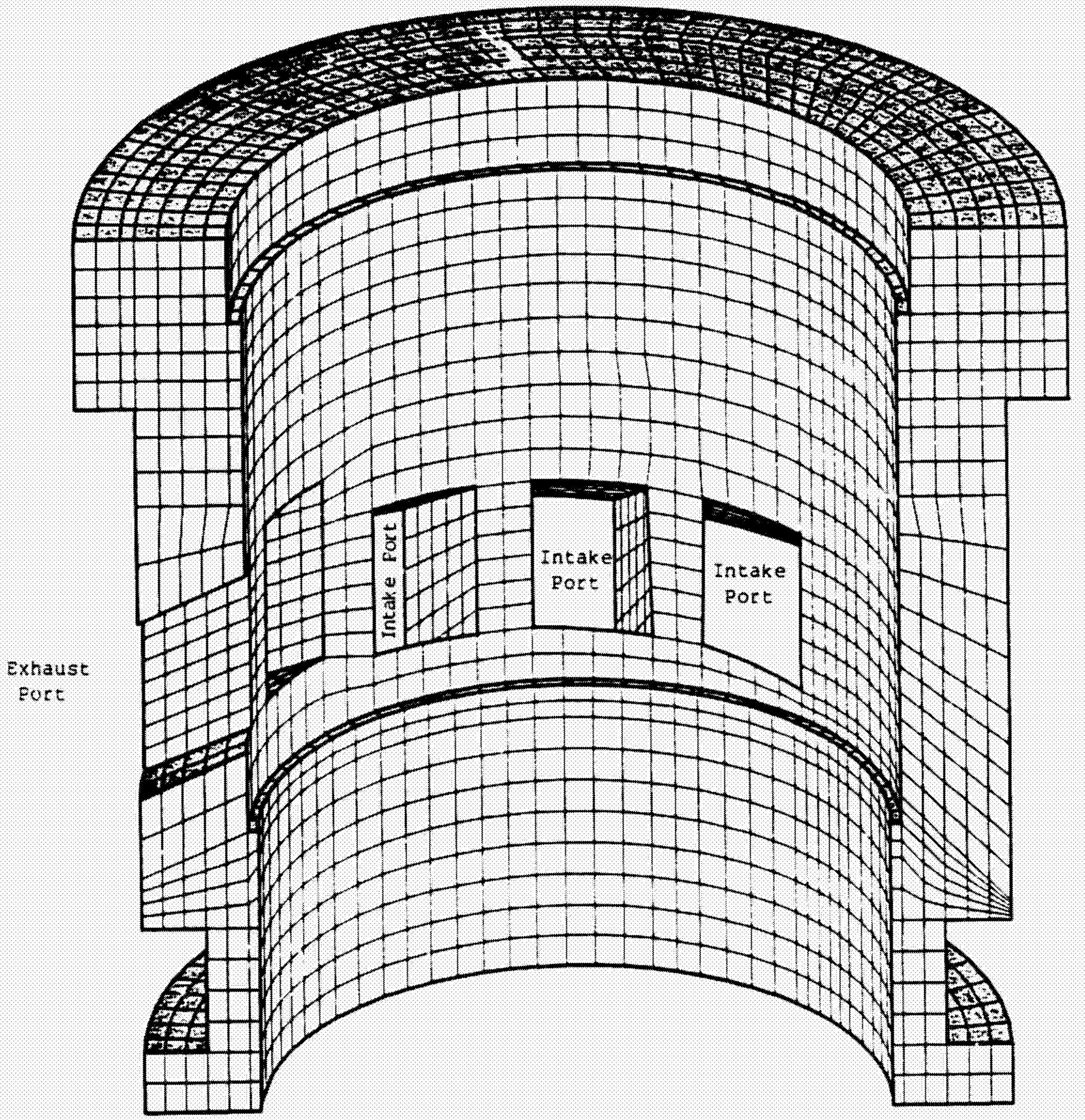

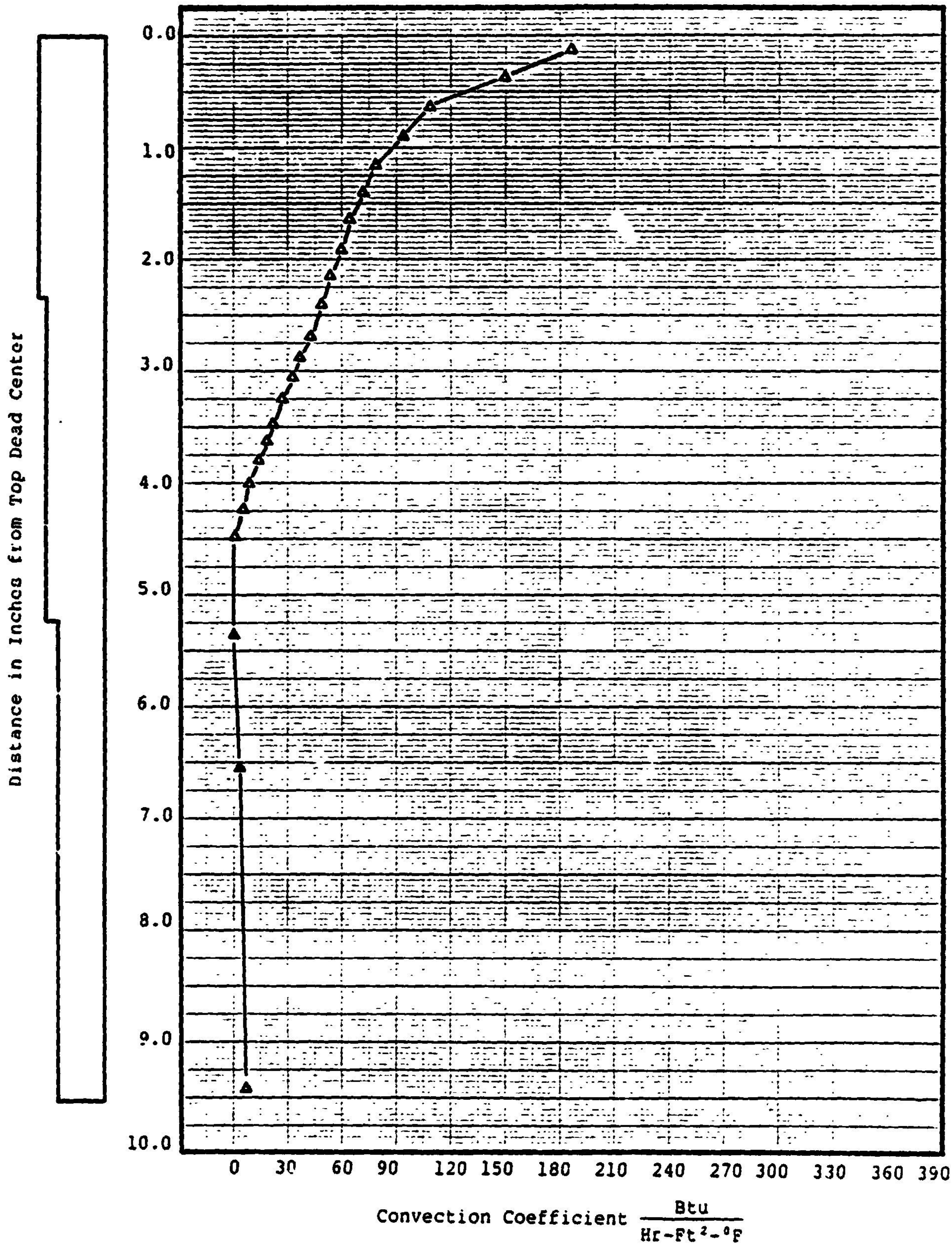

Figure 11A Convection Coefficient Along the Cylinder Liner (Zirconia Insulation)

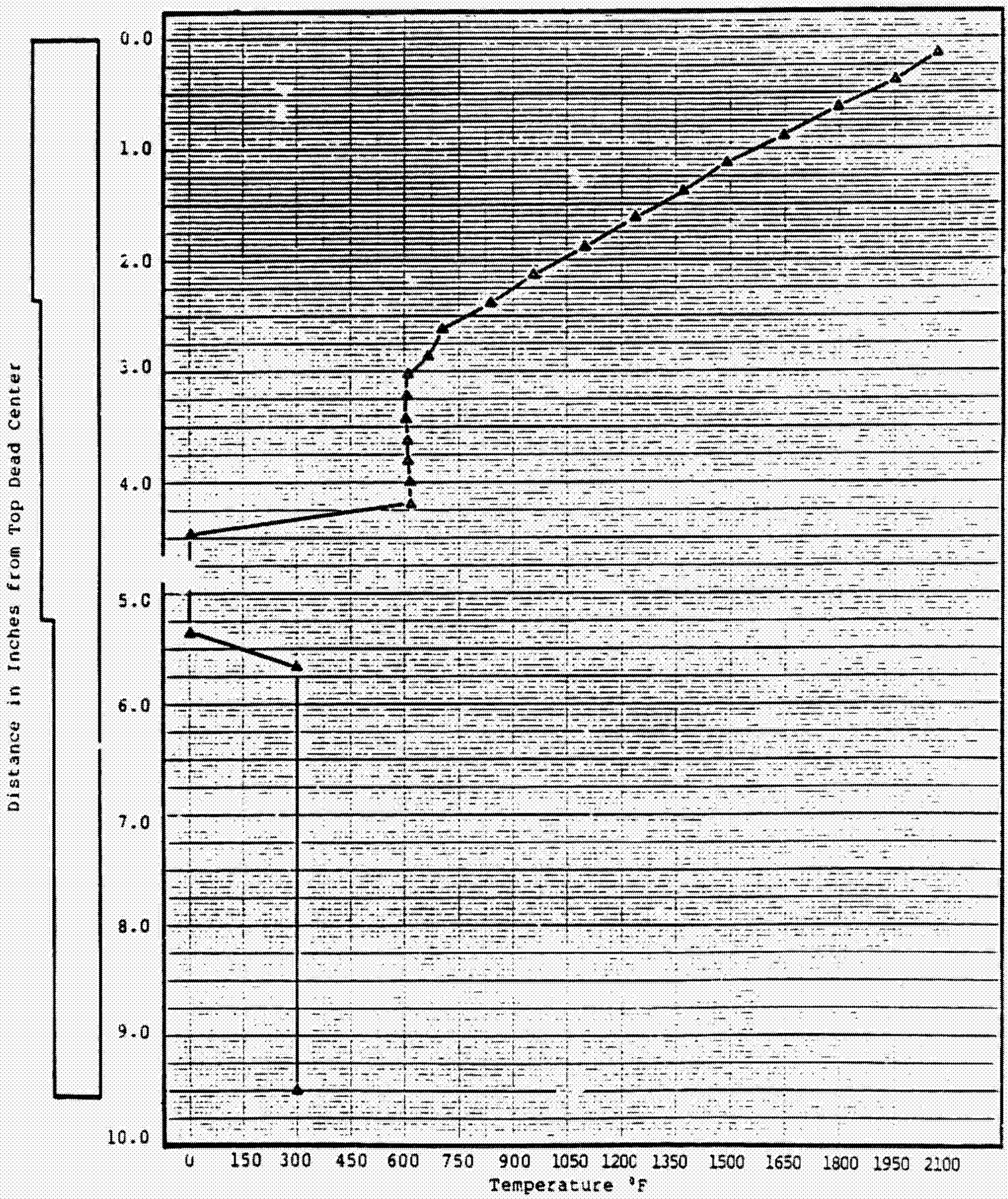

Figure 11B Gas Temperature Distribution Along Cylinder Liner (Zirconia Insulation)

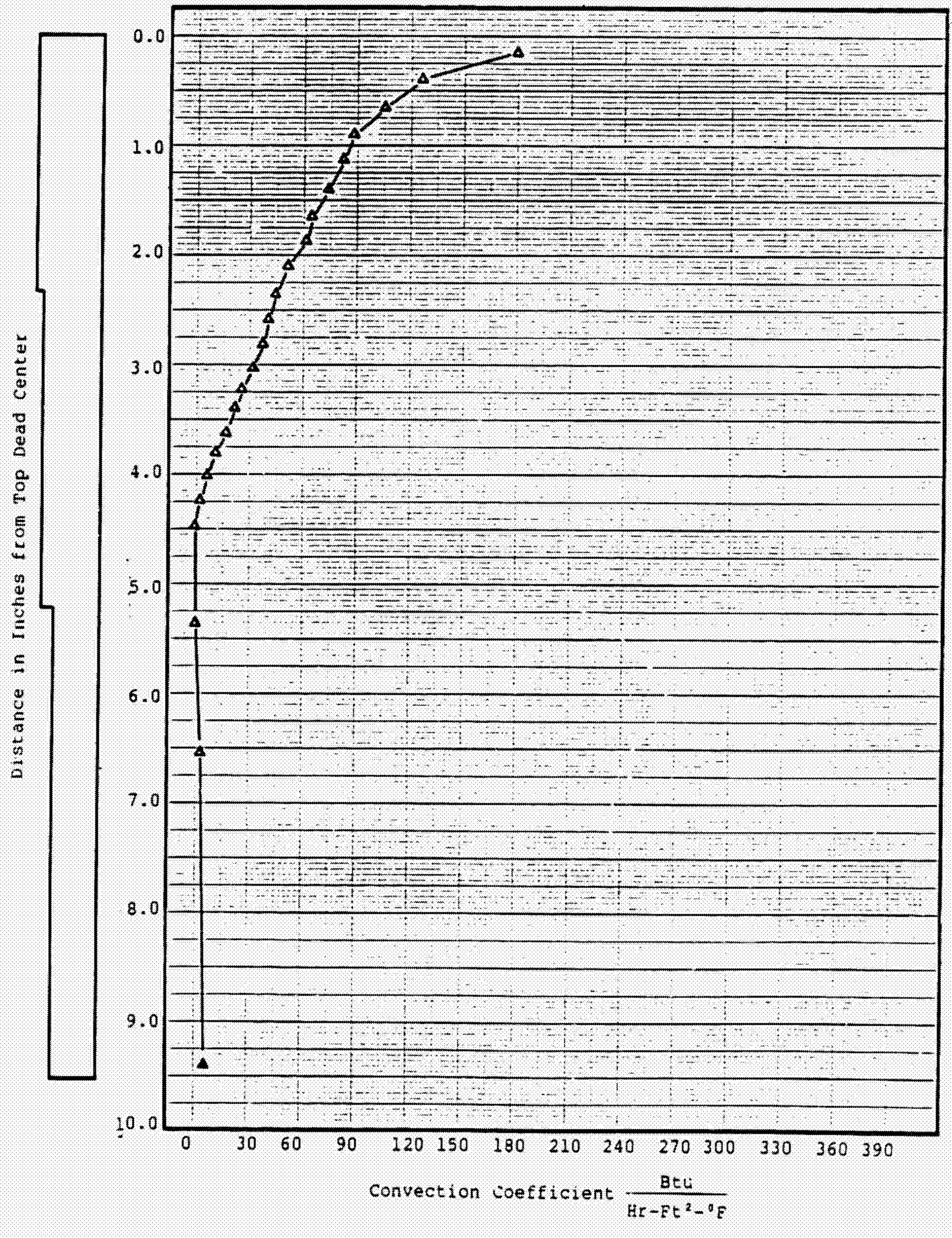

Figure 12A Convection Coefficient along the Cylinder Liner (Alumina Insulation)

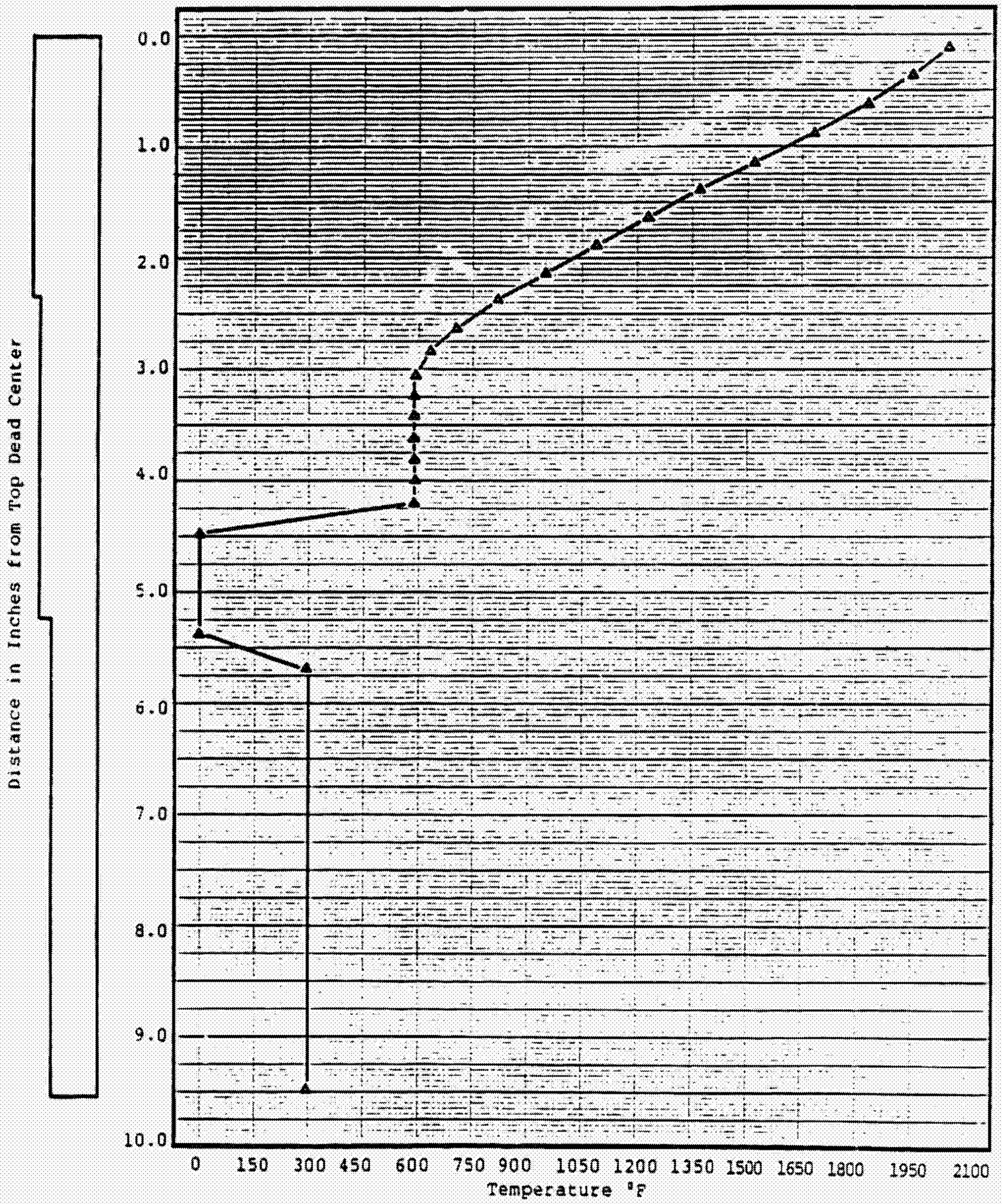

Figure 12B Gas Temperature Distribution Along Cylinder Liner (Alumina Insulation)

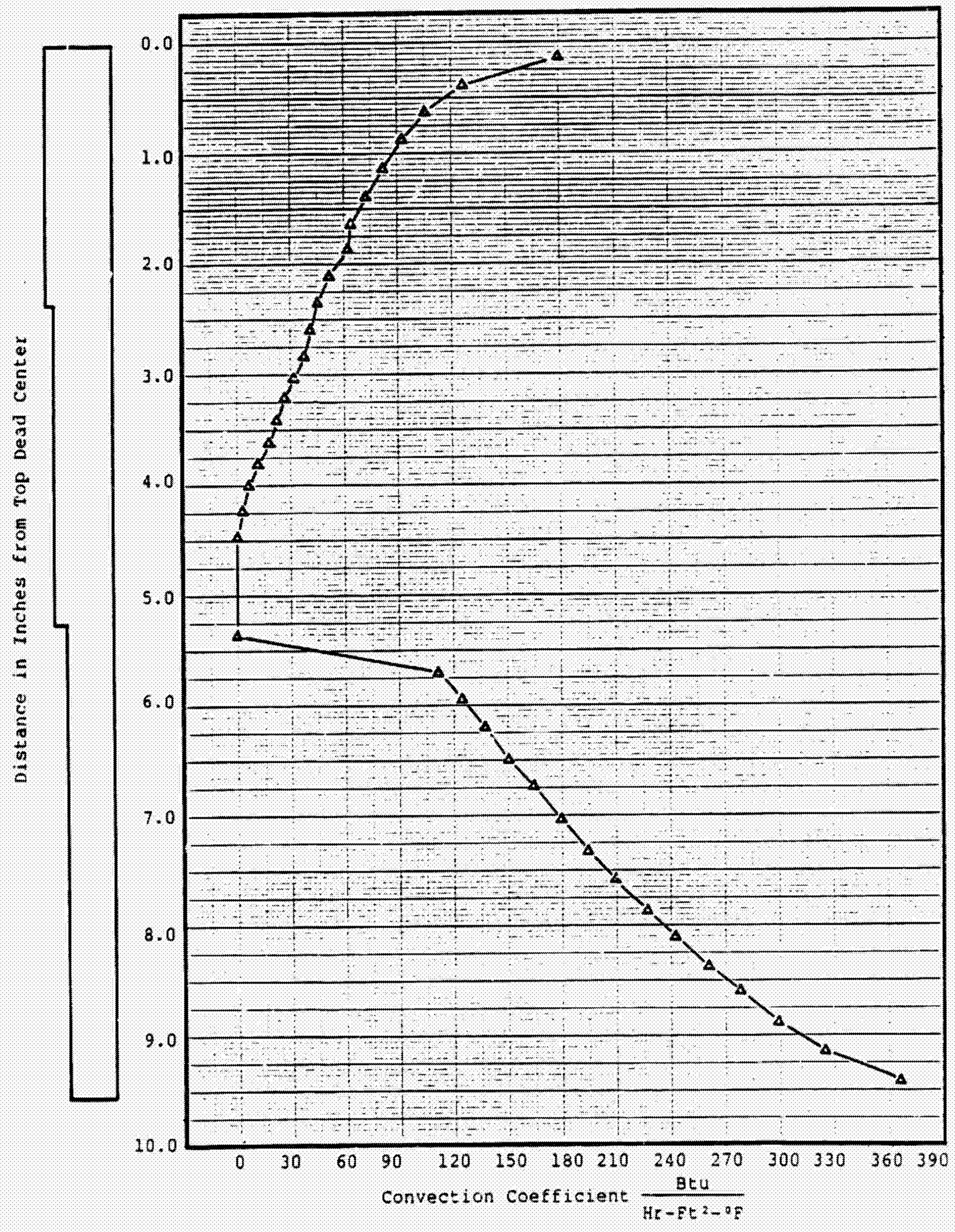

Figure 13 A Convection Coefficient along the Cylinder Liner (Silicon Nitride Insulation)

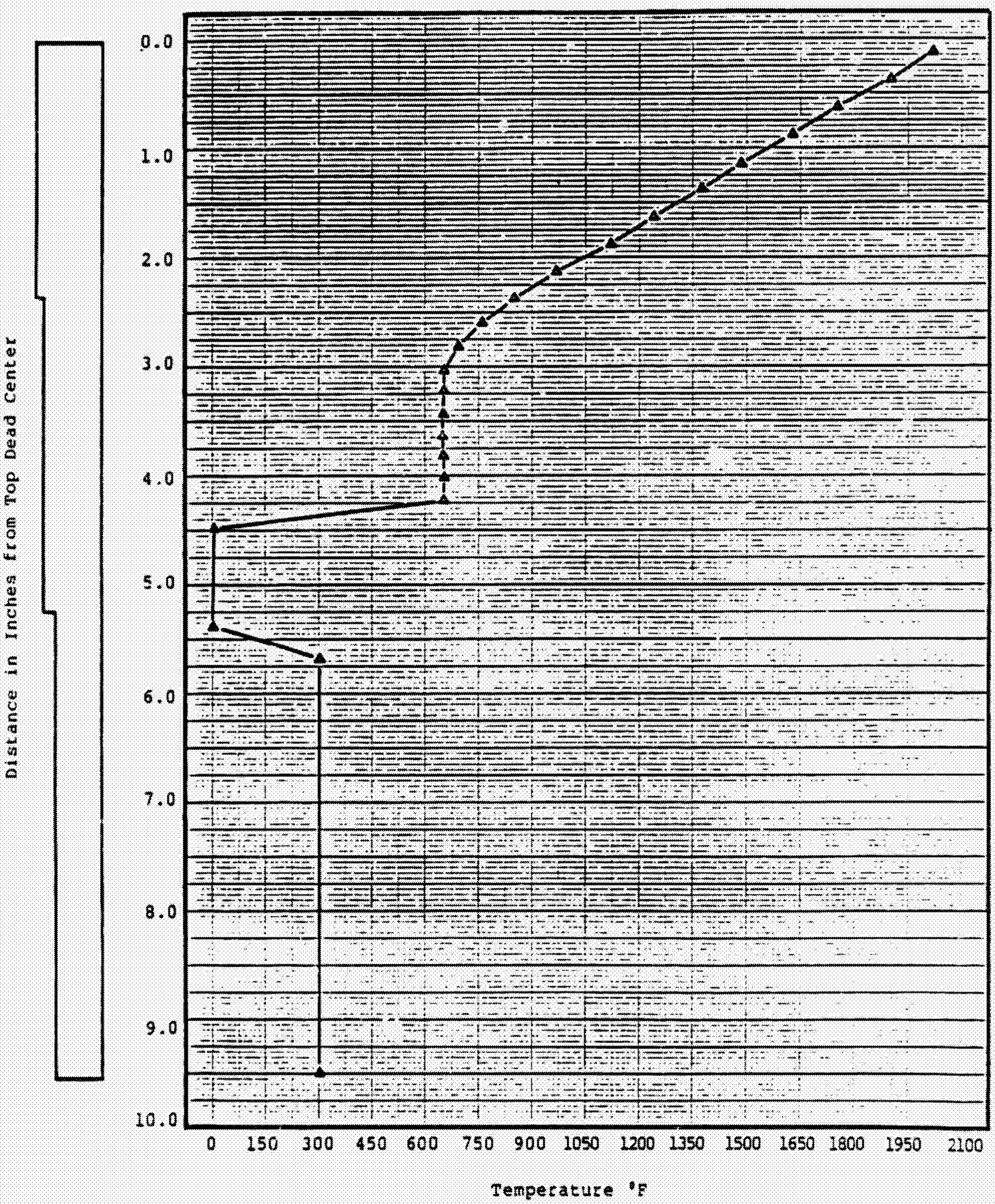

Figure 13 B Gas Temperature Distribution Along Cylinder Liner (Silicon Nitride Insulation)

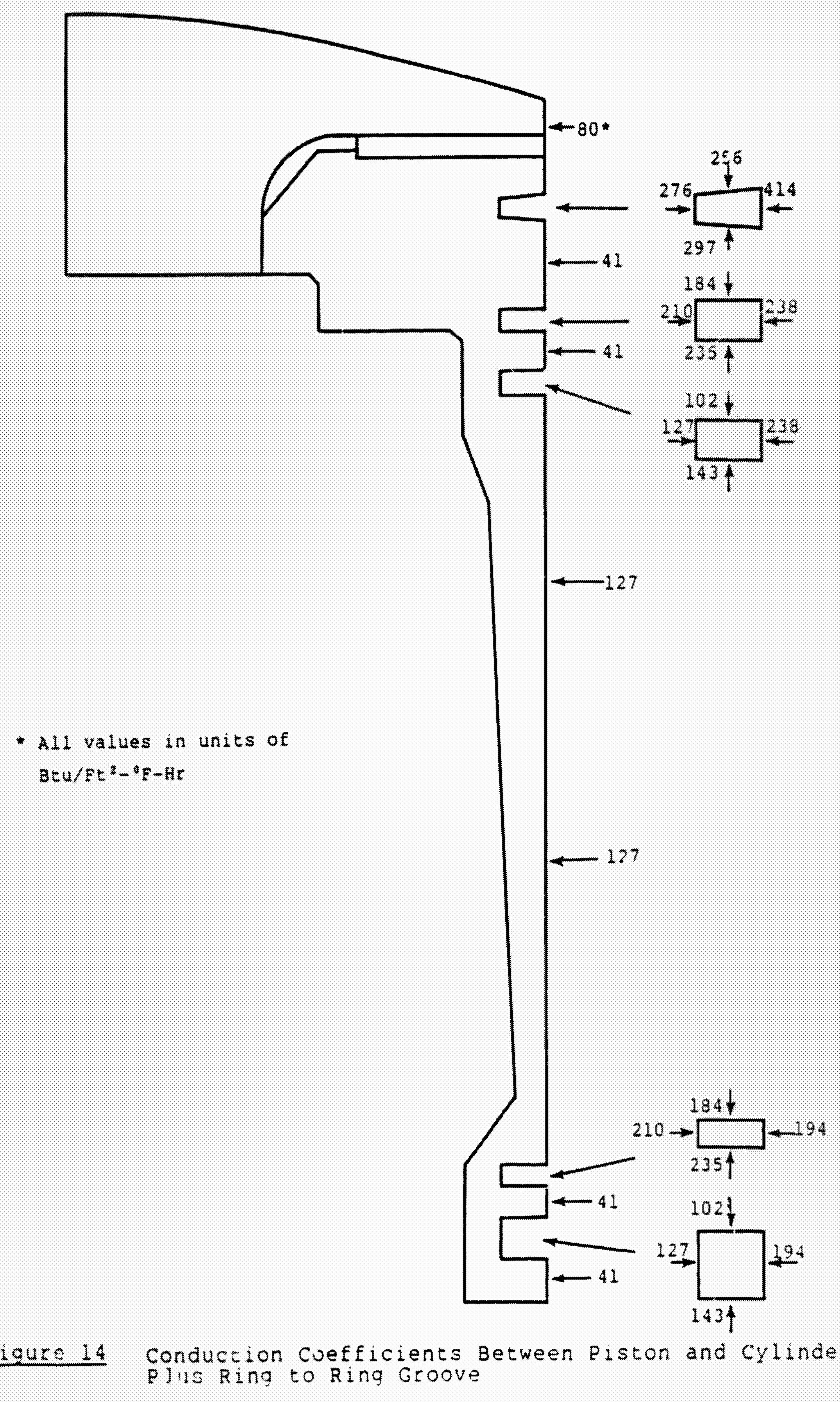

Figure 14 Conduction Coefficients Between Piston and Cylinder Plus Ring to Ring Groove

The piston conducts to the portion of the cylinder it comes into contact with during the stroke. The conduction coefficient is time weighted to distribute the heat to the cylinder properly.

$$H = 1.54 \times 10^{\text{[illegible]}} \frac{\text{Btu}}{\text{sec-in}^2\text{-}^\circ\text{F}}$$

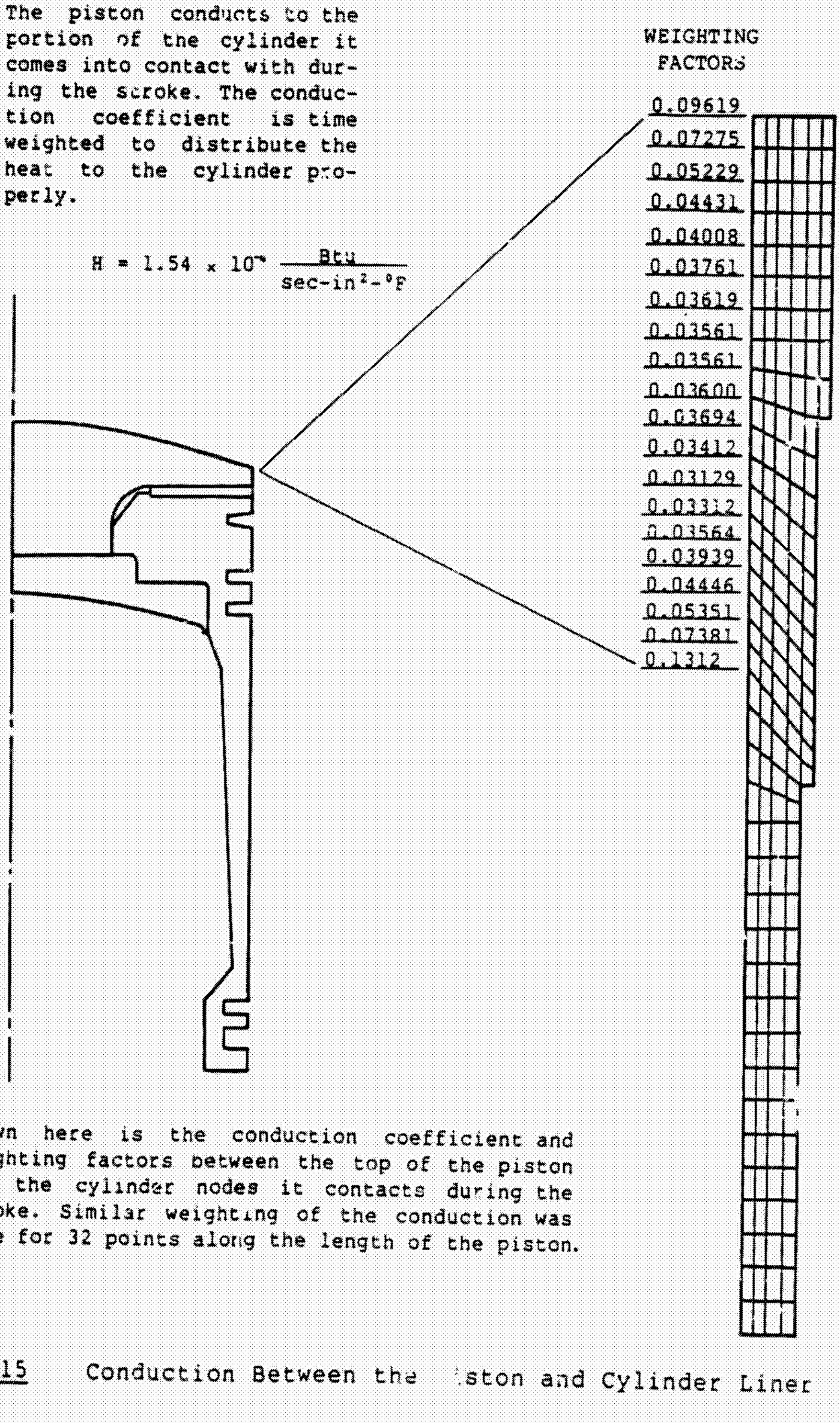

Shown here is the conduction coefficient and weighting factors between the top of the piston and the cylinder nodes it contacts during the stroke. Similar weighting of the conduction was done for 32 points along the length of the piston.

Figure 15 Conduction Between the Piston and Cylinder Liner

Figure 16A Combustion Bowl and Head Temperature - Maximum Power - All Zirconia Insulation

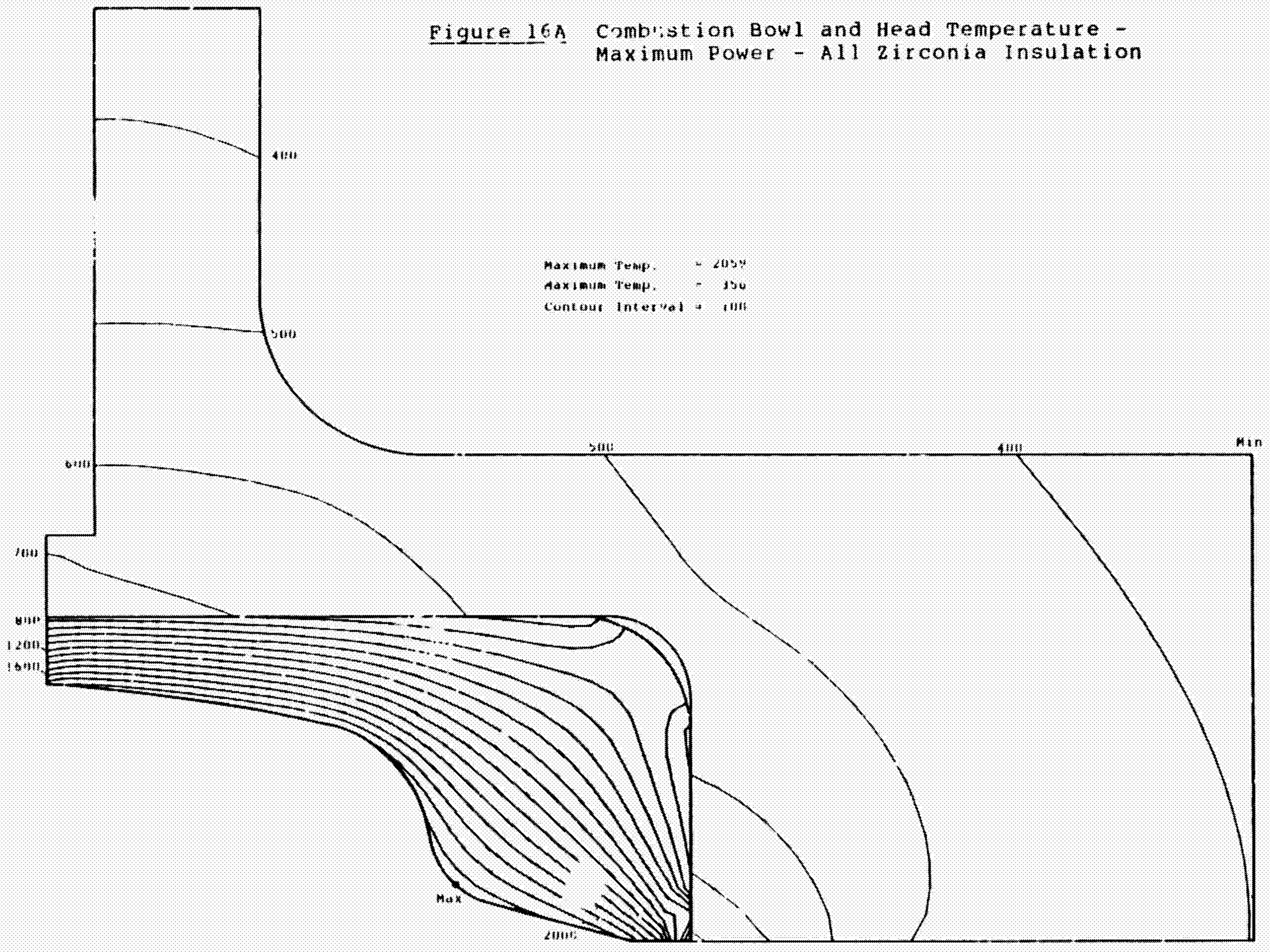

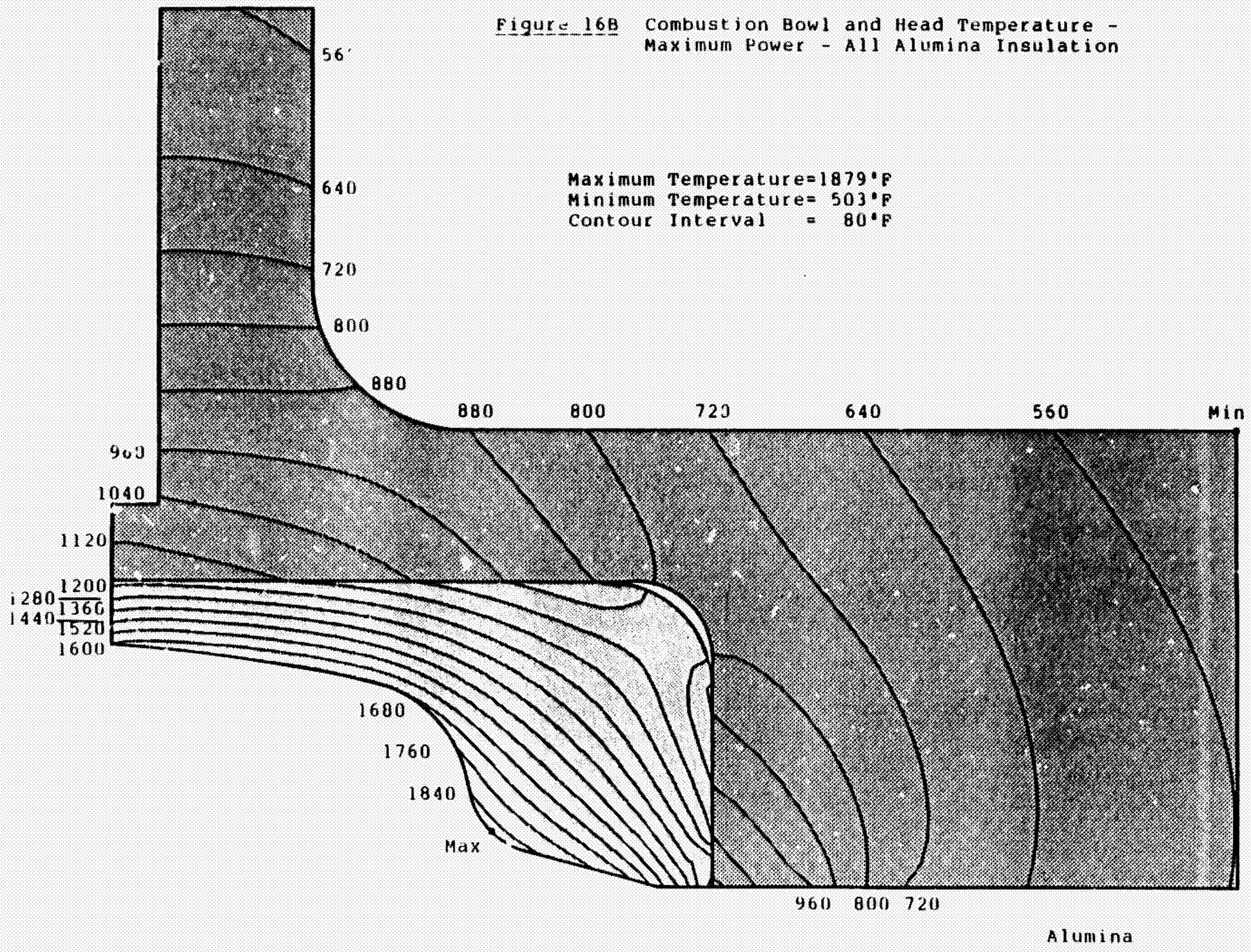

Figure 16B Combustion Bowl and Head Temperature - Maximum Power - All Alumina Insulation

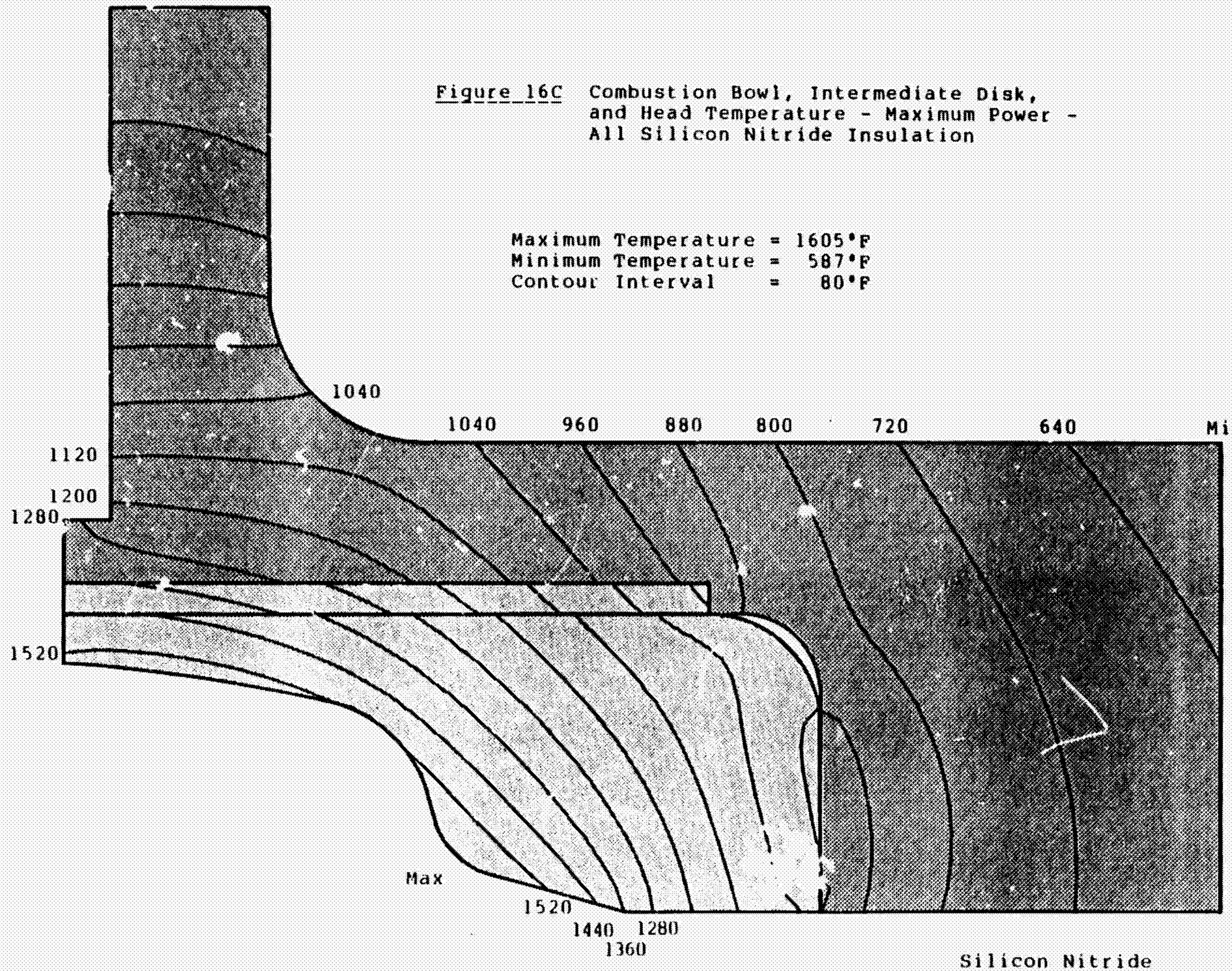

Figure 16C Combustion Bowl, Intermediate Disk, and Head Temperature - Maximum Power - All Silicon Nitride Insulation

Maximum Temperature = 1605°F
Minimum Temperature = 587°F
Contour Interval = 80°F

Figure 17A Piston Assembly Temperatures - Maximum Power - All Zirconia Insulation

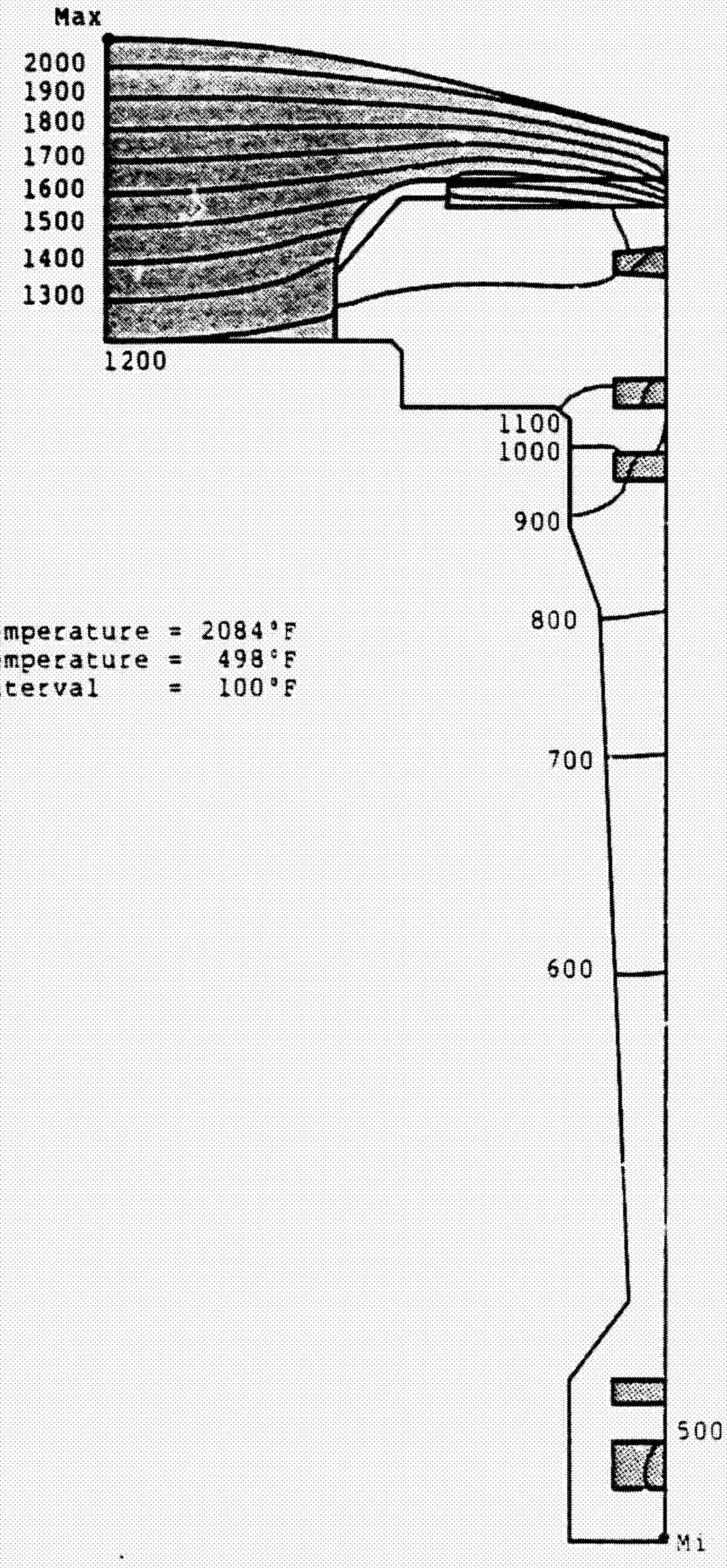

Maximum Temperature = 2084°F
Minimum Temperature = 498°F
Contour Interval = 100°F

Figure 17B Piston Assembly Temperatures - Maximum Power - All Alumina Insulation

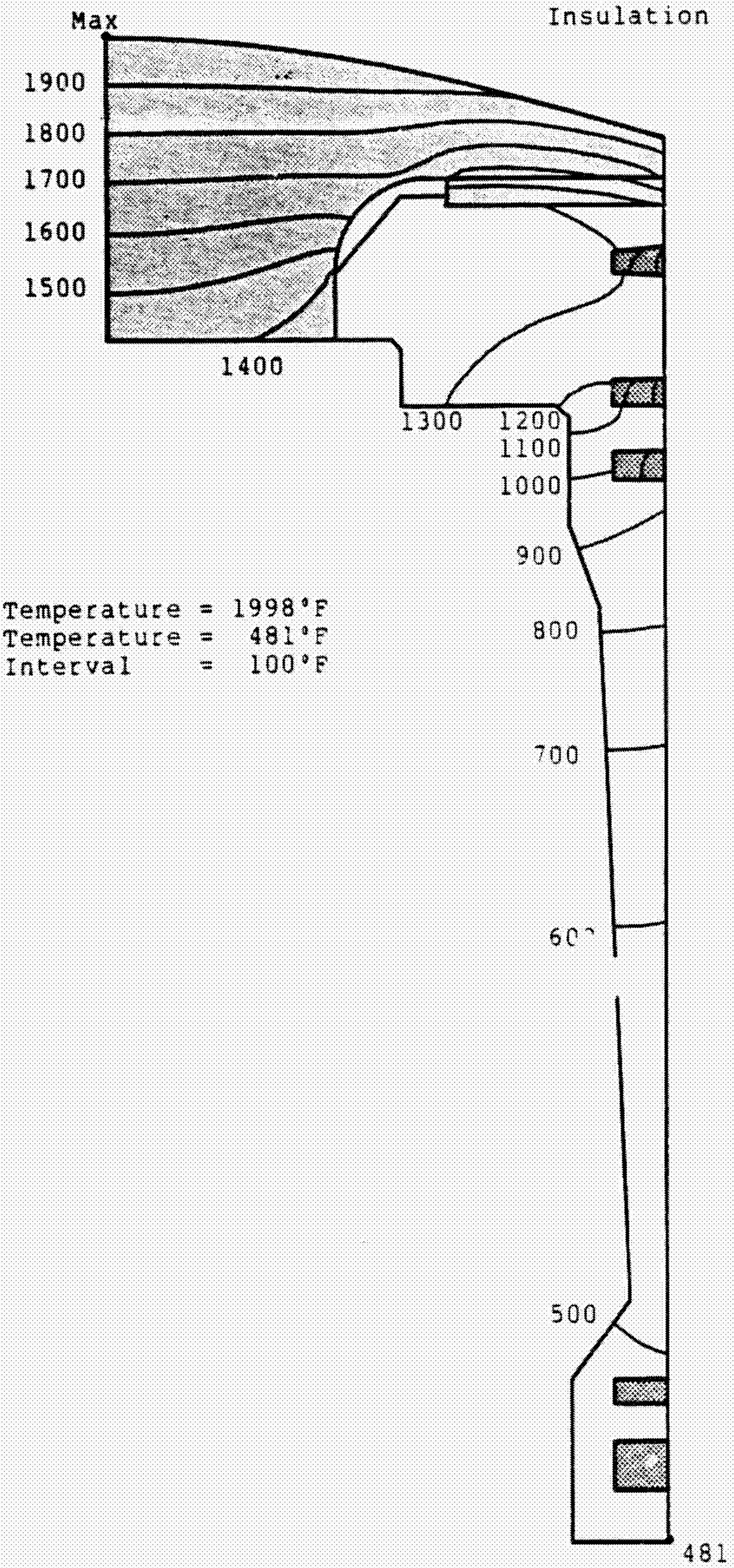

Maximum Temperature = 1998°F
Minimum Temperature = 481°F
Contour Interval = 100°F

<u>Figure 17C</u> Piston Assembly Temperatures - Maximum Power - All Silicon Nitride

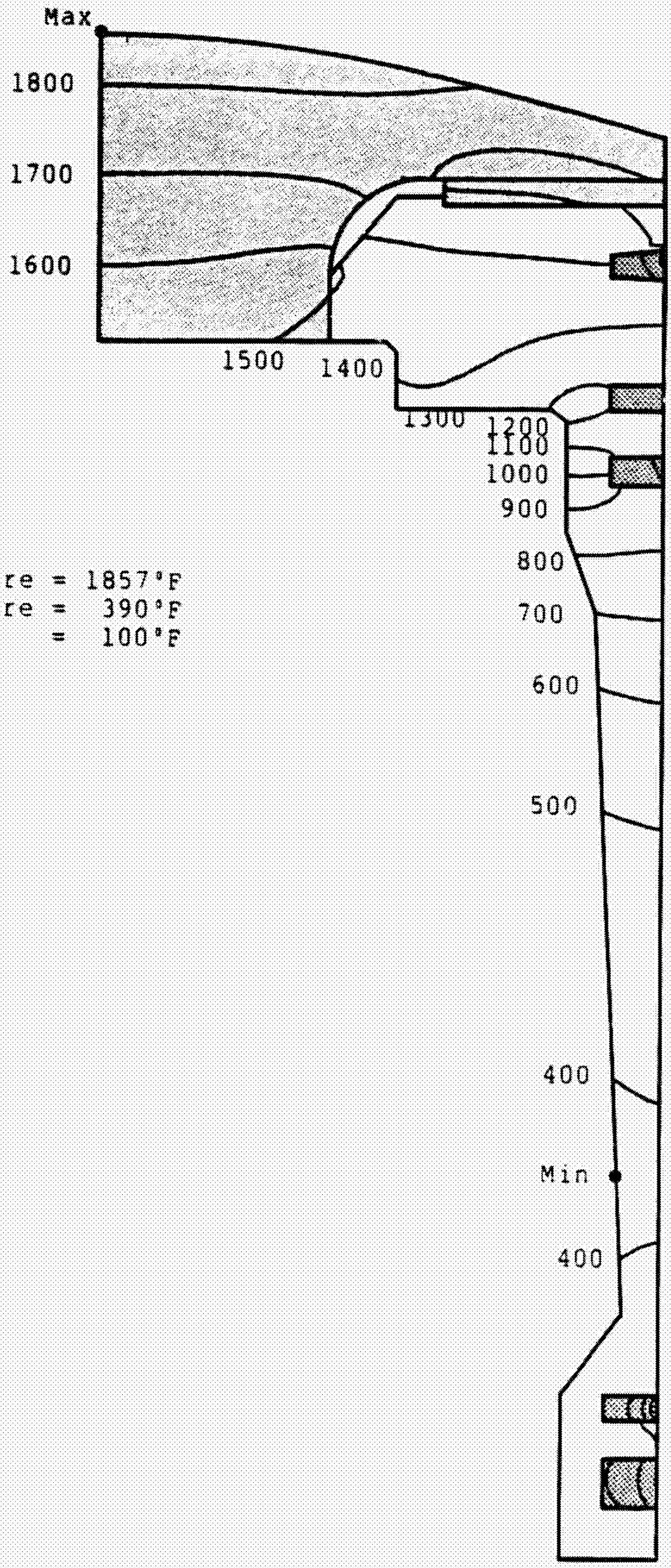

Maximum Temperature = 1857°F
Minimum Temperature = 390°F
Contour Interval = 100°F

Figure 18A ..rconia Liner Insert Temperature - Maximum Power

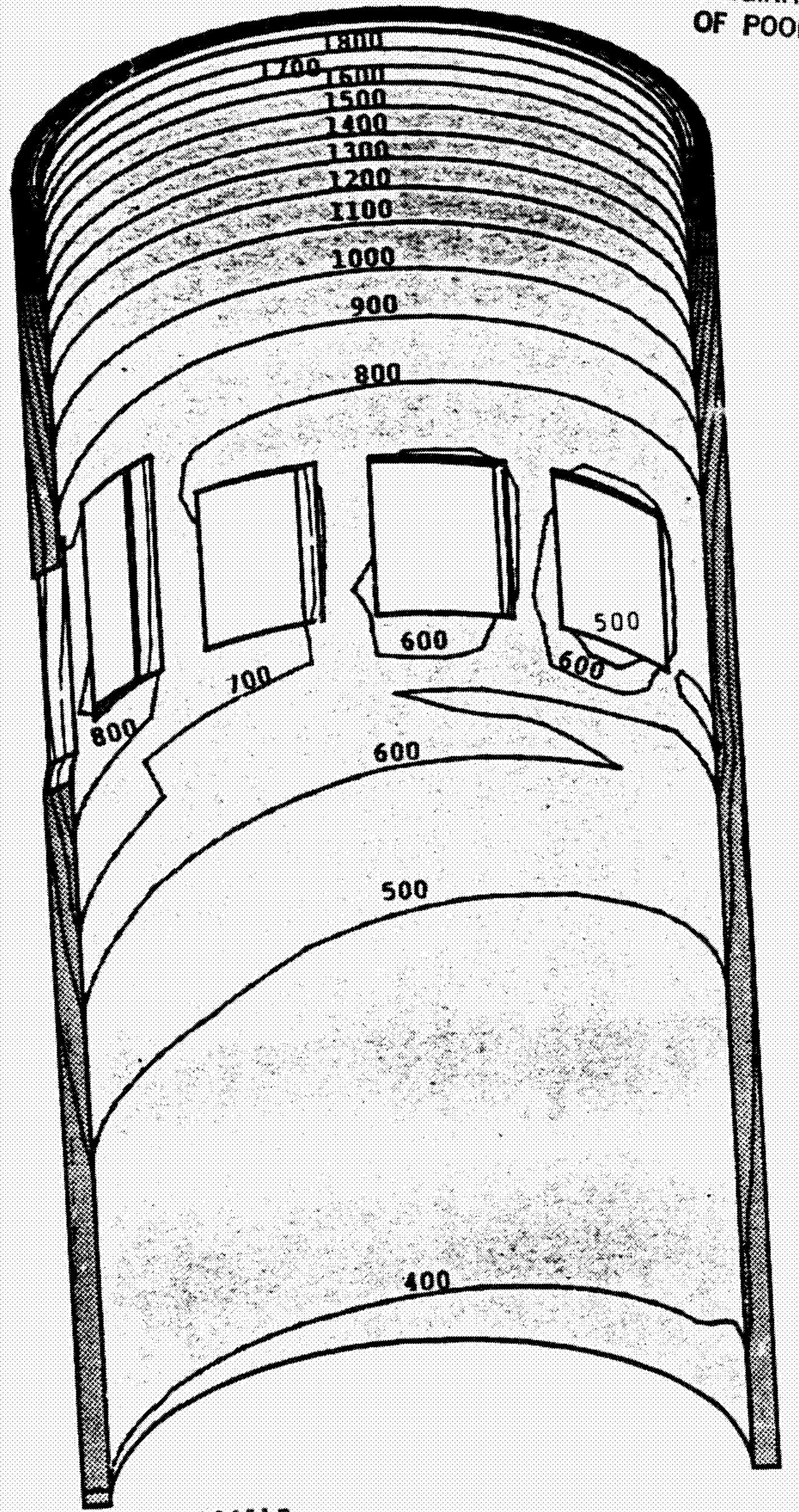

n m Temperature = 1865°F
um Temperature = 365°F
... Interval = 100°F

Figure 18B Zirconia Liner Insert Temperature - Maximum Power

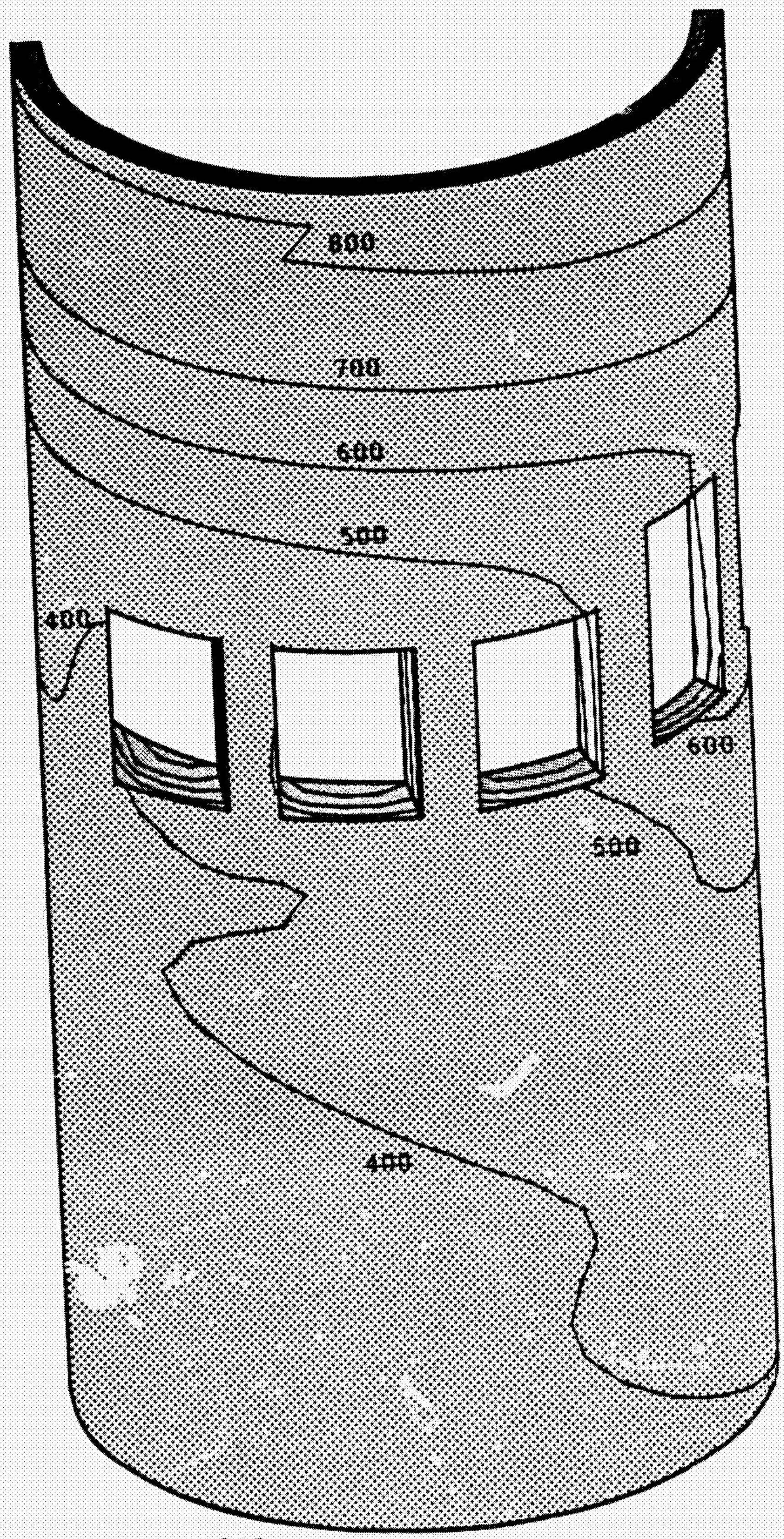

Maximum Temperature = 1865°F
Minimum Temperature = 365°F
Contour Interval = 100°F

Figure 19A Metal Reinforcing Cylinder Temperatures - Maximum Power - All Zirconia Insulated

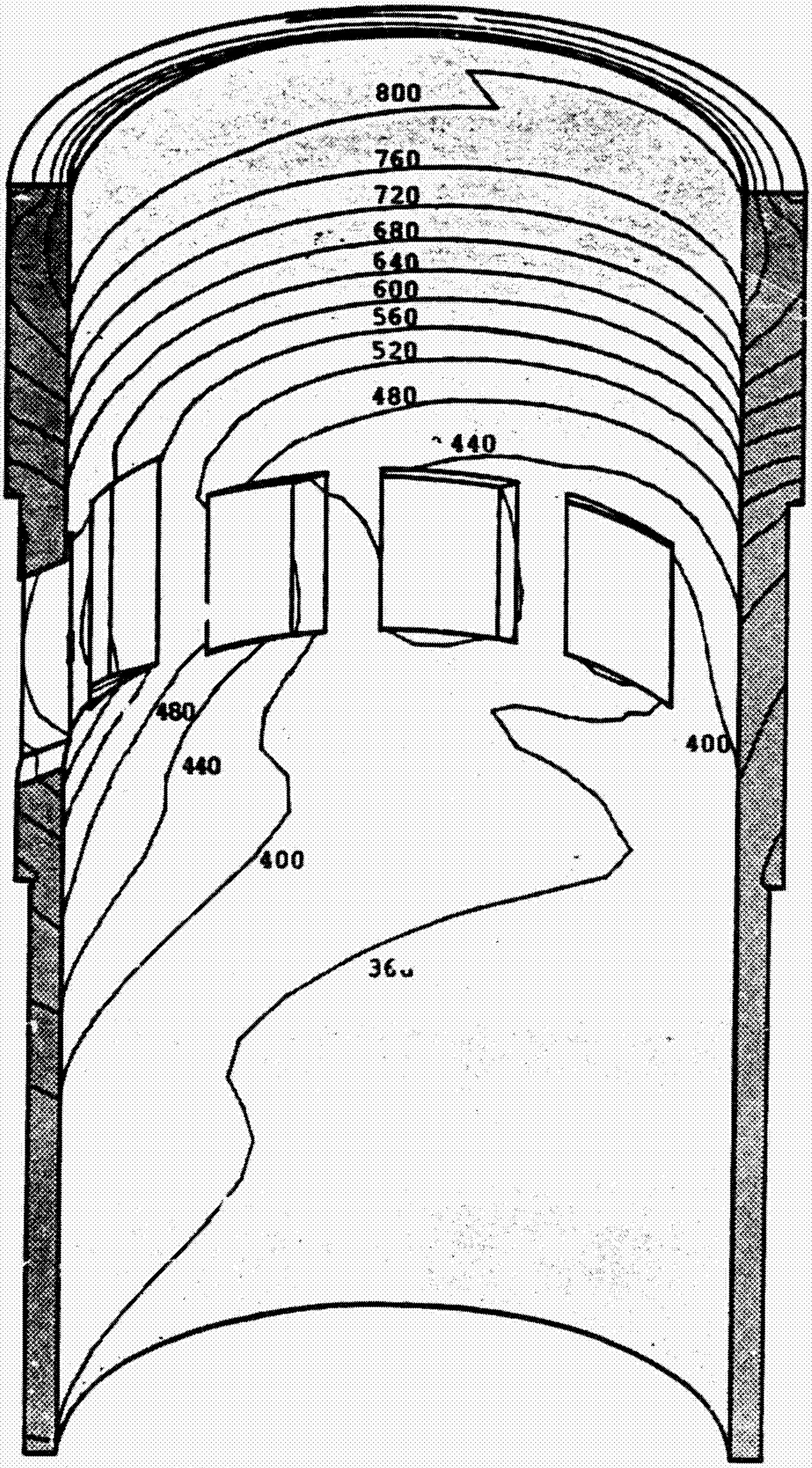

Maximum Temperature = 855°F
Minimum Temperature = 334°F
Contour Interval = 40°F

Figure 19B Metal Reinforcing Cylinder Temperatures - Maximum Power - All Zirconia Insulation

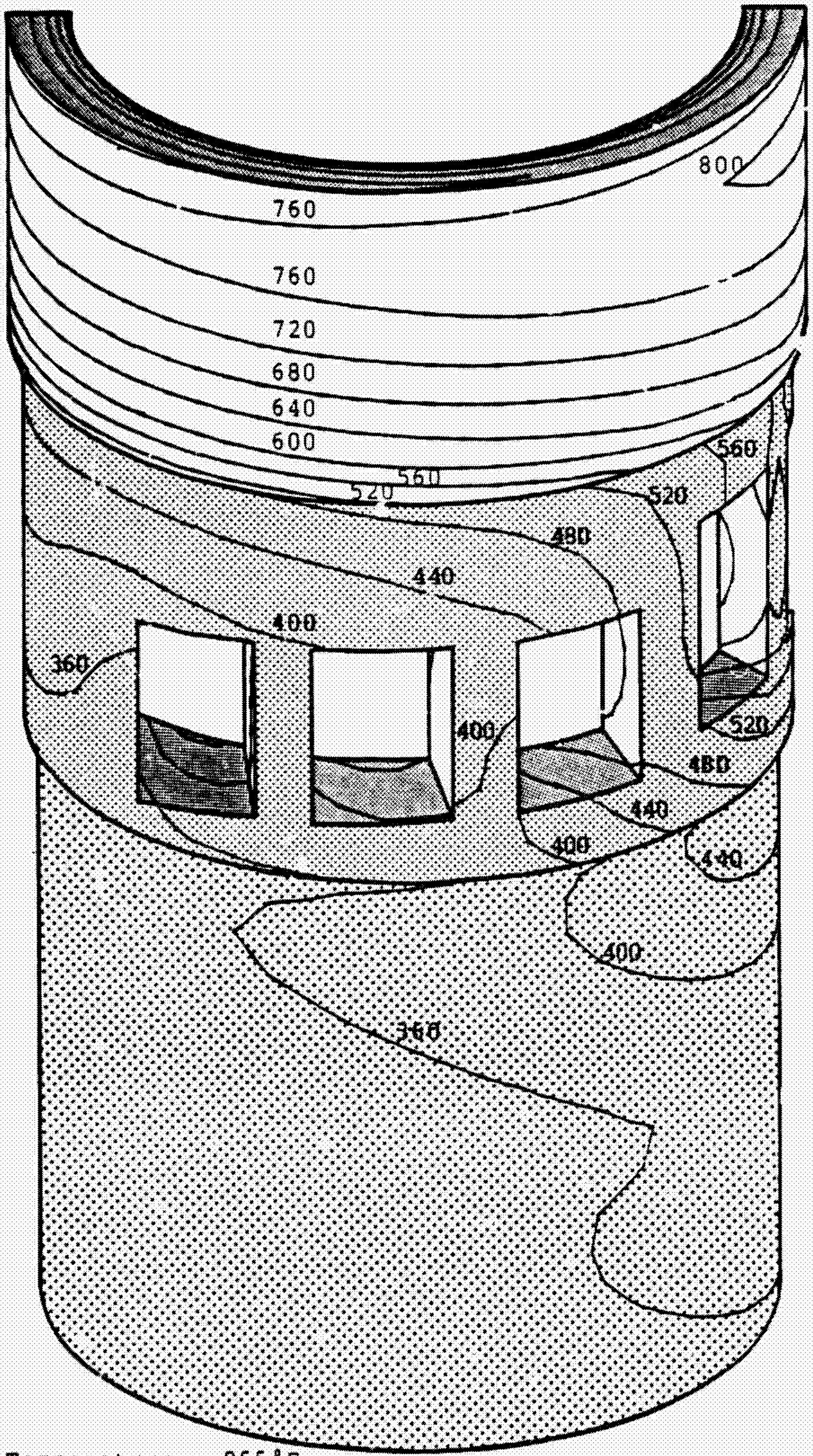

Maximum Temperature = 855°F
Minimum Temperature = 334°F
Contour Interval = 40°F

Figure 20A Block Temperature - Maximum Power - All Zirconia Insulated

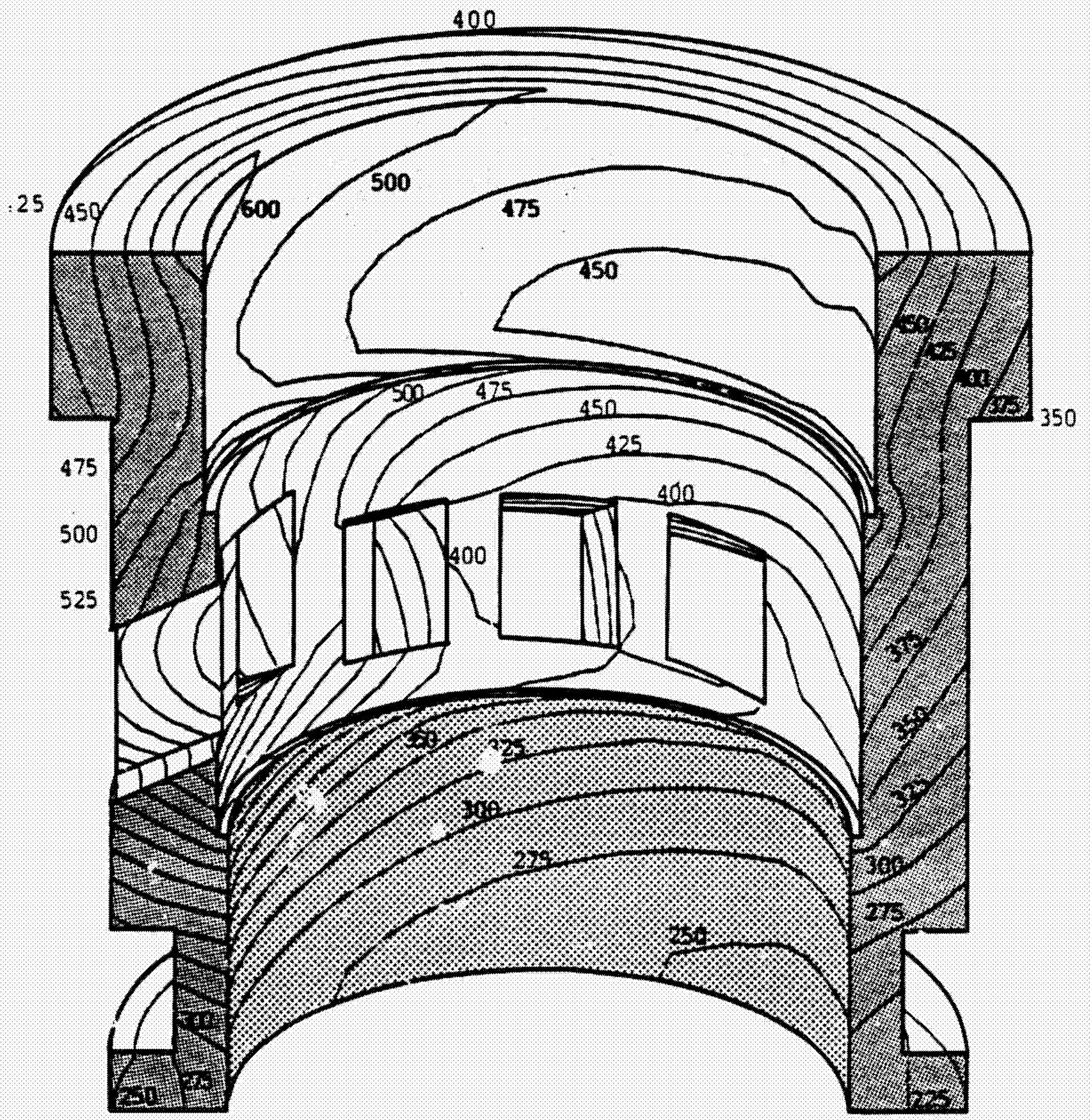

Maximum Temperature = 647°F
Minimum Temperature = 204°F
Contour Interval = 25°F

Figure 20B Block Temperature - Maximum Power - All Zirconia Insulated

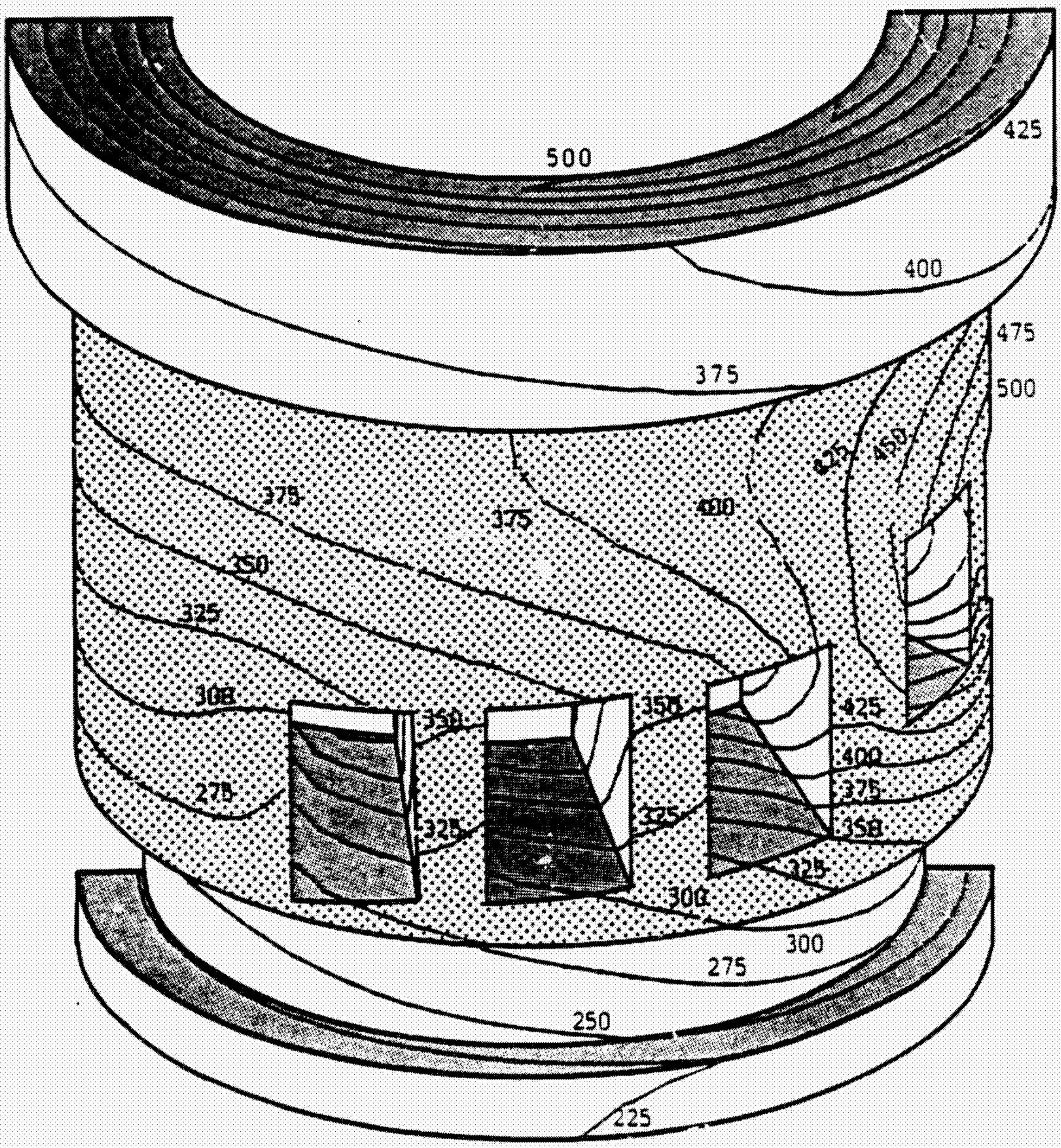

Maximum Temperature = 647°F
Minimum Temperature = 204°F
Contour Interval = 25°F

Figure 21A Alumina Liner Insert Temperature - Maximum Power

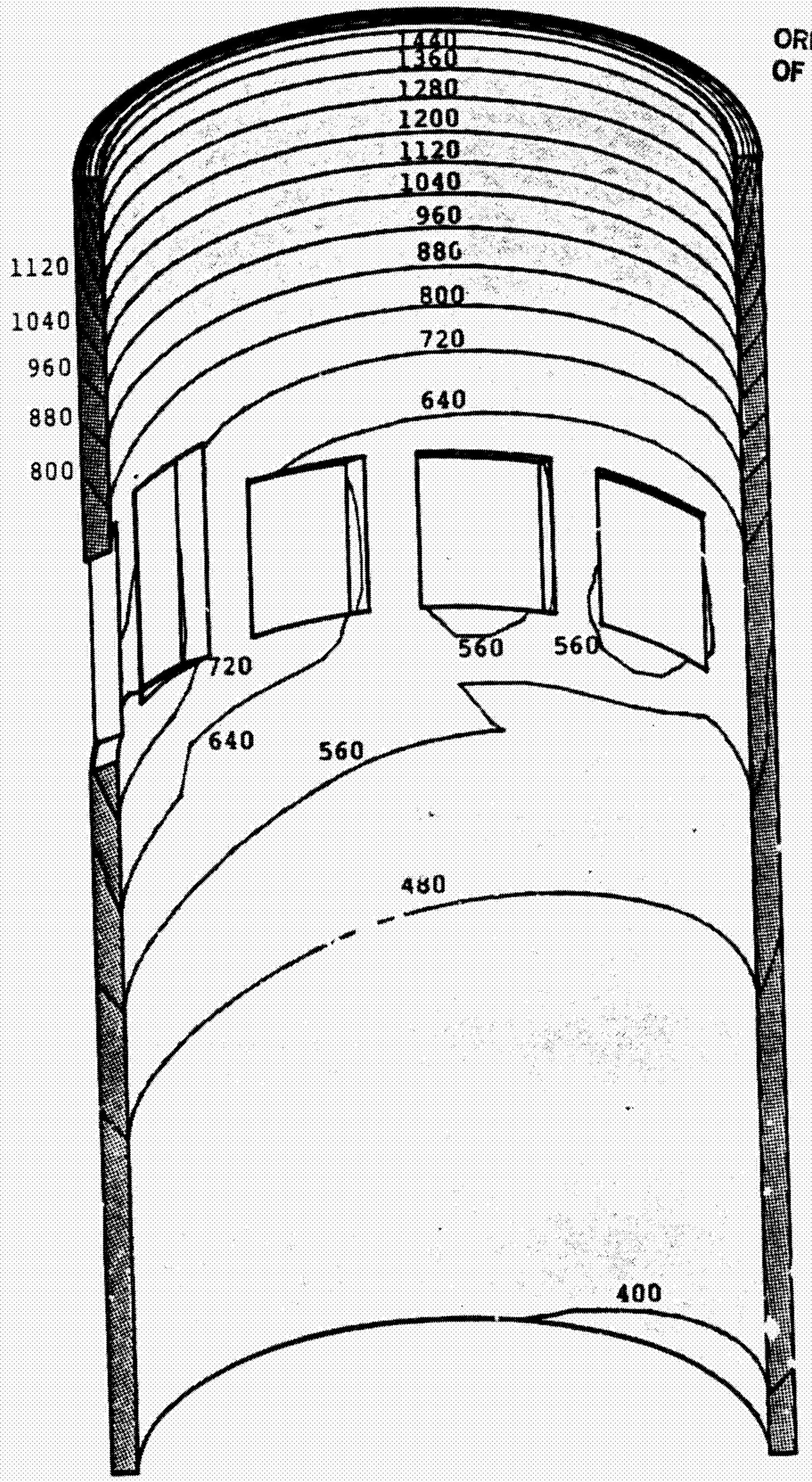

Maximum Temperature = 1572°F
Minimum Temperature = 394°F
Contour Interval = 80°F

Figure 21B Alumina Liner Insert Temperature - Maximum Power

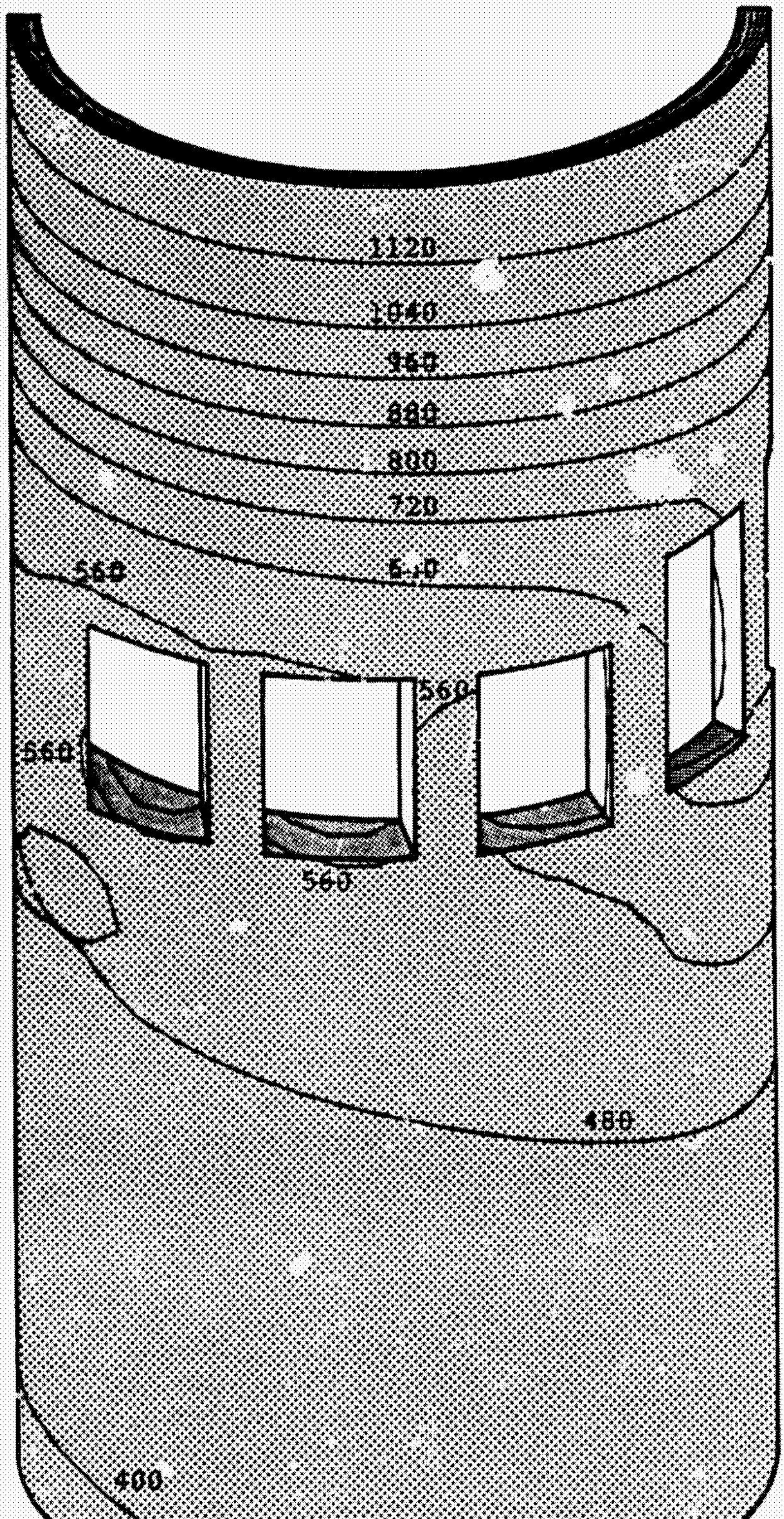

Maximum Temperature = 1572°F
Minimum Temperature = 304°F
Contour Interval = 80°F

Figure 22A Metal Reinforcing Cylinder Temperatures - Maximum Power All Alumina Insulation

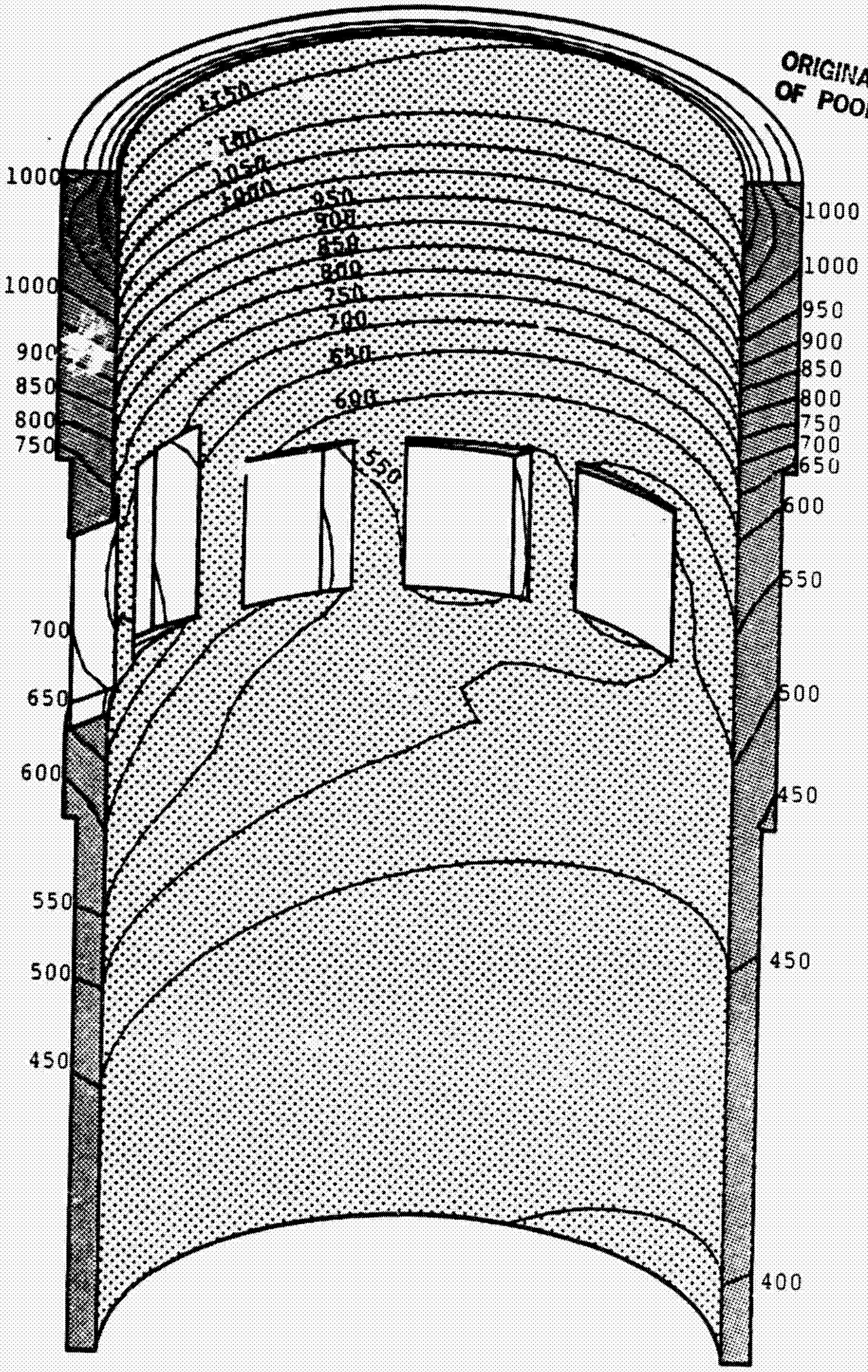

Maximum Temperature = 1170°F
Minimum Temperature = 395°F
Contour Interval = 50°F

C-3

Figure 22B Metal Reinforcing Cylinder Temperatures - Maximum Power - All Alumina Insulated

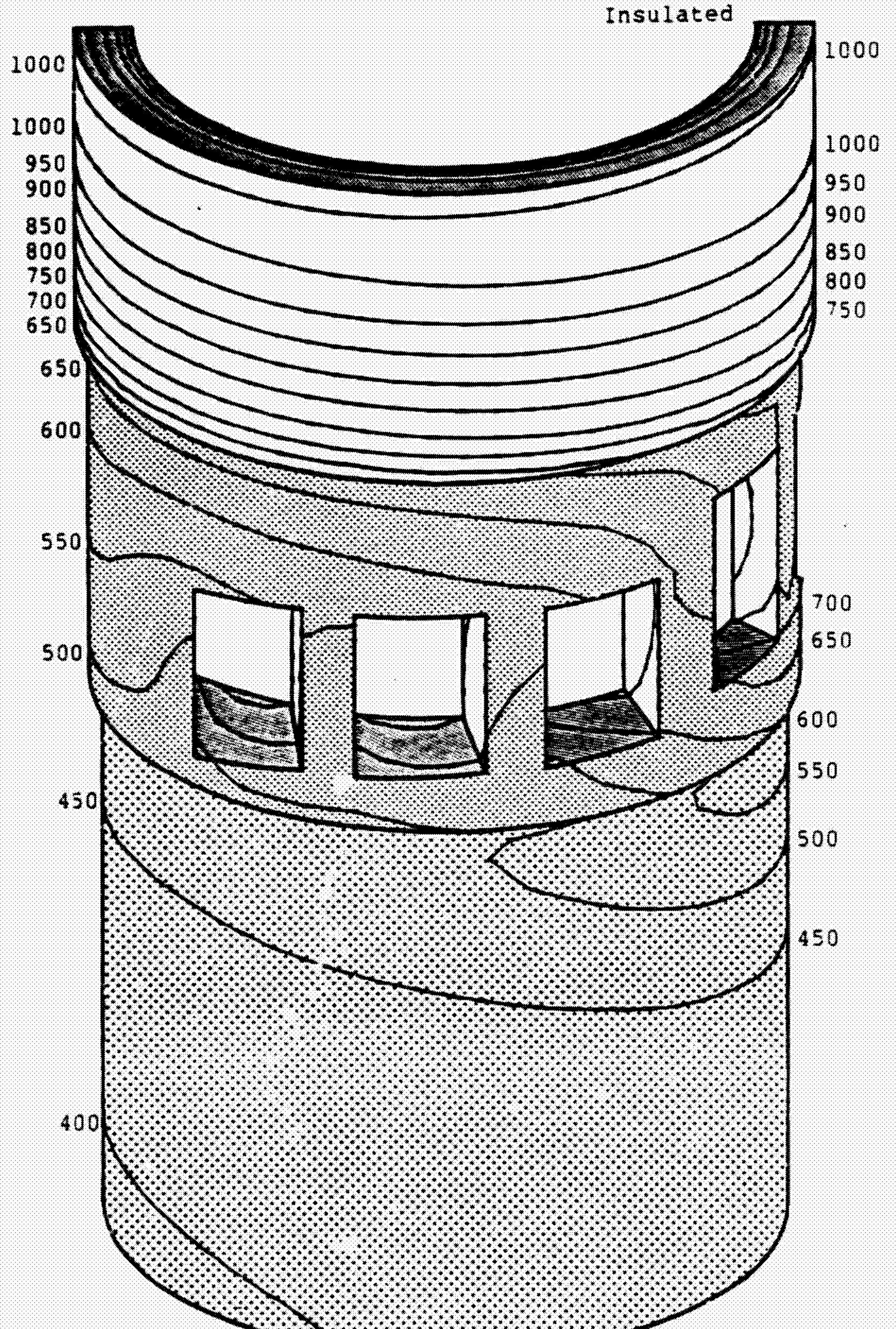

Maximum Temperature = 1170°F
Minimum Temperature = 395°F
Contour Interval = 50°F

Figure 23A Block Temperatures - Maximum Power - All Alumina Insulation

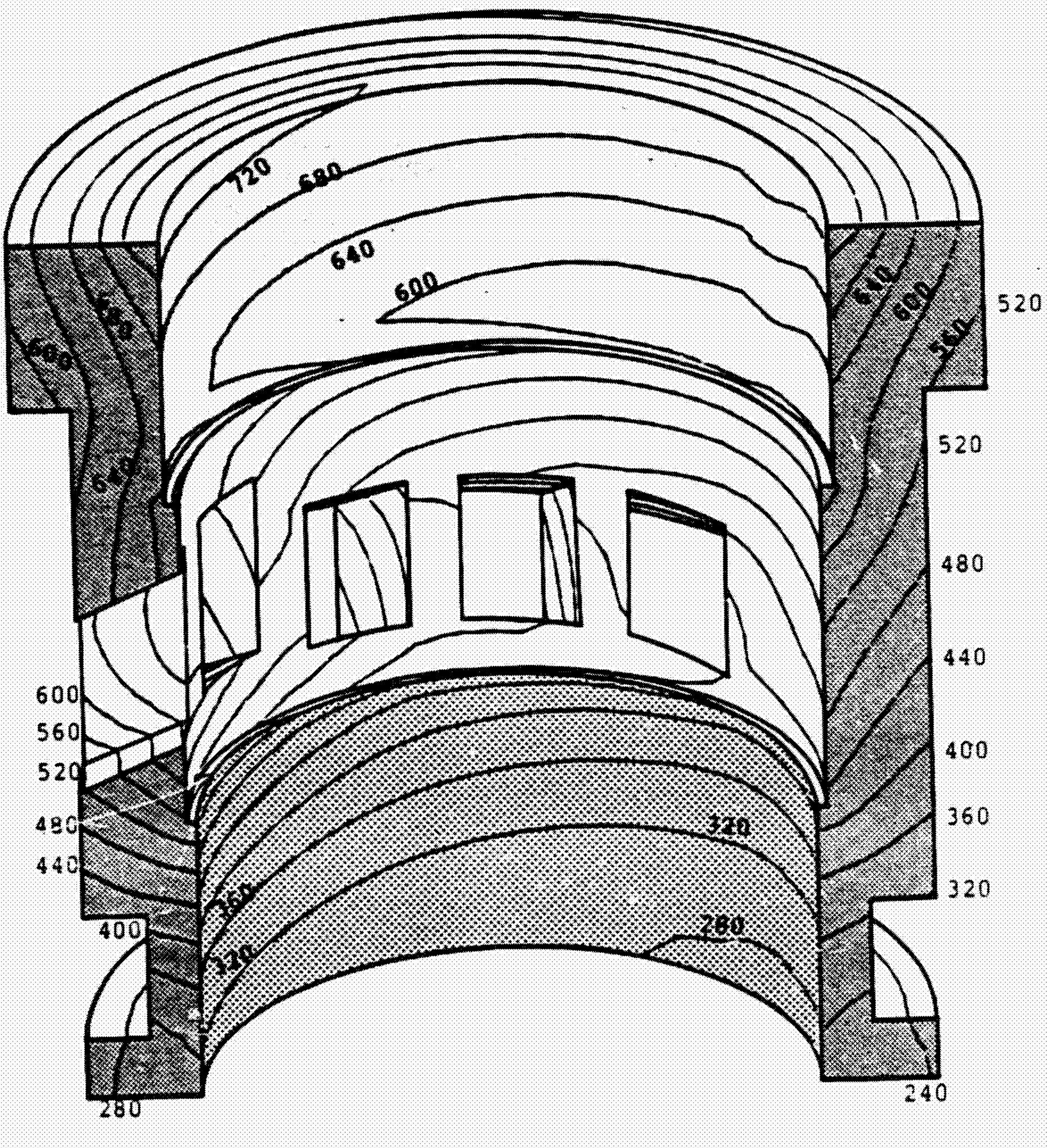

Maximum Temperature = 741°F
Minimum Temperature = 230°F
Contour Interval = 40°F

Figure 23B Block Temperatures - Maximum Power - All Alumina Insulation

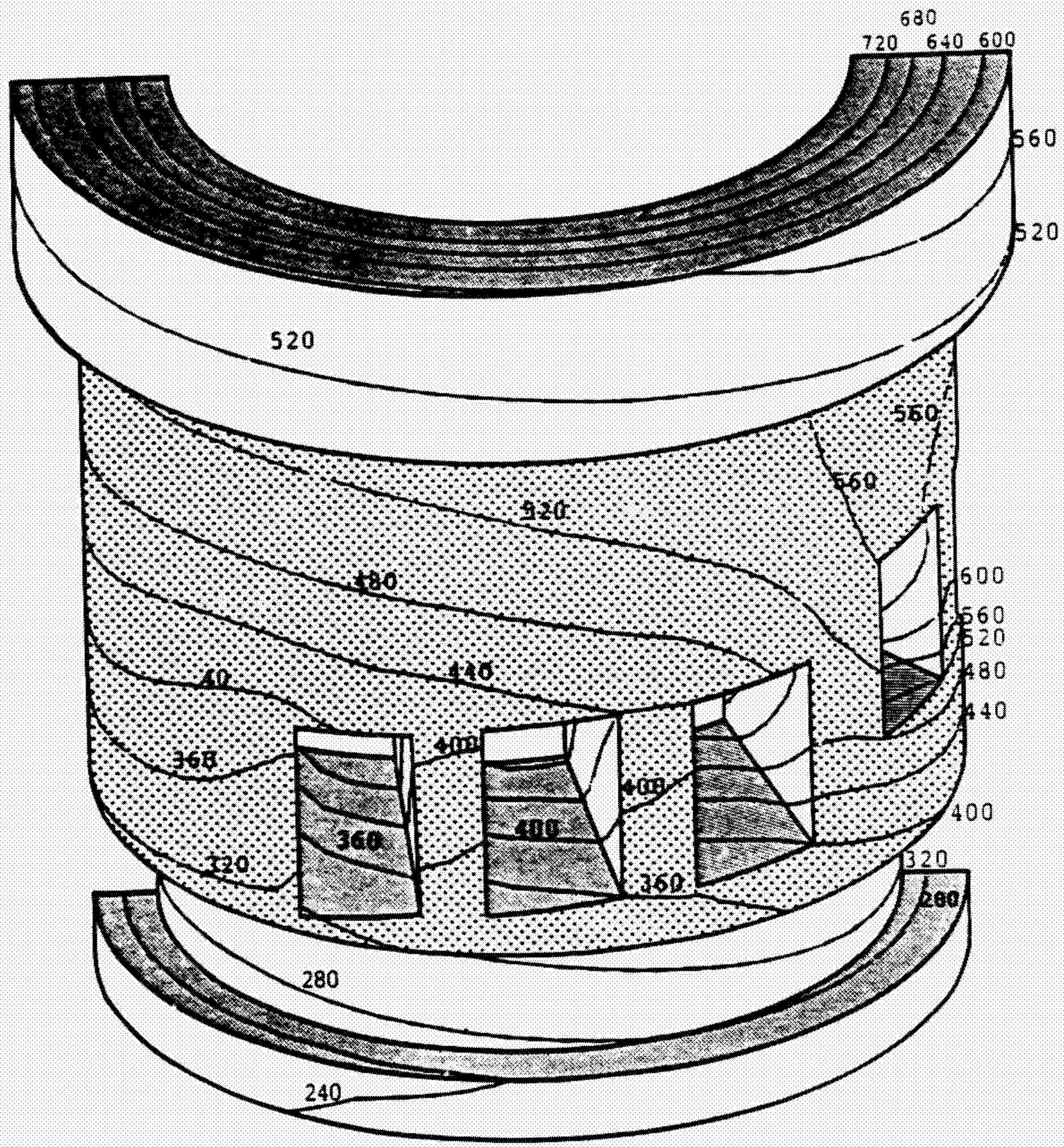

Maximum Temperature = 741°F
Minimum Temperature = 230°F
Contour interval = 40°F

Figure 24A Silicon Nitride Insert Temperatures - Maximum Power

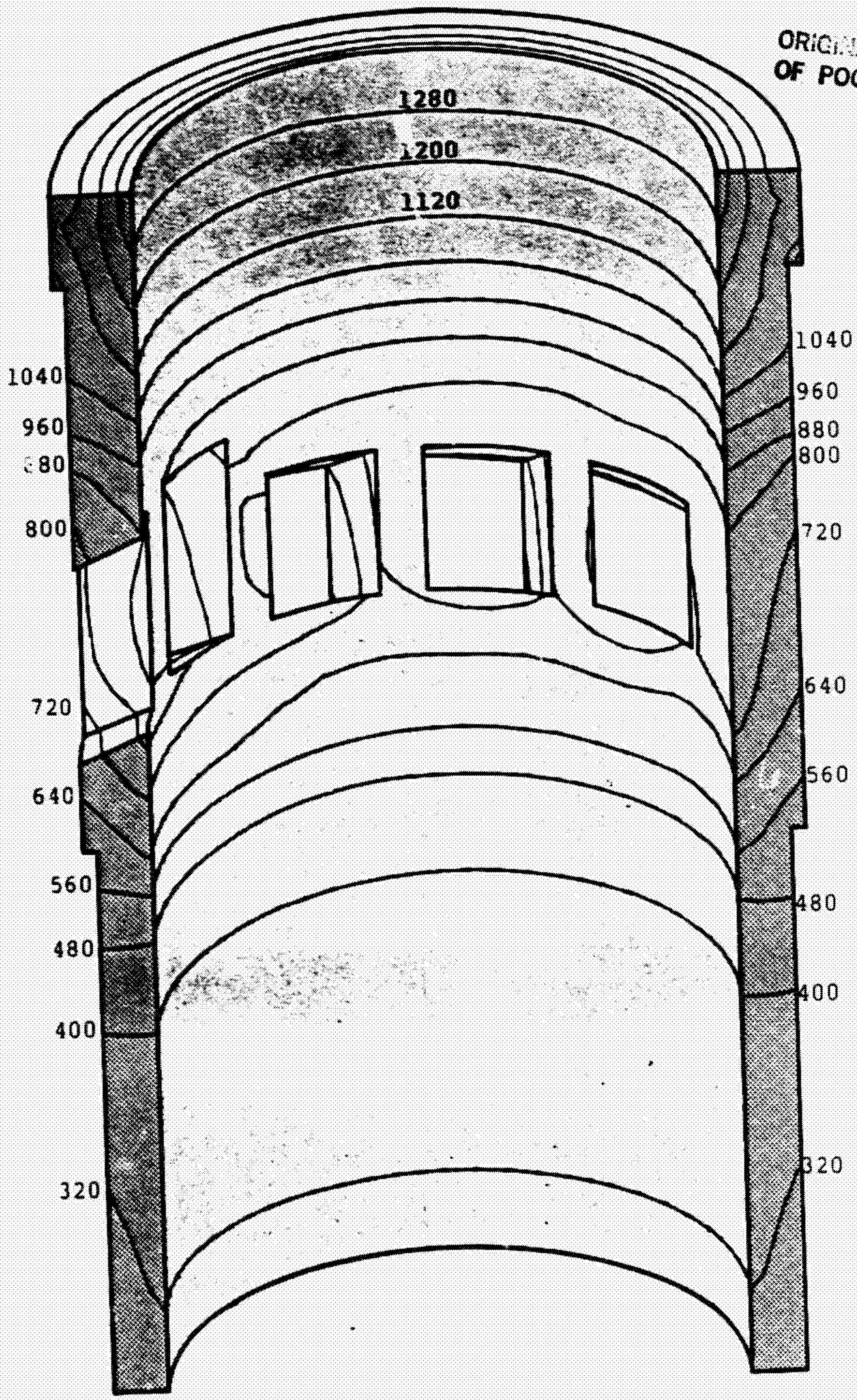

Maximum Temperature = 1364°F
Minimum Temperature = 303°F
Contour Interval = 80°F

<u>Figure 24B</u> Silicon Nitride Insert Temperatures - Maximum Power

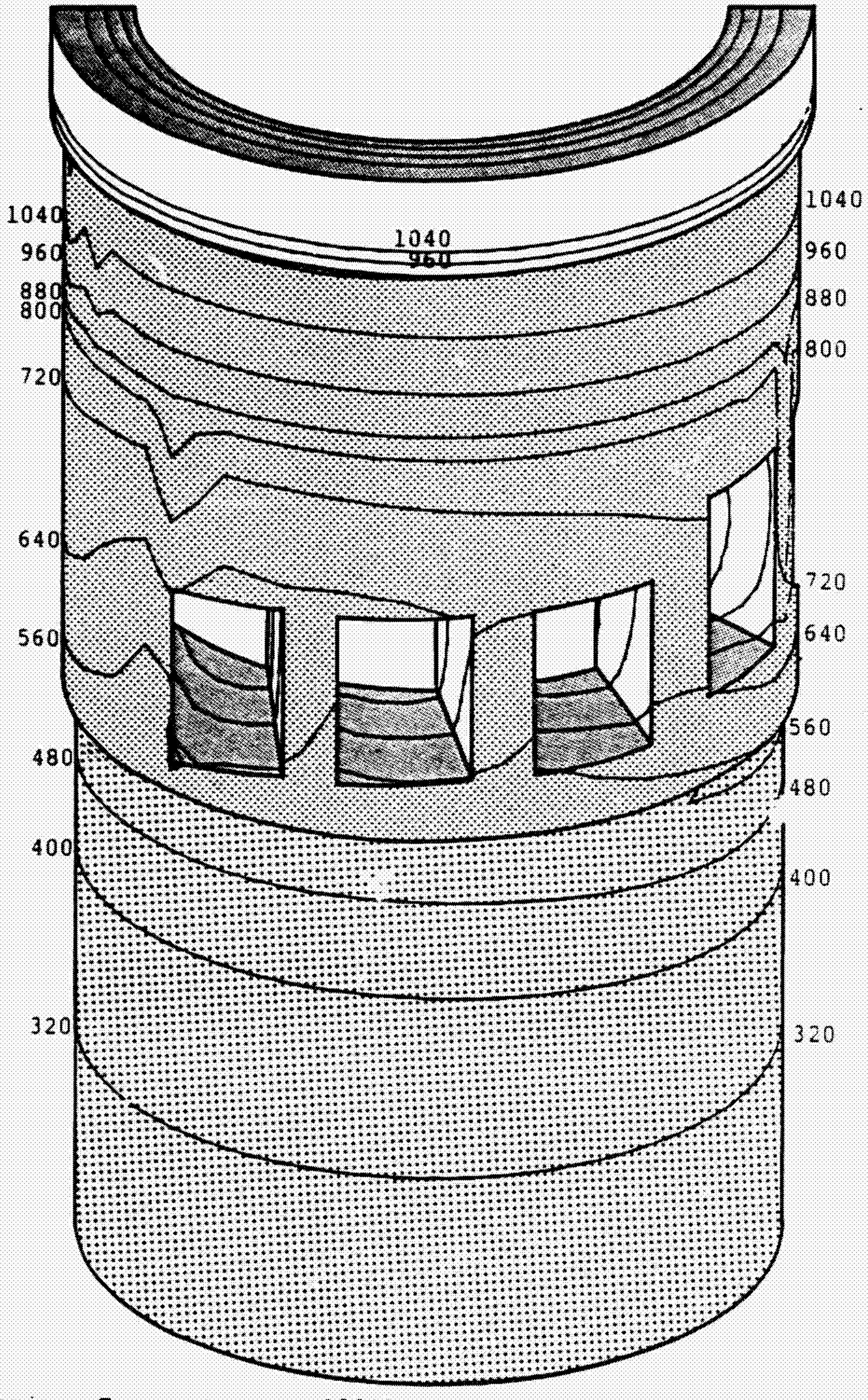

Maximum Temperatures = 1364°F
Minimum Temperatures = 303°F
Contour Interval = 80°F

Figure 25A Block Temperatures - Maximum Power - All Silicon Nitride Insulation

ORIGINAL PAGE IS OF POOR QUALITY

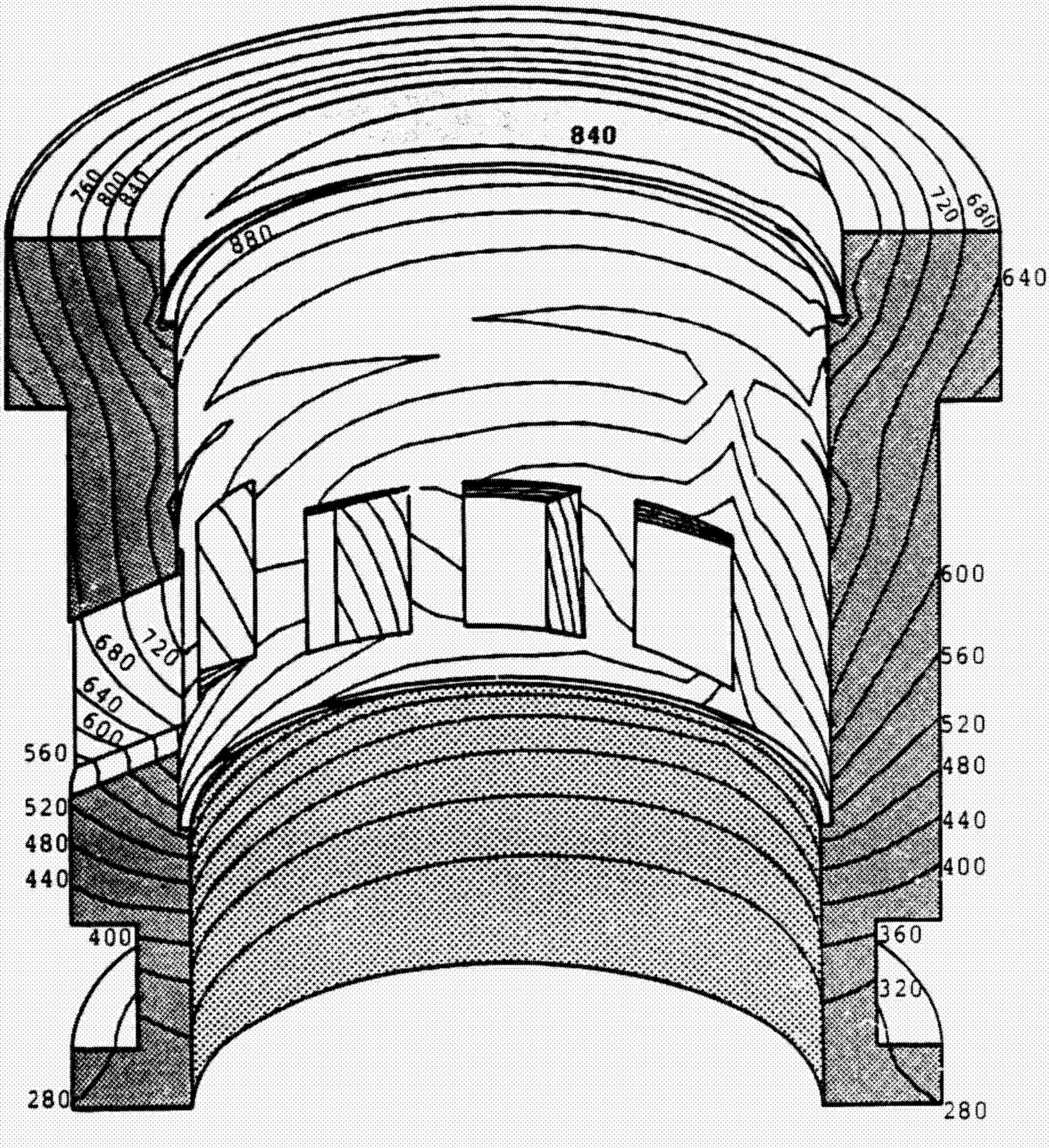

Maximum Temperature - 896°F
Minimum Temperature = 260°F
Increase = 40°F

<u>Figure 25B</u> Block Temperature - Maximum Power - All Nitride Insulation

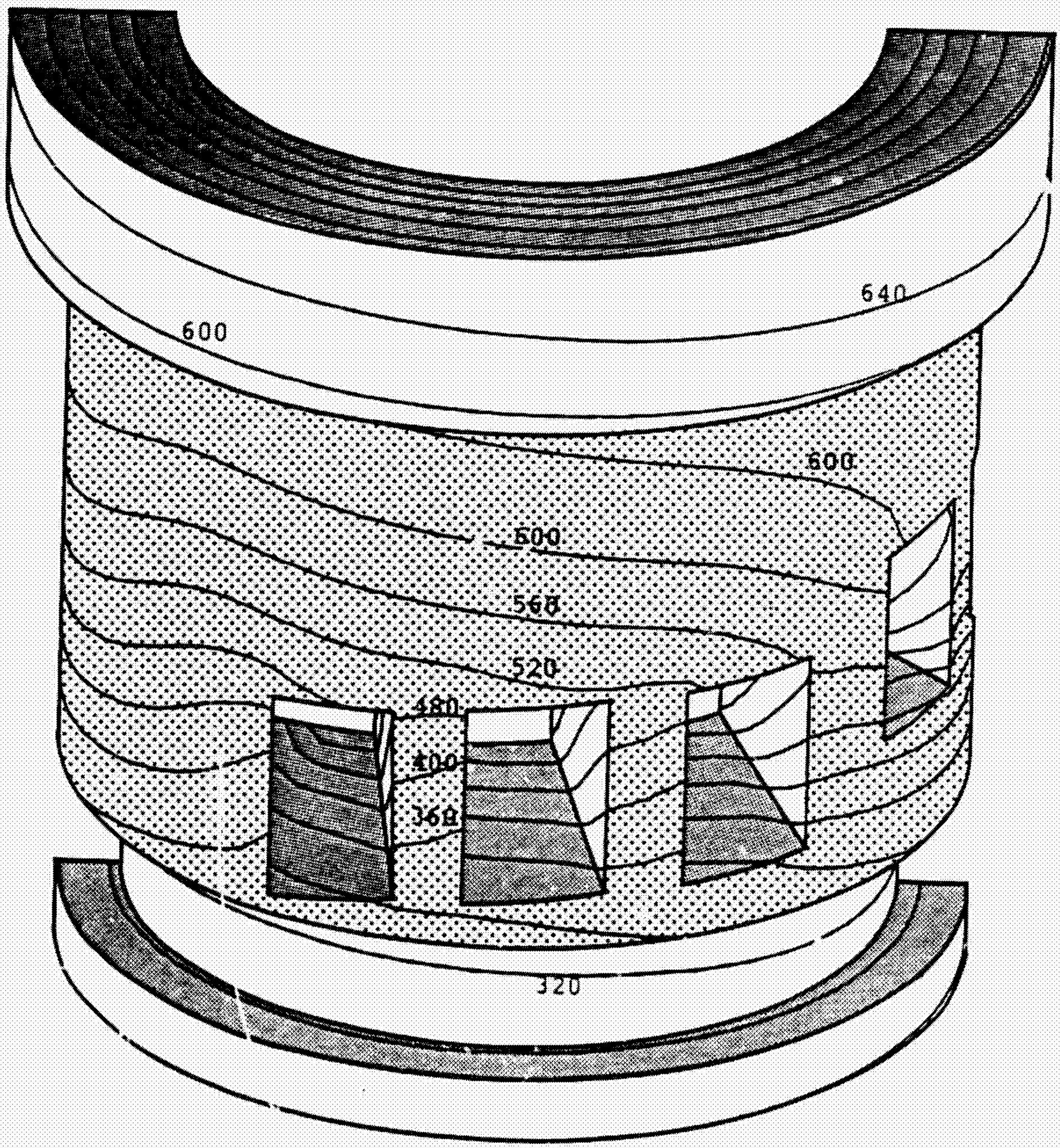

Maximum Temperature = 896°F
Minimum Temperature = 260°F
Increase = 40°F

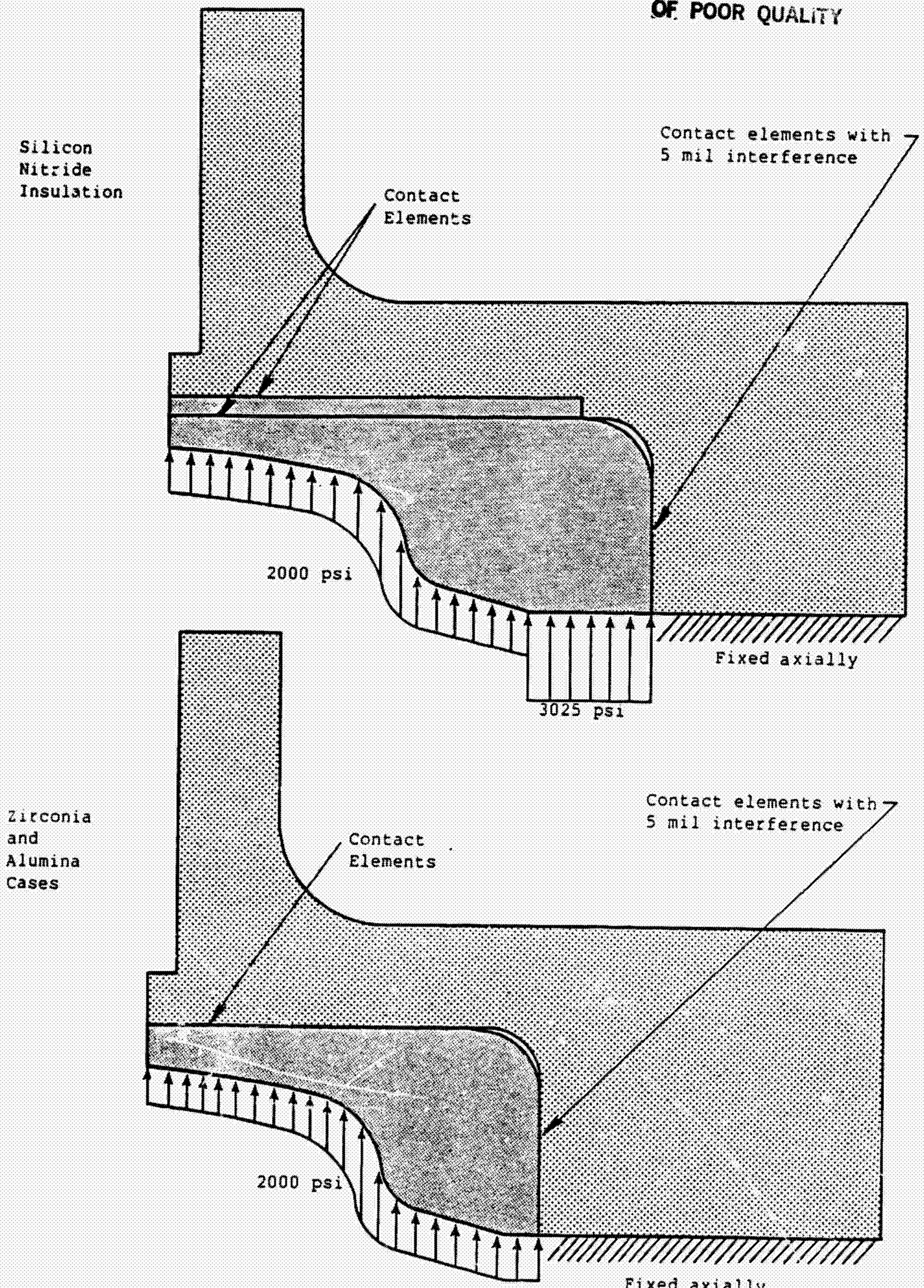

Figure 26 Head Structural Boundary Conditions

Figure 27A Combustion Bowl Stresses - Maximum Power - All Zirconia Insulated

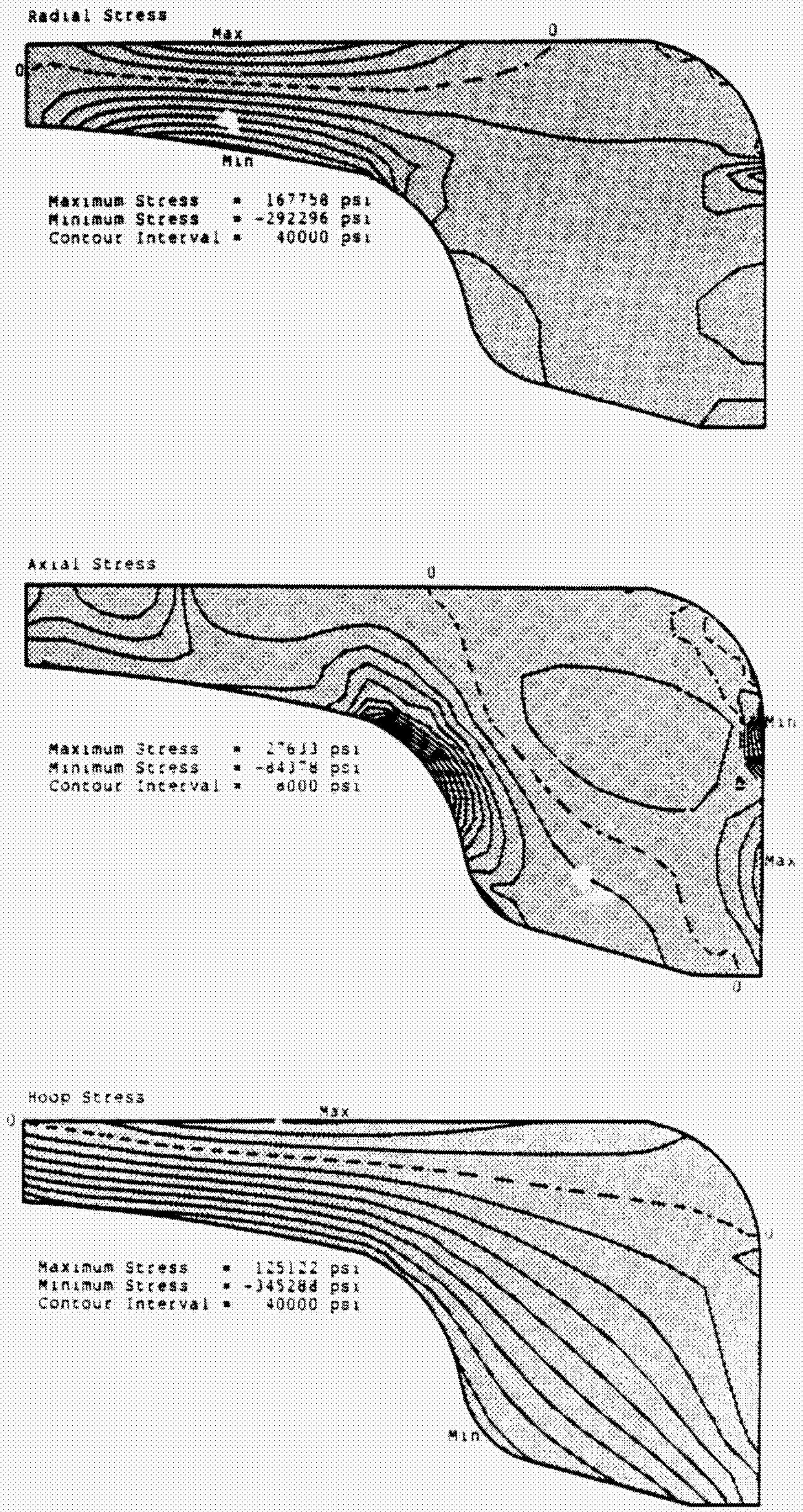

Figure 27B Combustion Bowl Stresses - Maximum Power - All Alumina Insulated

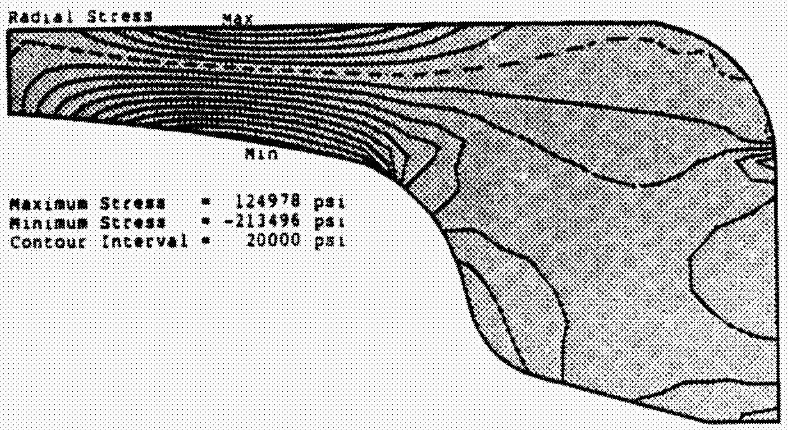

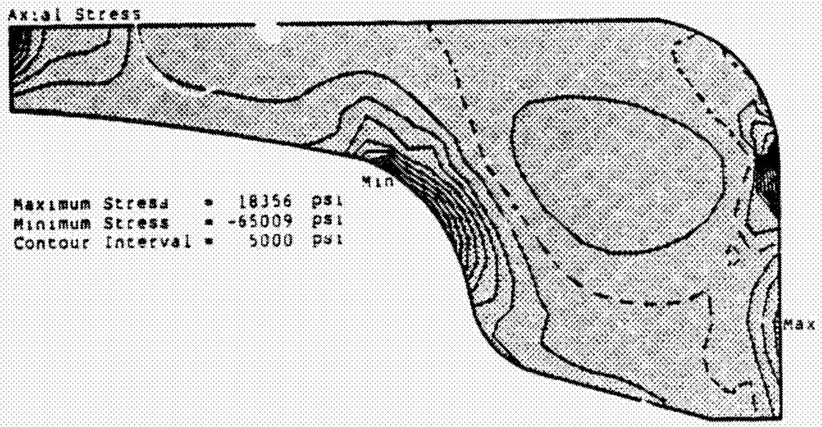

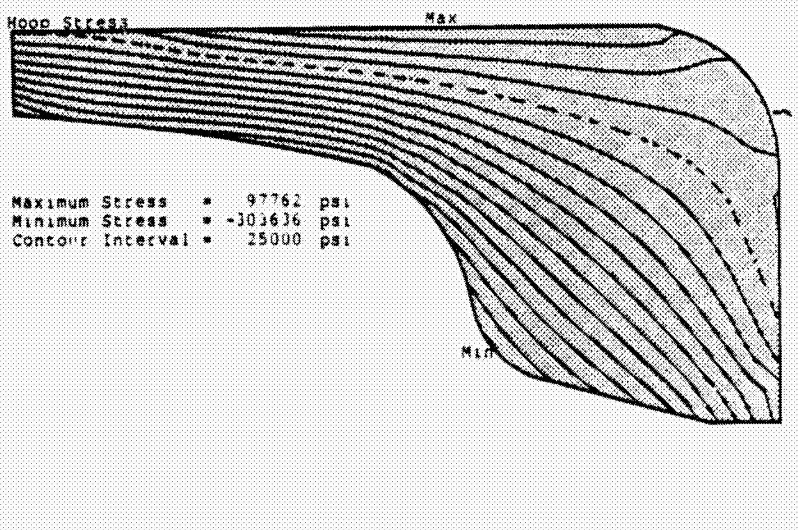

Figure 27C Combustion Bowl Stresses - Maximum Power - All Silicon Nitride Insulated

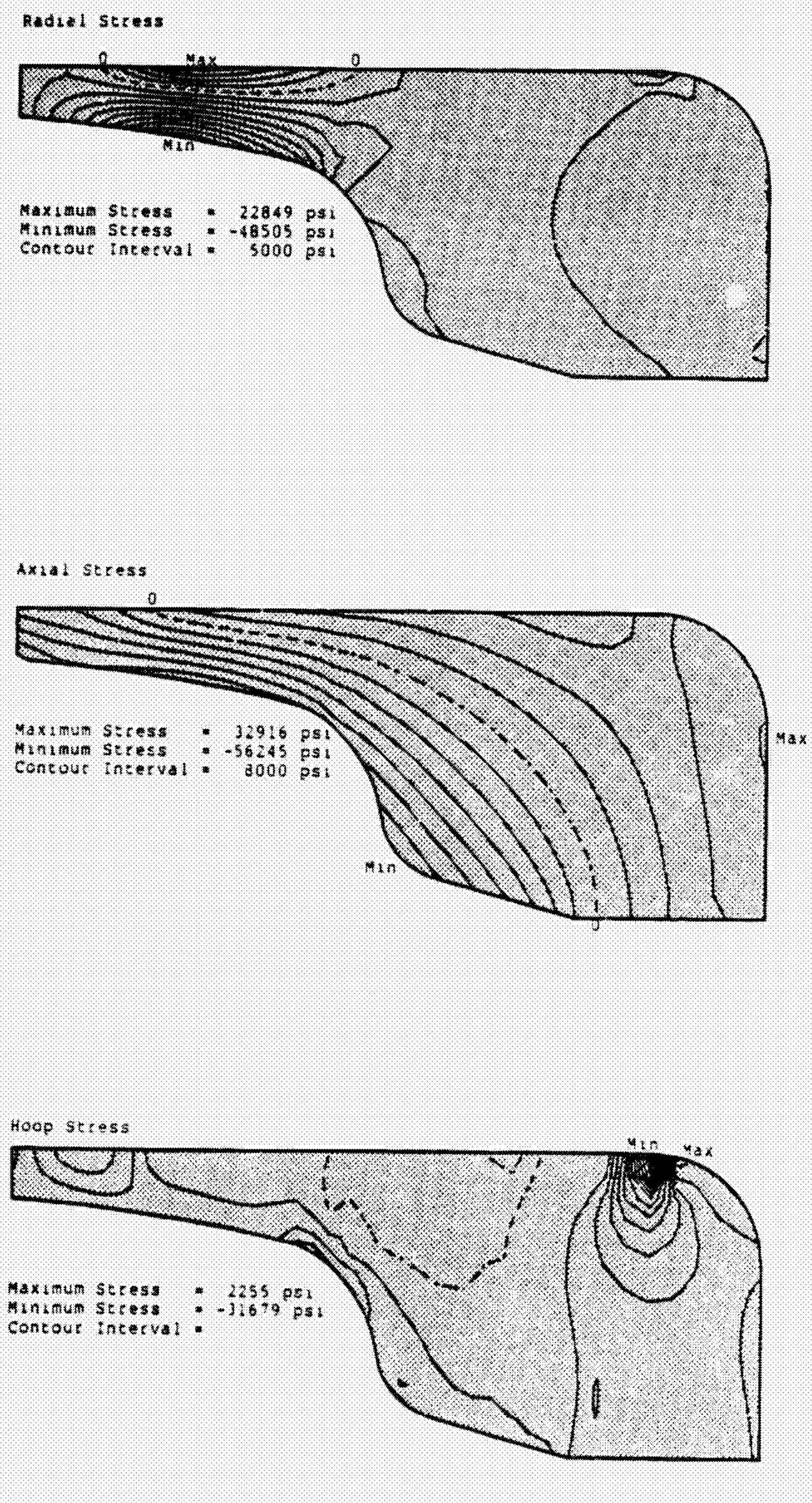

Figure 28 Head Intermediate Insulating Disk Stresses - Maximum Power - All Silicon Nitride Insulated

Radial Stress

Maximum Stress = 9504 psi
Minimum Stress = -22084 psi
Contour Interval = 2000 psi

Axial Stress

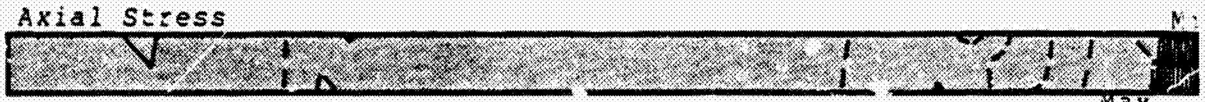

Maximum Stress = 4531 psi
Minimum Stress = -90827 psi
Contour Interval = 8000 psi

Hoop Stress

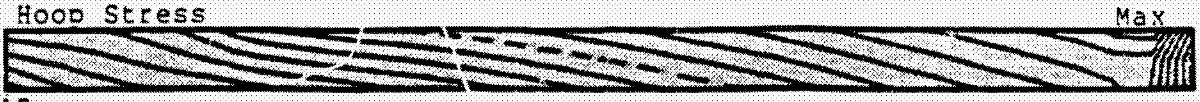

Maximum Stress = 30038 psi
Minimum Stress = -34211 psi
Contour Interval = 4000 psi

Figure _A Metal Portion of Head Assembly Stresses - Maximum Power - All Zirconia Insulated

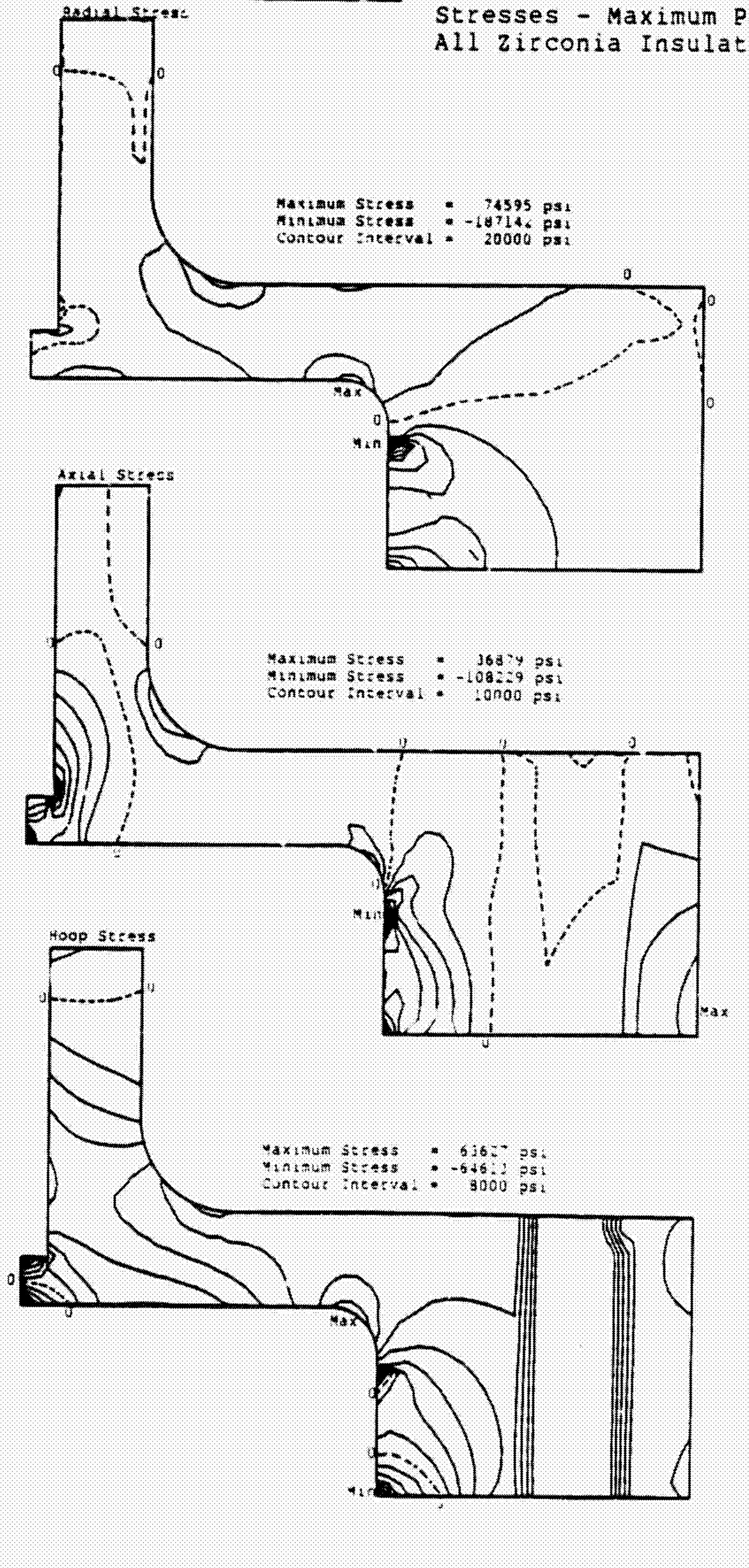

Figure 29B All Metal Portion of Head Assembly Stresses - Maximum Power - All Alumina Inulated

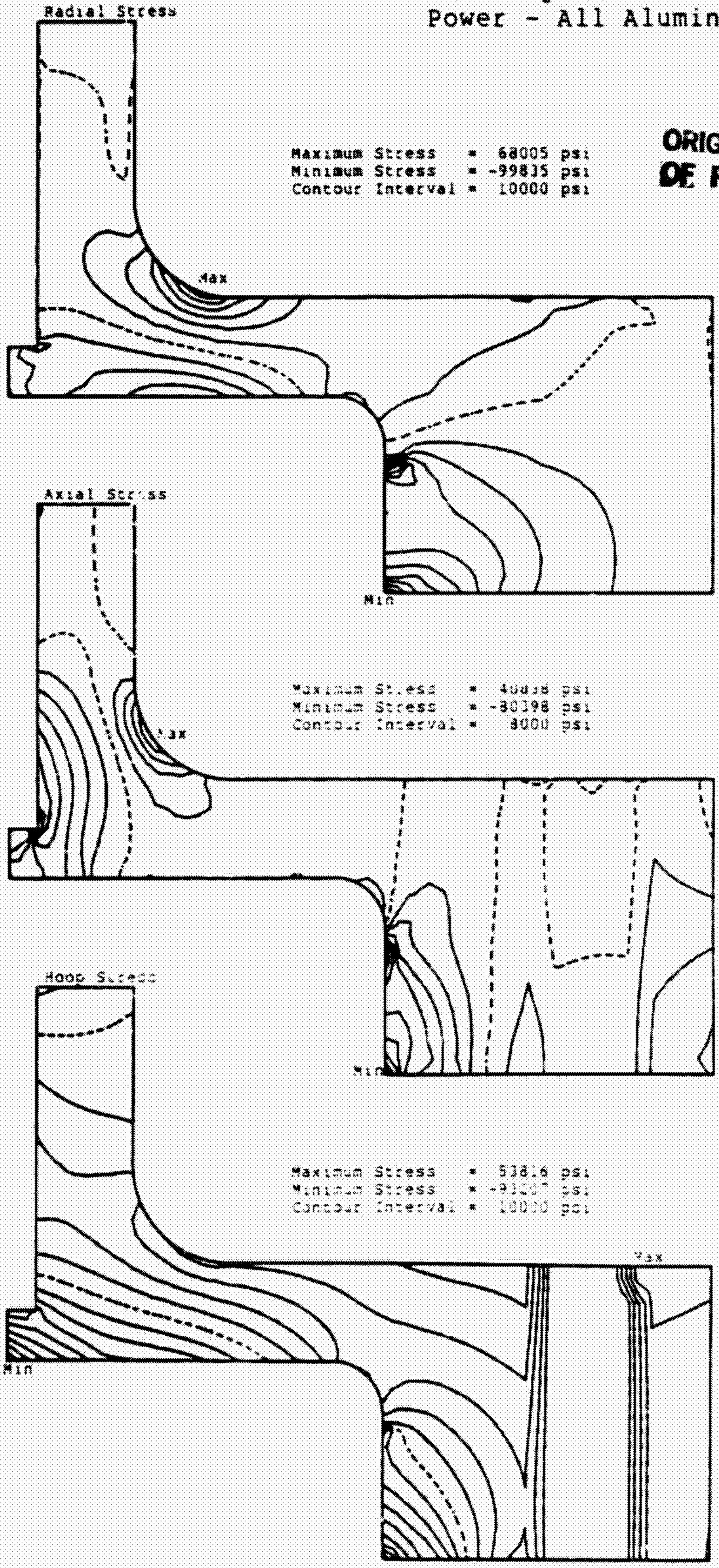

<u>Figure 29C</u> Metal Portion of Head Assembly Stresses - Maximum Power - All Silicon Nitride Insulation

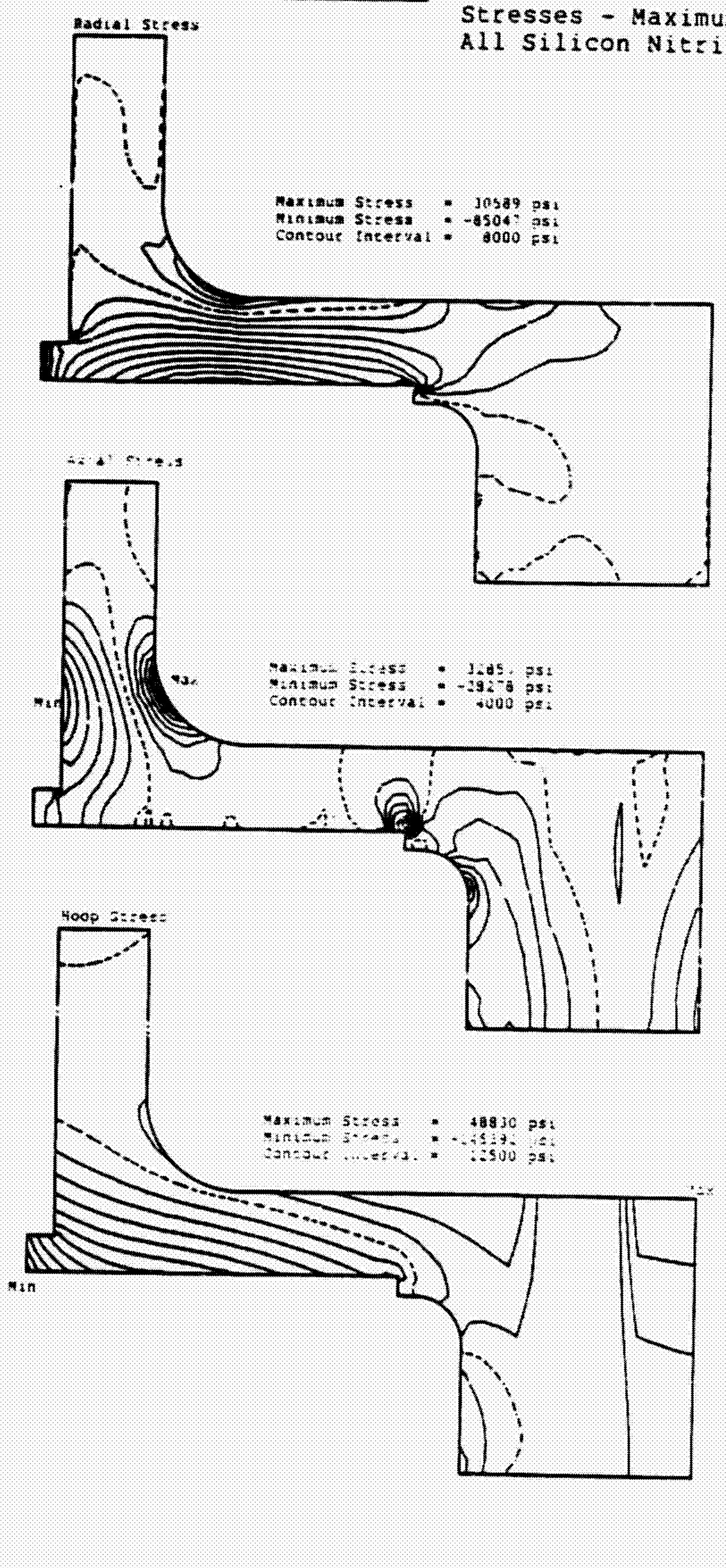

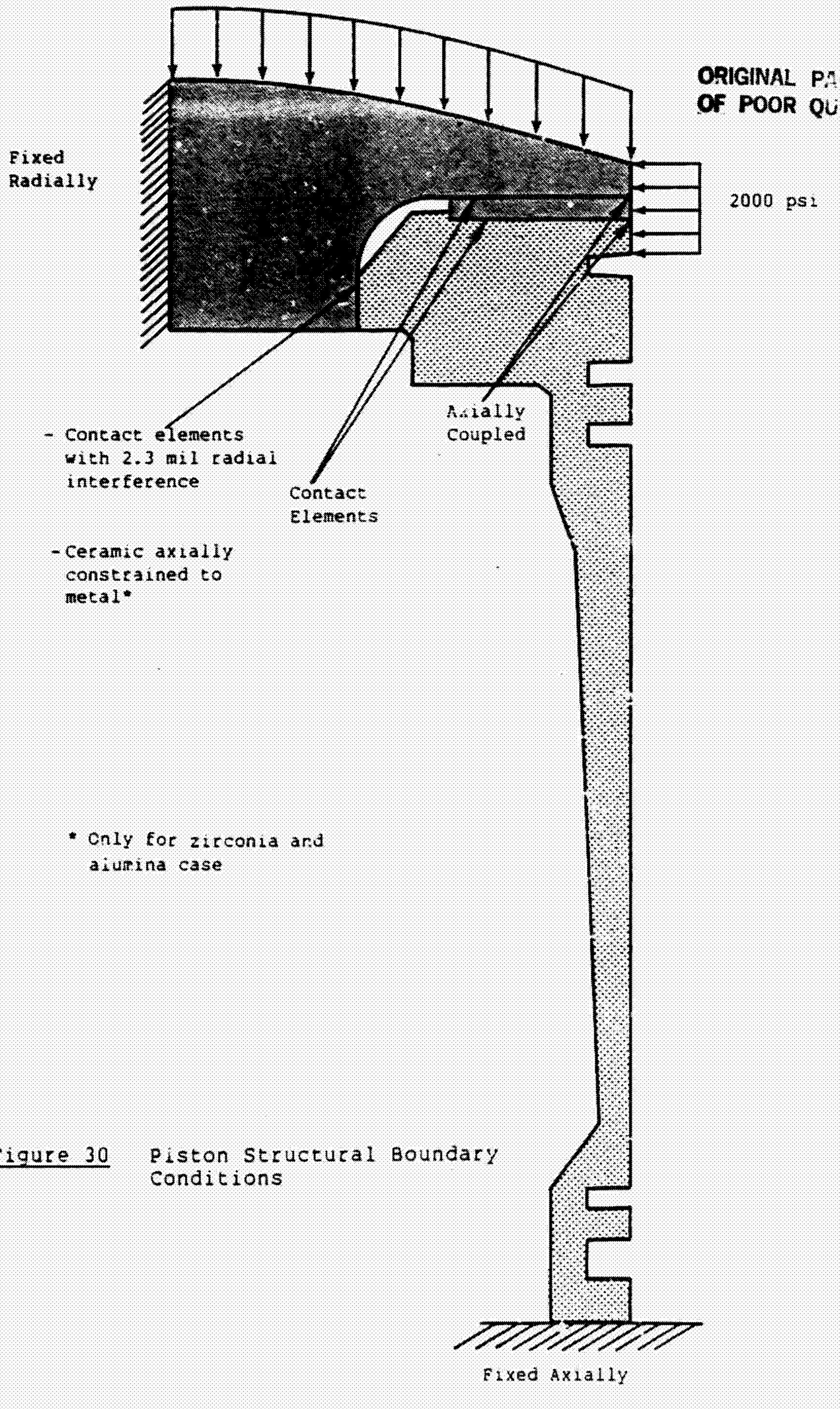

Figure 30 Piston Structural Boundary Conditions

<u>Figure 31A</u> Piston Cap Stresses - Maximum Power - All Zirconia Insulated

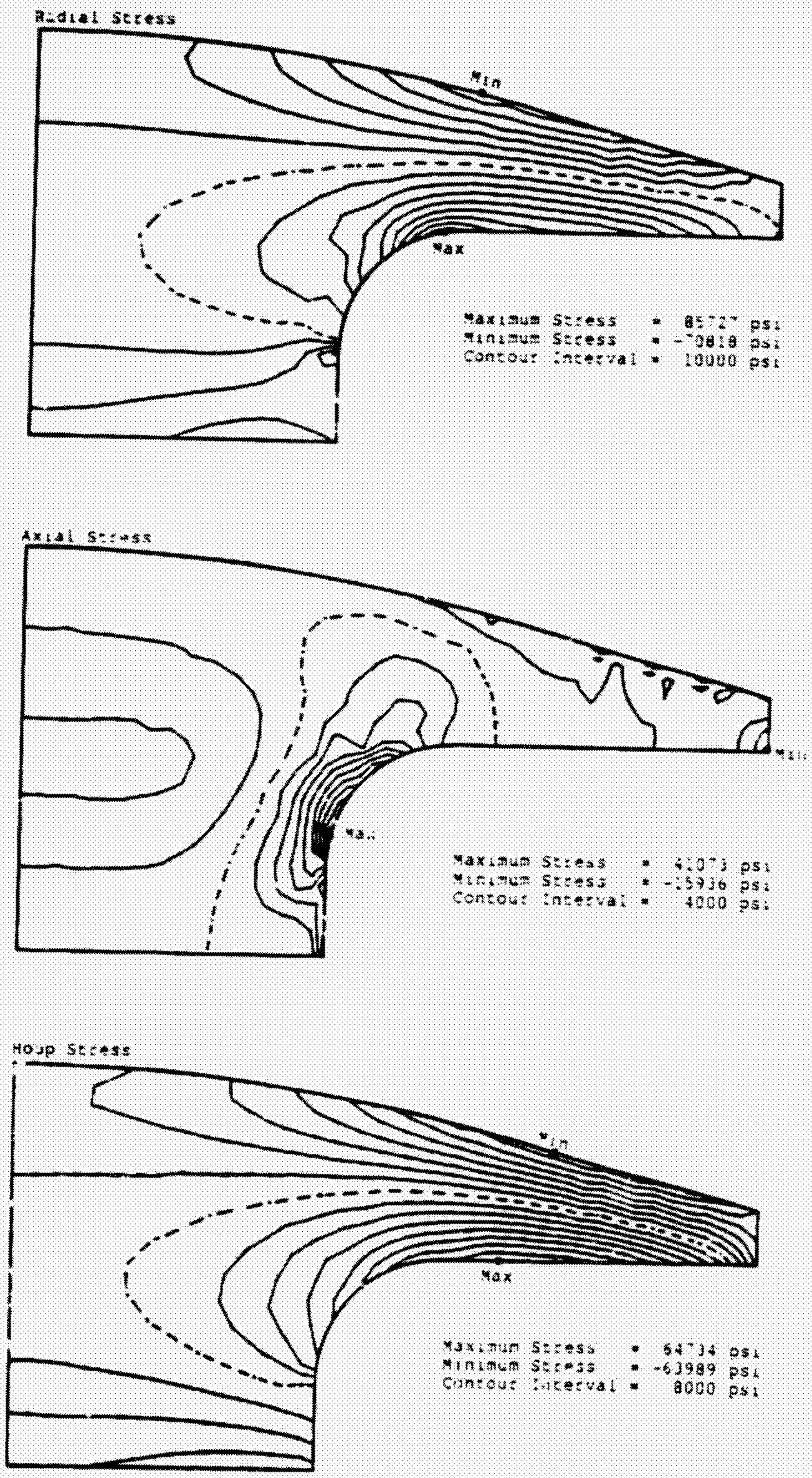

<u>Figure 31B</u> Piston Cap Stresses - Maximum Power - All Alumina Insulated

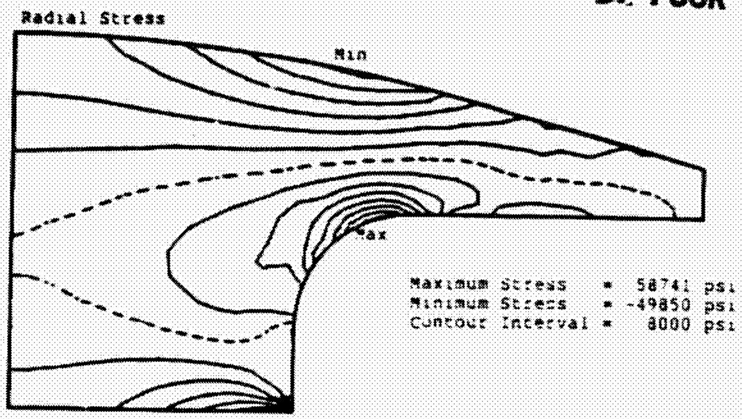

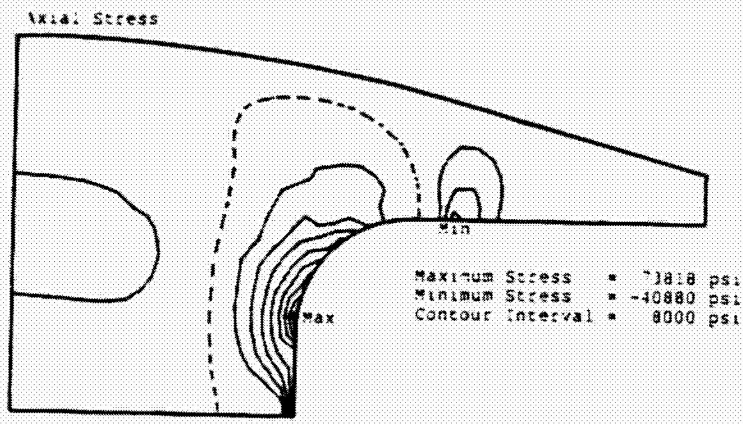

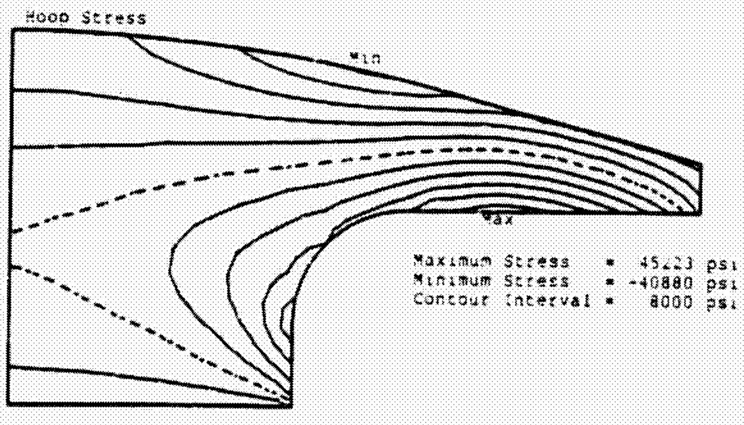

Figure 31C Piston Cap Stresses - Maximum Power - All Silicon Nitride Insulated

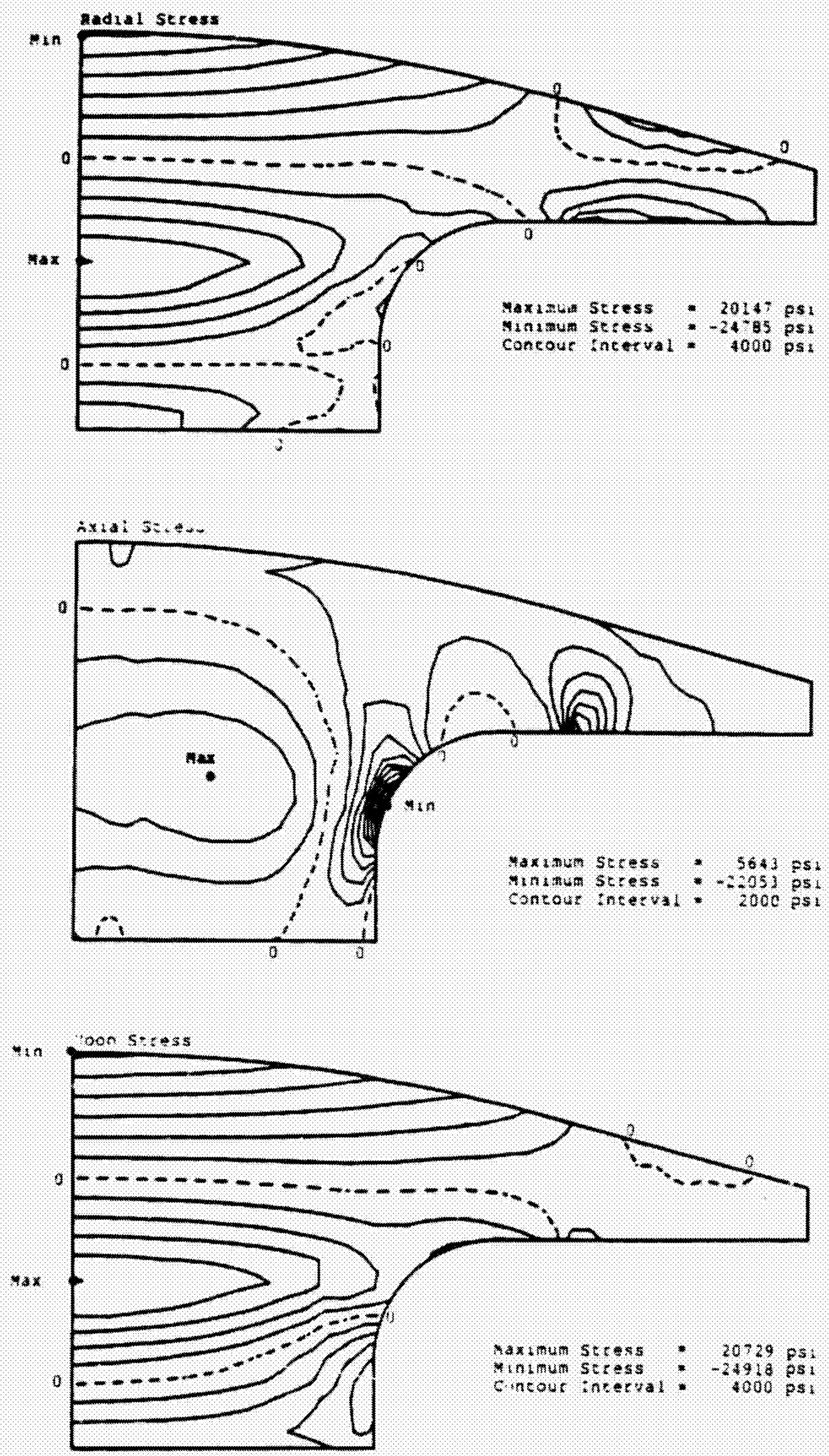

Figure 32A Piston Intermediate Insulation Disk Stresses - Maximum Power - All Zirconia Insulated

Radial Stress

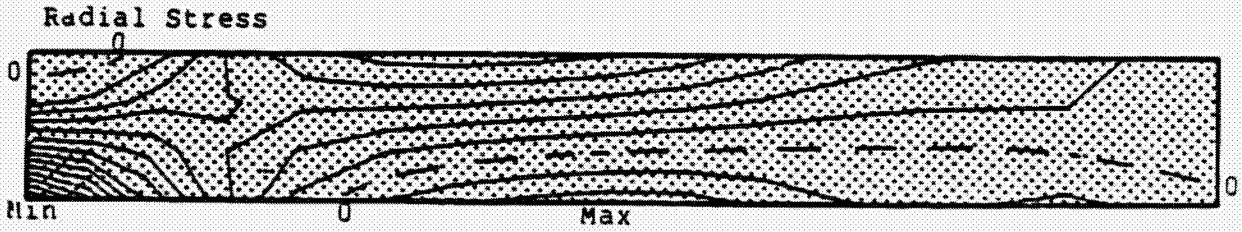

Maximum Stress = 12674 psi
Minimum Stress = -70220 psi
Contour Interval = 5000 psi

Axial Stress

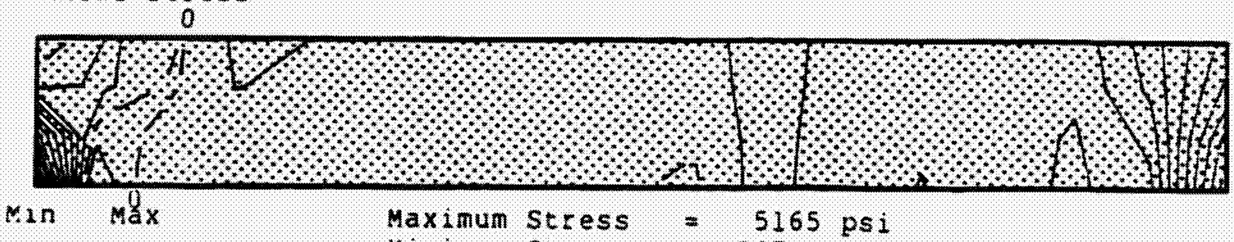

Maximum Stress = 5165 psi
Minimum Stress = -30744 psi
Contour Interval =

Hoop Stress

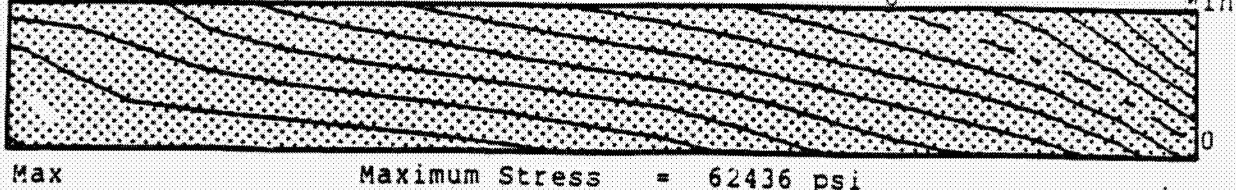

Maximum Stress = 62436 psi
Minimum Stress = -45378 psi
Contour Interval = 8000 psi

Figure 32B Piston Intermediate Insulation Disk Stresses
Maximum Power - All Alumina Insulation

Radial Stress

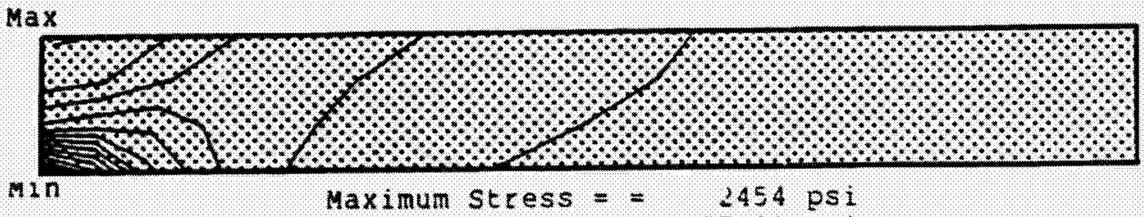

Maximum Stress = = 2454 psi
Minimum Stress = -277101 psi
Contour Interval = 20000 psi

Axial Stress

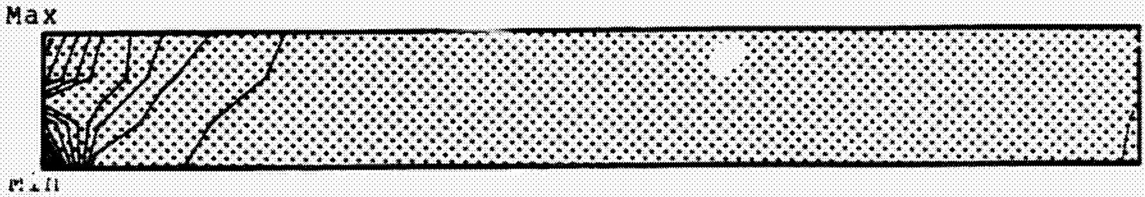

Maximum Stress = 7056 psi
Minimum Stress = -113915 psi
Contour Interval = 8000 psi

Hoop Stress

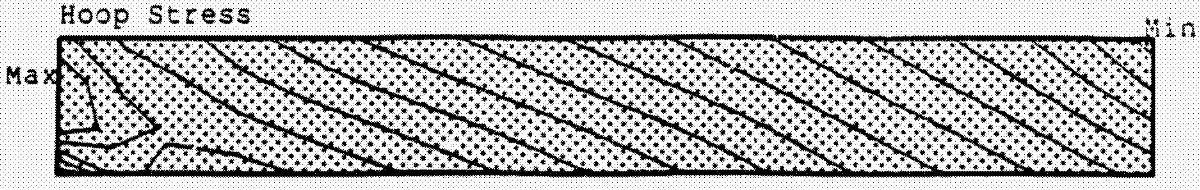

Maximum Stress = 159918 psi
Minimum Stress = 36466 psi
Contour Interval = 8000 psi

Figure 32C Piston Intermediate Insulation Disk Stresses - Maximum Power - All Silicon Nitride Insulation

Radial Stress

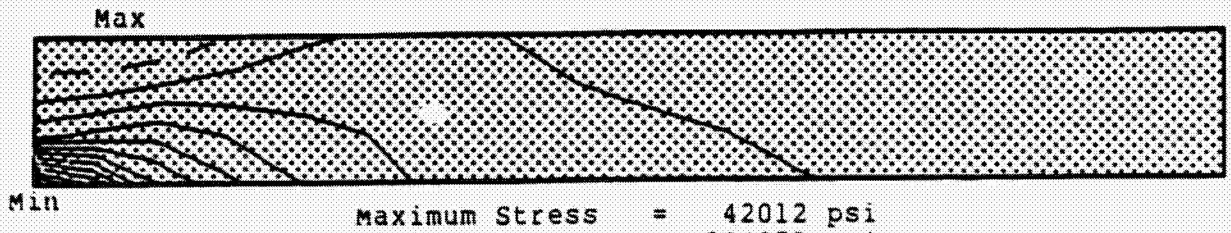

Maximum Stress = 42012 psi
Minimum Stress = -504075 psi
Contour Interval = 40000 psi

Axial Stress

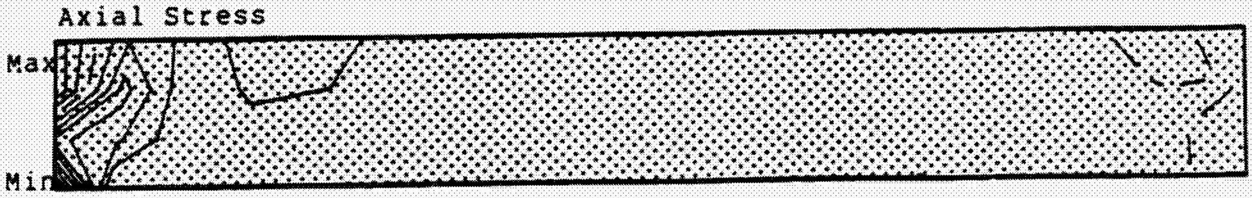

Maximum Stress = 23790 psi
Minimum Stress = -78152 psi
Contour Interval = 8000 psi

Hoop Stress

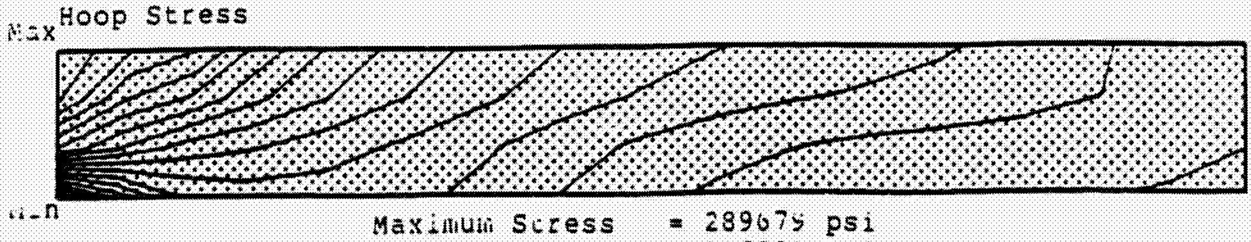

Maximum Stress = 289679 psi
Minimum Stress = 116282 psi
Contour Interval = 10000 psi

Figure 33A Piston Stresses - Maximum Power - All Zirconia Insulated

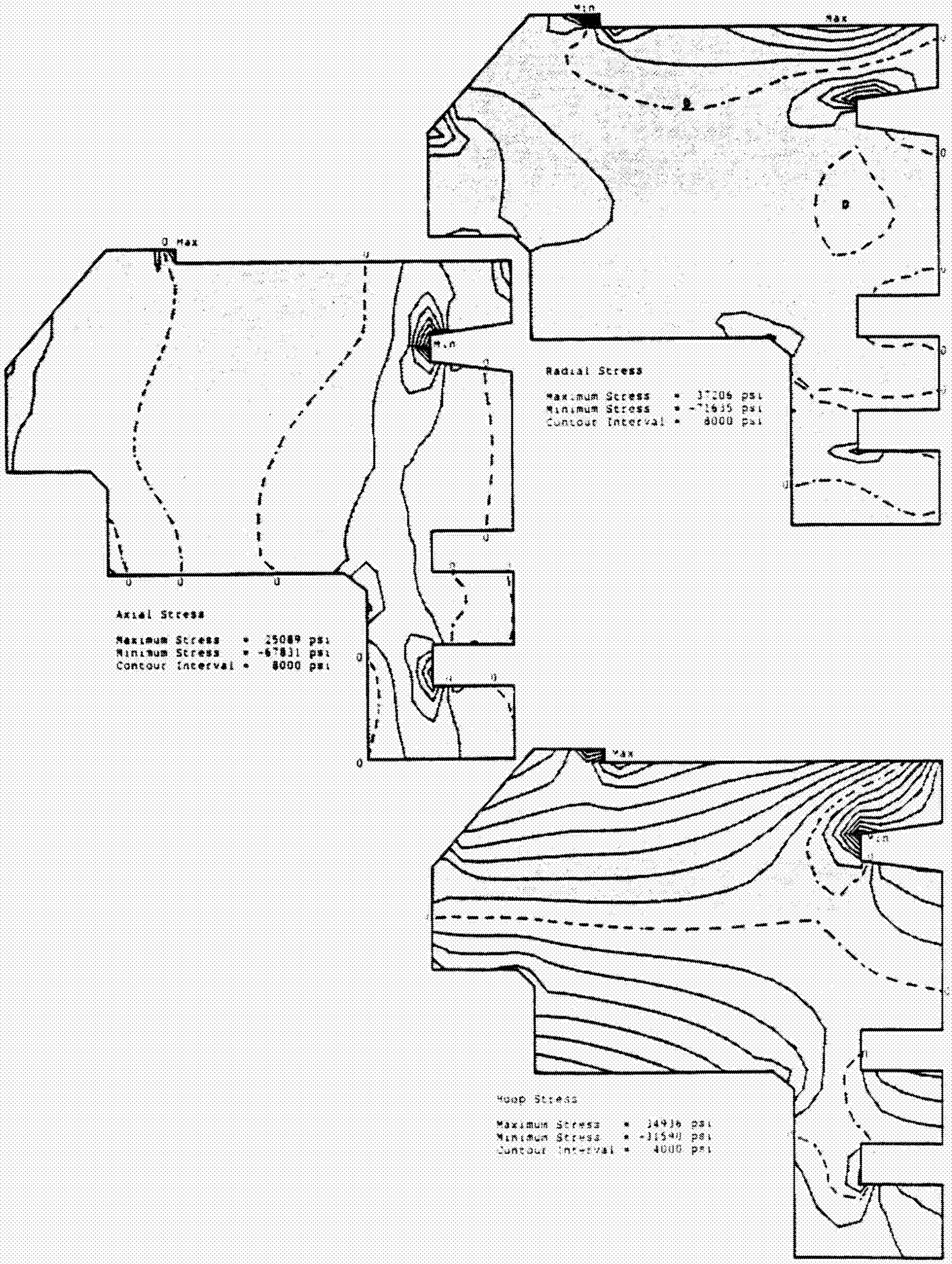

Figure 33B Piston Stresses - Maximum Power - All Alumina Insulated

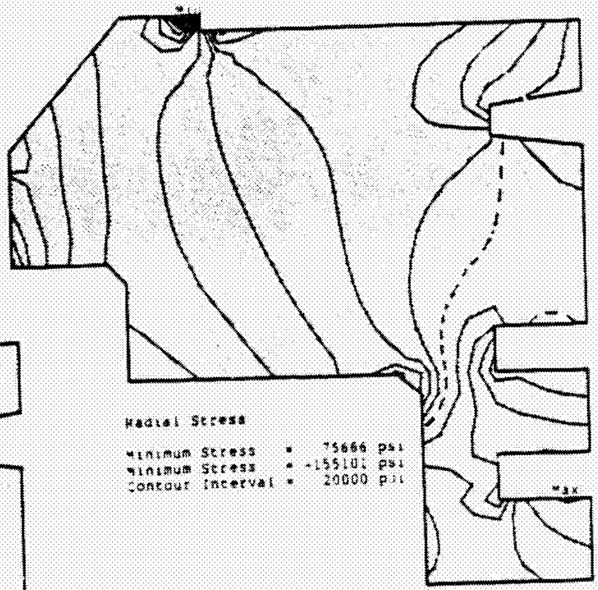

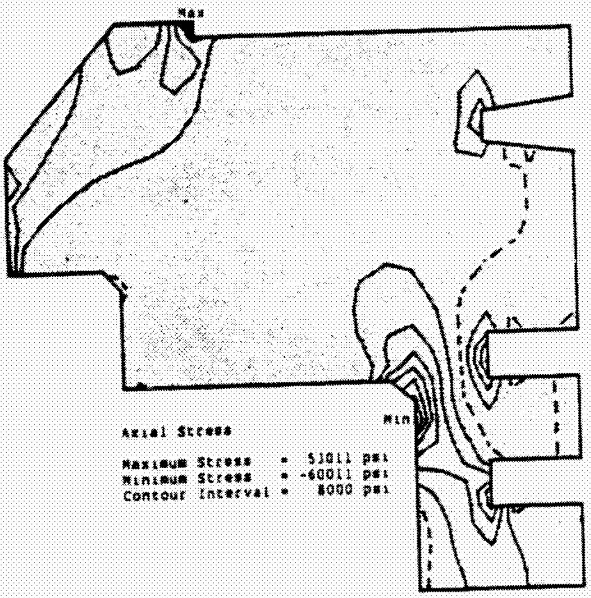

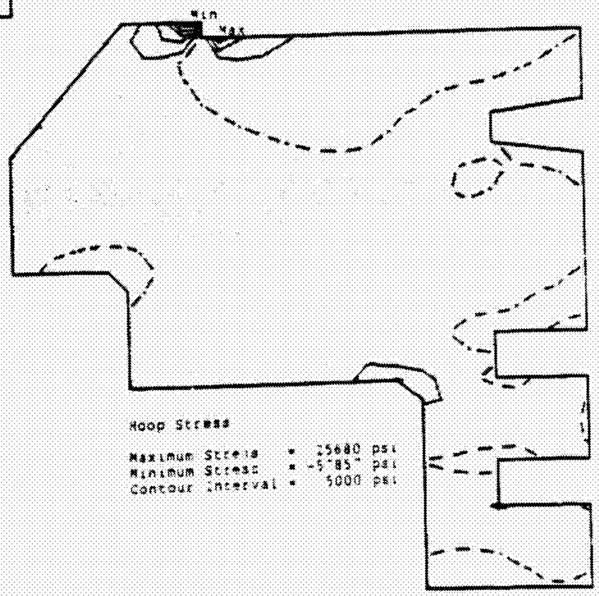

Figure 33C Piston Stresses - Maximum Power - All Silicon Nitride Insulation

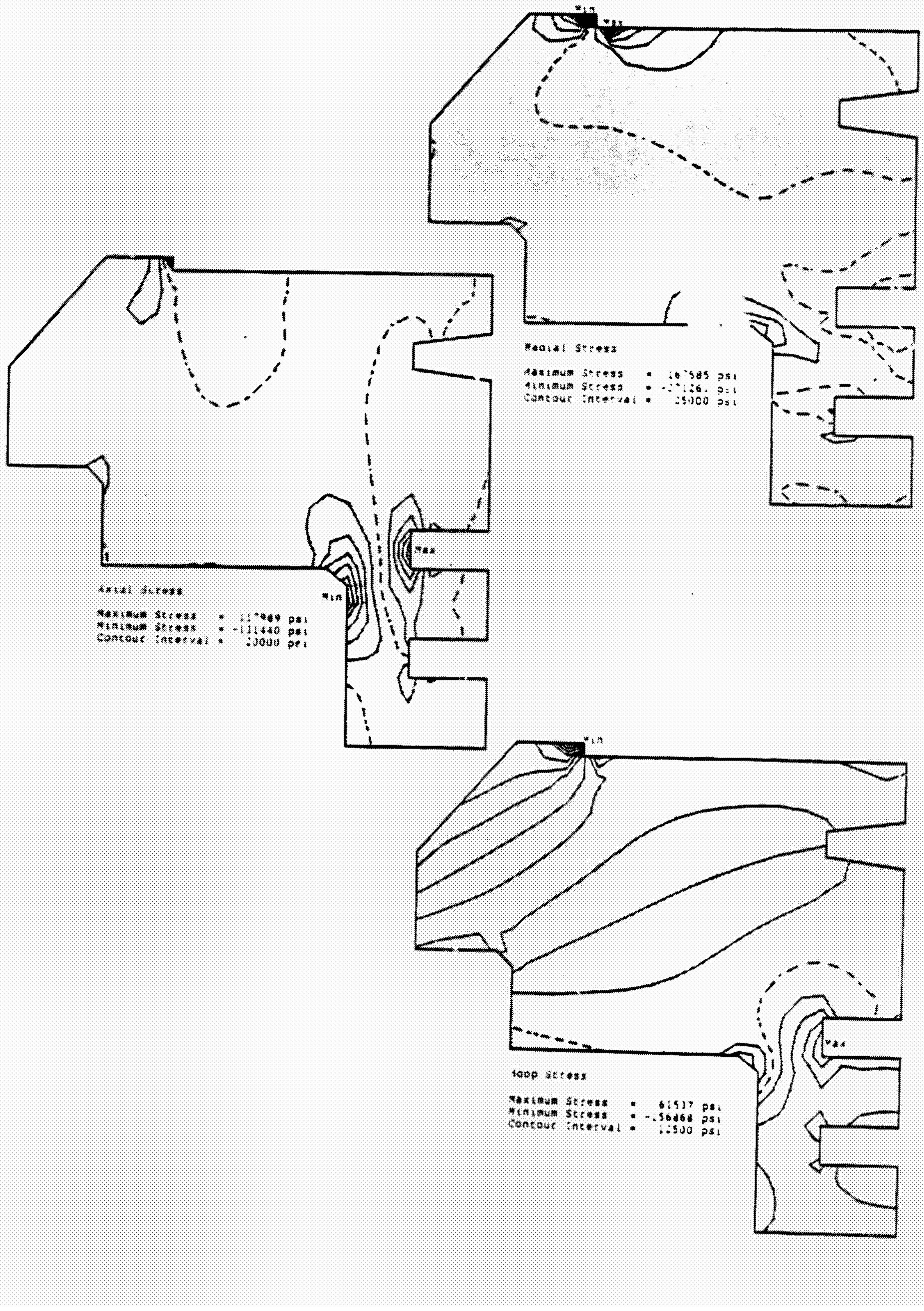

Figure 34 Ceramic Cylinder Liner - Maximum Principal Stress Due to Maximum Power Thermal and 0.010 Inch Diametral Interference - All Zirconia Insulation

ORIGINAL PAGE IS OF POOR QUALITY

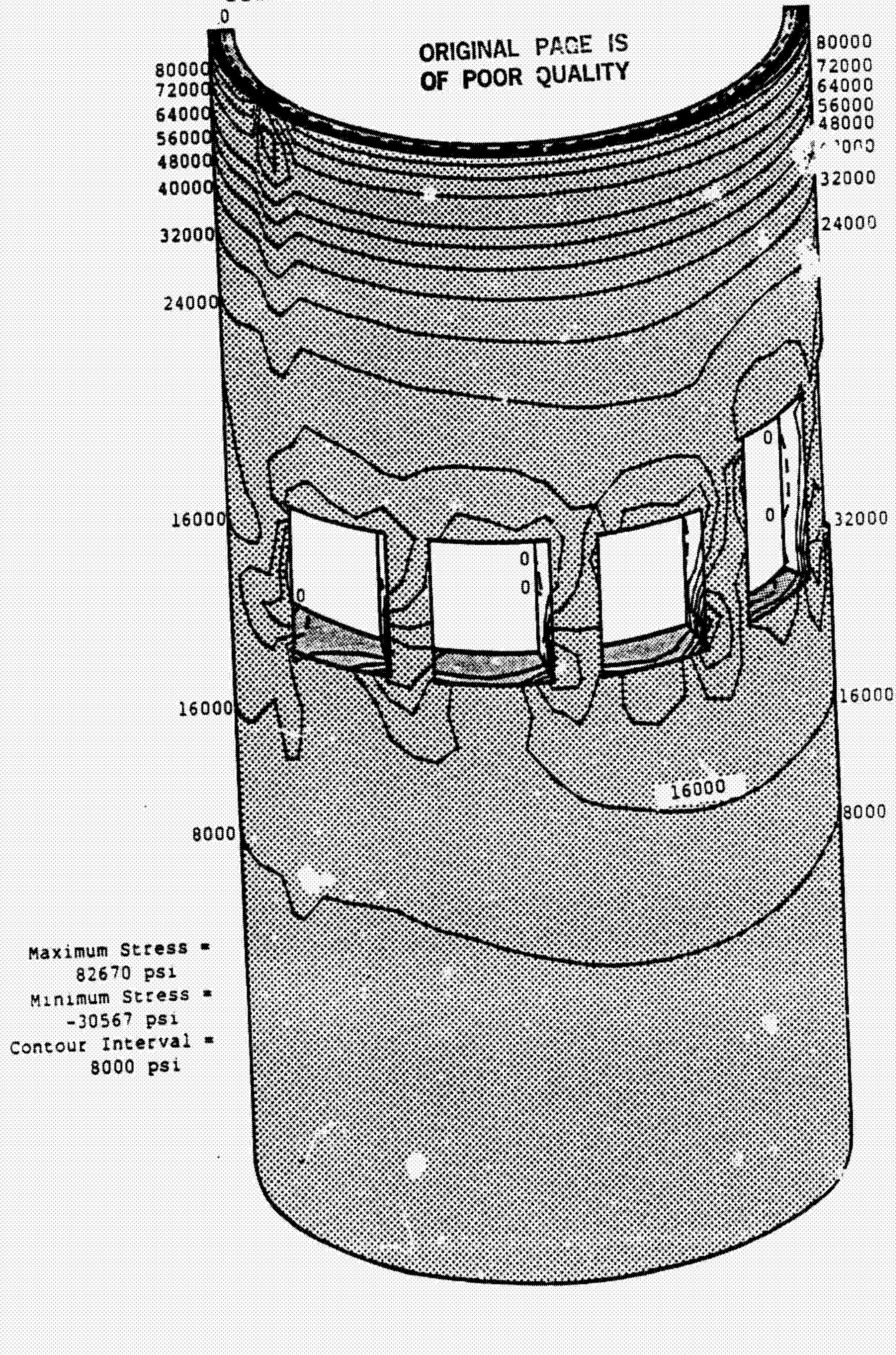

Figure 35 Ceramic Cylinder Liner - Minimum Principal Stress Due to Maximum Power Thermal and 0.010 Inch Diametral Interference All Zirconia Insulation

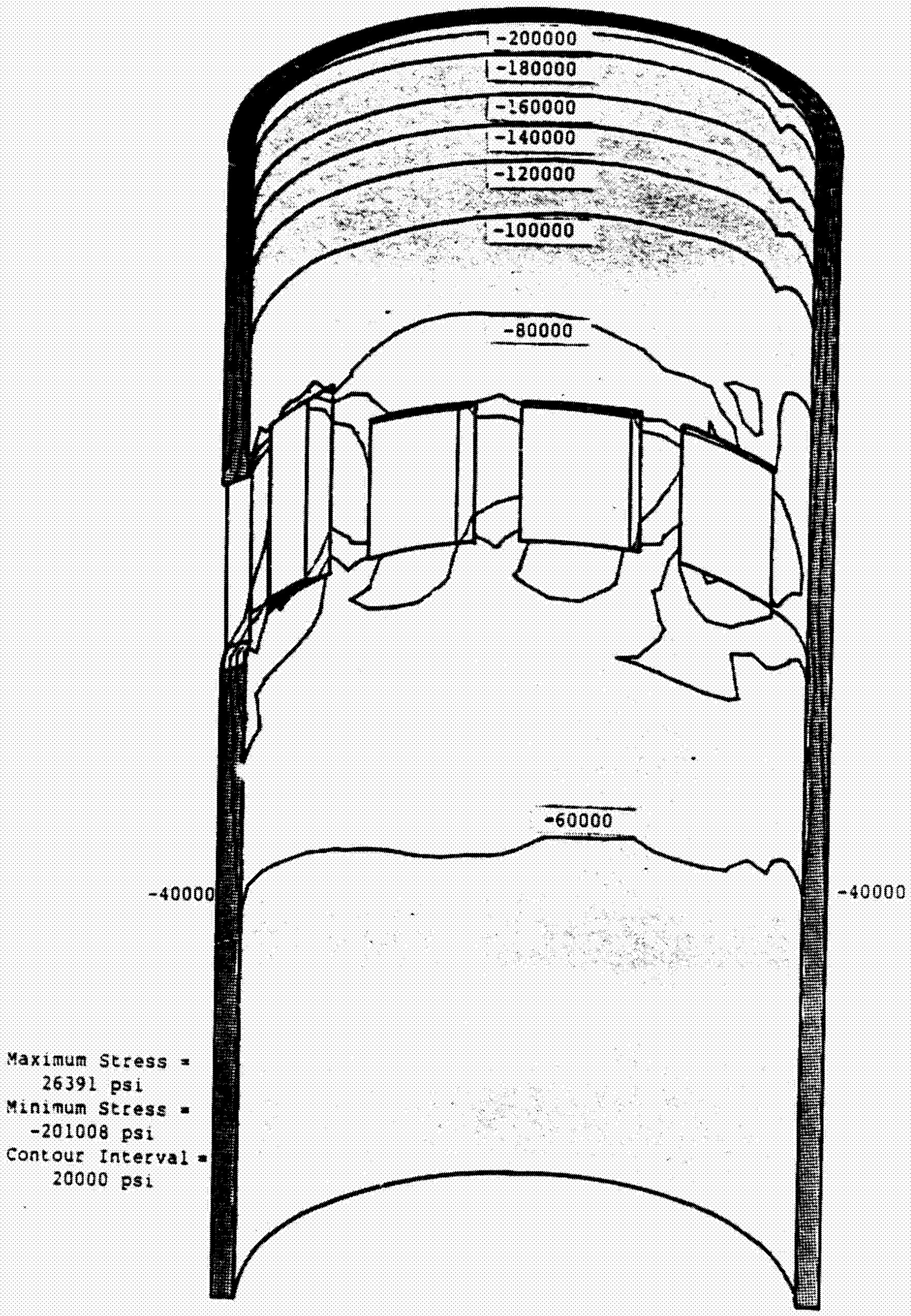

Figure 36 Ceramic Cylinder Liner - Maximum Principal Stress Due to Maximum Power Thermal and 0.010 Inch Diametral Interference - All Alumina Insulation

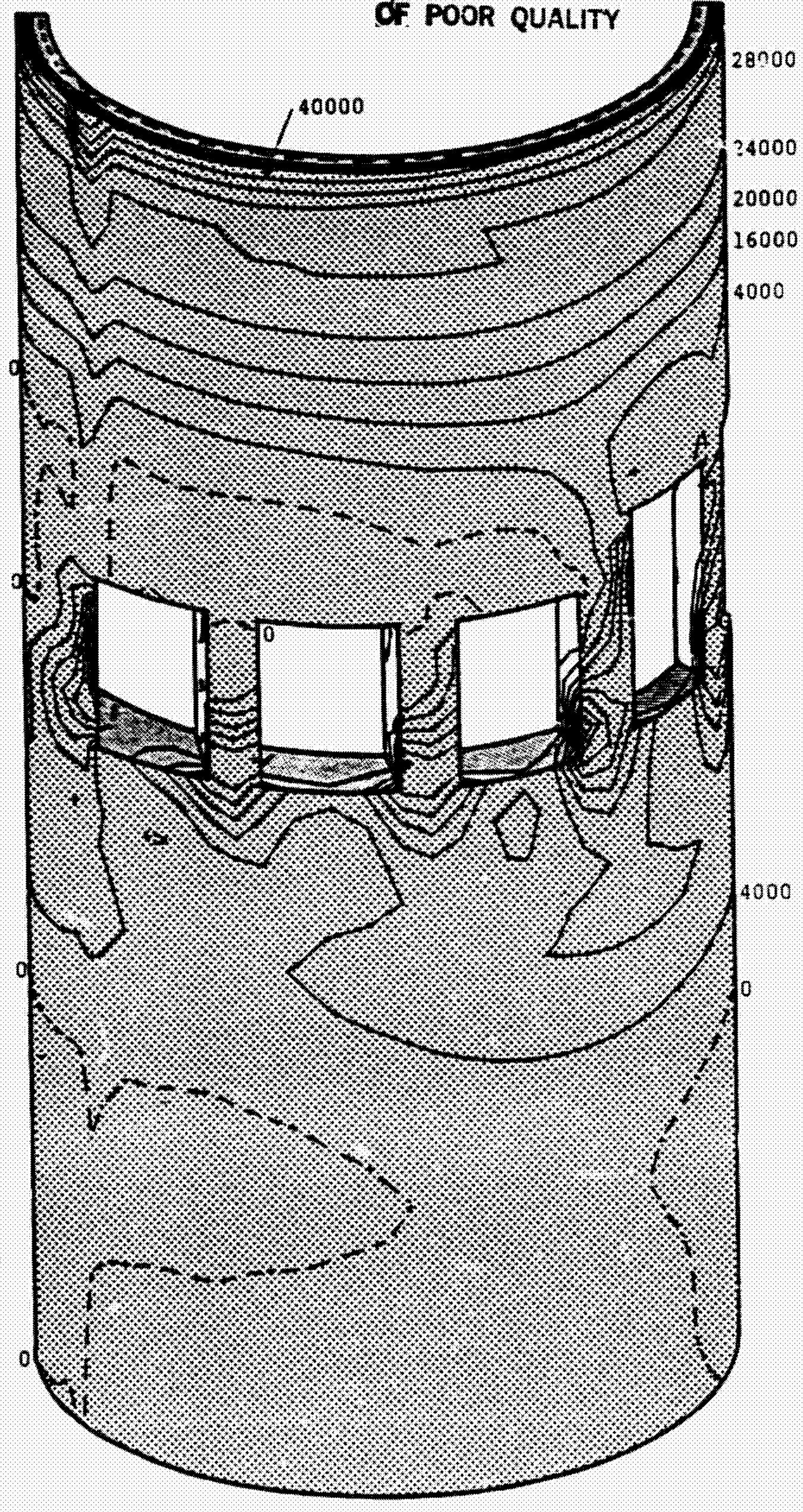

Maximum Stress = 45619 psi
Minimum Stress = -7338 psi
Contour Interval = 4000 psi

Figure 37 Ceramic Cylinder Liner - Minimum Principal Stress Due to Maximum Power Thermal and 0.010 Inch Diametral Interference - All Alumina Insulation

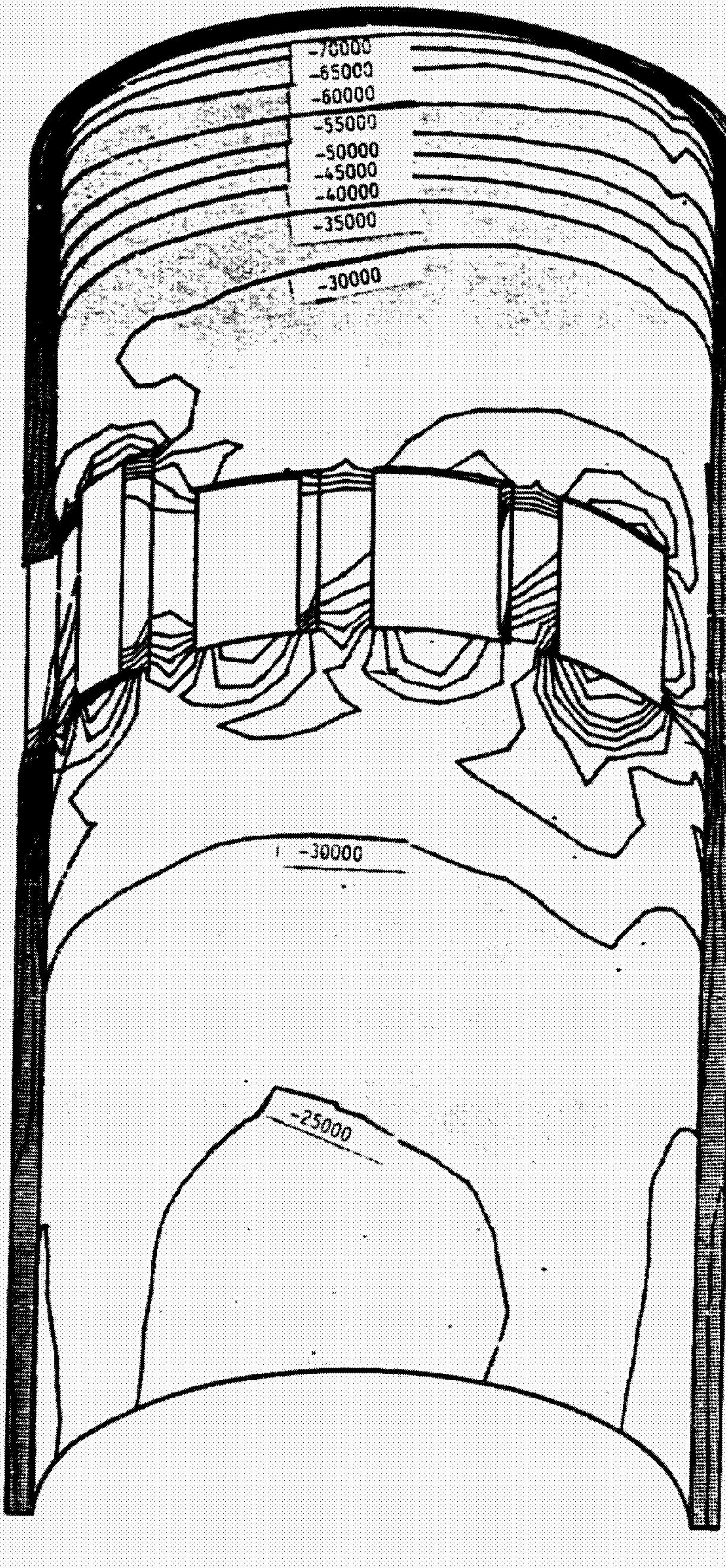

Maximum Stress = 6388 psi
Minimum Stress = -74242 psi
Contour Interval = 5000 psi

Figure 38 Ceramic Cylinder Insert - Maximum Principal Stress Due to Maximum Power Thermal - All Silicon Nitride Insulation

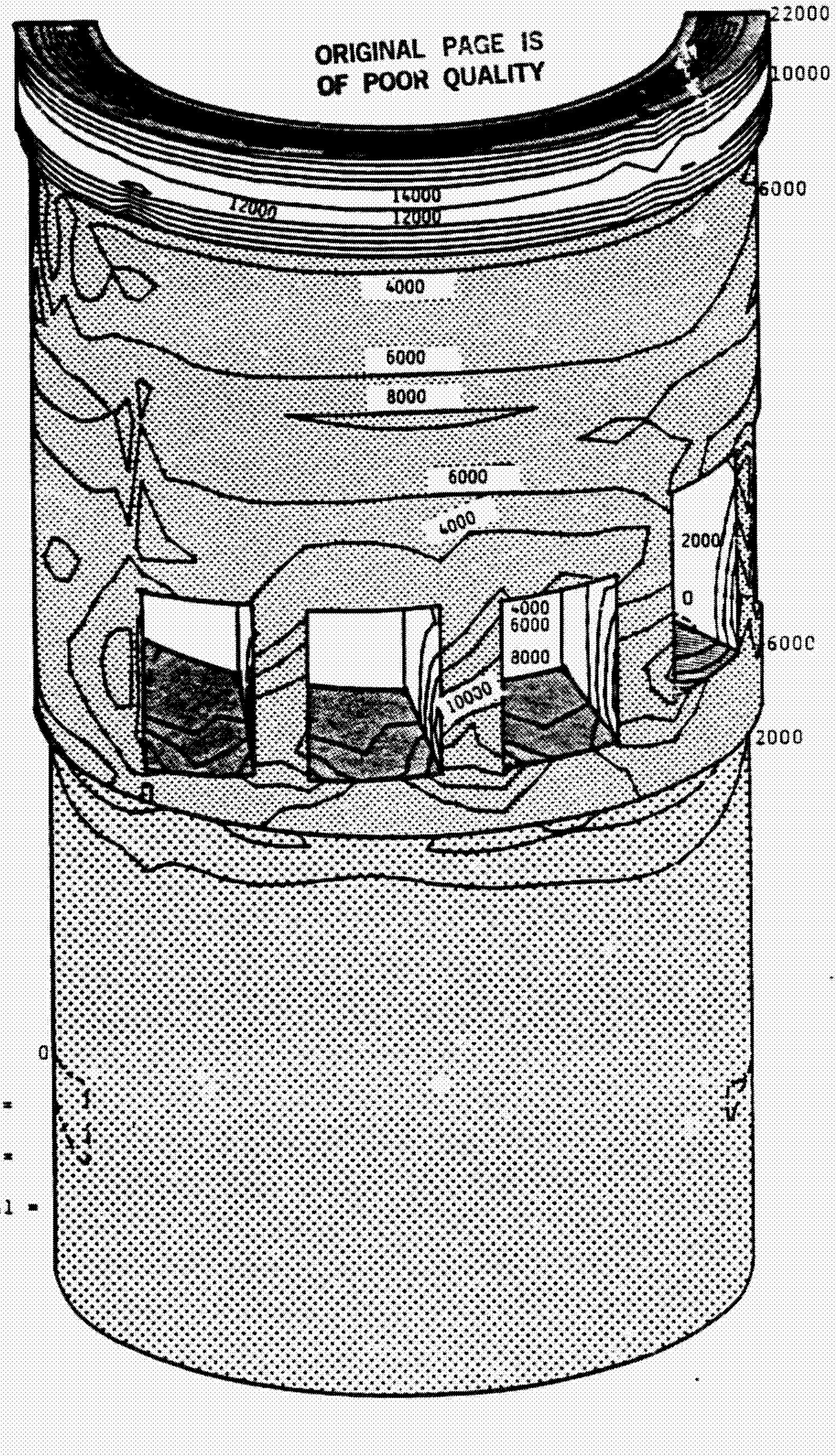

Maximum Stress = 23507 psi
Minimum Stress = -2849 psi
Contour Interval = 2000 psi

Figure 39 Ceramic Cylinder Insert - Minimum Principal Stress Due to Maximum Power Thermal - All Silicon Nitride Insulation

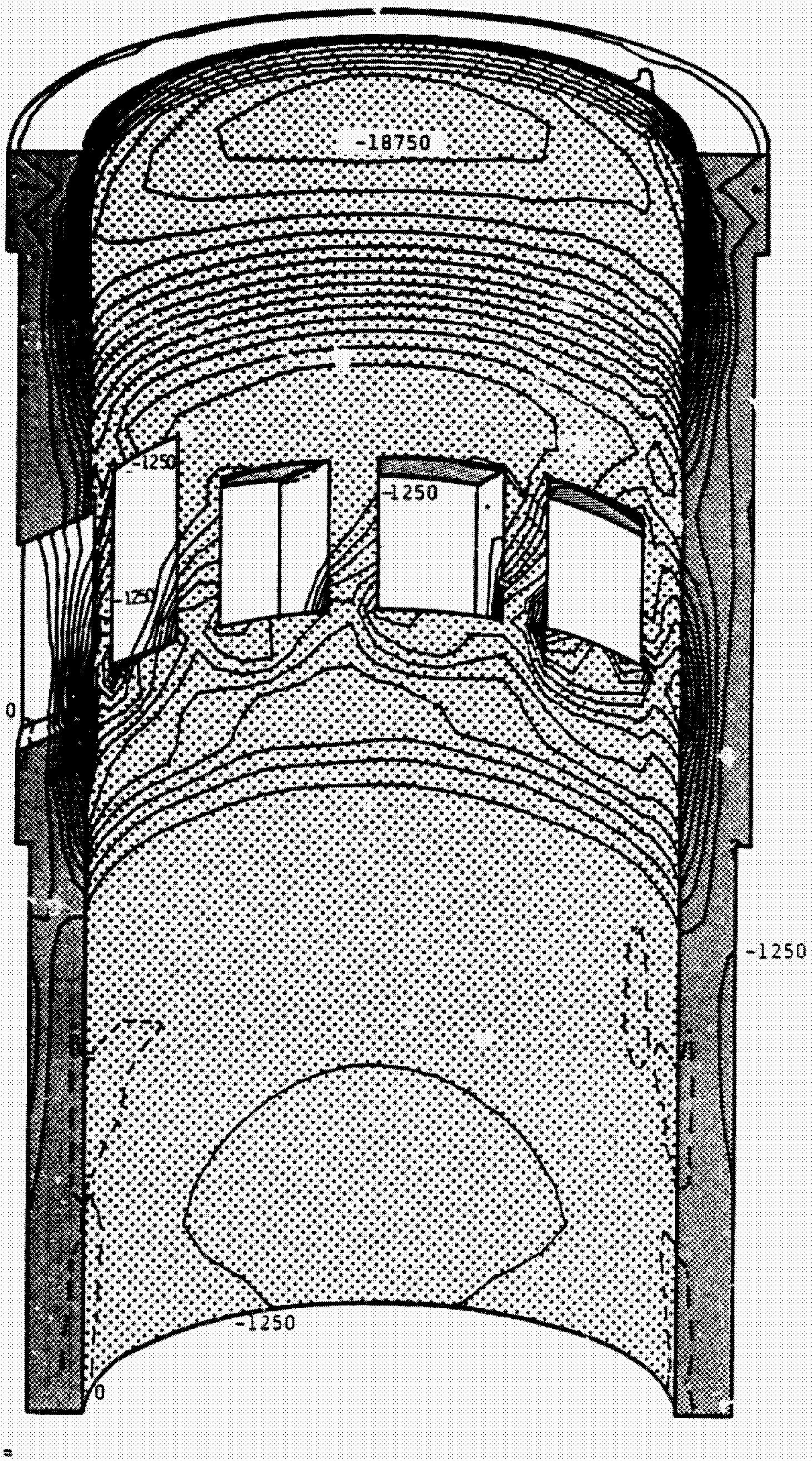

Maximum Stress = 1566 psi
Minimum Stress = -18791 psi
Contour Interval = 1250 psi

Table 1 Material Properties

				HEAD & BLOCK	PISTON
	ZIRCONIA	ALUMINA	SILICON NITRIDE	410 STAINLESS	CAST IRON
MODULUS ELASTICITY (PSI)	27E6	56E6		24E6	24E6
POISSON'S RATIO	0.3	0.22	0.3	0.3	0.3
COEFFICIENT OF THERMAL EXPANSION	4.28E-6 (70°F) 4.58E-6 (200°F) 4.92E-6 (400°F) 5.14E-6 (600°F) 5.28E-6 (800°F) 5.42E-6 (1000°F) 5.53E-6 (1200°F) 5.66E-6 (1400°F) 5.85E-6 (1600°F) 6.02E-6 (1800°F) 6.2 E-6 (2000°F)	1.9E-6 (77°F) 3.6E-6 (392°F) 4.1E-6 (932°F) 4.4E-6 (1472°F) 4.5E-6 (1832°F) 4.6E-6 (2192°F)	2.0E-6	5.6E-6 (212°F) 5.9E-6 (392°F) 6.1E-6 (572°F) 6.4E-6 (752°F) 6.5E-6 (932°F) 6.5E-6 (1112°F) 6.6E-6 (1292°F) 6.8E-6 (1472°F) 7.1E-6 (1652°F) 7.6E-6 (1832°F)	5.75E-6 (70°F) 5.93E-6 (200°F) 6.3 E-6 (400°F) 6.56E-6 (600°F) 6.8 E-6 (800°F) 7.06E-6 (1000°F) 7.3 E-6 (1200°F) 7.74E-6 (1400°F) 8.05E-6 (1600°F) 8.35E-6 (1800°F) 8.70E-6 (2000°F)
THERMAL CONDUCTIVITY $\frac{BTU}{HR\text{-}FT^2}$	1.0	3.64 (1472°F) 5.6 (1150°F)	13.75	15.7	27

A P P E N D I X   V

PROJECT SUMMARY REPORT
OF
ELECTRONICALLY CONTROLLED
FUEL INJECTION SYSTEM
FOR
GENERAL AVIATION
DIESEL ENGINE

PROJECT SUMMARY REPORT
ON
ELECTRONICALLY CONTROLLED
FUEL INJECTION SYSTEM
FOR
GENERAL AVIAION
DIESEL ENGINE

SEPTEMBER 13, 1984

PREPARED FOR

TELEDYNE CONTINENTAL MOTORS
GENERAL PRODUCTS DIVISION
MUSKEGON, MICHIGAN

PREPARED BY

ALLIED-BENDIX
ENGINE PRODUCTS DIVISION
JACKSONVILLE, FLORIDA

(REF: BENDIX JER0106M)

Engineering Laboratory Report

REPORT #JER0106

PROJECT SUMMARY REPORT ON ELECTRONICALLY CONTROLLED FUEL INJECTION SYSTEM FOR GENERAL AVIATION DIESEL ENGINE

DATE September 13, 1984

PREPARED BY
K. Stuckas, Project Engineer

APPROVED BY
W. Morton, Supervisory Engineer

APPROVED BY H. Dingman
H. Dingman, Engineering Manager

APPROVED BY
D. Baker, Director of Engineering

Bendix Engine Products Division

Jacksonville, Fl

ORIGINAL PAGE IS
OF POOR QUALITY

SUBJECT

This is a final project report summarizing the work which was done under Contract 70410 to build and test electronically controlled fuel injection systems for use by Teledyne Continental Motors, General Products Division (TCM-GPD). The project was initiated to support work being done by TCM-GPD in their NASA Lewis Research Center Contract NAS3-22218, "Two-Stroke Diesel, Single-Cylinder Technology Enablement".

I. BACKGROUND

The original technical proposal, EP007, May 1, 1981, (Ref. 1) proposed a high pressure, intensifier type, electronically controlled fuel injection system for use on the TCM-GPD single-cylinder technology demonstration diesel aircraft engine. The injector design was to be a modification of the Garrett AiResearch CCTE unit, scaled up to inject the required 90 mm^3 per stroke. Table 1 shows a comparison between the engine specifications of the CCTE and TCM-GPD diesel engines. The need for such an injector in the TCM program was clearly established: conventional mechanical diesel fuel injection systems did not have the flexibility to optimize engine performance by varying injection timing and duration during operation.

The original project plan outlined in report 4045, REV. 1, February 5, 1982, (Ref. 2) called for the new unit to be manufactured in the Experimental Machining Department in Sidney with a 44-week delivery after receipt of order (Fig. 1). Communications with TCM showed their displeasure with the projected delivery time. They were requesting a 26-week delivery period. Concern was also expressed over the suitability of the Garrett CCTE design injectors in view of the problems which were encountered during development.

As a result of the latter concern, report 4071, May 12, 1982 (Ref. 3) was written to address each problem and the subsequent solutions. A literature survey of the Garrett contract reports was made along with personal contacts with the Garrett project people and M. Gage of Bendix. The survey showed that the reasons for all of the problems were understood and satisfactory solutions were found.

In regard to the objectionable 44-week delivery period, the entire plan to design a higher capacity version of the CCTE unit was rethought. The risk of getting involved in a development program after the unit was designed and built seemed great. Even if the unit were merely scaled up there would be some risk, but because of the configuration of the air-cooled cylinder head more design changes would have to be made to the compact injector to adapt it.

An alternative proposal was prepared (EP021, May 24, 1984 (Ref. 4)) that seemed to solve these problems. The capacity of the existing "John Deere" injector design was shown to be suitable for the TCM diesel program with some minor design modifications to allow the unit to adapt to the TCM cylinder head and to provide a passage for needle lift measurement. The advantages of this unit over the CCTE design, which is functionally equivalent, were that outsource vendors were already in place to manufacture all the component parts, no great amount of design time would be needed, the "John Deere" unit had undergone hundreds of hours of testing on test benches and multi-cylinder engines at D.E.C. under Ted Watson's group, and was capable of performing to the TCM diesel's fuel delivery and speed specifications.

Prior to suggesting the use of the "John Deere" unit as a tool for the TCM-GPD development program, one of the original injectors, with a one-piece primary/intensifier piston assembly that had been used as a display model, was taken to the lab and operated at speeds up to 9,600 injections per minute to prove that speed was not a limiting factor (Fig. 4). That, and reassurances from D.E.C. that they saw no reason why the unit would not be satisfactory for the job in its present state of design, led us to propose its use with what turned out to be a great degree of overconfidence.

In fact, most of the D.E.C. operation had been on a four-stroke-cycle engine at considerably slower speeds (one injection per two engine revolutions) than required for the two-stroke aircraft diesel.

As to the operation on Jet A fuel, no particular problems were anticipated. As a straight-run middle distillate with an even narrower distillation curve temperature range than diesel #1, one would not have suspected there would be any more difficulty in operation on Jet A than on diesel #1. Past experience has shown that Jet A fuel would run successfully with conventional mechanical fuel injection equipment, as does diesel #1.

EP021 was submitted to TCM in June, 1982, as an unsolicited proposal with a total program cost of $81,000, all of which was to be paid by TCM. The delivery time of 44 weeks was reduced to 12 weeks based on vendor quotes for the parts.

On December 3, 1983, we received approval to go ahead with the revised proposal work outlined in EP021. See Table 2 for an historical summary of events leading up to contract award.

II. THE PROGRAM PLAN

Figure 1 shows the revised program plan. Had the program gone according to plan, the first unit would have been delivered in mid-March of 1983.

All purchase orders were prepared and sent out on time (12/8/82) but even by mid-March all the parts still had not been received. Parts inspection delays in Sidney and the need to rework parts pushed testing out to mid-May.

III. THE DEVELOPMENT PROGRAM

There wasn't supposed to be a development program on this project, and that's the reason the work was eventually halted in June, 1984. At the outset, careful investigation of historical testing including problems that had cropped up with the "John Deere" injectors seemed to indicate that there would be no problem with the units as supplied by the vendors. Finally, when the parts did arrive and were, in some case, reworked to print, we encountered a series of vexing problems.

Bottom Intensifier Body Failures - The first problem encountered involved the cracking of the bottom intensifier bodies at the ball check valve hole which allowed high pressure fuel to leak from the unit. A check with Ted Watson and his people at D.E.C. showed they had never had this problem before. (The injector was originally designed in Sidney and D.E.C. had made many changes in design and materials since then). Reducing ball check lift to reduce seating stresses and retempering the body did not work. The material was analyzed and found to be correct per the print (although different than the original Sidney design material).

Eventually, the probable cause of these failures was traced to a combination of improper heat treat and a poor design tolerance specified on the drawing which permitted two intersecting holes to be drilled beyond the point of intersection thereby weakening the area under the ball check seat as shown in Figures 2 and 3. The original Sidney design had a very thick section between the ball check seat and the intersecting fuel supply holes. The redesigned D.E.C. version reduced this section considerably to reduce injector length. The drawing was changed to prevent overdrilling of the intersecting holes, the seat section was thickened by 0.10 inches, the material was changed from the A2 to the AISI, Type D3 tool steel with a heat treat specification to give maximum toughness at some small sacrifice in hardness. That solved the problem.

Piston Seizures - One of the requirements of the TCM statement of work was that the units be capable of operating on Jet A fuel. Now that we had a runnable unit, we switched from operation on VISCOR test fluid to Jet A fuel. On Jet A, there was almost immediate seizure of the intensifier piston in its bore.

In several consultations with two authorities on the subject, one from General Motors Research Labs and one from Kodak, we learned that the problem stemmed from the poor compatibility of the D3 tool steel running against itself under conditions of marginal boundary lubrication, Jet A being a poorer lubricant than VISCOR or #2 diesel fuel. At the same time, in a conversation with Ted Watson of D.E.C., he revealed that they had just received a set of seized pistons from Volvo in Sweden who had been testing a set of identical injectors. It turned out after a later inquiry that they had been using a less viscous fuel as well--something similar to #1 diesel fuel.

The suggested solution to the problem was to change one of the materials to something more compatible with the high chromium (12%) D3. It was decided to make the pistons from SAE 52100 steel (2% Cr) and to plate them with a copper flash followed by 10-millionths of an inch of silver. This solved the problem so we could concentrate on endurance and performance testing. An agreement with TCM was reached to the effect that 10 hours of durability on each unit would be sufficient, if the disassembled parts showed no sign of distress afterwards.

Cavitation Erosion - Further endurance running uncovered a third problem--cavitation erosion of the spool valve. The debris from the erosion would cause the operation of the injector to cease as a result of the spool valve hanging up. Once disassembled and cleaned, however, the valve would again function normally. The cavitation was symmetric and confined to a thin annular ring near the edge of the valve land that controls supply pressure flow to the top of the primary piston. Although the magnified area appears to be cavitation erosion, there is some doubt, no other cause being apparent in explaining the damage while running on Jet A fuel.

Needle Seat Fatigue - The nozzles designed for this unit are of the low sac volume type, the nozzle holes being located on the needle seat area just downstream of the needle seat contact area instead of in a large sac volume. This provides a sharper start and end of injection with little afterspray. What appears to be surface fatigue occurred on the needle seat after extended running on Jet A fuel.

Needle End Fatigue - The hemispherical end of the needle where it contacts the spring button showed signs of surface fatigue. This might be due to a combination of high Herzian contact stress and poor lubrication since no force reversals are available to permit fuel to enter the area and provide a squeeze film to protect the parts. The hemispherical needle end also may not provide enough surface area to reduce the contact stresses to an acceptable value.

Coil Epoxy Swelling - A phenomenon called "runout" had plagued the program from the beginning. At higher speeds and loads the operation of the unit would cease in an exponentially decreasing manner over a period of a couple of seconds or less. The problem was avoided at first by running at low speeds. Eventually, when enough of the problems described earlier had been solved to run for longer periods at higher speeds and loads, the problem could no longer be avoided. The problem was tracked to a heat buildup in the coil. Although the coil is fuel cooled with the residual fuel used to move one end of the spool valve, at higher loads the increased temperatures caused the epoxy to swell, decreasing the gap between the coil and armature. Several suggestions were proposed to provide either temporary or permanent solutions. Among the solutions were plans to externally liquid cool the coil, increase the coil-to-armature gap, reduce the coil current and recess the epoxy by 1/32" from the face of the coil. A coil redesign was also proposed for a more permanent long term fix. The redesign might include integrated external cooling means and a coil with smaller gauge wire and more turns. Don Louden was studying the problem and was to prepare a report on the subject.

IV. CONCLUSIONS AND RECOMMENDATIONS

The latest version of the "John Deere" injector, that had been used during the strobe testing work to further characterize the quality of the spray, had come a long way toward meeting the TCM objectives. Some problems with the unit had been solved and the remainder were clearly identified as to cause, and changes were suggested necessary to permit the unit to operate successfully as originally intended.

ORIGINAL PAGE IS OF POOR QUALITY

In spite of the apparent lack of success in fulfilling the requirements of the TCM contract, it is important to note that a great deal of progress was made in advancing the state-of-the-art with this injector. No other high speed, electronically controlled diesel fuel injection unit capable of operation on fuels lighter than diesel #2 has yet been made public.

The unit in its present state has been capable of operation of Jet A fuel (and therefore, presumably, on diesel #1 as well). Also, it is the considered opinion of the engineers who participated in this testing that the remaining problems are amenable to engineering solutions.

REFERENCES

1. Technical Proposal No. EP007, "Electronic Controlled Diesel Fuel Injection System for Light Aircraft Diesel.", May 1. 1981.

2. Engineering Report No. 4045, REV. 1. "Electronically Controlled Diesel Fuel Injector for Teledyne Continental Motors.", M. Gage, February 5, 1982.

3. Engineering Report No. 4071, "Analysis of Defects and Problems with the Bendix Electronically Controlled Fuel Injection System from Testing During the Garrett AiResearch CCTE Program.", K. Stuckas, May 12, 1982.

4. Technical Proposal No. EP021, "Electronically Controlled Fuel Injection System for General Aviation Diesel Engine," May 24, 1982.

5. Engineering Report No. 4085, "Failure Analysis of Bottom Intensifier Body (P/N 2195138) from Electronically Controlled Fuel Injection System (P/N DCX-3028) for General Aviation Diesel Engine," K. Stuckas, June 13, 1983.

6. Engineering Report No. 4086, "Progress Report on Electronically Controlled Diesel Fuel Injectors for Teledyne Continental Motors, General Products Division," K. Stuckas, August 10, 1983.

7. Engineering Report No. 4087, "Progress Report on Electronically Controlled Diesel Fuel Injectors for Teledyne Continental Motors, General Products Division," K. Stuckas, October 27, 1983.

8. Engineering Report No. JER0060, "Progress Report on Electronically Controlled Diesel Fuel Injectors for Teledyne Continental Motors," M. Morton, April 3, 1984.

ORIGINAL PAGE IS OF POOR QUALITY

TABLE 1

COMPARISON OF ENGINE SPECIFICATIONS

	Garrett CCTE	TCM-GPD Diesel
Type of Diesel	2-stroke cycle	[illegible]-stroke cycle
Scavenging	Curtiss Loop	Curtiss Loop
Displacement Per Culinder (in^3)	16.64	[illegible]
Bore (inches)	2.58	[illegible]
Stroke (inches)	2.95	[illegible]
Bore-Stroke Ratio	0.91	[illegible]
Compression Ration, Nominal	15.00	[illegible]
Compression Ration, Effective	9.60	[illegible]
Scavenge Ratio	1.452	[illegible]
Maximum Rated Speed (rpm)	8000.0	[illegible]
Mean Piston Speed (ft/min)	3930.0	[illegible]
Maximum Indicated HP Per Cyl.	111.64	[illegible]
IMEP (psi)	332.0	223.2
Maximum Cylinder Pressure (psia)	4500.0	[illegible]
Fuel Volume Per Injection (mm^3)	47.0	90.0
Fuel-Air Ratio (lbm/lbm)	0.0257	0.0364
Duration of Injection (crank angle degrees)	19.2	[illegible]
Duration of Injection (ms)	0.4	[illegible]

TABLE 2 - History of Bendix EnPD/TCM-GPD/NASA Involvement Prior to Contract Award

.6/80	Initial contact by TCM indicating interest in Bendix fuel injection system similar to that developed for Garrett/AiResearch.
.11/80	Joint Bendix/TCM/NASA meeting in Sidney to discuss Bendix' capabilities. Received preliminary copy of fuel injection spec.
.12/80	TCM requested "Ball Park" quote of electronic fuel injection system for single cylinder diesel engine.
.1/81	Bendix quoted budgetary price estimate of $64,000, 6-8 months ARO for 2 electronically controlled fuel injectors and system support equipment. Total cost of program $87,000 ($23,000 absorbed by Bendix).
.2/81	Bendix prepared Project Plan per Engineering Report #4045.
.3/81	TCM requested a firm quotation.
.5/81	Bendix Technical proposal EP007 was prepared and dated 5/1/81.
.6/81	Disclosure agreement between Bendix and TCM was negotiated.
.11/81	Firm quotation for work covered by EP007 was given to TCM - quoted $82,000 and 44 weeks delivery. Progress payments to be negotiated at time of order.
.3/82	TCM advised NASA is on verge of approving 2 1/2 year program to continue work on aircraft diesel engine program.
.6/82	Bendix submitted revised proposal EP021 based on use of existing "John Deere" design injector. Program total cost reduced to $81,087 and time to 12 weeks.
.12/82	Go-ahead received from TCM.

ELECTRONICALLY CONTROLLED DIESEL FUEL INJECTOR FOR TELEDYNE CONTINENTAL MOTORS
REVISED PROGRAM PLAN

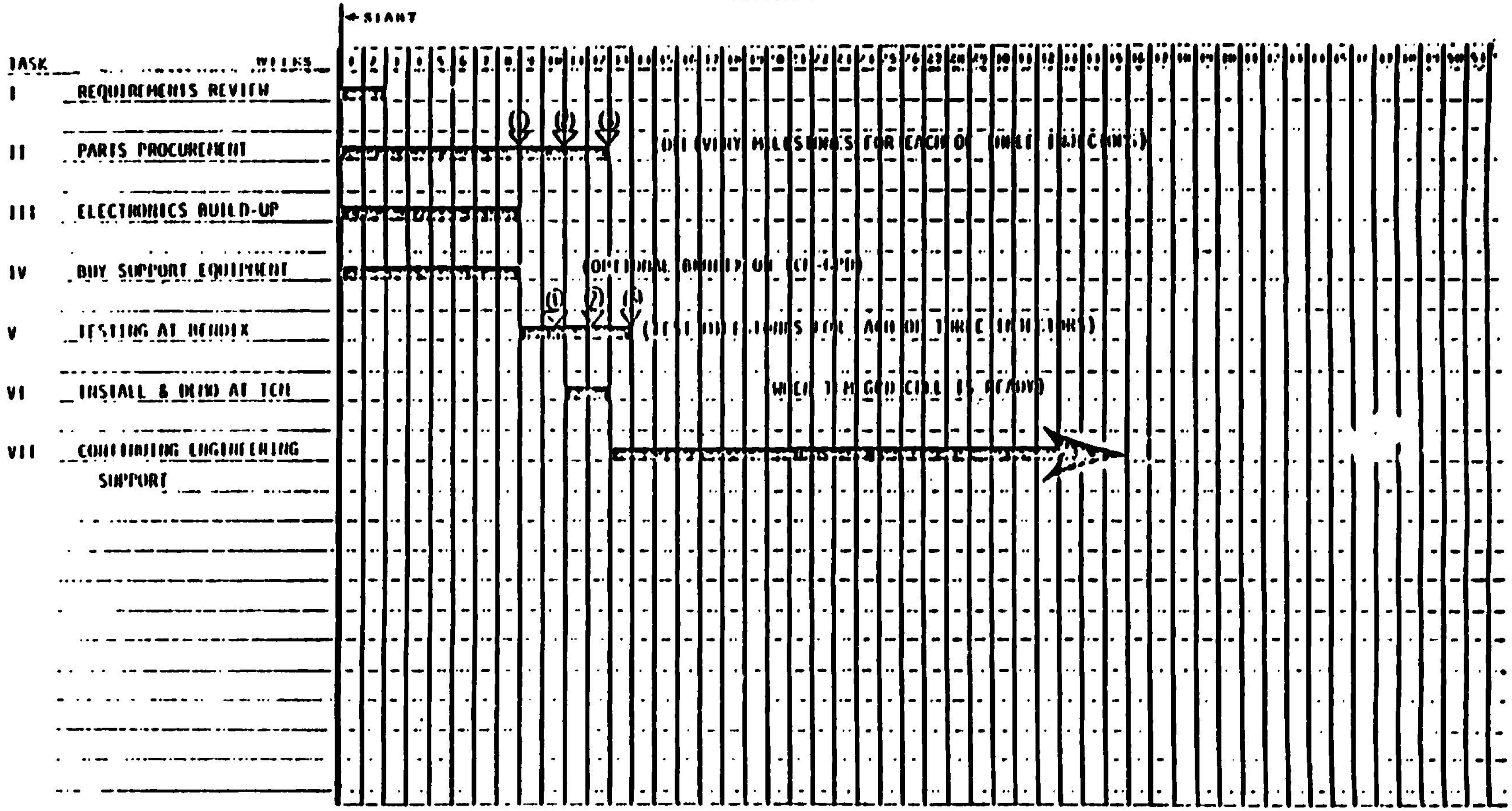

FIGURE 1

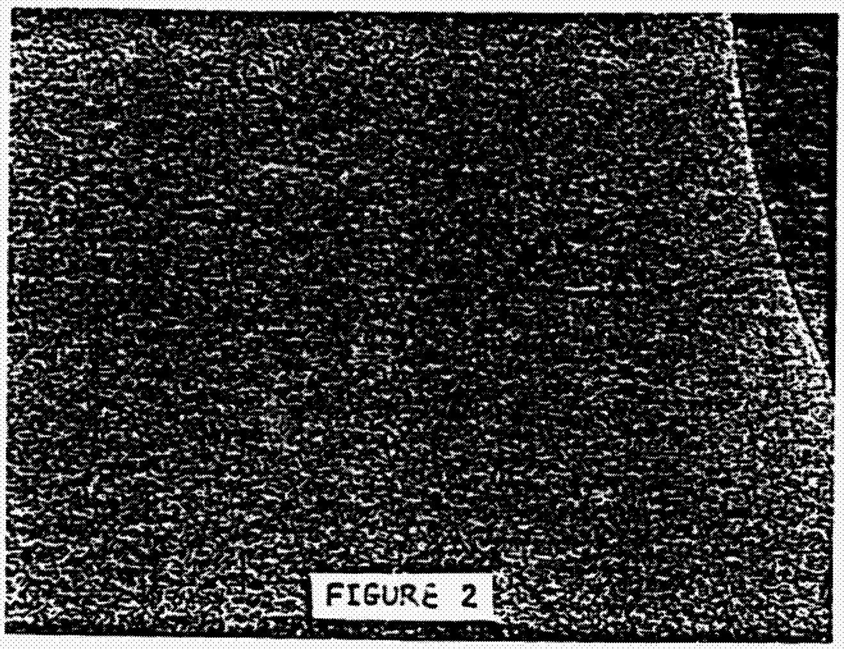

FIGURE 2

ORIGINAL PAGE IS
OF POOR QUALITY

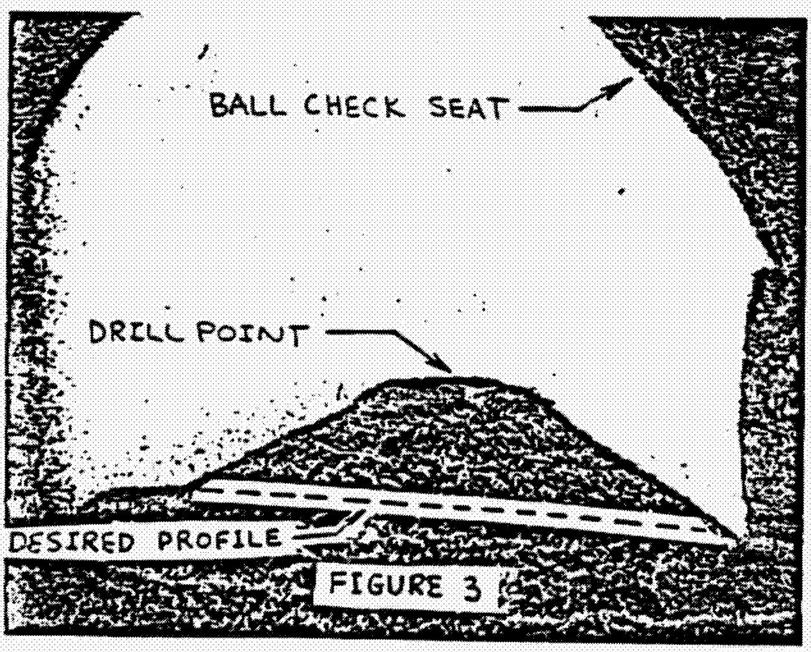

FIGURE 3

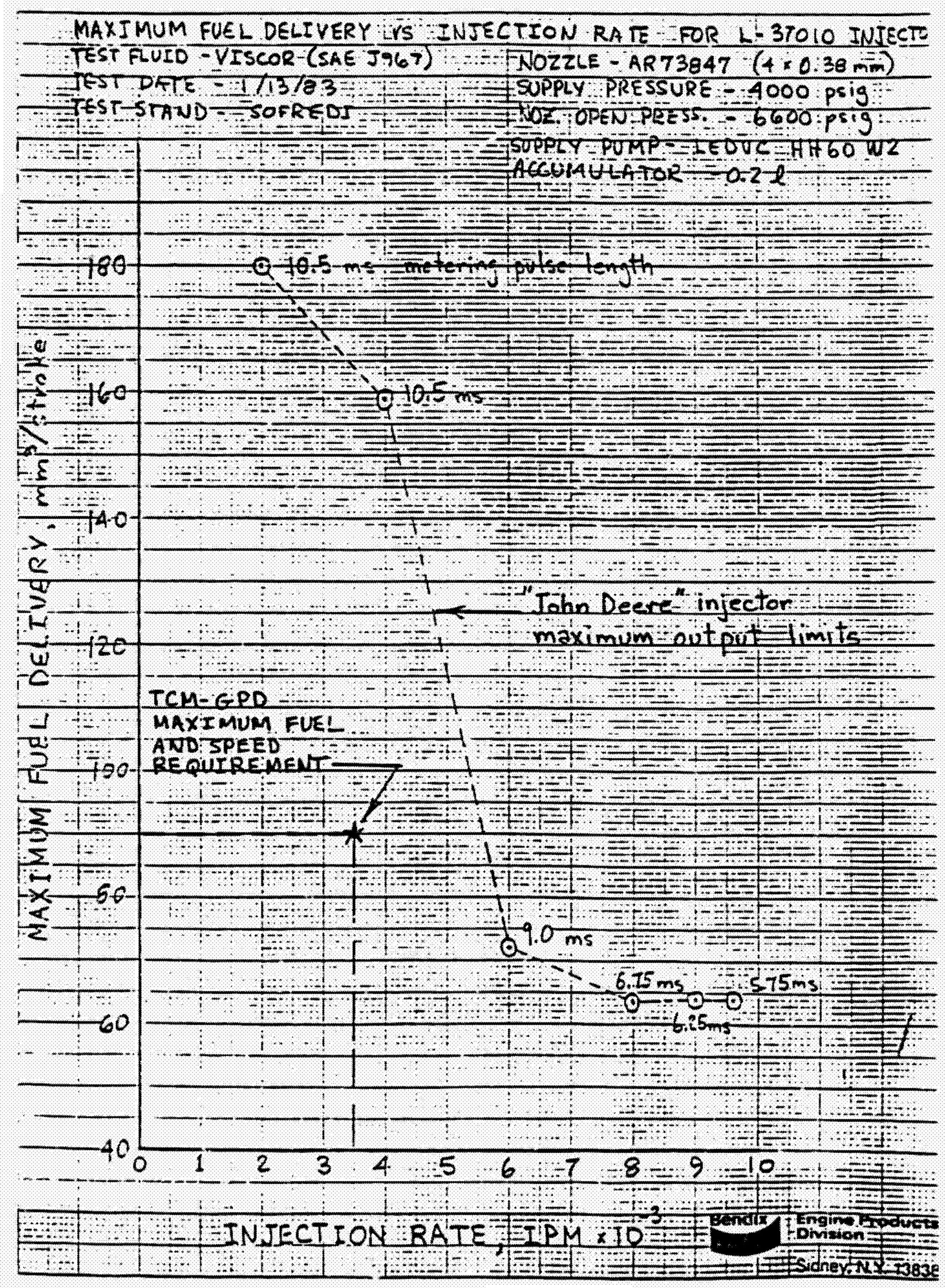
MAXIMUM FUEL DELIVERY VS INJECTION RATE FOR L-37010 INJECTO
TEST FLUID - VISCOR (SAE J967)
TEST DATE - 1/13/83
TEST STAND - SOFREDI
NOZZLE - AR73847 (4 x 0.38 mm)
SUPPLY PRESSURE - 4000 psig
NOZ. OPEN PRESS. - 6600 psig
SUPPLY PUMP - LEDUC HH60 W2
ACCUMULATOR - 0.2 l
MAXIMUM FUEL DELIVERY, mm³/stroke
INJECTION RATE, IPM x10⁻³
18.5 ms metering pulse length
10.5 ms
"John Deere" injector maximum output limits
TCM-GPD MAXIMUM FUEL AND SPEED REQUIREMENT
9.0 ms
6.75 ms
6.25ms
5.75ms
180
160
140
120
100
80
60
40
0
1
2
3
4
5
6
7
8
9
10
Bendix
Engine Products Division
Sidney, N.Y. 13838

FIGURE 4.

A P P E N D I X V I

EVALUATION OF K-1000F PISTON RING SET FROM
A 4.252" Ø TWO CYCLE AIRCRAFT ENGINE
RM 1652

KOPPERS COMPANY INC.,
PISTON RING AND SEAL DIV.
BALTIMORE, MARYLAND

TELEDYNE CONTINENTAL MOTORS: MUSKEGAN

EVALUATION OF K-1000F PISTON RING SET FROM A 4.252" Ø TWO CYCLE AIRCRAFT ENGINE

RM 1652

REFERENCE: TECHNICAL SERVICE

M.W.O.: 340000

DATE: August 1, 1983

AUTHOR: J. B. DISNEY

APPROVED BY: J. E. Cromwell
J. E. CROMWELL

INTRODUCTION:

A 4.252" Ø piston ring set was received for evaluation when scuffing occurred after running at full load for 1/2 hour in Teledyne's two-cycle aircraft diesel test engine in Muskegan, Michigan. Prior to scuffing, the engine ran successfully for 12-1/2 hours at partial load. The cylinder liner surface is chrome plated and the top and second compression rings are plasma coated with K-1000F. The five ring piston set consisted of the following:

TOP RING:	Crown Plasma K-1000F Keystone Compression Ring Bevel Back K-28, P/N B-7792.
SECOND RING:	Plasma Coated K-1000F Crown Face Bevel Back K-28 Compression Ring, P/N B-7794.
THIRD & FOURTH RINGS:	Crown Face Bevel Back K-Iron Compression Ring, P/N B-7793.
OIL RING:	Conformable K-28 Oil Ring, P/N B-7796.

Teledyne's end clearance and free gap measurements before and after the test are documented on Attached Sheet B.

OBJECT:

Document the condition of the ring set and, if possible determine the cause of scuffing.

CONCLUSIONS:

1. An end clearance of (.024") on the top compression ring apparently was too tight to accommodate the high temperatures of a full load operation. Butting of the top compression ring resulted in scuffing and an end clearance change of .029".

2. Distress on the ring joints of the second and third compression rings indicates contact with the liner intake/exhaust ports. The current point protrusion specification for these rings is +.0007 to - .0005.

3. The fourth compression ring had a ΔEC of .002" as compared to a ΔEC of .014" for the third compression ring. Although both rings are manufactured from K-Iron material, the difference in wear is attributed to the fact that the fourth ring is always below the intake/exhaust ports and therefore is not gas loaded.

4. The K-28 ductile iron oil ring experienced extremely heavy O.D. wear resulting in a ΔEC .040" and localized heavy wear at the joints. The cause of the heavy oil ring wear is suspected as being the very tight end clearance of .014" which may have caused ring butting.

RECOMMENDATIONS:

1. Increase ring end clearances as indicated below:

	PART NUMBER	END CLEARANCE
Top Ring	B-7792	.040 - .050
Second Ring	B-7794	.030 - .040
Third Ring	B-7793	.030 - .040
Fourth Ring	B-7793	.030 - .040
Oil Ring	B-7796	.025 - .035

2. Increase the amount of negative point protrusion on the second and third compression rings to 0.000 to -.0017.

3. Reduce Unit Pressure on oil ring from 225 psi to 175 psi.

SUMMARY OF RESULTS:

1. All five rings show varying degrees of abrasive wear across the O.D. surface. The heaviest wear is noted on the plasma coated top compression ring (ΔEC .029") and the fifth K-28 oil ring (ΔEC .040"). The plasma coating on the top compression ring is severely scuffed and pulled out. Carbon is noted in the areas of coating pullout. Heavy abrasive face wear due to metal-to-metal contact caused sharp edges and burrs along top/bottom O.D. rails. Wear on the plasma coated second compression ring is similar to (but not as severe as) that of the top ring with evidence of port clipping at the ring joint areas. However, the plasma coating has not chipped or spalled in this location. Second compression ring had .003" ΔEC. Abrasive wear patterns are noted on the third (ΔEC .014") and fourth (ΔEC .002") K-Iron compression rings and the K-28 oil ring (ΔEC .040"). All three rings exhibit varying degrees of localized wear at the joint areas. Reference Sheet A documents the condition of the ring set. Sheet B shows Teledyne's free gap and end clearance measurements before and after engine test.

2. Photographs on Sheet C are believed to be typical of the wear experienced by this ring set.

3. A close examination of the top compression ring reveals a build-up of heavily packed carbon at the left joint end which indicates that the ring butted and caused the coating to scuff and pull out. (Sheet D).

4. Port clipping is evident on the second compression ring being most prominent on the top O.D. surface. It is interesting to note that the coating has not chipped or spalled as a result of joint clipping. Joint ends of ring show burnished areas that indicate a ring butting condition, Sheet E.

5. Heavy localized wear at the joint area of the third (K-Iron) compression ring is believed to be due to port clipping. Photographs presented on Sheet F indicate wear to be more pronounced along the top O.D. surface. The heavy O.D. wear (ΔEC .014") on this third compression ring may be attributed to the softer K-Iron material wearing against the distressed liner surface caused by top ring scuffing.

6. The fourth K-Iron compression ring (ΔEC .002") shows only slight evidence of localized wear at the joint areas; however, burnished spots on joint ends indicates that the ring may have butted, Sheet G.

7. The K-28 oil ring shows evidence of very heavy abrasive wear around O.D. circumference (ΔEC .040") and heavy localized wear at the joint areas. A photograph of the ring near 180° indicates that wear was heavy enough to cause burrs on the edges of the O.D. rails, being most prominent on the bottom rail, Sheet H. Since the motion of the piston is such that the oil ring does not traverse the intake/exhaust ports, the heavy distress noted at the joint cannot be attributed to port clipping. Therefore, it is believed that the heavy O.D. wear may have been caused by the tight original end clearance of .014" that could not accommodate the thermal expansion of the ring. It should be noted that at full load the exhaust temperatures were reported to be approximately 1000°F and the top turn-around point of the oil ring is close to the vicinity of the exhaust ports.

SUMMARY OF RESULTS - CONT'D.

8. A close examination of the oil ring indicates that the top rail width varies around the ring circumference due to off-centered venting operation, Sheet I.

9. The microstructure of the plasma coated top and second comression rings is presented on Sheets J and K. Despite the heavy wear experienced, the K-1000F plasma coating exhibits good adhesion along the base metal interface. Porosity is within acceptable limits. Coating thickness is also within a specified tolerance of .004" - .009" for P/N B7792 and P/N B-7794.

   Microstructure of ring base material consists of spheroidal graphite (100% types 1 and 2) in a matrix of tempered martensite. Hardness of the top ring is 43.5 - 43.8 and for the second ring 44.6 - 44.8 HRC within a specified tolerance of 40 - 46 HRC. Both the top and second compression rings are considered to be manufactured from good ductile iron material.

10. The microstructure of the third and fourth K-Iron compression rings consists primarily of flake type graphite (100% type AC*), Sizes 6,7 and 8. The matrix is pearlite with a non-continuous network of steadite. Hardness of both rings ranges from 80 - 82 HRG and is within manufacturing specification of 77.5 - 91 HRG according to their ring dimensions. (See Sheet L).

11. Photomicrographs presented on Sheet M, further confirm the heavy abrasive O.D. wear that caused plastic deformation on the oil ring rails. The ring's microstructure consists of spheroidal graphite (100% types 1 and 2) in a matrix of tempered martensite with a hardness of 42 - 43 HRC within a specified range of 40 - 46 HRC for K-28 ductile iron.

12. O.D. profile traces were obtained on the compression rings (particularly top and second rings) in an area where the face wear was not too severe. Sheet N shows the top ring to have a wear profile exhibiting top edge bearing with a 1^{o} taper on the top side near 270^{o} from the right joint.

    The second compression ring shows a wear profile indicating slight wear toward the bottom side near 90^{o}.

    At 180^{o}, both the third and fourth compression rings have a wear profile exhibiting bottom edge bearing.

DISCUSSION:

An end clearance of (.024") which was too tight to accommodate the high temperatures of a full load operation, apparently caused the top compression ring to butt resulting in scuffing and heavy wear (.029" ΔEC).

Distress on the ring joints of the second and third compression rings indicate contact with the liner intake/exhaust ports. The current point protrusion specification for these rings is +.0007 to -.0005. Burnished areas on the joint ends of these rings indicate evidence of a butting condition.

The fourth compression ring had a ΔEC of .002" as compared to a ΔEC of .014" for the third compression ring. Although both rings are manufactured from K-Iron material, the difference in wear is attributed to the fact that the fourth ring does not traverse the intake/exhaust ports.

DISCUSSION - CONT'D.

The K-28 ductile iron oil ring experienced extremely heavy O.D. wear resulting in a ΔEC of .040" and localized heavy wear at the joints. The cause of heavy oil ring wear is believed to be related to the very tight end clearance of .014' which may have caused ring butting. Since the manufacture of these rings Teledyne has run a test with a top ring end clearance of .045". This test ran successfully for 35 hours until another component failure shut the engine down. For any future tests it is recommended that the minimum allowable end clearance be increased to .040" for the top ring, P/N B-7792, .030" for the second, third and fourth rings, P/N B-7794, P/N B-7793 and .025" for oil ring, P/N B-7796.

INDEX OF INCLUDED SHEETS

CONTENTS	SHEETS
Ring Measurements and General Appearance	A
Free Gap and End Clearance Measurements	B
Photographs of Piston Ring Set	C
O.D. Photographs of Compression Rings and Oil Ring	D - I
Microstructure of Five Ring Piston Set	J - M
O.D. Profile Traces	N

RING MEASUREMENTS AND GENERAL APPEARANCE

			P/N B-7792	P/N B-7796	P/N B-7793	P/N B-7793	P/N B-7797
Ring No.			TOP COMPRESSION (A)	SECOND COMPRESSION (B)	THIRD COMPRESSION (C)	FOURTH COMPRESSION (D)	OIL RING (E)
Type Coating			K-1000F			K-IRON	K-28
SPEC		Wall	.172/.182	.172/.182	.172/.182	.172/.182	.145/.155
SPEC		Width	.115 Ref.	.097/.098	.097/.098	.097/.098	.176/.177
MEASUREMENT	WALL	Gap	.172	.176	.171	.173	.146
MEASUREMENT	WALL	90°	.172	.176	.173	.179	.144
MEASUREMENT	WALL	180°	.171	.176	.172	.176	.145
MEASUREMENT	WALL	270°	.172	.176	.173	.173	.145
MEASUREMENT	WALL	Gap	.171	.176	.172	.173	.147
MEASUREMENT	WIDTH	Gap	.116	.098	.098	.098	.177
MEASUREMENT	WIDTH	180°	.116	.098	.098	.098	.177
MEASUREMENT	WIDTH	Gap	.116	.098	.098	.098	.177
GENERAL APPEARANCE			O.D. - Coating worn off at joint. Carbon build-up in worn areas. Coating severly scuffed and pulled out. Carbon evident in areas of pullout. Heavy abrasive face wear caused sharp edges and burrs along top/bottom O.D. Areas of heavy carbon build-up at left joint end indicates ring may have butted. I.D. - Light carbon. TOP SIDE - Carbon build-up near O.D. BOTTOM SIDE - Burnished with dirt chaining and fretting wear most prominent near I.D.	O.D. - Wear similar to top ring with evidence of port clipping but no evidence of coating chipping or spalling at joint areas. EVIDENCE OF RING BUTTING I.D. - Mostly free of carbon TOP SIDE - Tan appearance. BOTTOM SIDE - Mostly burnished.	O.D. - Heavy abrasive face wear caused sharp edges and burrs along top/bottom O.D. Port clipping most evident at right joint (0°). EVIDENCE OF RING BUTTING I.D. - Free of carbon. TOP/BOTTOM SIDES - are mostly burnished.	Wear patterns similar to third compression ring. Some evidence of localized wear at joint areas. Light chaining evident on top side. EVIDENCE OF RING BUTTING	O.D. - Heavy abrasive wear caused burrs on edges of rails. Top rail width varies around the ring due to off centered venting operation. Heavy localized wear at ring joint areas. EVIDENCE OF RING BUTTING I.D. - No unusual wear patterns. TOP/BOTTOM SIDES - Mostly burnished.

RM 1652
Sheet A

FREE GAP AND END CLEARANCE MEASUREMENTS BEFORE AND AFTER TEST MEASUREMENTS AS REPORTED BY TELEDYNE

RING IDENTIFICATION		FREE GAP (INCHES)		(WHEN CLOSED TO 4.250" Ø) END CLEARANCE (INCHES)	
		BEFORE	AFTER	BEFORE	AFTER
Top,	P/N B-7792	.547	.406	.024	.053
Second,	P/N B-7794	.390	343	.021	.024
Third,	P/N B-7793	.546	.531	.020	.034
Fourth,	P/N B-7793	.547	*.640	.017	.019
Oil,	P/N B-7796	.266	.234	.015	.055

KOPPERS SPECIFICATIONS

P/N B-7792	.58 Approx.	.010/.023
P/N B-7794	.42 Approx.	.010/.020
P/N B-7793	.73 Approx.	.010/.020
P/N B-7793	.73 Approx.	.010/.020
P/N B-7796	.32 Max.	.010/.025

*Increase in Free Gap is believed to be due to an error in recording.

ORIGINAL PAGE IS
OF POOR QUALITY

K-1000F PLASMA COATED RING SET

PHOTOGRAPHS APPROX. 3.4X

RIGHT JOINT

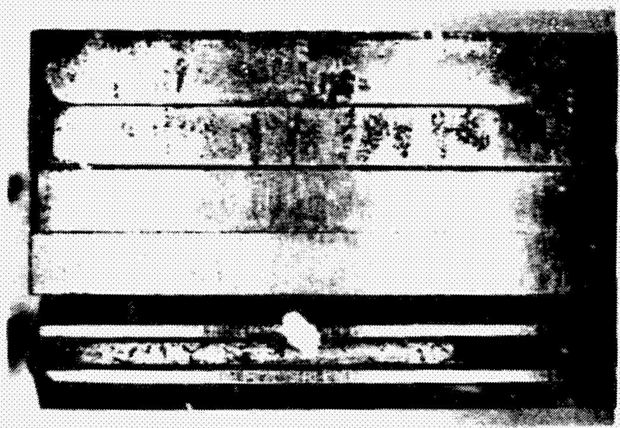

LEFT JOINT

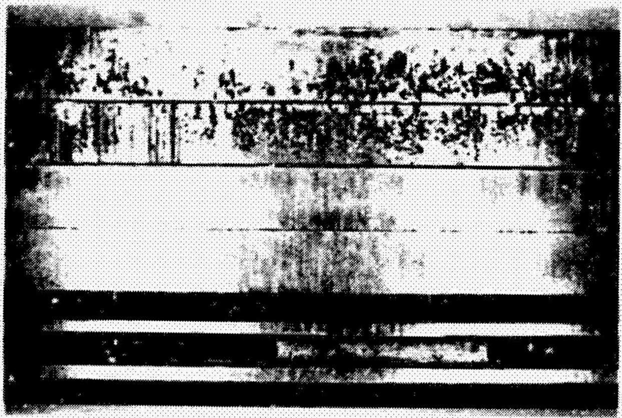

180°

Entire ring set shows the effects of heavy wear. Scuffing is evident on the K-1000F plasma coated top and second compression rings. Carbon is packed in the areas of pullout. The third and fourth K-Iron compression rings and the K-28 oil ring all show heavy abrasive wear.

PLASMA COATED TOP COMPRESSION RING, P/N B-7792

ALL PHOTOGRAPHS APPROX. 14X

O.D. SURFACE

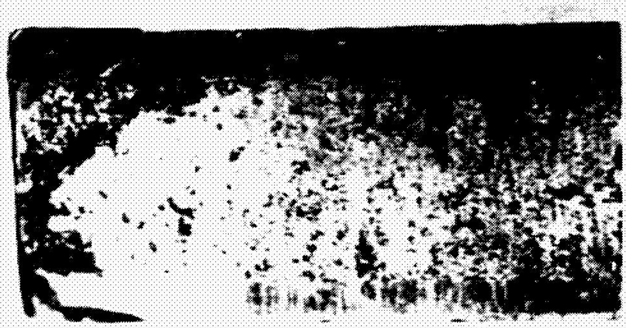

Right Joint

Left Joint

Photographs show heavy abrasive and adhesive wear at the ring joint area. Plasma coating has been pulled out and some of the voids are packed with carbon.

Joint Tip Ends

Photograph shows carbon build-up at ring joint ends. Black arrow indicates notch at right joint. Small areas (white arrows) of heavy carbon build-up on left joint end indicates that the ring may have butted and caused plasma coating to scuff and pull out.

ORIGINAL PAGE IS OF POOR QUALITY

RM 1652
Sheet E

K-1000F PLASMA COATED SECOND COMPRESSION RING, P/N B-7794

PHOTOGRAPHS APPROX. 14X

Right Joint

Left Joint

Port clipping appears to be most evident along top O.D. surface as indicated by arrows. It is interesting to note that coating has not chipped or spalled at joint area as a result of port clipping.

Joint ends of ring before cleaning show light carbon build-up on the surface.

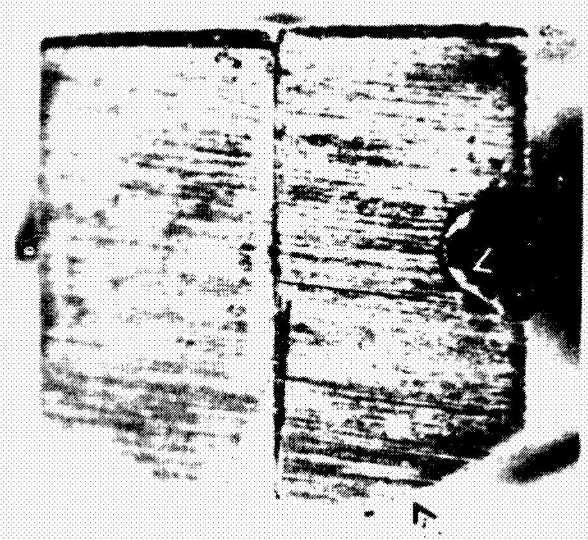

Joint ends of ring after cleaning . Burrs on notched end of right joint (white arrow) and high spot on bottom side at I.D. interface are burnished and indicate that ring may have butted.

THIRD (K-IRON) COMPRESSION RING - P/N B-7793

PHOTOGRAPHS APPROX. 14X

O.D. SURFACE

Right Joint

Left Joint

Heavy localized wear at the ring joint area is believed to be due to port clipping. Arrows indicate wear to be more pronounced along the top O.D. surface. Abrasive scoring extends across ring face.

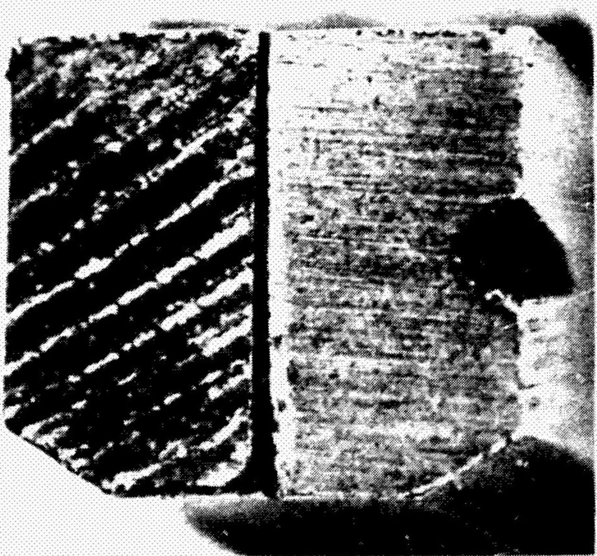

Burnished spots and burrs on joint ends of third compression ring indicate the ring may have butted.

FOURTH (K-IRON) COMPRESSION RING, P/N B-7793

PHOTOGRAPHS APPROX. 14X

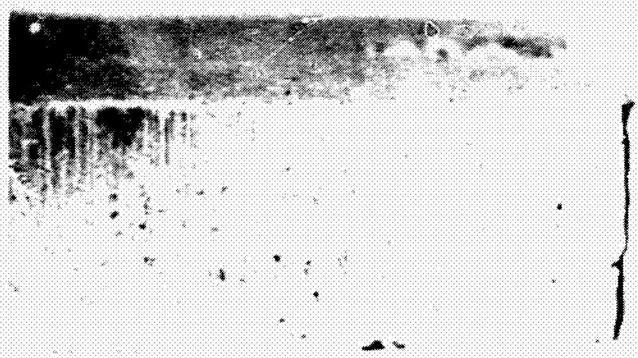

Right Joint

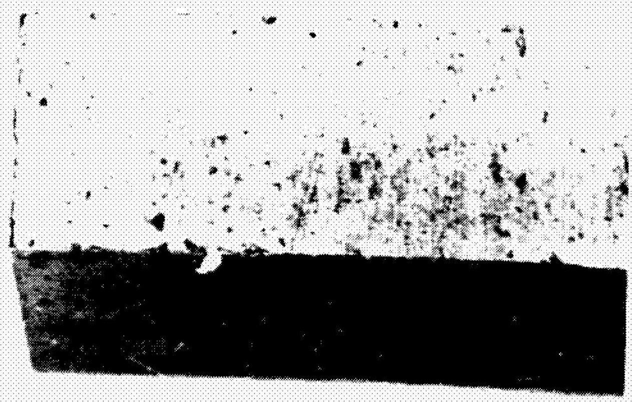

Left Joint

O.D. surface of ring shows abrasive scoring and some slight evidence of localized wear at the joint area.

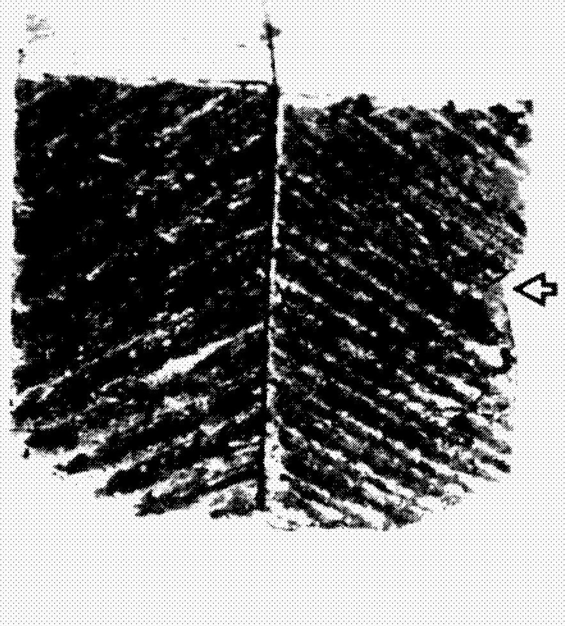

Burnished spots on joint ends of fourth compression ring indicates that ring may have butted.
Arrow indicates notch at right joint.

O.D. RAILS OF K-28 OIL RING, P/N B-7796
PHOTOGRAPHS APPROX. 14X

Right Joint

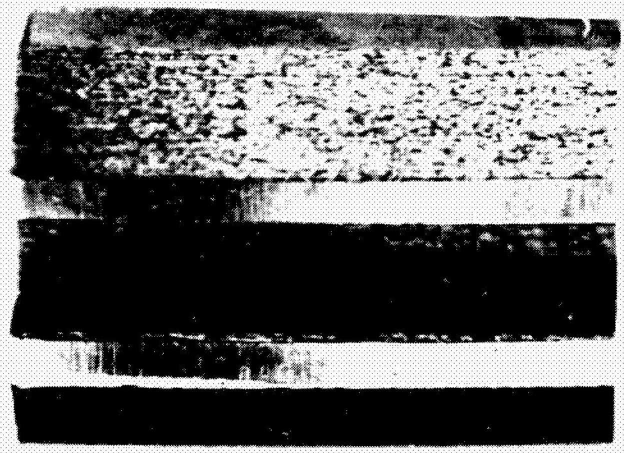

Left Joint

Wear on oil ring rails appears to be most evident along bottom rail.

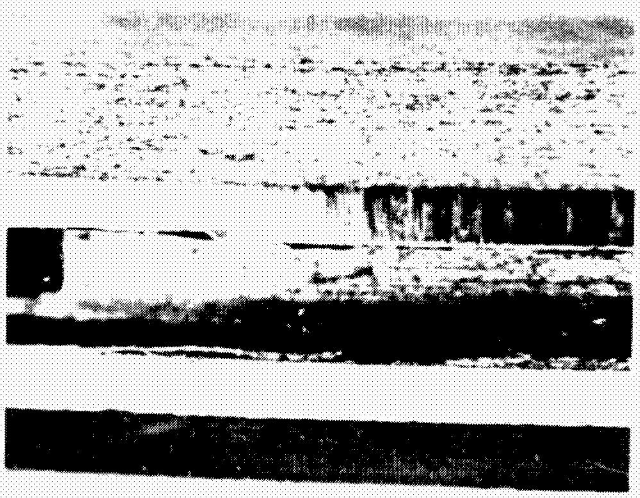

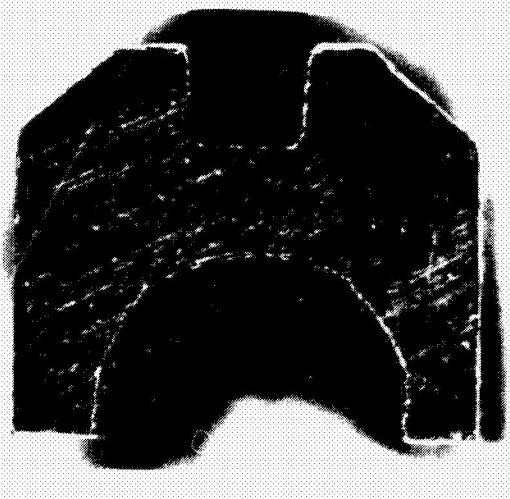

Right Joint End

Heavy abrasive wear caused burrs on edges of rails. Condition most evident along bottom rail near 180°.

Photographs on the right show the left and right joint ends of the oil ring. High spots and burrs on the surface may have been caused by butting.

Left Joint End

O.D. RAILS OF (K-28) OIL RING, P/N B-7796

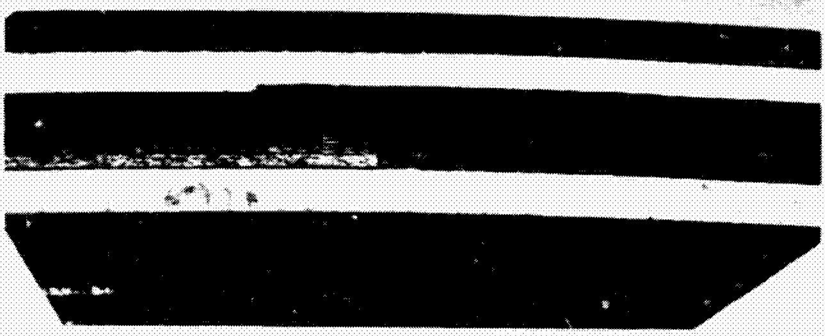

Approx. 9X

Top rail width varies around the ring circumference due to off centered venting operation.

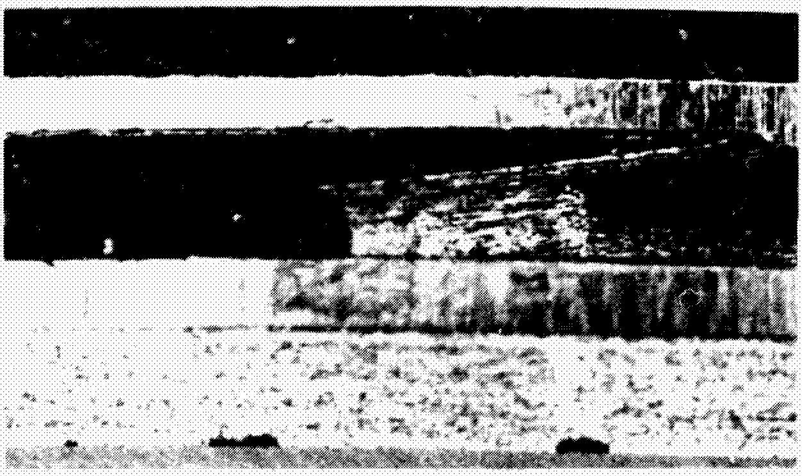

Approx. 14X

A different area around the ring O.D. at a higher magnification shows the same type of condition described above.

PHOTOMICROGRAPHS OF (K-1000F) TOP COMPRESSION RING

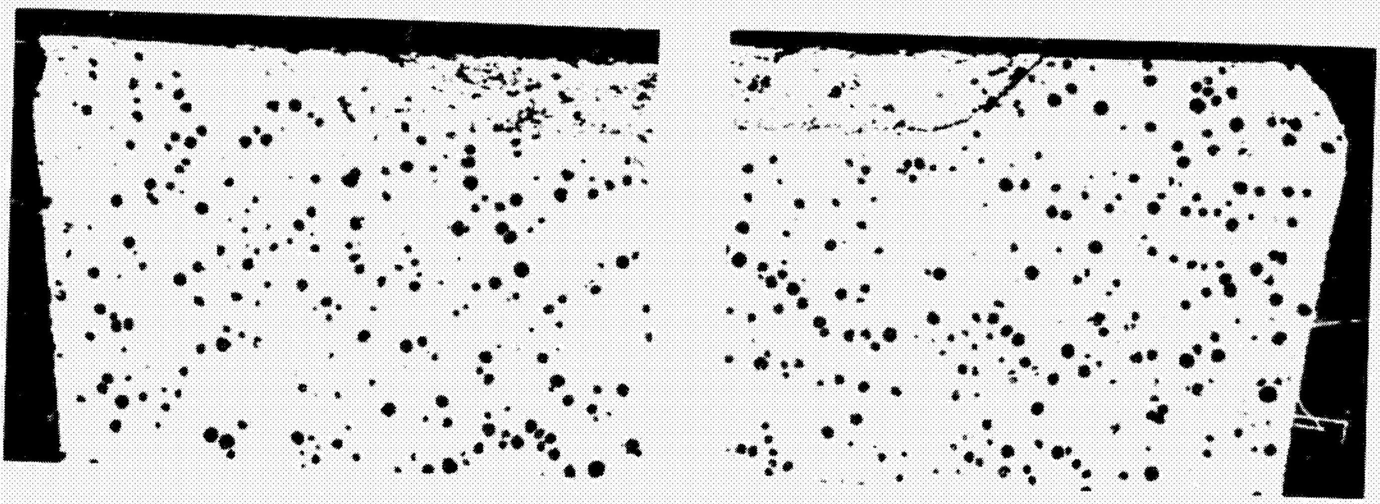

Top 100X Bottom

Right joint (0^o) area of ring - coating thickness .004". Heavy abrasive wear caused a burr on the edge of the top base metal shoulder. Bottom shoulder does not show this type of condition.

Coating shows good adhesion along base metal interface. Porosity is within acceptable limits. Coating thickness is on the low side, but still within new ring specification of .004" - .009", P/N B-7792.

Microstructure of base material shows a good dispersion of spheroidal graphite consisting of 100% types 1 and 2. Hardness is 43.5 - 43.8 RC within a specified tolerance of 40 - 46 RC for K-28 ductile iron.

PHOTOMICROGRAPH OF (K-1000F) SECOND COMPRESSION RING

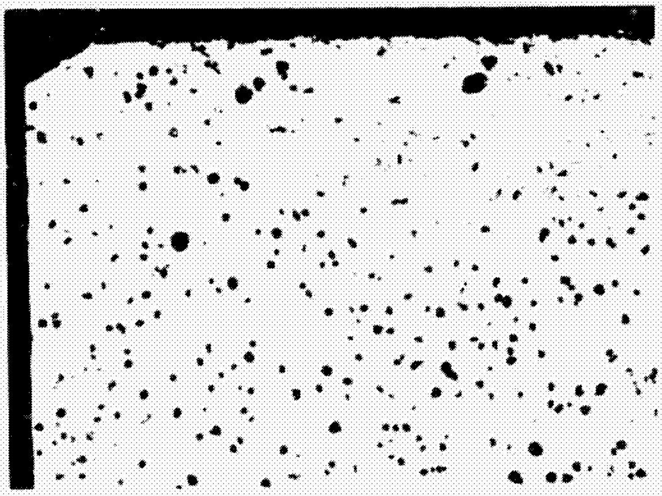

Coating thickness is .009" along top O.D. surface near right joint.

Coating thickness specifications: .004 - .009", P/N B-7794

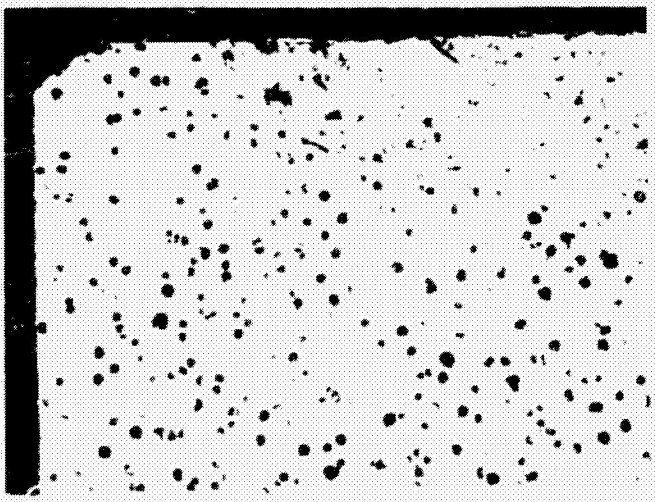

Coating thickness is .007" along top O.D surface near 90° from the right joint. Top base metal shoulder shows uniform wear with no evidence of a burr at the top edge.

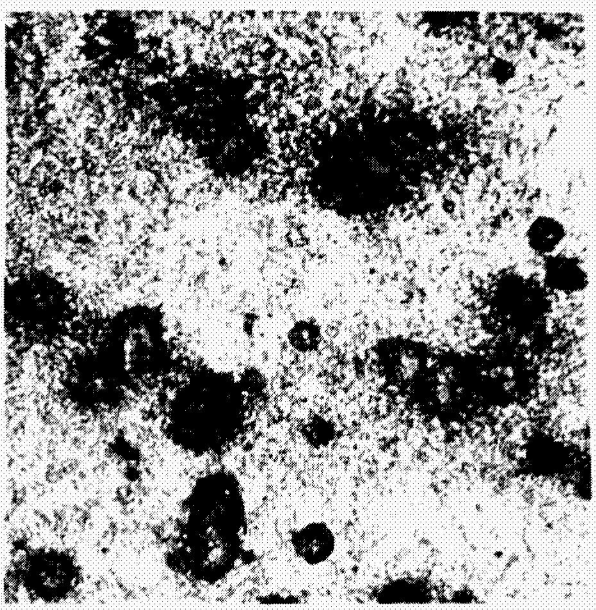

Etched condition of ring's base material shows a matrix of tempered martensite with a hardness of 44.6 - 44.8 HRC, within a specified range of 40 - 46 HRC for K-28 ductile iron. Both the top and second compression rings are considered to be manufactured from good piston ring material.

MICROSTRUCTURE OF K-IRON COMPRESSION RINGS

TYPICAL STRUCTURE OF THIRD AND FOURTH RINGS, P/N B-7793

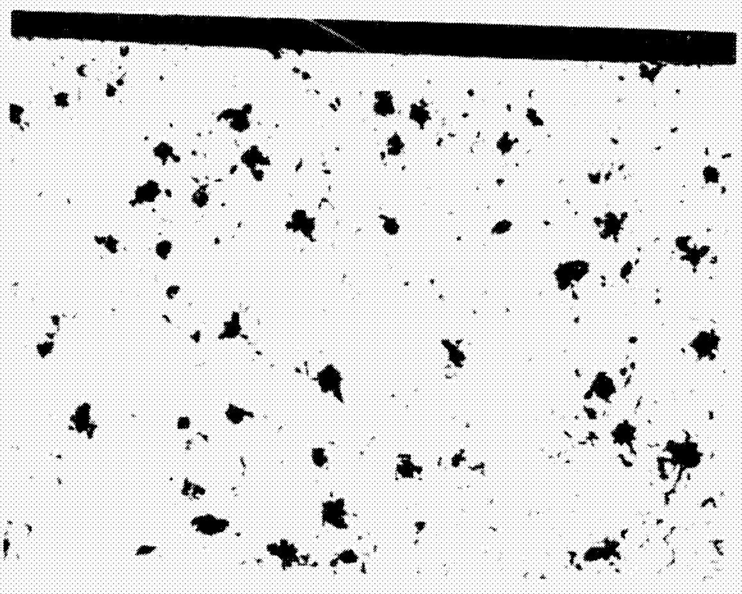

Graphite structure along O.D. wear surface consists of flake type graphite. (100% AC*), sizes 6,7, & 8

100X

O.D. WEAR SURFACE Matrix is pearlite with a non-continuous network of steadite. Hardness of both rings is 80 - 82 HRG within manufacturing specifications of 77.5 - 91 HRG according to ring dimensions.

400X

ORIGINAL PAGE IS
OF POOR QUALITY

RM 1652
Sheet M

PHOTOMICROGRAPHS OF K-28 OIL RING, P/N B-7797
O.D. SURFACE

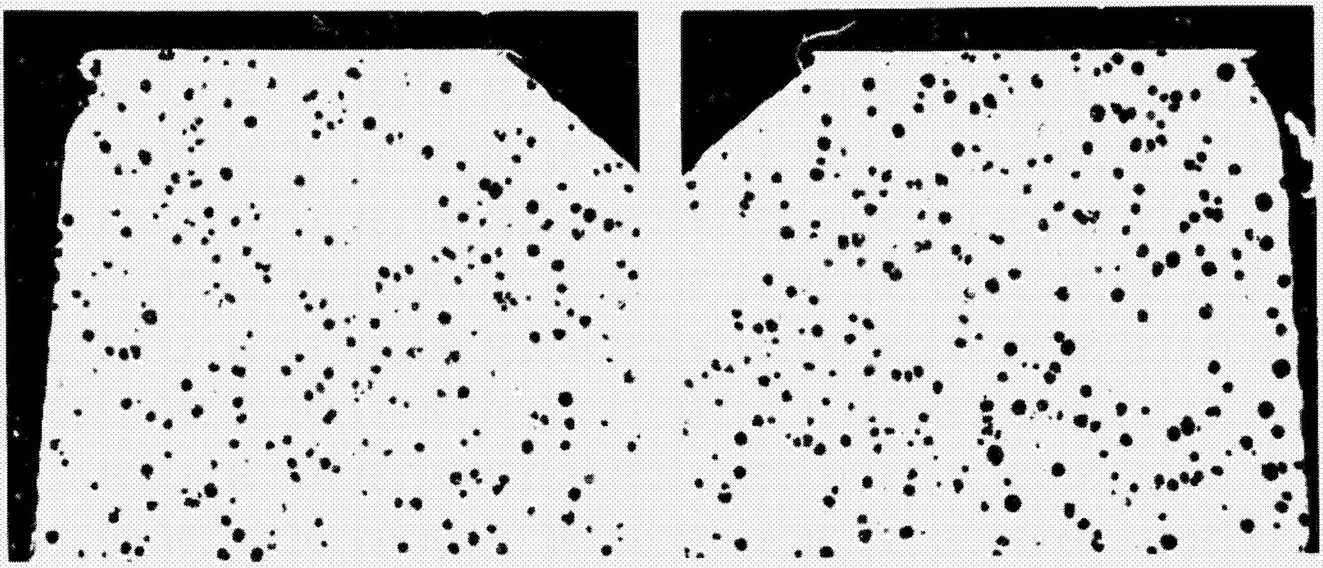

Top Rail 100X Bottom Rail

Heavy abrasive wear caused burrs on the edges of the O.D. rails

This ring is considered to be manufactured from good quality ductile iron. Spheroidal graphite consists of 100% types 1 and 2.

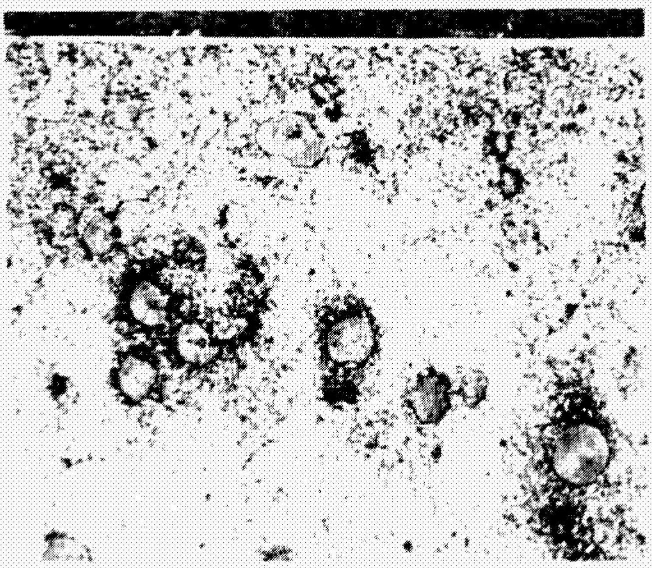

400X

O.D. Surface of Rail

A nital etchant reveals smeared metal on the O.D. rail caused by severe abrasive wear.

The matrix consists of tempered martensite. Hardness is HRC 42-43 within HRC 40-46 specifications for this ductile iron material.

O.D. PRO.ILE TRACES OF COMPRESSION RINGS

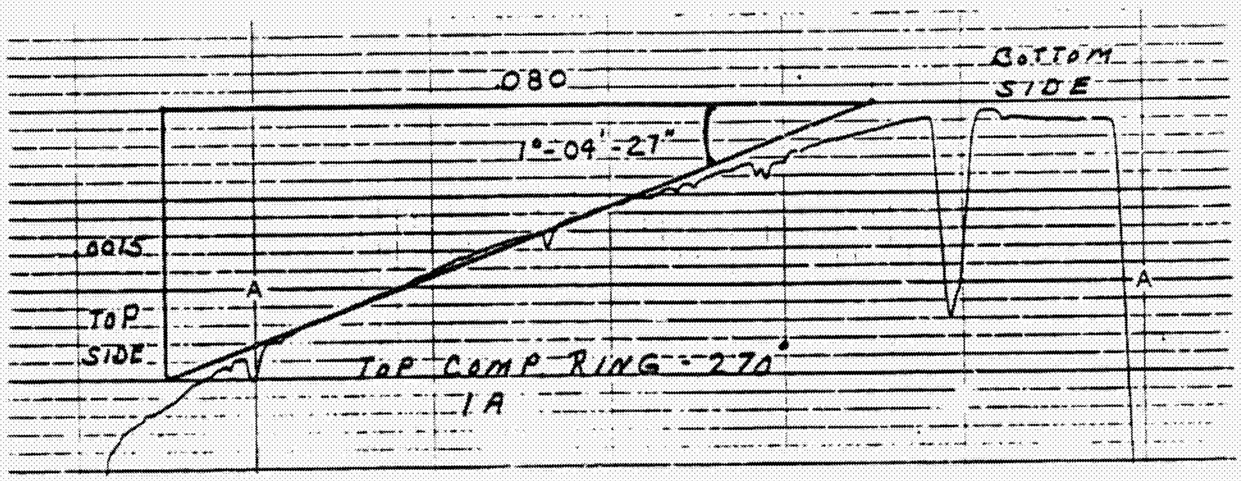

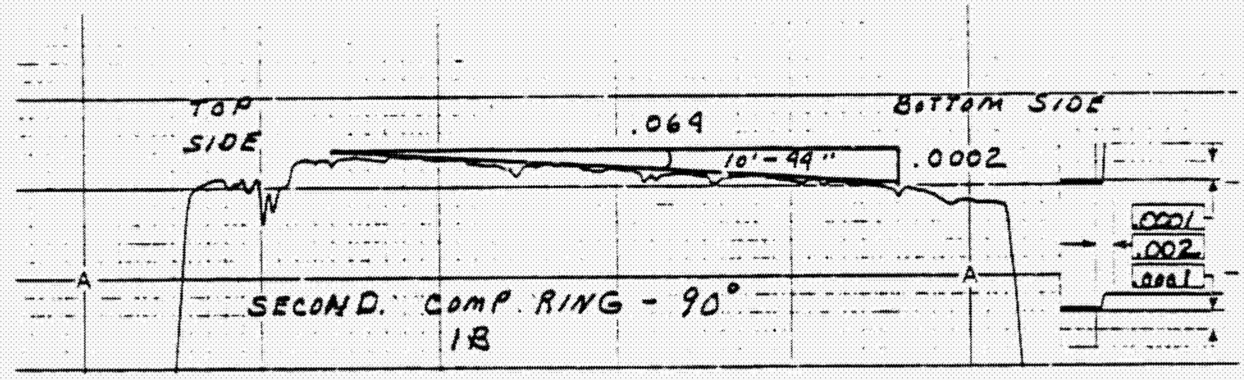

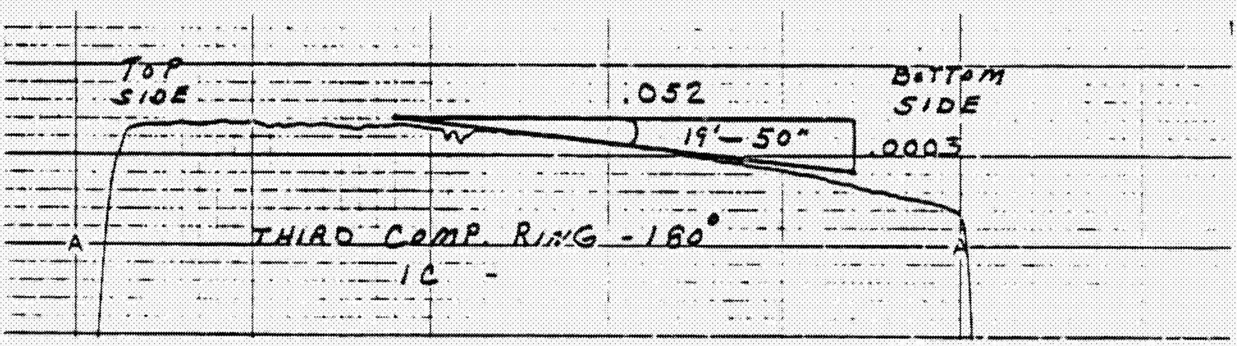

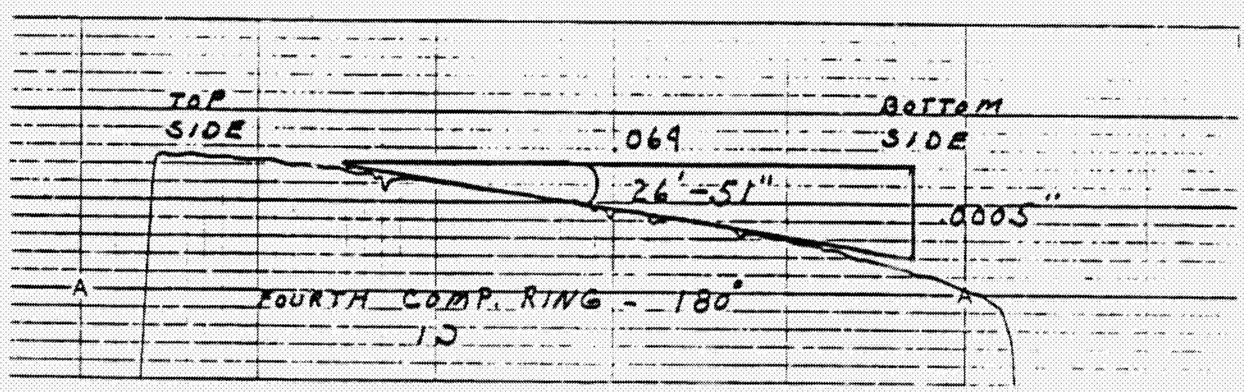

A P P E N D I X   V I I

EVALUATION OF TELEDYNE 4.252" DIAMETER RINGS AND PISTON WITH STEEL CROWN AND ALUMINUM SKIRT

ENGINEERING REPORT #160
December 2, 1984

EVALUATION OF TELEDYNE 4.252" DIAMETER RINGS AND PISTON WITH STEEL CROWN AND ALUMINUM SKIRT

INTRODUCTION

A recent test of Teledyne Continental Motor's 4.252" diameter two cycle diesel engine scuffed after just eight hours of running at half load (45 HP) and 3500 RPM. The cylinder bore was chrome plated. The compression rings were coated with Koppers K-1000F plasma coating. The ring set consisted of part number B7792 in the top groove, part number B7794 in the 2nd and 3rd grooves, part number B7793 in the 4th groove, and part number B7795 in the oil ring groove.

PURPOSE

To determine the cause of scuffing.

CONCLUSIONS

1. A "pinching in" effect of the top ring groove when hot resulted in the top ring standing "proud" causing it to scuff. This "pinching in" effect is caused by the high rate of thermal expansion of the aluminum skirt forcing the bottom side of the steel groove up while at the same time the thermal expansion of the steel crown is forcing the top of the groove down (Figure 7).

2. The piston lands below the 2nd ring and below the 4th ring are distressed reflecting contact with the cylinder liner. This may have contributed to the scuffing of the rings by removing the lubricating oil films from the cylinder liner.

RECOMMENDATION

If the aluminum skirted piston is used again, the top ring side clearance should be increased and the piston lands below the 2nd and 4th rings should be cut back.

DISCUSSION

The scuffing appears to have originated with the top compression ring. This is indicated by the fact that the top ring has the heaviest amount of coating pull-out and the wear measurements show that it experienced the heaviest wear of all the rings (Table 1). There is also evidence that the top ring was not precessing freely in its groove. This is reflected by the very localized carbon staining on the piston land below the top ring (Figure 1) caused by the top ring end clearance dwelling in one place. In addition, the O.D. surface of the ring has several very distinct areas where there is no coating pull-out (Figure 2). The width of these areas (approximately .270") correspond to the width of the port bridges in the liner. This effect, more commonly referred to as port milling, also indicates that the top ring wasn't precessing freely in the groove. Although the top ring wasn't stuck in its groove when removed from the engine, it appears that when the piston is hot the ring becomes stuck in its groove. Examination of the top and bottom sides of the top ring reflect localized areas of unusually heavy wear after just eight hours of running. On the top side of the ring several shiny spots between 180° (from the joint notch) and 270° are indicative of contact with the top side of the groove (Figure 3). On the bottom side, a shiny wear band is evident at the O.D. edge of the ring for 360°. This is generally a desirable condition indicating a good bottom side seal and a front edge bearing condition. However, examination of the bottom side wear pattern under magnification in the same region corresponding to the localized wear noted in the top side of the ring shows that there was heavy plastic deformation and wear of the ring surface (Figure 4). This is clearly illustrated by the profile trace of the bottom side of the ring shown in Figure 5. The .00045" depth of wear near the O.D. is extremely heavy for just eight hours of running. A profile trace of the bottom side away from the region of heavy wear is shown in Figure 6 and is more typical of what is normally seen after eight hours. The piston top ring groove was inspected and found to be within the dimensions allowed by the specification. Also, the width of the top ring was checked and found to be slightly thin in several places (Table 2). This is attributed to the fact that the width of the ring was checked in the region of wear near the O.D. of the ring. These measurements show that the side clearance of the ring in the piston groove was not any less than what was allowed by the design. The calculated mean side clearance according to the nominal values of the design is .0065 and is typically sufficient side clearance for a keystone top ring in a two cycle application. It is suspected that the piston design with a steel crown threaded onto an aluminum skirt results in the top ring groove closing up when hot. It is thought, as illustrated in Figure 7, that as the aluminum skirt expands it forces the bottom side of the top groove up while at the same time the expansion of the crown causes the top side of the groove to close down. This condition would result in a reduction of the ring side clearance such that as the piston rocks over from combustion, the ring could stand "proud" in the groove causing scuffing.

George Sauter

George W. Sauter
KOPPERS COMPANY, INC.
December 2, 1984

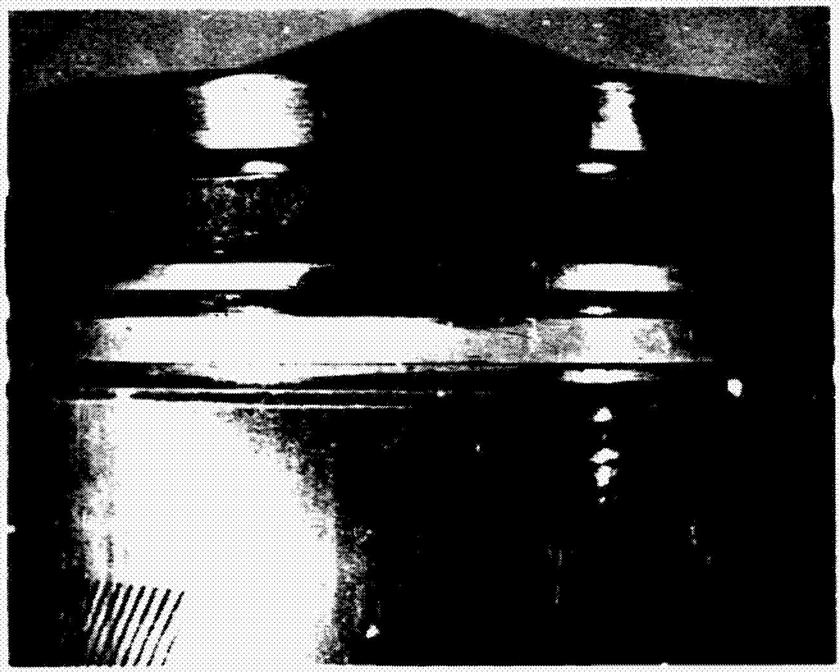

FIGURE 1

Note carbon formation just below the top ring groove and the carbon staining on the aluminum land just above the second ring.

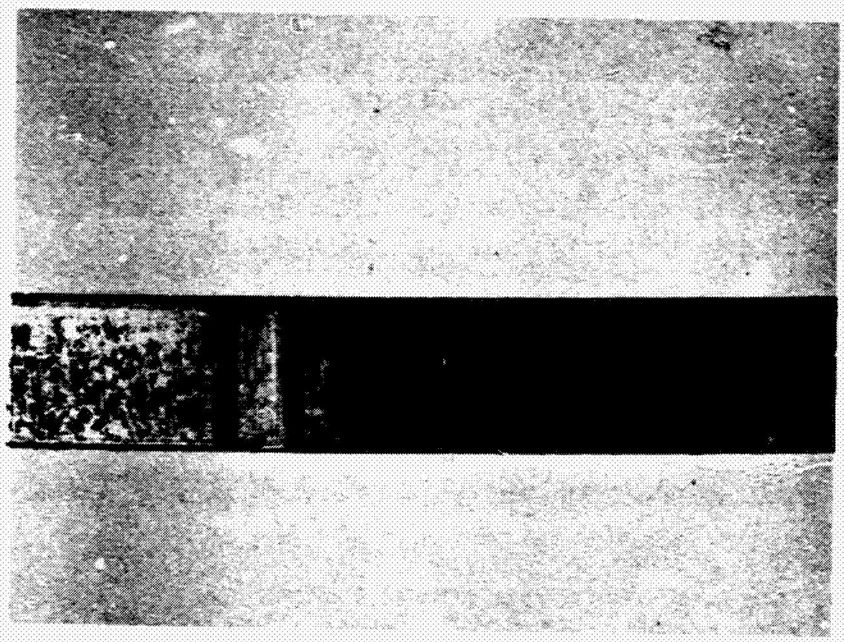

FIGURE 2

Area on O.D. of top ring .270" wide indicative of port milling.

FIGURE 3

Areas on top side of the ring showing contact with the top side of the ring groove.

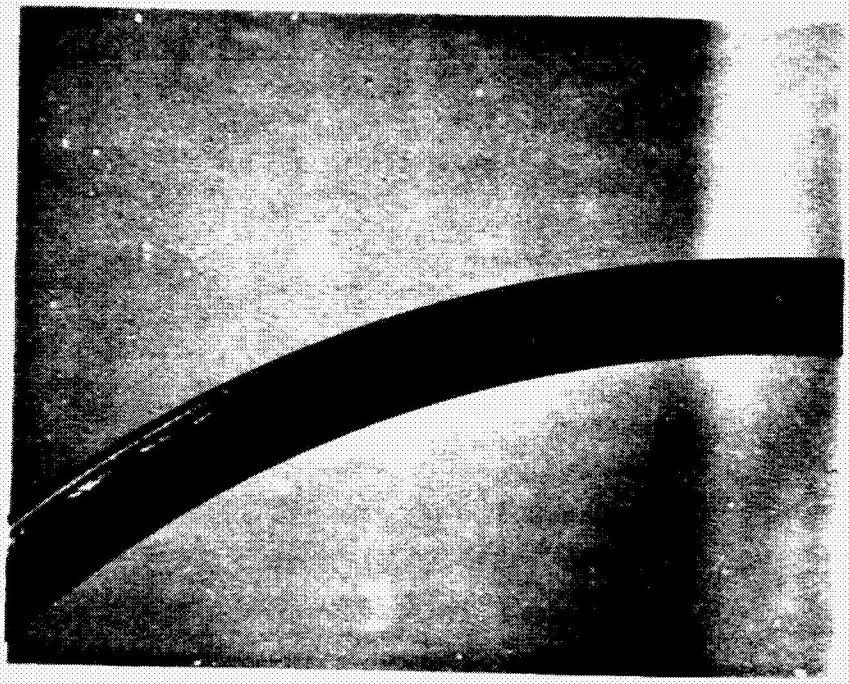

FIGURE 4

Bottom side of ring showing region
at O.D. where heavy wear occurred.

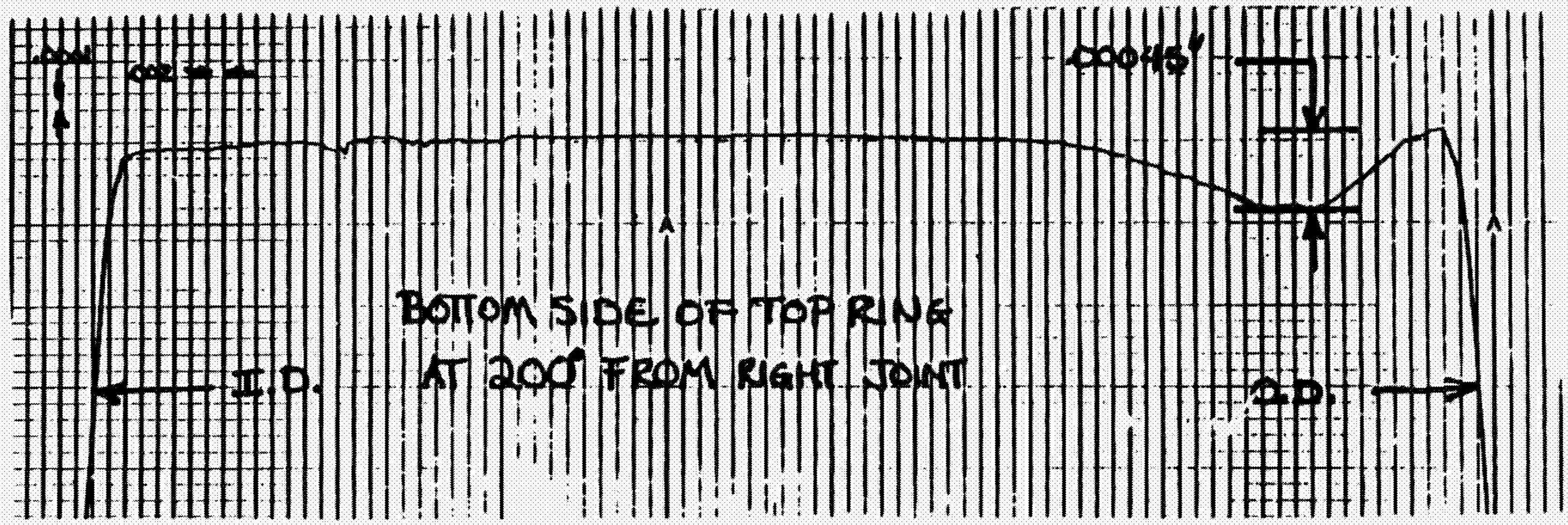

FIGURE 5

Profile trace of bottom side of top ring showing .00045" wear near O.D.

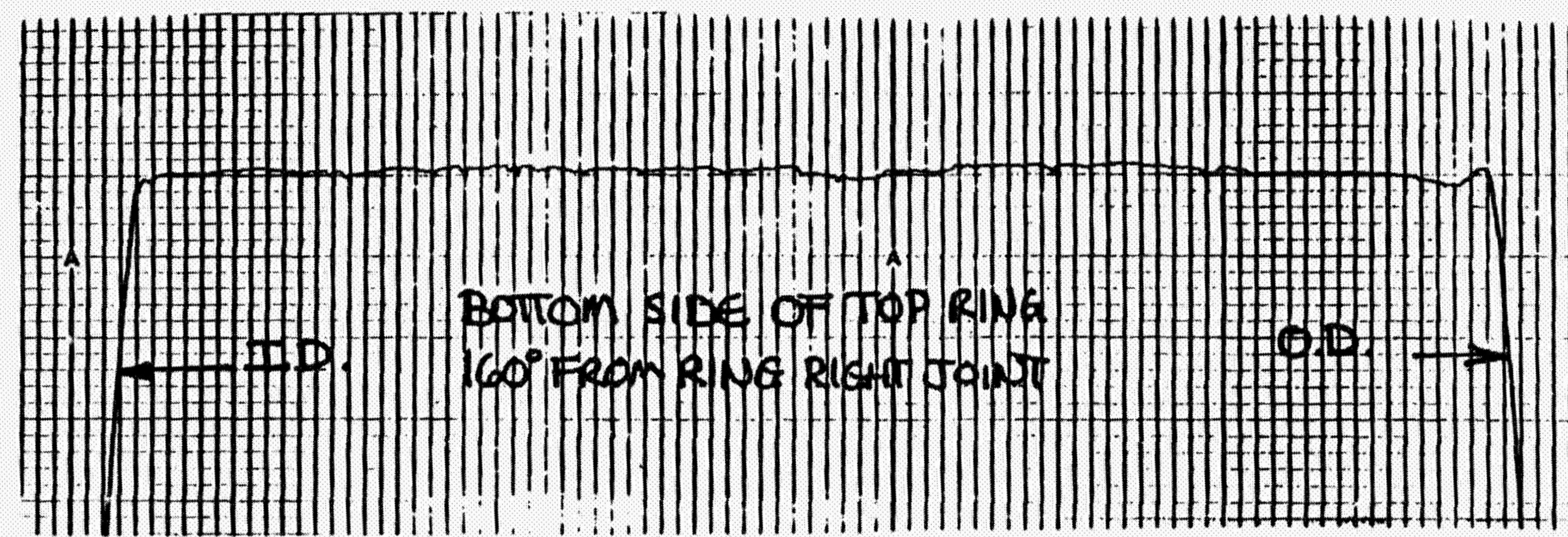

FIGURE 6

Bottom side of top ring showing
no appreciable wear.

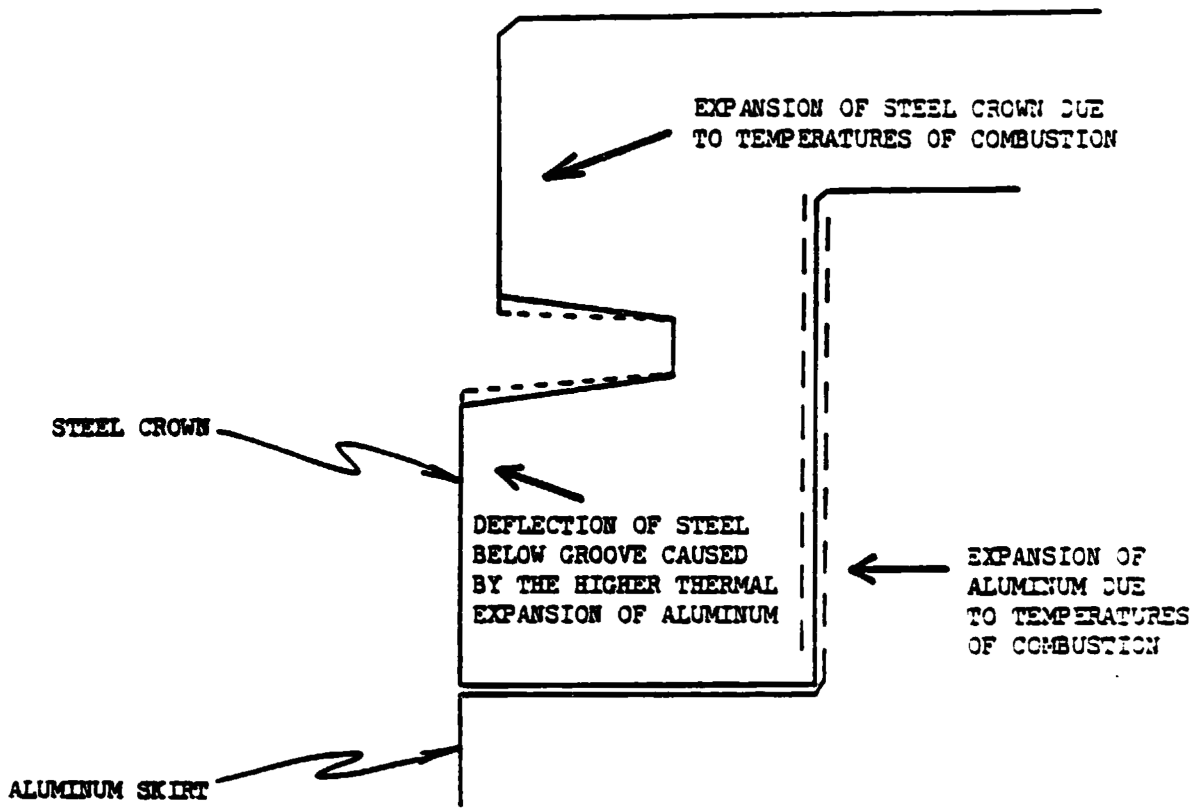

FIGURE 7

Illustration showing the closing
down of the top ring groove due
to thermal expansion.

TABLE 1

RING WEAR

	PART NUMBER	END CLEARANCE BEFORE	END CLEARANCE AFTER	CHANGE IN END CLEARANCE
Top Ring	B7792	.046	.063	.017
2nd Ring	B7794	.038	.042	.004
3rd Ring	B7794	.034	.043	.009
4th Ring	B7793	.020	.025	.005
Oil Ring	B7796	.025	.034	.009

APPENDIX VIII

FUEL AND LUBRICATING OIL SPECIFICATIONS

Engine testing was conducted at the Teledyne Contintental Motors engine laboratories over a period of years. Numerous batches of fuel and oil were used over that time period, and detailed fuel analysis for each batch is not available. Specifications for the fuel and oils used throughout the program include:

FUEL:

1.	Military diesel fuel	VV-F-800B
2.	Commercial jet fuel (Similar to military)	Jet A JP-5

OIL

1.	Military lubricating oil	MIL-L-2104C
2.	Stauffer Oil Company	Propritary Lubricant

The following tables are included for these specifications.

ORIGINAL PAGE IS
OF POOR QUALITY

TABLE I. Physical and chemical requirements

Properties	Values			
	Grade DF-A	Grade DF-1	Grade DF-2: CONUS	Grade DF-2: OCONUS
Gravity, °API	Report	Report	Report	32.9 to 41.0
Flash point, °F(°C) min.	100(37.8)	100(37.8)	125(51.7)	133(56)
Cloud point, °F(°C) max.	-60(-51)	1/	1/	2/
Pour point, °F(°C) max.	Report	Report	Report	3/
Kinematic viscosity @ 100°F.(37.8°C), cSt	1.2 to 2.5	1.4 to 3.0	2.0 to 4.3	1.8 to 9.5
Distillation, °F(°C):				
50% evaporated	Report	Report	Report	Report
90% evaporated, max.	550(288)	550(288)	640(338)	675(357)
End point, max.	572(300)	626(330)	700(371)	700(371)
Carbon residue on 10% bottoms, % wt., max.4/	0.10	0.15	0.35	0.20
Sulfur, % wt., max.	0.25	0.50	0.50	0.70
Copper strip corrosion, 3 hrs. @122°F(50°C) max. rating	3	3	3	1
Ash, % wt., max.	0.01	0.01	0.01	0.02
Water & Sediment, % max.	0.01	0.01	0.01	0.01
Accelerated stability, total insolubles, mg/100 ml, max.5/	1.5	1.5	1.5	1.5
Neutralization number, TAN, max.	0.05	--	--	0.10
Particulate contamination, mg/liter, max.	8	8	8	8
Cetane number, min.	40	45	45	45

1/ See Appendix I for limiting temperature value.

2/ DF-2 destined for Europe and S. Korea shall have a maximum limit of 9°F (-13°C). For other OCONUS areas, the maximum limit must be specified by the procuring activity.

3/ DF-2 destined for Europe and S. Korea shall have a maximum limit of 0°F(-18°C). For other OCONUS areas, the maximum limit must be specified by the procuring activity.

4/ See Appendix II. The maximum limits do not apply for samples containing cetane improvers. In those instances, the test must be performed on the base fuel blend.

5/ This requirement is applicable only for military bulk deliveries intended for tactical, OCONUS, or long term storage (greater than six months) applications (i.e., Army depots, etc.).

TABLE II. - SUMMARIZED DATA FOR GRADE JP-5 MILITARY AVIATION TURBINE FUELS

	1970	1971	1972	1973	1974	1975	1976	1977	1978	1979	1980
Number of fuels	10	10	12	8	7	8	8	7	7	7	5
Gravity, °API	41.0	42.0	41.6	41.7	41.6	41.5	41.5	41.4	41.7	41.2	40.9
Distillation 1/											
Temperature:											
10% recovered, °F	381	380	388	387	389	388	390	385	390	387	381
50% do. , °F	416	414	419	422	419	418	422	420	419	423	422
90% do. , °F	461	459	460	469	462	462	470	470	465	470	476
Recovered at 400 F, %	31.5	36.2	25.0	23.4	23.2	25.9	21.6	24.1	23.6	24.1	24.1
Reid vapor pressure, lb	-	-	-	-	-	-	-	-	-	-	-
Freezing point, °F	-58	-57	-59	-56	-58	-56	-54	-56	-55	-57	-58
Viscosity, kinematic, -30 F, cs	10.2	10.2	10.1	10.5	10.5	9.0	10.2	9.7	7.1	10.4	-
Aniline point, °F	140.0	140.8	139.7	144.6	144.0	142.1	143.3	143.0	142.9	142.5	141.9
Aniline-gravity constant, No.	5,740	5,914	5,714	6,059	5,990	5,840	5,971	5,920	5,959	5,869	5,804
Water tolerance, ml	0.2	0.03	-	-	0.1	0.1	0.3	3/ 0.0	0.5	0.7	2/ 1.0
Sulfur:											
Total, wt %	0.045	0.053	0.037	0.096	0.065	0.061	0.059	0.068	0.057	0.044	0.020
Mercaptan, wt %	0.0004	0.0003	0.0009	0.0007	0.0015	0.0006	0.0004	0.0006	0.0004	0.0003	0.0004
Naphthalenes, wt %	-	-	1.21	-	-	-	-	2/ 1.0	-	2/ 1.0	-
Aromatic content, vol %	15.9	16.4	15.7	16.0	16.0	15.2	16.9	16.0	15.3	16.4	17.4
Olefin content, vol %	1.0	1.1	0.6	0.8	1.0	1.2	0.8	0.9	1.4	0.8	0.6
Smoke point, mm	22.4	22.2	21.7	22.2	22.3	22.9	22.3	22.6	21.8	21.9	20.9
Gum, mg/100 ml:											
Existent, at 450 F	0.5	0.9	1.3	1.3	0.6	1.0	0.8	1.1	1.0	0.7	0.8
Potential, at 212 F	2.2	2.7	2.2	2.6	-	-	2/ 1.0	2/ 1.0	-	-	-
Heat of combustion, net, Btu/lb	18,514	18,534	18,515	18,526	18,539	18,522	18,538	18,533	18,535	18,530	18,525
…uminometer number	44	-	-	-	-	-	2/ 48	2/ 48	-	-	-
Thermal Stability:											
Pressure drop, in. Hg	0.01	0.08	0.14	0.5	0.2	0.16	0.16	0.4	0.3	0.2	0.2
Water separometer index, No.	95	97	96	94	95	94	92	96	95	94	84

1/ Distillation data reported on evaporated basis prior to 1972.
2/ Represents one sample.
3/ Represents two samples.

ORIGINAL PAGE IS
OF POOR QUALITY

TABLE III. - SUMMARIZED DATA FOR GRADE A JET COMMERCIAL JET FUELS

	1970	1971	1972	1973	1974	1975	1976	1977	1978	1979	1980
Number of fuels	57	57	64	65	63	66	65	65	60	60	67
Gravity, °API	42.7	42.8	43.0	42.9	42.9	42.9	43.1	41.2	42.9	42.7	42.6
Distillation 1/											
Temperature:											
10% recovered, °F	371	371	372	369	369	370	37[illegible]	370	374	375	375
50% do. , °F	417	416	415	415	413	414	415	414	416	416	417
90% do. , °F	477	473	474	473	472	472	474	472	473	473	473
Recovered at 400 F, %	34.2	35.6	35.7	36.3	37.2	36.8	35.3	37.6	33.9	34.5	32.3
Reid vapor pressure, lb	0.3	0.2	0.2	0.1	-	0.2	0.2	0.2	-	-	-
Freezing point, °F	-50	-50	-50	-51	-51	-50	-51	-50	-49	-49	-48
Viscosity, kinematic, -30 F, cs	9.45	9.45	9.38	9.12	9.21	9.22	9.32	9.4	9.2	8.8	8.78
Aniline point, °F	144.4	144.1	144.8	143.2	142.6	143.4	144.2	143.6	143.6	142.4	142.1
Aniline-gravity constant, No.	6,166	6,182	6,241	6,143	6,118	6,152	6,244	6,206	6,160	6,072	6,025
Water tolerance, ml	0.2	0.2	0.3	0.5	0.5	0.4	0.5	0.3	0.4	0.6	0.5
Sulfur:											
Total, wt %	0.04?	0.045	0.048	0.045	0.054	0.054	0.060	0.061	0.053	0.050	0.053
Mercaptan, wt %	0.0005	0.0006	0.0004	0.0006	0.0009	0.0008	0.0009	0.0008	0.0007	0.0008	0.0008
Naphthalenes, wt %	1.91	1.85	1.79	1.80	1.82	1.67	1.70	1.70	1.78	1.80	1.99
Aromatic content, vol %	16.4	16.1	16.1	16.3	16.7	16.9	17.0	17.2	17.4	17.9	17.5
Olefin content, vol %	1.1	1.0	1.1	1.2	1.2	1.0	1.1	1.2	1.0	0.9	1.2
Smoke point, mm	23.3	23.4	23.2	23.3	22.9	22.9	23.1	23.1	22.7	22.6	22.5
Gum, mg/100 ml:											
Existent, at 450 F	0.6	0.7	0.8	0.7	0.8	0.9	0.8	0.9	0.8	1.0	1.0
Potential, at 212 F	1.5	1.4	1.6	1.6	1.9	1.9	2.2	1.5	2.3	2.5	-
Heat of combustion, net, Btu/lb	18,586	18,584	18,589	18,583	18,582	18,622	18,609	18,589	18,584	18,598	18,574
Luminometer number	48.9	49	50	49	50	50	50	50	49	49	-
Thermal Stability:											
Pressure drop, in. Hg	0.15	0.21	0.23	0.35	0.33	0.26	0.29	0.3	0.4	0.3	0.2
Water separometer index, No.	95	96	95	95	95	95	96	94	95	95	94

1/ Distillation data reported on evaporated basis prior to 197?

TABLE IV. CHEMICAL AND PHYSICAL REQUIREMENTS AND TEST METHODS

Requirements	Fuel Grade JP-4	Fuel Grade JP-5	Test Method ASTM Standards
Total acid number, mg KOH/g, max	0.015	0.015	D974 1/
Aromatics, vol percent, max	25.0	25.0	D1319
Olefins, vol percent, max	5.0	5.0	D1319
Mercaptan sulfur, weight percent, max 2/	0.001	0.001	D1219 or D1323
Sulfur, total, weight percent, max	0.40	0.40	D1266 or D2622
Distillation temperature, deg F (deg C):			D86 3/
Initial boiling point	4/	4/	
10 percent recovered, max temp	4/	400 (204)	
20 percent recovered, max temp	290 (143)	4/	
50 percent recovered, max temp	370 (188)	4/	
90 percent recovered, max temp	470 (243)	4/	
End point, max temp	4/	550 (288)	
Residue, vol percent, max	1.5	1.5	
Loss, vol percent,	1.5	1.5	
Percent recovered [illegible] °F (204°C)	4/	- -	
Explosiveness, percent, max	- -	50	5/
Flash point, deg F (deg C), min	- -	140 (60)	D93
Gravity, °API, min (sp gr, max)	45.0 (0.802)	36.0 (0.845)	D287
Gravity, °API, max (sp gr, min)	57.0 (0.751)	48.0 (0.788)	D287
Vapor pressure, 100°F, psi (g/cm^2), min	2.0 (140.6)	- -	D323 or D2551
Vapor pressure, 100°F, psi (g/cm^2), max	3.0 (210.9)	- -	D323 or D2551
Freezing point, deg F (deg C), max	-72 (-58)	-51 (-46)	D2386
Viscosity, centistokes at -30°F (-34°C), max	- -	16.5	D445
Heating value, Aniline-gravity product, min or Net heat of	5,250	4,500	D1405
Combustion, BTU/lb, min	18,400	18,300	D240 or D2382
Luminometer number, min	60	50	D1740
or Smoke point, mm, min	- -	19.0	D1322 6/
or Smoke volatility index, min	52.0	- -	7/
Copper strip corrosion, 2 hr at 212°F (100°C), max	1b	1b	D130

TABLE V. - DESCRIPTION OF TEST LUBRICANT

DESCRIPTION	ASTM METHOD NO.	
Specification		MIL-L-2104C
Grade		OE/HDO-30
Properties		
Viscosity, cSt	D 445	
at 99°C(210°F)		11.90
at 38°C (100°F)		120.0
Viscosity Index	D 2270	96
TAN	D 664	2.0
TBN	D 2896	12.0
Flash Point, °F	D 92	440